Section I

Reprints of Published Articles

July 1969-June 1970

EVIDENCE FOR A TENSOR EFFECTIVE TWO-BODY INTERACTION IN THE ^{14}N(p, p') 2.31 MeV EXCITATION

G. M. CRAWLEY, S. M. AUSTIN* and W. BENENSON**
Michigan State University, East Lansing, Michigan 48823, *USA*

and

V. A. MADSEN, F. A. SCHMITTROTH and M. J. STOMP***
Oregon State University, Corvallis, Oregon 97331, *USA*

Received 27 April 1970

The cross section for the excitation of the 2.31 MeV state in ^{14}N by 24.8 MeV protons has been measured. Calculations have been performed with both central and tensor charge exchange forces. Inclusion of the tensor term greatly improves the agreement betweeen the calculated and the experimental angular distribution.

In DWBA studies of nuclear inelastic scattering and charge exchange the microscopic model has enjoyed considerable success and shown much promise as a spectroscopic tool. The usual formulation of the theory includes an arbitrary exchange mixture but uses only a central effective interaction. If one assumes only such central forces, then for the 1^+ ($T = 0$) to 0^+ ($T = 1$) transition in ^{14}N, the normally dominant $L = 0$ contribution to the inelastic scattering cross section should be almost vanishing. This conclusion is based on the fact that the inelastic scattering matrix element is nearly proportional to that for the Gamow-Teller beta decay of ^{14}C which is strongly inhibited [1]. One would therefore expect the $L = 2$ component to dominate the cross section for a purely central effective force.

This same matrix element is involved in the cross section for the ^{14}C(p, n)^{14}N G. S. reaction and therefore in this case there should also be a dominance of the $L = 2$ cross section. However in both the (p, p') reaction discussed here and the (p, n) reaction [2] the $L = 2$ contribution fits the angular distributions poorly.

The nucleus ^{6}Li, with a proton and neutron in the 1p shell, has a similar transition to the one under study in ^{14}N. However the ^{6}He-^{6}Li beta decay is not hindered and the $L = 0$ term dominates the cross section. In this case, the measured inelastic scattering cross section is larger than for ^{14}N and a central force calculation gives a reasonably good fit to the strong forward peak of the angular distribution [3].

One is naturally led to consider the effects of a possible tensor component in the charge-exchange spin-flip interaction. Since tensor forces are known to be important in free nucleon-nucleon scattering and in nuclear structure calculations, it would not be surprising if they are also important in nucleon-nucleus scattering. Such a possibility has been considered by Schmittroth [4] and by Anderson et al. [5], who noted considerable improvement in the calculated angular distribution for ^{14}C(p, n)^{14}N G. S. when the tensor interaction was included.

Charge-exchange scattering occurs in the inelastic scattering through the $\tau_1 \cdot \tau_2$ terms in the interaction. Evidence is presented here that as in the (p, n) reaction the central force is inadequate and that tensor terms must be included.

We give here a brief shetch of the theoretical considerations needed for inclusion of the tensor interaction. A more complete treatment is given in refs. [2, 5].

To the usual central charge exchange

$$V_{01} = [V_\tau(\tau_0 \cdot \tau_1) + V_{\sigma\tau}(\sigma_0 \cdot \sigma_1)(\tau_0 \cdot \tau_1)] f_c(r_{01}) \quad (1)$$

* Alfred P. Sloan Fellow.
** Research supported in part National Science Foundation.
*** Research supported in part by U. S. Atomic Energy Commission.

we add a tensor term

$$V_T(0,1) = V_T[3(\sigma_0 \cdot \hat{r}_{01})(\sigma_1 \cdot \hat{r}_{01}) - \sigma_0 \cdot \sigma_1](\tau_0 \cdot \tau_1) f_T(r_{01}). \quad (2)$$

As the tensor radial form factor we take a "regularized" spherical Hankel function

$$f_T(r) = h_2^{(1)}(i\alpha r) - \left(\frac{\beta}{\alpha}\right)^3 h_2^{(1)}(i\beta r) \quad (3)$$

and for $f_c(r_{01})$ we use a Yukawa form of range α. The first term in eq. (3) is the one-pion tensor form where $\alpha = 0.71$ fm^{-1} and the second term, which we take to have short range of $\beta = 2.0$ fm^{-1}, subtracts out the r^{-3} and r^{-2} singularities in $h_2^{(1)}$ leaving only the r^{-1} singularity. The spherical harmonic expansion of eq. (2) in r_0 and r_1 with $f_T(r_{01})$ given by eq. (3) is continuous with a discontinuous derivative at $r_0 = r_1$, whereas the expansion of eq. (2) with just the first term of eq. (3) is discontinuous. Because the tensor force is a rank-two, parity-conserving tensor operator on space coordinates, there are now two different orbital-angular-momentum transfers: L for the projectile and λ for the nucleus, such that $\lambda = L$, $L \pm 2$. In the absence of spin orbit distortions the cross section is incoherent in L but coherent in λ.

The 35° proton spectrum for the ^{14}N(p, p') reaction is shown in fig. 1. The 2.31 MeV $T = 1$ state, which requires $\Delta T = 1$ is weak compared to other states in the spectrum. All these other states are $T = 0$ and therefore can proceed by the usually dominant $\Delta T = 0$ term in the interaction. In addition these transitions are presumably enhanced by collective effects whereas the $\Delta T = 1$ transitions are probably not. In fig. 2 the experimental differential section for the 2.31 MeV transition is shown along with results of calculations using Visscher-Ferrell wave functions which give cancellation of the beta decay matrix element [6, 7]. The curve labelled "central only" was calculated using a value of $V_{\sigma\tau} = 6.2$ MeV and $\alpha = 0.7$ fm^{-1} which fits other inelastic scattering [8] and (p, n) data [9, 10] in this mass range. The angular distributions calculated with this central force are in poor agreement with the data, and the inclusion of the tensor term in the interaction produces a substantial improvement. The tensor-central mixture used was $V_T = 3.9$ MeV, $V_{\sigma\tau} = 6.2$ MeV for $\alpha = 0.71$ fm^{-1}. The dip at about 150° in the calculated angular distribution remains a persistent feature of the tensor calculation even if the optical potential and tensor radial form are varied.

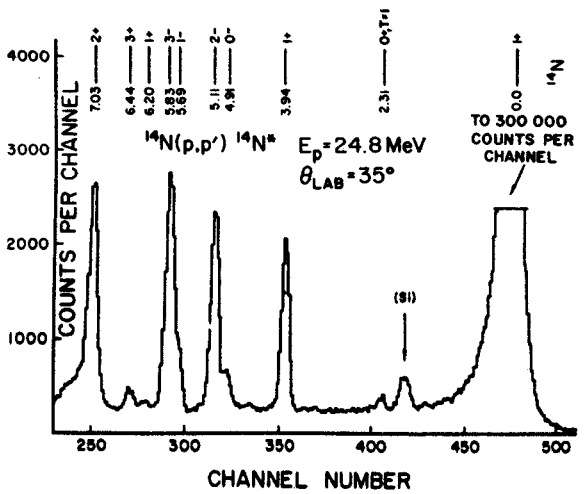

Fig. 1. Spectrum of protons from the ^{14}N(p, p')^{14}N reaction. The peak marked (Si) arises from the excitation of the 1.78 MeV state of ^{28}Si by proton reactions in the solid state detector.

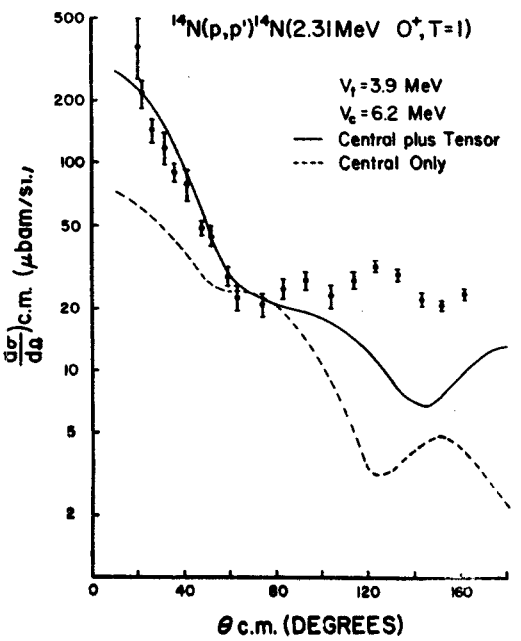

Fig. 2. Angular distribution of inelastic protons which excite the 2.31 MeV state in ^{14}N. The solid line indicates a DW calculation using central plus tensor interaction. The dotted line is the same calculation using the central force only.

It is interesting that the angular distribution produced by the central-tensor mixture resembles neither the $L = 0$ dominated central-force results of using $(1p_{1/2})^2$ configuration nor the $L = 2$ dominated central result of using Visscher-Ferrell wave functions. This is in contrast to the recent discovery by Rost and Kunz [11] that the tensor interaction in (^{3}He, t) transitions to unnatural parity states is characteristic of the central-force angular distribution including only the higher of the two-permitted j-values, thus solving the problem of the L-anomaly [12, 13]. The potential form factor giving rise to the tensor results shown in fig. 2 is predominantly $L = 0$, but it has a very different radial character than a typical central $L = 0$ term due to the regularizing term in eq. (2). The (^{3}He, t) reaction is apparently sensitive only to the asymptotic part of the form factor because of the strong absorption and hence is not significantly affected by the regularizing term.

The strength for the (^{3}He, t) projectile-target nucleon interaction can be calculated from the corresponding (p, n) strength using the results of Wesolowski et al. [14], which can also be applied to the tensor force. The result is $V_T = 5.1$ and $V_c = 8.1$ MeV compared to values [11] of from $V_c = V_T = 6.4$ to 13.6 MeV for various abnormal parity states in ^{54}Co. The results are not particularly sensitive to the tensor-central mixture for our case, since the central $L = 0$ contribution to the cross section is essentially zero, and the tensor $L = 0$ contribution is several times the central-plus-tensor $L = 2$ contribution. The (p, p') tensor strength is in reasonable agreement with the (^{3}He, t) results.

Our (p, p') strength of 3.9 MeV is also near the one-pion strength of 3.7 MeV, although the closeness of the agreement is probably fortuitous since we have not included exchange effects and since the regularized form factor of eq. (3) is slightly weaker than the one-pion form factor.

References

[1] C. A. Levinson and M. K. Bannerjee, Annals of Phys. 2 (1957) 471.
[2] C. Wong et al., Phys. Rev. 160 (1967) 769.
[3] S. M. Austin and G. M. Crawley, Phys. Letters 27B (1968) 570.
[4] F. A. Schmittroth, Oregon State University thesis (1968) unpublished.
[5] J. D. Anderson, C. Wong, V. A. Madsen, F. A. Schmittroth and M. J. Stomp, to be published.
[6] V. M. Visscher and R. A. Ferrell, Phys. Rev. 107 (1957) 781.
[7] H. J. Rose, O. Hausser and E. K. Warburton, Revs. Mod. Phys. 40 (1968) 591.
[8] S. M. Austin, P. J. Locard, W. Beneson and G. M. Crawley, Phys. Rev. 176 (1968) 1227.
[9] A. S. Clough et al., Nucl. Phys. A137 (1969) 222.
[10] J. D. Anderson et al., Phys. Rev. 177 (1969) 1416.
[11] E. Rost and P. Kunz, Phys. Letters 30B (1969) 231.
[12] P. Kossanyi-Demay, P. Roussel, H. Faraggi and R. Schaeffer, to be published.
[13] S. I. Hayakawa, J. J. Kraushaar, P. D. Kunz and E. Rost, Phys. Letters 29B (1969) 327.
[14] J. J. Wesolowski, E. H. Schwarcz, P. G. Roos and C. A. Lundeman, Phys. Rev. 169 (1968) 878.

* * * * *

$^{16}O(p,d)^{15}O$ Form Factors*

B.M. Preedom, J.L. Snelgrove**, and E. Kashy

Cyclotron Laboratory, Michigan State University
East Lansing, Michigan 48823

ABSTRACT

Two methods of obtaining distorted-wave form factors which provide fits to the $^{16}O(p,d)$ reaction are investigated. Both apply a radial damping term to a Woods-Saxon eigenfunction. One method employs a correction for the density dependence of the interaction along with the usual local-energy-approximation correction terms for nonlocality and finite range. The other method applies a simple empirical two-parameter damping term. The calculations are compared with data for $1p_{1/2}$ and $1p_{3/2}$ neutron transfers at energies from 25 to 45 MeV.

---

* Work supported in part by the National Science Foundation.

** Present Address: Argonne National Laboratory
Argonne, Illinois 60439

Reprinted from THE PHYSICAL REVIEW C, Vol. 1, No. 1, 270–275, January 1970
Printed in U. S. A.

Production of the Light Elements Lithium, Beryllium, and Boron by Proton Spallation of ^{12}C†

CARY N. DAVIDS,* HELMUT LAUMER, AND SAM M. AUSTIN
Cyclotron Laboratory, Physics Department, Michigan State University, East Lansing, Michigan 48823
(Received 30 July 1969)

Cross sections for the production of the light elements lithium, beryllium, and boron by proton bombardment of ^{12}C were measured for proton energies between 21.7 and 44.0 MeV. Time-of-flight methods were used to identify the masses of ions recoiling from a thin target into a semiconductor detector. The results are related to current models on the origin of these light elements, and are consistent with a suggestion that the $^{11}B/^{10}B$ isotopic ratio has remained unaltered at its formation value.

I. INTRODUCTION

THE origin of the light elements lithium, beryllium, and boron (LiBeB) is an interesting astrophysical problem. These elements are negligibly present in the sequence of charged-particle fusion reactions which synthesize heavier elements from hydrogen and helium. In addition, they are too fragile to survive the temperatures found in the deep interiors of stars, the site of nearly all the element-synthesizing nuclear processes. It was originally suggested by Fowler *et al.*[1] that the LiBeB isotopes were produced on the surfaces of stars by proton spallation of heavier elements.[2–4] In later articles,[5,6] they expanded this suggestion, and incorporated it into a model for the origin of the planets. In their scheme the site of the spallation reactions was in meter-sized "icy planetesimals," remote from the early sun, but coupled to it by magnetic forces. Protons, originating from surface flares and having a mean energy of 500 MeV, would spiral along the magnetic lines of force and bombard the planetesimals. The LiBeB would be produced primarily from the targets ^{16}O, ^{24}Mg, and ^{28}Si.

In the absence of cross-section data, the authors assumed that the production values of the isotopic ratios $^7Li/^6Li$ and $^{11}B/^{10}B$ were unity. In addition to the LiBeB, large numbers of neutrons would be produced. After thermalization these neutrons would react with ^6Li and ^{10}B, which both have large low-energy neutron cross sections, thus depleting these isotopes and producing the observed terrestrial and meteoritic $^7Li/^6Li$ and $^{11}B/^{10}B$ isotopic ratios of 12.5 and 4.1, respectively.[7]

With the development of mass spectrometric tech-

† Work supported in part by the National Science Foundation.
* Present address: Center for Nuclear Studies, University of Texas, Austin, Tex. 78712.

[1] W. A. Fowler, G. R. Burbidge, and E. M. Burbidge, Astrophys. J. Suppl. 2, 167 (1955).

[2] Recent calculations of big-bang nucleosynthesis (Ref. 3) indicate the possibility of synthesizing ^7Li in a cosmic fireball, but no ^6Li or heavier elements are produced. Computations of nucleosynthesis in exploding objects (Ref. 4) yield ^7Li, ^9Be, ^{10}B, and ^{11}B in addition to heavier elements, but again no observable ^6Li is produced. These two cases do not diminish the importance of the spallation hypothesis, but do provide possible alternative routes for synthesizing *some* of the LiBeB.

[3] R. V. Wagoner, W. A. Fowler, and F. Hoyle, Astrophys. J. 148, 3 (1967).

[4] R. V. Wagoner, Astrophys. J. Suppl. 162, 247 (1969).

[5] W. A. Fowler, J. L. Greenstein, and F. Hoyle, Geophys. J. 6, 148 (1962).

[6] D. S. Burnett, W. A. Fowler, and F. Hoyle, Geochim. Cosmochim. Acta 29, 1209 (1965).

[7] M. Shima, J. Geophys. Res. 67, 4251 (1962); D. Krankowsky and O. Muller, Geochim. Cosmochim. Acta 28, 1625 (1964).

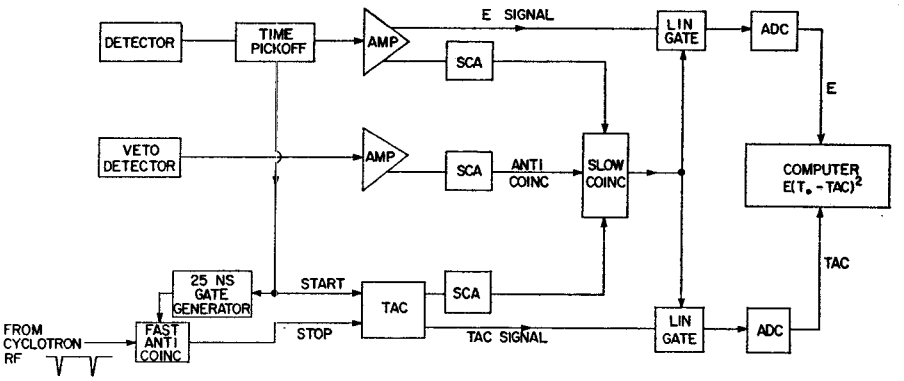

FIG. 1. Block diagram of charged-particle time-of-flight electronics.

niques enabling identification of extremely small quantities of LiBeB isotopes,[8] the Orsay mass spectrometry group was able to begin measuring spallation cross sections in ^{12}C and ^{16}O at several energies.[9,10] On the basis of their experimental results and studies of the systematics of spallation reactions, they formulated a different theory of the origin of LiBeB.[11] They suggested that each star produces LiBeB in the stellar atmosphere by proton spallation of the abundant elements ^{12}C, ^{14}N, ^{16}O, and ^{20}Ne. In their scheme the solar system ^{11}B/^{10}B ratio remains unchanged from its formation value, but the ^{7}Li/^{6}Li ratio has increased from the production value of about 2.5 to its observed value of 12.5. This change is ascribed to (p, α) reactions on ^{6}Li at temperatures which would be found near the bottom of the convection region of the primitive sun. Under these conditions the isotopes ^{7}Li, ^{9}Be, ^{10}B, and ^{11}B are depletedonly negligibly. Thus the need for neutrons to deplete ^{6}Li and ^{10}B is removed, and the site of the LiBeB production is placed in the stellar atmosphere. The presence of icy planetesimals is not essential to their theory, thereby relaxing the requirement of high energy for the bombarding protons.

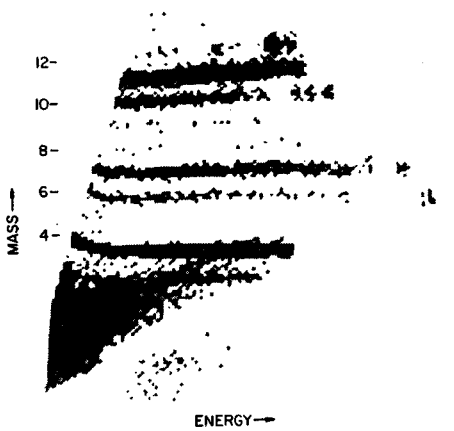

FIG. 2. Computer oscilloscope display of ET^2 (mass) versus E, showing mass bands.

Experimental proton spallation cross sections for LiBeB are required to test the validity of the various approaches. In particular, knowledge of the ^{11}B/^{10}B formation ratio should enable one to choose between the speculations outlined above. The targets of interest are ^{12}C, ^{14}N, ^{16}O, ^{20}Ne, ^{24}Mg, and ^{28}Si, while proton energies from threshold to somewhat below 100 MeV are most important for the production of LiBeB. The observed steep energy behavior of the proton flux from solar flares ($\sim E^{-4}$) markedly reduces the contribution from protons with higher energies.

The available data on production cross sections have recently been reviewed.[12] Most of the cross sections have been measured by radioactivity and mass spectrometric techniques. Little information is available on the production of ^{9}Be, ^{10}B, and ^{11}B, particularly for energies below 100 MeV.

A program has been initiated in this laboratory to measure spallation cross sections relevant to the production of LiBeB. The $A=10$ and $A=11$ data have been reported in Ref. 13. Reported here are the results on production of isotopes with $6 \leq A \leq 11$ from a target of ^{12}C, for proton bombarding energies between 21.7 and 44.0 MeV.

II. EXPERIMENTAL METHOD

The techniques that have been used for measuring spallation cross sections, namely, radioactivity and mass spectrometry, each suffer from the disadvantage of not being equally sensitive to all isotopes simultaneously. The determination of a total production cross section by the usual methods of nuclear physics involves measuring the angular distribution of the reaction products and integrating this quantity over all angles. In order to apply this method to the present problem, it is neces-

[8] E. Gradsztajn, M. Epherre, and R. Bernas, Phys. Letters 4, 257 (1963).
[9] R. Bernas, M. Epherre, E. Gradsztajn, R. Klapisch, and F. Yiou, Phys. Letters 15, 147 (1965).
[10] F. Yiou, M. Baril, J. DuFaure de Citres, P. Fontes, E. Gradsztajn, and R. Bernas, Phys. Rev. 166, 968 (1968).
[11] R. Bernas, E. Gradsztajn, H. Reeves, and E. Schatzman, Ann. Phys. (N.Y.) 44, 426 (1967).
[12] J. Audouze, M. Epherre, and H. Reeves, in *High-Energy Nuclear Reactions in Astrophysics*, edited by B. S. P. Shen (W. A. Benjamin, Inc., New York, 1967), p. 255.
[13] C. N. Davids, H. Laumer, and S. M. Austin, Phys. Rev. Letters 22, 1388 (1969).

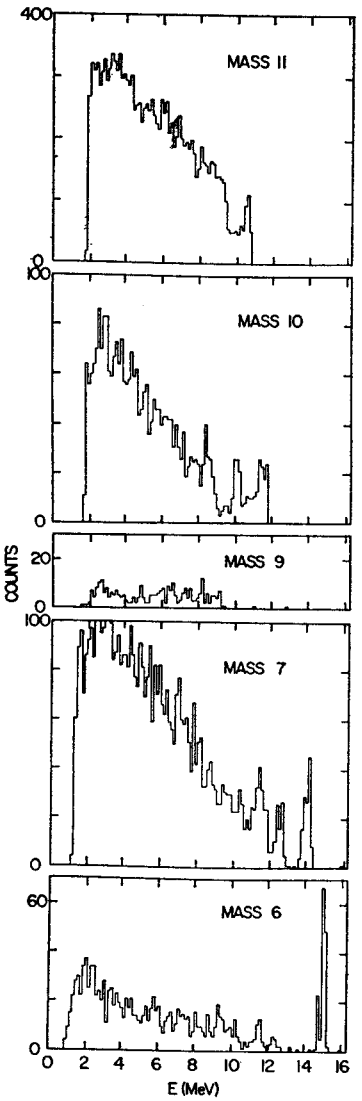

FIG. 3. Energy spectra of the various masses following the bombardment of ^{12}C by 39.8-MeV protons. The detector angle was 15° from the beam direction.

sary to ensure that (1) the target used is thin enough to allow the ions to emerge from it and proceed to the detector and (2) the detection system is able to identify and separate the isotopes of interest.

The first requirement is satisfied by a ^{12}C target with thickness less than about 100 $\mu g/cm^2$; the maximum energy lost by a recoiling particle is then less than 0.65 MeV, this loss occurring for a 4.4-MeV ^{11}C ion.

Particle identification can be accomplished in several ways. Two semiconductor counters in series, acting as energy loss (ΔE) and stopping (E) detector, respectively, can separate the various ions by mass and charge. However, ions stopping in the front detector cannot be identified. Because a large number of the heavier fragments produced by spallation have low energy, this is a serious limitation.

A second method, which avoids this difficulty, is to measure the total energy (E) and the time-of-flight (T) of each ion as it stops in a single detector. Such a measurement gives the particle mass (M), through the relation $ET^2=MD^2/2$, where D is the flight distance between target and detector. Knowing the mass turns out to be sufficient for the present purpose, as is explained in Sec. III below. Only the sensitivity of the time measurement circuit connected to the detector sets the lower energy limit. In addition, the system can be made insensitive to elastically scattered protons and other energetic light particles by proper choice of detector thickness.

A knowledge of the precise time that the ion left the target is required in order to apply this method. Such information is readily available using a pulsed beam, and the narrow ($\lesssim$0.2 nsec) burst width of the proton beam from the MSU sector-focused cyclotron is eminently suited to such a precise timing application. For all these reasons, the ET^2 particle identification method was chosen for this experiment.

Thin self-supporting ^{12}C targets were made by dipping a glass slide into a colloidal graphite suspension, allowing it to dry, and floating off the resulting thin films on water. Typical targets had thicknesses between 65 and 80 $\mu g/cm^2$, with less than 6% oxygen contamination. The target thickness was measured by comparing the elastic scattering yield from the unknown with the yield from a thick target. The thick target, in turn, was measured by an α-particle thickness gauge and also by weighing. An over-all uncertainty of $\pm 10\%$ due to the target thickness measurement has been assigned to the absolute cross sections.

A block diagram of the electronics is shown in Fig. 1.

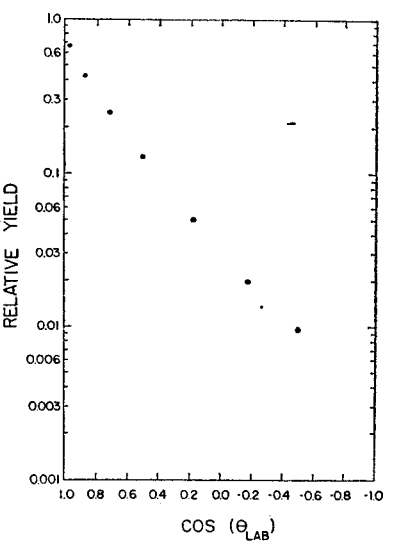

FIG. 4. Angular distribution of mass-7 particles measured at 39.8-MeV bombarding energy. The abscissa is $\cos\theta_{lab}$, so that the area under the curve is a measure of the total cross section. It is clear that the extrapolations to 0° and 180° introduce very little error.

A fast timing signal was derived from the fully depleted surface-barrier detector by means of an Ortec model 260 time pickoff. Cooling the detector with a dry ice and alcohol system resulted in improved time response. The dead layer of the detector caused energy losses for the heaviest ions which did not exceed 0.1 MeV. Detectors of thickness 78 and 68 μm were used, depending on the proton bombarding energy, with flight distances of the order of 28 cm. The time-to-amplitude converter (TAC) was started by a signal from the detector, and stopped by the next rf pulse from the cyclotron. This caused the time spectrum to be inverted, i.e., to be proportional to the quantity T_0-T, where T_0 is a constant, but ensured that the TAC was busy only for a real event. In addition, a fixed time of approximately 25 nsec was electronically added to each time interval measured, so that only the linear portion of the TAC was utilized. Maximum flight times between 52 and 72 nsec were determined by the cyclotron rf period at the various bombarding energies. This imposed a lower limit on the observable energies for the heavier masses, which fell between 1 and 2 MeV for the $A=11$ ions. The lower limit for ^{6}Li was set by the sensitivity of the time pickoff, and was typically 0.8 MeV. The veto counter caused the rejection of any particle which passed through the front detector.

The two signals E and TAC were digitized and sent to the Sigma-7 computer. Here, by means of the general-purpose code TOOTSIE,[14] the quantity $E(T_0-\text{TAC})^2$ was computed on line. This quantity is proportional to ET^2 for the correct value of T_0 and, when displayed versus E, causes the different masses to fall in bands. The parameter T_0 is adjusted by teletype input until the bands appear approximately horizontal on the display. A typical display of ET^2 versus E is shown in Fig. 2. The size of this array is 128×128 channels.

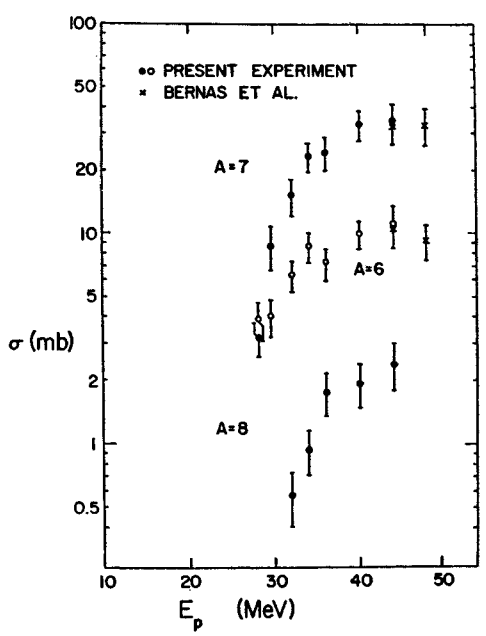

FIG. 5. Production cross sections of masses 6–8 from proton spallation of ^{12}C. The error bars represent the total uncertainty.

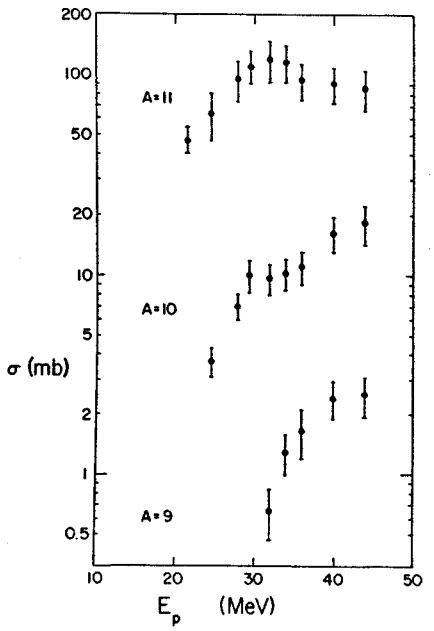

FIG. 6. Production cross sections of masses 9–11 from proton spallation of ^{12}C. The error bars represent the total uncertainty.

Using such a two-dimensional display, a given mass band can be outlined by computer-generated curves placed between the bands, and the events lying between two curves are projected on the E axis. In this way, energy spectra for all the masses of interest can be obtained. Figure 3 show spectra taken at a proton energy of 39.8 MeV, with the detector at an angle of 15° to the beam.

The peaks appearing in some of the spectra are due to reactions involving only two bodies in the final state, with the possibility that the detected particle and also the residual nucleus can be left with excitation. Only particle-stable states of the ion of interest will be observed, and all γ decays occur before the particle reaches the detector. These two-body reactions only account for a small percentage of the total yield for each isobar.

In general, the reactions proceed through multibody channels; the continuum in the energy spectrum is caused by the superpostion of yields from multibody final states of differing total energies, e.g., the mass-11 yield is due to the reactions ^{12}C$(p, d)^{11}$C, ^{12}C$(p, pn)^{11}$C, and ^{12}C$(p, 2p)^{11}$B, where in each case the ^{11}C and ^{11}B ions can be left in the ground state or in any of their particle-stable excited states. For the latter two reactions this means that the three-body system can emerge with eight or nine values of total kinetic energy. The sum of the many three-body distributions causes the spectrum to be peaked at low energy, but it must

[14] D. Bayer (private communication).

TABLE I. Production cross sections from proton spallation of ^{12}C.

E_p (MeV)	$\sigma(6)$ (mb)	$\sigma(7)$ (mb)	$\sigma(8)$ (mb)	$\sigma(9)$ (mb)	$\sigma(10)$ (mb)	$\sigma(11)$ (mb)
21.7	...	...	...	...	...	45±7
24.6	...	...	...	...	3.7±0.6	64±17
28.0	3.9±0.8	3.2±0.6	...	...	7.0±1.1	96±22
29.5	4.0±0.8	8.7±2.1	...	...	10.0±1.8	113±20
32.0	6.3±1.0	15.2±3.0	0.6±0.2	0.7±0.2	9.7±1.7	121±28
34.0	8.6±1.4	23.2±3.7	0.9±0.2	1.3±0.3	10.2±1.8	116±25
36.0	7.2±1.1	24.1±4.2	1.8±0.4	1.7±0.4	11.1±2.1	95±21
39.8	9.9±1.5	33.1±5.4	1.9±0.5	2.4±0.5	16.3±3.3	91±18
44.0	11.2±2.2	34.4±6.6	2.4±0.6	2.5±0.6	18.4±4.1	87±20

have the value zero at zero energy. This is because the Jacobian of the transformation from c.m. to laboratory coordinates is equal to the ratio $p/\bar{p}$, where p and $\bar{p}$ are the momenta in the laboratory and c.m. systems, respectively. In the spectra of Fig. 3, the peaking at low energies and down-turn toward zero at zero energy are evident for all masses except for mass 9. This unique case ^9Be is probably produced via the reaction $^{12}C(p, p^3He)^9Be$, which has only one open three-body channel. Thus no low-energy peak is expected.

Spectra were accumulated at seven or eight angles, ranging between 15° and 120° for the higher bombarding energies, and to smaller back angles for lower-energy runs. Angular distributions were measured at proton bombarding energies of 44.0, 39.8, 36.0, 34.0, 32.0, 29.6, 28.0, 24.6, and 21.7 MeV, as determined by the beam transport system analyzing magnets. For each run the product of target thickness and incident charge was normalized by means of a fixed monitor counter, which measured the protons elastically scattered from ^{12}C.

The individual energy spectra at each angle were extrapolated to zero energy in order to obtain the total yield. Allowance for the missing portions has been made by adding to the observed totals a representative average number of counts per channel for the energies below the low-energy cutoff. At each angle, half of the resulting contribution to the total cross section has been assigned as a conservative uncertainty. Added together, these errors account for most of the 15–30% uncertainty quoted for the final absolute cross sections. In all cases, the yields decreased rapidly as the detector was moved to back angles. Figure 4 shows a typical angular distribution, in this case measured for the mass-7 particles at 39.8 MeV. Extrapolation of the angular distributions to 0° and 180° produced an additional small uncertainty in the final result.

The experimental angular distributions were converted to absolute cross sections using the known solid angle, target thickness, and charge accumulation. A Faraday cup was used to provide the relation between incident charge and elastic yield as determined by the monitor counter.

III. RESULTS AND DISCUSSION

The total cross sections obtained from these measurements are given in Table I, and shown in Figs. 5 and 6, plotted against proton bombarding energy. Included are the mass spectrometry measurements of Bernas *et al.*[9] on mass-6 and mass-7 production in this energy region. Our results show good agreement with the mass spectrometry results where the two overlap.

For our proton bombarding energies, the mass-6 particles are ^6He and ^6Li. The mass-7 particles are ^7Li and ^7Be, while ^8B and ^9Be make up masses 8 and 9, respectively. Mass 10 consists of ^{10}Be, ^{10}B, and ^{10}C, with ^{11}B and ^{11}C comprising the mass-11 yield. It should be noticed that there is only one stable isobar for each mass (except for mass 8, which has none), and the radioactive isobars decay rapidly to it on an astrophysical time scale.[15] Thus for our purposes, a mass measurement is sufficient, and (mass 6)$\equiv^6Li$, (mass 7)$\equiv^7Li$, (mass 9)$\equiv^9Be$, (mass 10)$\equiv^{10}B$, and (mass 11)$\equiv^{11}B$.

A calculation of the abundances and isotopic ratios of the LiBeB elements produced by spallation could in principle be carried out. What is required are the experimental production cross sections as a function of energy, the abundances of the targets involved, and knowledge of the proton spectrum at the stellar surface. The results of such a calculation, when compared with the observations, would serve as a basis for determining whether or not other nuclear processes have been involved in the history of these elements. Fractionation, weathering, and other chemical effects must also be considered.

On the other hand, the isotopic ratios by themselves serve to provide information on the unique nuclear history of the LiBeB elements, since these ratios are unaffected by chemical processes.

From Fig. 5, it is seen that the production of ^{11}B from ^{12}C far exceeds that of ^{10}B. Using these cross sections and a proton spectrum varying as E^{-4}, a calculated $^{11}B/^{10}B$ ratio of about 8 is obtained for ^{12}C.

[15] Although ^{10}Be could be considered stable with its half-life of 2.7×10^6 yr, its production rate is expected to be negligible compared with the total mass-10 yield (Refs. 10, 11).

For the over-all $^{11}B/^{10}B$ ratio, one must consider the production of ^{11}B and ^{10}B separately from all the targets, weighted by the appropriate abundances. The solar photospheric abundances of the important targets ^{12}C, ^{14}N, and ^{16}O are in the approximate ratios 3:1:5.[16] Because of differing values of production thresholds, each of these three targets might be expected to contribute about equally to the formation of ^{11}B and ^{10}B. Preliminary values obtained in this laboratory for the $^{11}B/^{10}B$ ratios at 35 MeV for ^{14}N and ^{16}O are 0.5 and 8, respectively. Below 12 MeV only ^{11}B is produced from ^{14}N, via the $^{14}N(p, \alpha)^{11}C$ reaction. These results are consistent with the suggestion of Bernas *et al.*[11] that the solar system $^{11}B/^{10}B$ formation ratio has not been altered by subsequent nuclear processes.

The low value of the ^{9}Be production cross section is not surprising, in view of the fact that this nucleus has only one particle-stable state, compared to the nine or so states available in ^{11}B and ^{11}C. In addition, the formation of ^{9}Be via the direct $(p, p^{3}He)$ reaction is expected to depend strongly on the probability of finding ^{3}He clusters in the target nucleus, a situation likely to occur only infrequently.

Production of ^{7}Li from ^{12}C exceeds that of ^{6}Li by a factor of 2–3, in agreement with the estimates of Barnas *et al.*[11] A large $^{7}Li/^{6}Li$ ratio near threshold was not observed. Such a large ratio might have made it possible to explain the terrestrial and meteoritic $^{7}Li/^{6}Li$ ratio if, in addition, a spectrum of protons with energies extending only to about 25 MeV were postulated. The necessity of a secondary process to explain the terrestrial $^{7}Li/^{6}Li$ ratio remains, the most likely candidate being the $^{6}Li(p, \alpha)$ reaction. Slow neutrons do not seem to be the answer, since they would increase the $^{11}B/^{10}B$ ratio further.

Further measurements of proton spallation cross sections for LiBeB production from ^{14}N, ^{16}O, and heavier targets, as well as additional measurements on ^{12}C at higher energies, are required. It is hoped that such results will soon be available, enabling a better understanding of the origin of lithium, beryllium, and boron

[16] E. A. Muller, in *Origin and Distribution of the Elements*, edited by L. H. Ahrens (Pergamon Press, Oxford, 1968), p. 155.

NUCLEAR INSTRUMENTS AND METHODS 75 (1969) 109–112; © NORTH-HOLLAND PUBLISHING CO.

A SINGLE CRYSTAL Ge(Li) CONVERSION-COEFFICIENT SPECTROMETER

C. R. GRUHN, R. R. TODD, C. J. MAGGIORE and W. H. KELLY

Cyclotron Laboratory, Department of Physics, Michigan State University, East Lansing, Michigan* 48823, *U.S.A.*

R. E. DOEBLER and Wm. C. McHARRIS

Department of Chemistry† and Cyclotron Laboratory, Department of Physics, Michigan State University, East Lansing, Michigan* 48823, *U.S.A.*

Received 27 May 1969

We discuss the design and operation of a conversion-coefficient spectrometer in which a single small Ge(Li) crystal serves as the detector both for γ-rays and conversion electrons. We show a calibration curve for our detector and discuss both its advantages and faults as compared with a spectrometer that uses separate detectors for γ-rays and electrons.

1. Introduction

The impact of lithium-drifted germanium detectors on the field of γ-ray spectroscopy is well known, and now these detectors are being used to a greater extent to measure other radiations as well. In this laboratory, for example, they are used more or less routinely for the high-resolution detection of inelastically-scattered protons[1]). Also, recently several experimenters have noted the presence of conversion electrons in low-energy X-ray spectra observed with thin-window detectors[2]). A number of excellent "conversion-coefficient spectrometers" of the type developed by Easterday, Haverfield, and Hollander[3]) are now in use. These consist of a Ge(Li) detector for γ-rays used in conjunction with a Si(Li) detector for measuring the accompanying conversion electrons. By mounting the detectors and sources in fixed positions and calibrating the ensemble with well-known conversion standards, later measurements can be made in a very straightforward manner.

In this paper we explore the feasibility of using a small Ge(Li) detector in a thin-windowed mount to measure γ-ray and electron intensities simultaneously and consequently serve as a single crystal conversion-coefficient spectrometer. There are several advantages to such a system, principally in the fact that it uses fewer electronics and only one analyzer. (The Ge(Li)-Si(Li) system can use one analyzer by measuring γ-rays and electrons sequentially, but then live-time and half-life corrections become more cumbersome.) Also, a single efficiency curve can be made for the single-crystal Ge(Li) spectrometer, one that contains information about both γ-ray and electron intensities. (This is possible because the electron efficiency curve is a slowly varying function of energy.) Finally, the single-crystal spectrometer is potentially a powerful tool for coincidence experiments involving another detector because it would often mean the difference

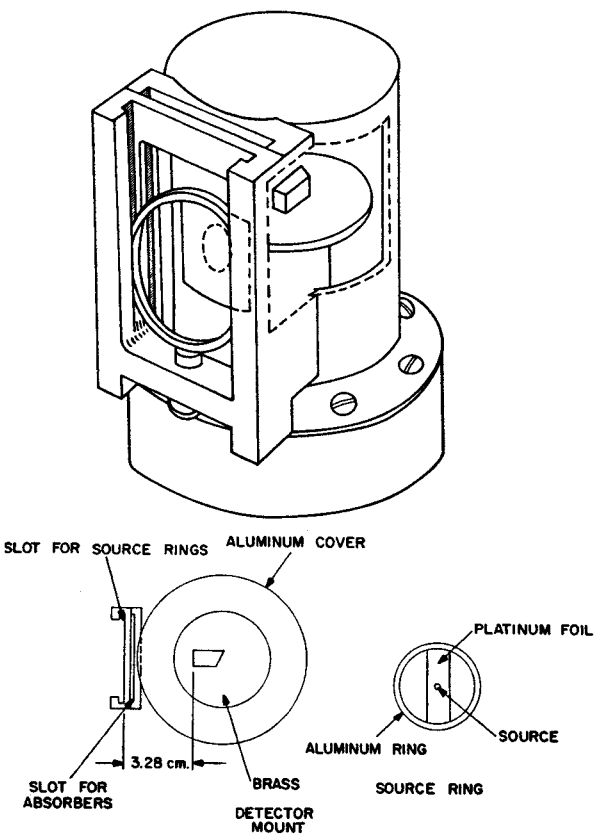

Fig. 1. Small Ge(Li) detector mounted in a dipstick cryostat having a 0.25-mil Havar foil window to permit the detection of γ-rays and conversion electrons simultaneously.

* Work supported in part by the U.S. National Science Foundation and by the National Aeronautics and Space Administration.

† Work supported in part by the U.S. Atomic Energy Commission.

between a double and triple coincidence or, again, sequential experiments. For short-lived, difficult-to-make nuclides, this can be important. Disadvantages of such a device are source strength, i.e., the detectors are necessarily small, so strong sources are required, and the straggling experienced by the electrons in passing through the window, which must be accounted for in stripping out the data and which affects the background of the spectra as a whole. In particular, the straggling makes it very difficult to separate the L and M electron peaks because of their small energy difference and large overlap. There also appears to be no single optimum size of detector to cover all energy regions, so one would be compelled to have an assortment of sizes.

2. Experimental apparatus

The particular detector used in these experiments, originally designed as a proton detector, was manufactured in this laboratory from Ga-doped Ge. The source material was an ingot of $\approx$ 16-ohm · cm, horizontally-grown Ge (Hoboken), with an etch-pit density of 700/cm^2 and a carrier lifetime of 400 μsec. The Li diffusion and drift techniques used were the standard ones reported in the literature. The resulting detector was a planar drift device with a drift depth of $\approx$ 7 mm and an active volume of $\approx$ 0.4 cm^3. It was mounted in a conventional dipstick cryostat having a window of 0.25-mil Havar foil. The orientation of the detector and source is indicated in fig. 1. Side entry geometry was used. When it was used with a Canberra 1408C room-temperature FET preamplifier and 1417 linear amplifier with pole-zero compensation, we obtained a resolution of 1.8 keV fwhm for the ^{137}Cs 661.6-keV γ.

The relative efficiencies were found to depend sensitively on source shape and position. To insure uniform reproducibility, the sources were vaporized through 3-mm dia. masks onto 0.25-mil Pt foil backings. These were mounted on Al rings machined to fit into the slot shown in fig. 1. The rings were positioned vertically by means of a simple screw at the base of the mount. Initially the screw was adjusted to optimize the vertical source position in front of the detector in order to minimize the outscattering of electrons caused by the small solid angle presented to the source by the detector. The source holder was made of brass with a slot to contain the rings, and all excess brass was removed to reduce the amount of brass in the vicinity of the source. The source holder was positioned on the detector with a strap encircling the can and fixed in place after being centered horizontally about the window.

3. Performance characteristics

The efficiency of the detector was calibrated by using well-known standards whose conversion coefficients had been determined precisely. These are listed in table 1. In addition, an efficiency curve was obtained

TABLE 1

Conversion coefficient calibration standards.

Nuclide	γ-energy	Multi-polarity	α_K experimental	Ref.	α_K theoretical[8]
^{113}Sn	391.7	M4	$4.38 \pm 0.08 \times 10^{-1}$	4)	4.48×10^{-1}
^{134}Cs	795.8	E2	$2.46 \pm 0.30 \times 10^{-3}$	5)	2.58×10^{-3}
^{134}Cs	1365	E2	$6.8 \pm 0.5 \times 10^{-4}$	5)	8.19×10^{-4}
^{137}Cs	661.595	M4	$8.94 \pm 0.10 \times 10^{-2}$	6)	9.28×10^{-2}
^{207}Bi	569.6	E2	$1.56 \pm 0.07 \times 10^{-2}$	7)	1.59×10^{-2}
^{207}Bi	1064	M4	$9.0 \pm 0.9 \times 10^{-2}$	7)	9.70×10^{-2}

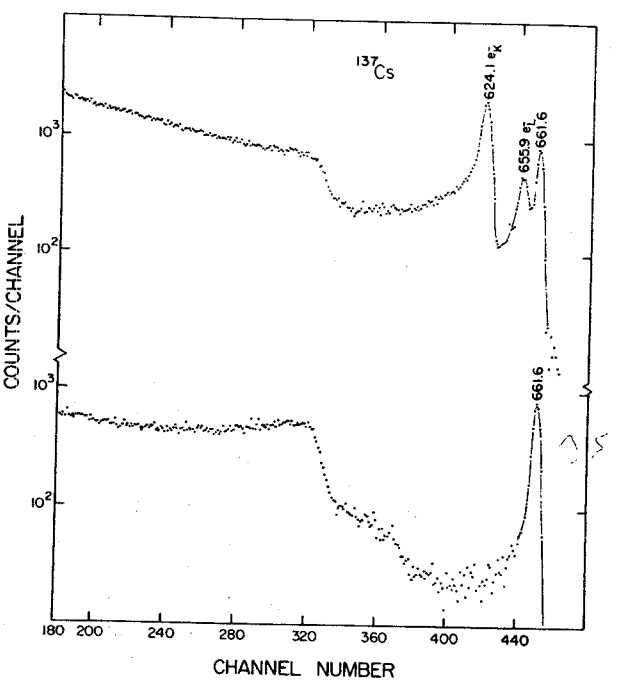

Fig. 2. Top: ^{137}Cs spectrum showing the 661.6-keV γ and its K and L conversion electrons.
Bottom: ^{137}Cs spectrum taken with an Al absorber between the source and the detector to block the electrons. By subtracting the bottom spectrum from the top one a clean electron spectrum can be obtained.

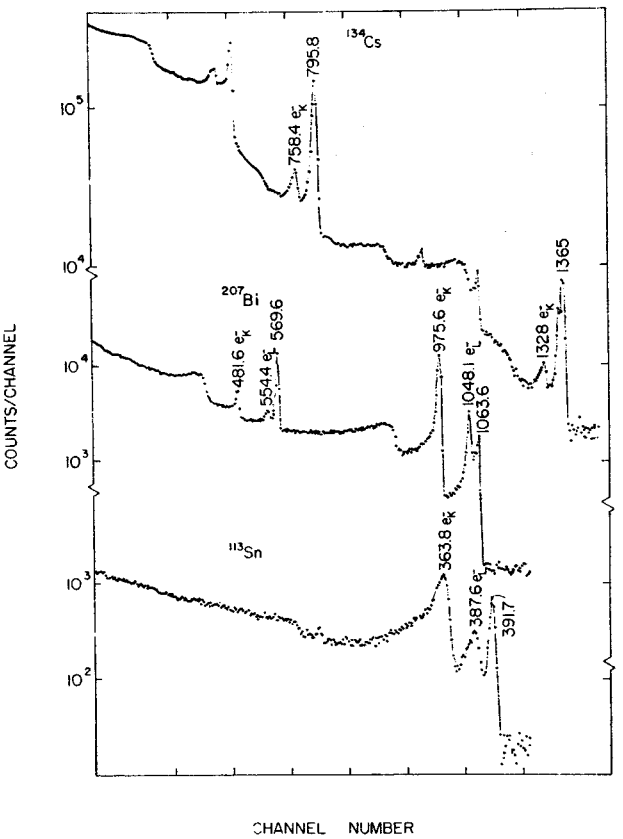

Fig. 3. Three spectra demonstrating the response of the detector to radiations of different energies. Note that the gains were adjusted to utilize the entire analyzer for each spectrum, so the energy scales are not aligned. Top: ^{134}Cs (only the transitions of interest are labelled). Middle: ^{207}Bi. Bottom: ^{113}Sn (note the broadening of the electron peaks at this relatively low energy).

using theoretical values of conversion coefficients determined by interpolation of the results of R. S. Hager and E. C. Seltzer[8]). The intensities of the electron peaks were determined by first taking a spectrum of both electrons and γ-rays, as shown for ^{137}Cs in fig. 2a. Then an Al absorber of sufficient thickness to stop the electrons completely was placed between the source and the detector, and a spectrum was taken (with the same electronics settings) that contained only the γ-rays, as in fig. 2b. By overlapping the spectra and subtracting, the electron intensities were easily obtained. (After some practice, we found that we could obtain precision electron intensities even without the second spectrum, but for complex spectra it is needed).

The spectra for ^{113}Sn, ^{134}Cs, and ^{207}Bi are shown in fig. 3. These demonstrate both the range and the limitations of the present detector. To determine conversion coefficients most precisely, the efficiencies for detecting electrons and γ-rays should be comparable, at least within several orders of magnitude. This means that a small detector is required, particularly for lower energies, where the Compton backgrounds from the γ-rays can easily obscure the electron peaks, especially when the latter have been broadened by straggling in passing through the window. This problem is evident in the ^{113}Sn spectrum. At higher energies the γ-ray efficiency becomes very small and so do most conversion coefficients, so this becomes the limitation. Our present detector has a useful range from approximately 200 to 1300 keV. A larger detector would be more useful for higher energies, and a smaller (thinner, to lower the γ-ray efficiency) at lower energies. In addition, the window thickness could be reduced to 0.1 mil or less, and, in fact, straggling could be essentially eliminated by using a vacuum interlock to allow one to place the source inside the can with the detector.

The efficiency curve for the present detector is shown in fig. 4. It takes the form of the relative efficiencies for γ-rays and electrons, i.e.,

$$C = D(\gamma)/D(e^-),$$

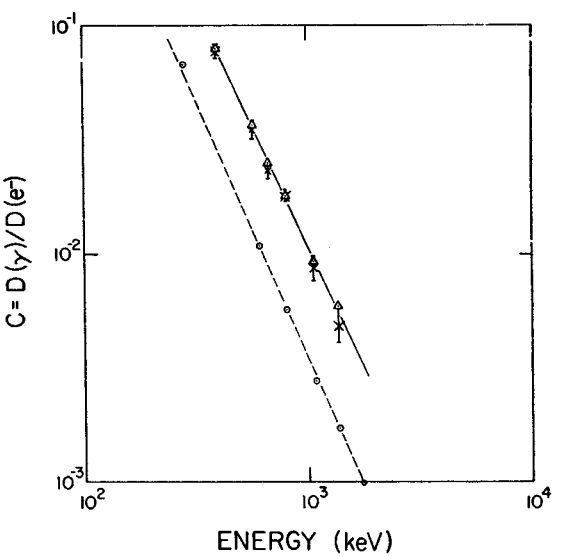

Fig. 4. Efficiency curve for determining conversion coefficients from the Ge(Li) single-crystal conversion-coefficient spectrometer. The solid curve represents the composite γ-ray-electron efficiencies. Δ's, calculated from theoretical conversion coefficients; $\times$'s, from experimental conversion coefficients (cf. table 1). The error bars apply to the $\times$'s. For comparison, the dashed line shows a relative γ-ray efficiency curve; this has been shifted down so as not to overlap with the solid curve.

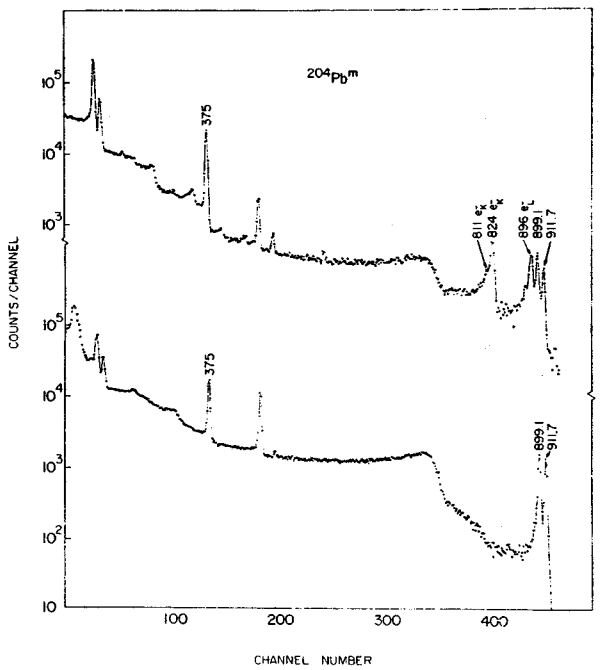

Fig. 5. $^{204}Pb^{m}$ spectra. Only the $^{204}Pb^{m}$ transitions are labelled; the others occur in Tl isotopes following the decay of other Pb isotopes. Top: Spectrum showing both γ-rays and electrons. Bottom: Spectrum taken through an Al absorber to remove the electrons.

vs the γ-ray energy, E_γ. (For purposes of illustration, we have compressed our data onto a single graph. In actual practice, one has to account for the differences in binding energy for different elements.) To obtain the conversion coefficient of a transition, one merely obtains an experimental intensity ratio for the γ-rays and electrons and multiplies this by the corresponding ordinate from fig. 4, i.e.,

$$\alpha = C(A_e/A_\gamma) .$$

Because the efficiency for electrons varies very slowly, the above efficiency curve is very nearly the same as the efficiency curve for γ-rays alone. The latter curve is presented in fig. 4 with an offset scale for comparison.

4. Example of use of the system

An example of the use of the detector is shown in fig. 5, where spectra for $^{204}Pb^{m}$ are shown. The difference between α_K for the 899.1-keV E2 and the 912.0-keV E5 transitions is striking. Our measured values for these are given in table 2, where they are compared with the theoretical values of ref.[8]). The agreement is quite good, as is the agreement with previously measured values[9]). We also include the K/L ratio for the E5 transition, but one cannot extract a reliable K/L for the E2 because of the complexity of this portion of the spectrum.

TABLE 2

$^{204}Pb^{m}$ conversion data.

Transition energy (keV)	Multipolarity	α_K experimental	α_K theoretical[8])	K/L experimental	K/L theoretical[8])
899.1	E2	0.0072±0.0022	0.0065		
912.0	E5	0.0545±0.0045	0.046	1.66±0.25	1.73

In conclusion, a small Ge(Li) detector mounted in a cryostat with a thin window to allow the simultaneous counting of γ-rays and conversion electrons shows considerable promise as a convenient piece of equipment for measuring conversion coefficients from spectra that are not too complex.

References

1) C. R. Gruhn, Bull. Am. Phys. Soc. **13** (1968) 1363, presented at 1968 Fall Meeting of the American Physical Society.
2) R. H. Pehl, F. S. Goulding, D. A. Landis and M. Lenzlinger, Nucl. Instr. and Meth. **59** (1968) 45.
3) H. T. Easterday, A. J. Haverfield and J. M. Hollander, Nucl. Instr. and Meth. **32** (1965) 333.
4) J. H. Hamilton, cited in C. M. Lederer, J. M. Hollander and I. Perlman, *Table of isotopes*, 6th ed. (Wiley, New York, 1967).
5) R. A. Brown and G. T. Ewan, Nucl. Phys. **68** (1965) 325; W. van Wyngaarden and R. C. Conner, Can. J. Phys. **42** (1964) 42.
6) J. S. Merritt and J. G. V. Taylor, Anal. Chem. **37** (1965) 351.
7) K. Siegbahn, Nucl. Phys. **A93** (1967) 63.
8) R. S. Hager and E. C. Seltzer, Nucl. Data **A4** (1968) 1.
9) C. J. Herrlander, R. Stockendal, J. A. McDonell and I. Bergström, Nucl. Phys. **1** (1956) 643.

Reprinted from THE PHYSICAL REVIEW, Vol. 188, No. 4, 1875–1880, 20 December 1969
Printed in U. S. A.

Neutron-Deficient Members of the $A=139$ Decay Chain. II. 4.5-h Pr^{139}

D. B. BEERY* AND W. H. KELLY

Cyclotron Laboratory,† Department of Physics, Michigan State University, East Lansing, Michigan 48823

AND

WM. C. MCHARRIS

Department of Chemistry‡ and Cyclotron Laboratory,† Department of Physics, Michigan State University, East Lansing, Michigan 48823

(Received 28 April 1969)

The γ rays emitted following the decay of 4.5-h Pr^{139} have been investigated with Ge(Li) and NaI(Tl) detectors in singles and anticoincidence configurations. Twelve transitions having the following energies (and relative intensities) were observed: 254.7 (53), 1320.0 (13), 1347.4 (≡100), 1375.7 (33), 1563.6 (9), 1596.6 (10), 1630.6 (70), 1653.3 (8), 1730.2 (1.6), 1818.4 (7.0), 1907.9 (3.5), and 2015.9 keV (3.0). Using energy sums and the anticoincidence results, we placed states in Ce^{139} at 0 ($\frac{3}{2}+$), 254.7 ($\frac{1}{2}+$), 1320.0 ($\frac{3}{2}, \frac{5}{2}, \frac{7}{2}$), 1347.4 ($\frac{7}{2}+$), 1596.6 ($\frac{3}{2}, \frac{5}{2}, \frac{7}{2}$), 1630.6 ($\frac{3}{2}, \frac{5}{2}+$), 1818.4 ($\frac{3}{2}, \frac{5}{2}+$), 1907 ($\frac{3}{2}, \frac{5}{2}+$), 1984.9 ($\frac{3}{2}, \frac{5}{2}+$), and 2015.9 keV ($\frac{3}{2}, \frac{5}{2}, \frac{7}{2}+$). The assignments were made on the basis of logft values and relative photon intensities. The single particle versus collective behavior of the states is also discussed.

I. INTRODUCTION

THE $_{59}Pr_{80}^{139}$ is twice removed from stability in the $A=139$ decay chain and decays with a 4.5-h $t_{1/2}$ to 140-day Ce^{139}. Pr^{139} was first produced in 1950 by Stover,[1] who bombarded Ce with 20- and 32-MeV p's and attributed a 4.5-h activity to the reaction, $Ce^{140}(p, 2n)Pr^{139}$. Since that time, there have been a number of papers on its decay,[2–9] including two recent, rather complete studies[8,9] in which Ge(Li) detectors were used to observe the γ rays following its decay.

We have just completed an extensive investigation[10] of the decays of Nd^{139m+g}. During the course of that investigation we, of course, observed γ rays from the decay of the daughter Pr^{139}. It was necessary to make careful observations of these γ rays in order to avoid inadvertently confusing them with γ rays in the complex Nd^{139m+g} spectra. This led to our producing Pr^{139} separately from Nd^{139m+g}, and we were able to obtain somewhat more precise and more extensive information than that which had been published already. Thus, we found it worthwhile to investigate the Pr^{139} γ rays more completely. To date, very little has been published on the interpretation of the states in $_{58}Ce_{81}^{139}$ (closed $g_{7/2}$ proton subshell, one neutron hole in the $N=82$ shell). Therefore, we here present a discussion of the structures of the states in terms of the shell model and in relation to states in other nuclei in this region.

II. SOURCE PREPARATION

We prepared Pr^{139} sources by bombarding reagent grade $CeNO_3$ (88.5% Ce^{140}, 11.07% Ce^{142}, 0.250% Ce^{138}, and 0.193% Ce^{136}) with 29-MeV p's from the Michigan State University sector-focused cyclotron. Typically, ≈100-mg targets were bombarded with a 1.5-μA beam for ≈1 h. The sources were usually aged some 5 h before starting counting, and at that time the primary activities were Pr^{139}, 17.2-h Ce^{135}, and 19.2-h Pr^{142}, although 19.5-h La^{135}, 33-day Ce^{141}, and 140-day Ce^{139} were also noted as the sources aged. These contaminant activities were so weak that they did not interfere significantly with the measurements on the Pr^{139} decay. The counting was done over a period of several days, with careful attention being given to the growth and decay of the various peaks. In this way, γ rays from the different activities were easily distinguished.

Pr^{139} was also made as a by-product of our Nd^{139m+g} sources[10] through the reaction chain

$$Pr^{141}(p, 3n)Nd^{139m+g} \xrightarrow{\beta^+/\epsilon} Pr^{139}.$$

---

* Present address: Manchester College, North Manchester, Ind. 46962.

† Work supported in part by the U.S. National Science Foundation.

‡ Work supported in part by the U. S. Atomic Energy Commission.

[1] B. J. Stover, Phys. Rev. 81, 8 (1951).
[2] T. Handley and E. L. Olson, Phys. Rev. 96, 1003 (1954).
[3] G. Danby, J. Foster, and A. Thompson, Can. J. Phys. 36, 1487 (1958).
[4] Y. Carver and W. Turchinetz, Proc. Phys. Soc. 73, 110 (1959).
[5] O. Borello, S. Costa, and F. Ferrero, Nucl. Phys. 27, 25 (1961).
[6] E. Biryukov, V. T. Novikova, and N. S. Shimanskaya, Izv. Akad. Nauk SSSR, Ser. Fiz. 27, 1408 (1963).
[7] I. D. Goldman, Y. Miyao, I. C. Nascimento, N. L. Da Costa, and A. G. De Pinho, Nuovo Cimento 47, 306 (1967).
[8] J. D. King, N. Neff, and H. W. Taylor, Nucl. Phys. A99, 433 (1967).
[9] D. De Frenne, J. Demuynck, K. Heyde, E. Jacobs, M. Dorikens, and L. Dorikens-Vanpraet, Nucl. Phys. A106, 350 (1968).
[10] D. B. Beery, W. H. Kelly, and Wm. C. McHarris, preceding paper, Phys. Rev. 188, 1851 (1969).

These sources confirmed some of the Pr^{139} γ rays, but the multitude of high-intensity γ rays from Nd^{139m+g} decay obscured much of the Pr^{139} spectrum.

III. EXPERIMENTAL RESULTS

A. γ-Ray Singles Spectra

A 7-cm^3 five-sided coaxial Ge(Li) detector manufactured in this laboratory[11] was used to obtain singles γ-ray spectra. The detailed methods used, including standards and spectrum analysis, are given in Ref. 10. We show some resulting spectra for the low- and high-energy regions in Figs. 1(a) and 1(b), respectively. A $\frac{5}{8}$-in. graded Pb absorber was employed while recording the high-energy spectrum in order to enhance the weak higher-energy γ rays.

A summary of the Pr^{139} γ-ray energies and intensities measured in this investigation is given in Table I. Each entry is the weighted average of a number of determinations performed at different times and with different electronics. In addition to purely statistical errors, the errors in both the energies and intensities reflect their reproducibilities, peak heights above background, and estimated uncertainties in the standards.[10] Also shown for comparison in Table I are the results of King, Neff, and Taylor[8] and of de Frenne *et al.*,[9] the two recent studies of Pr^{139} decay that used Ge(Li) detectors.

By careful intensity measurements at several different times after bombardment and by the use of graded Pb absorbers to allow the enhancement of the counting rate at high energies, we were able to confirm clearly the presence of the weak 1730.2- and 2015.9-keV γ's, which had been seen by de Frenne *et al.*, but not by King, Neff, and Taylor. We were also able to place an upper limit of 0.5 (relative to 100 for the 1347.4-keV γ intensity) on the intensity of a 1575.7-keV γ that had been reported by King, Neff, and Taylor. In several of our spectra, we did observe a 1575.9-keV γ in this energy region, but this γ ray proved to result from a 19.2-h Pr^{142} contaminant activity produced by the Ce^{142} $(p, n)Pr^{142}$ reaction.

Only the 254.7-, 1347.4-, 1375.8-, and 1630.6-keV γ's from Pr^{139} decay were seen in the Pr^{139} sources produced as decay products from Nd^{139m+g}. The remaining γ rays were either weak enough to be hidden by the intense Nd^{139m} γ rays or corresponded closely to a Nd^{139m} γ ray; e.g., the 254.7-keV γ was obscured at all times by the 254.9-keV γ from Nd^{139m} decay.

B. γ-γ Anticoincidence Study

From the Pr^{139} disintegration energy[6,12] of 2110±20 keV and the measured γ-ray energies of Table I, it is clear that the cascades that are energetically allowed must involved only the 254.7-keV γ. Unfortunately, as can be seen from Fig. 1(a), coincidence experiments gated on this γ ray are not terribly practicable because of its relative weakness and the intense background upon which it rides. However, a γ-γ coincidence was performed by de Frenne *et al.*,[9] in which they gated on all γ rays having energies greater than 1.5 MeV, and this experiment indicated

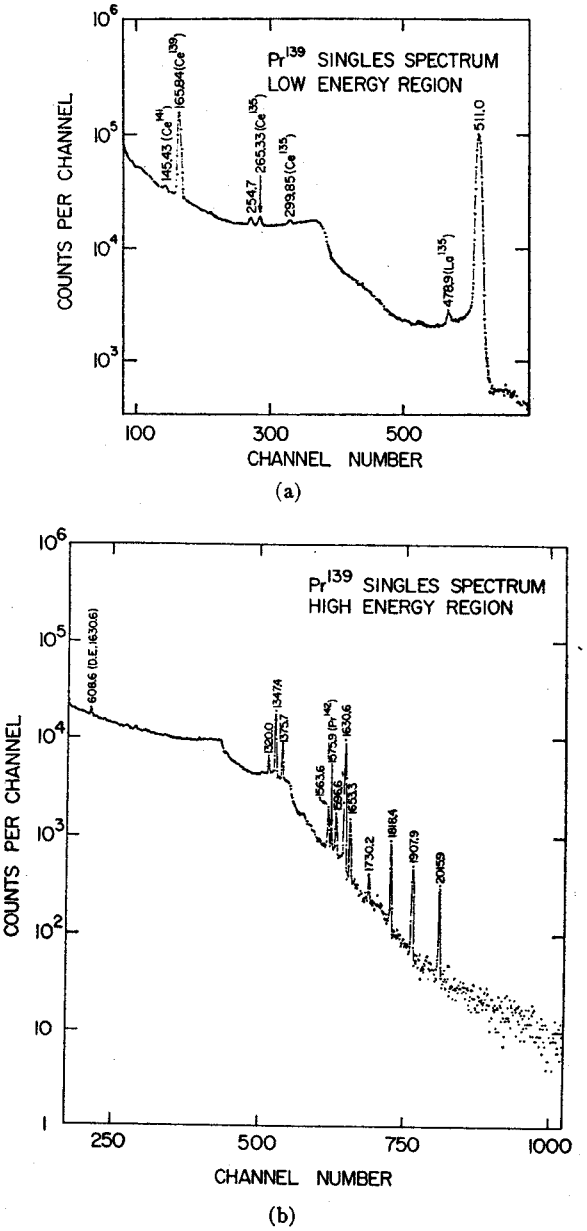

FIG. 1. Pr^{139} singles γ-ray spectrum taken with a 7-cm^3 Ge(Li) detector: (a) low-energy portion; (b) high-energy portion. A $\frac{5}{8}$-in. graded Pb absorber was placed between the source and the detector to lower the low-energy counting rate for spectrum (b).

[11] This detector was constructed by Dr. G. Berzins working with Dr. C. R. Gruhn, to both of whom we express our thanks.

[12] J. H. E. Mattauch, W. Thiele, and A. H. Wapstra, Nucl. Phys. 67, 1 (1965); 67, 32 (1965); 67, 73 (1965).

TABLE I. Pr^{139} γ rays.

Energy (keV) Present work	King, Neff, and Taylor[a]	de Frenne *et al.*[b]	Relative intensity Present work	King, Neff, and Taylor[a]	de Frenne *et al.*[b]
254.7±0.3	254.7±0.1	255.15±0.2	53±5	37.7	47±5
511.0($\gamma^{\pm}$)	511.0	511.0	3600±400	3280	4000±200[c]
1320.0±0.3	1320.4±0.4	1320.0±0.5	13±3	7.6	16±3
1347.4±0.2	1347.4±0.2	1346.8±0.5	≡100	≡100	100±10
1375.7±0.2	1375.8±0.3	1375.3±0.5	33±2	22.6	25±2
1563.6±0.3	1563.8±0.2	1563.6±0.5	9±2	5.7	9±1
(1576)[d]	1575.7±0.4		<0.5	(2.26)	
1596.6±0.3	1597.5±0.4	1595.6±0.5	10±2	4.5	7±1
1630.6±0.3	1630.6±0.2	1630.7±0.5	70±7	53	65±7
1653.3±0.3	1652.0±0.4	1653.3±0.5	8±2	5.3	7±1
1730.2±0.4		1729.8±0.9	1.6±0.5		1.5±0.5
1818.4±0.3	1818±1	1818.0±0.5	7.0±1.0	3.4	6.5±1
1907.9±0.4	1905±1	1907.0±0.9	3.5±0.5	<2	3±1
2015.9±0.5		2015.0±0.9	3.0±0.5		3±1

[a] Reference 8.
[b] Reference 9.
[c] Assuming that the "2000±100" in Fig. 3 of Ref 9 indicates β^+ intensity relative to 100 for the 1347-keV γ ray.
[d] We did not observe a γ ray of this energy and can only place an upper limit on its intensity.

that one or more of these is in cascade with the 254.7-keV γ.

In order to determine which of the 11 higher-energy γ rays are the ones in coincidence with the 254.7-keV γ and to search for additional weak γ rays that might have passed unobserved in other measurements, we employed an 8×8-in. NaI(Tl) split annulus[13] in an anticoincidence experiment with the 7-cm³ Ge(Li) detector. The single-channel gate on the signals from the annulus was chosen to be open for all γ rays having energies greater than 100 keV. Each Pr^{139} source was placed inside the annulus tunnel on top of the Ge(Li) detector, which blocked one end of the tunnel. An additional 3×3-in. NaI(Tl) anticoincidence detector was placed in the tunnel above the sources and the Ge(Li) detector in order to reduce further the sharp Compton edges caused by back-scattering in the Ge(Li) detector.

The high-energy region of one of the anticoincidence spectra which resulted is shown in Fig. 2. In Table II, we compare the relative intensities of the Pr^{139} γ rays as obtained from singles and anticoincidence data. These intensities are averages taken over several runs

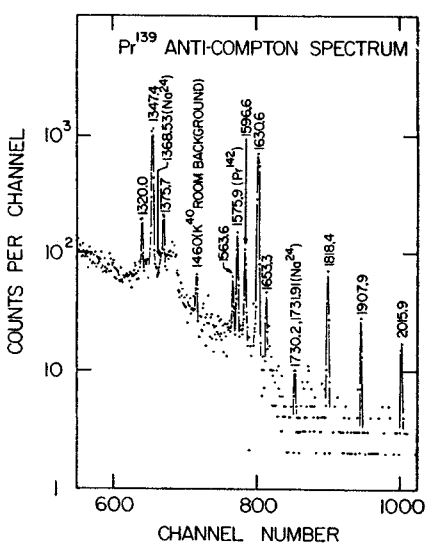

FIG. 2. Pr^{139} anticoincidence spectrum recorded by the 7-cm³ Ge(Li) detector when placed inside the tunnel of an 8×8-in. NaI(Tl) split annulus, with a 3×3-in. NaI(Tl) detector at the other end of the tunnel. For details, see the text or Ref. 13.

TABLE II. Pr^{139} relative photon intensities in singles and anticoincidence experiments.

Energy (keV)	Relative intensity Singles (S)	Anticoincidence (A)	Intensity ratio A/S
254.7	53±5	18±2	0.34[b]
511.0	3600±400	363±60	0.10[b]
1320.0	13±3	11±1	0.85[c]
1347.4[a]	≡100	≡100	1.00[c]
1375.7	33±2	10±1	0.30[b]
1563.6	9±2	4±0.8	0.4[b]
1596.6	10±2	8±1	0.8[c]
1630.6	70±7	72±6	1.0[c]
1653.3	8±2	2±0.3	0.25[b]
1730.2	1.6±0.5	0.5±0.1	0.3[b]
1818.4	7.0±1.0	5.3±0.6	0.8[c]
1907.9	3.5±0.5	2.8±0.3	0.8[c]
2015.9	3.0±0.5	2.6±0.3	0.9[c]

[a] The high intensity of this γ ray suggests that it is a ground-state transition.
[b] The low A/S ratio suggests that these transitions are involved in coincidences.
[c] The high A/S ratio suggests that these transitions are primarily fed by ϵ decay and proceed directly to the ground state.

[13] R. L. Auble, D. B. Beery, G. Berzins, L. M. Beyer, R. C. Etherton, W. H. Kelly, and Wm. C. McHarris, Nucl. Instr. Methods 51, 61 (1967).

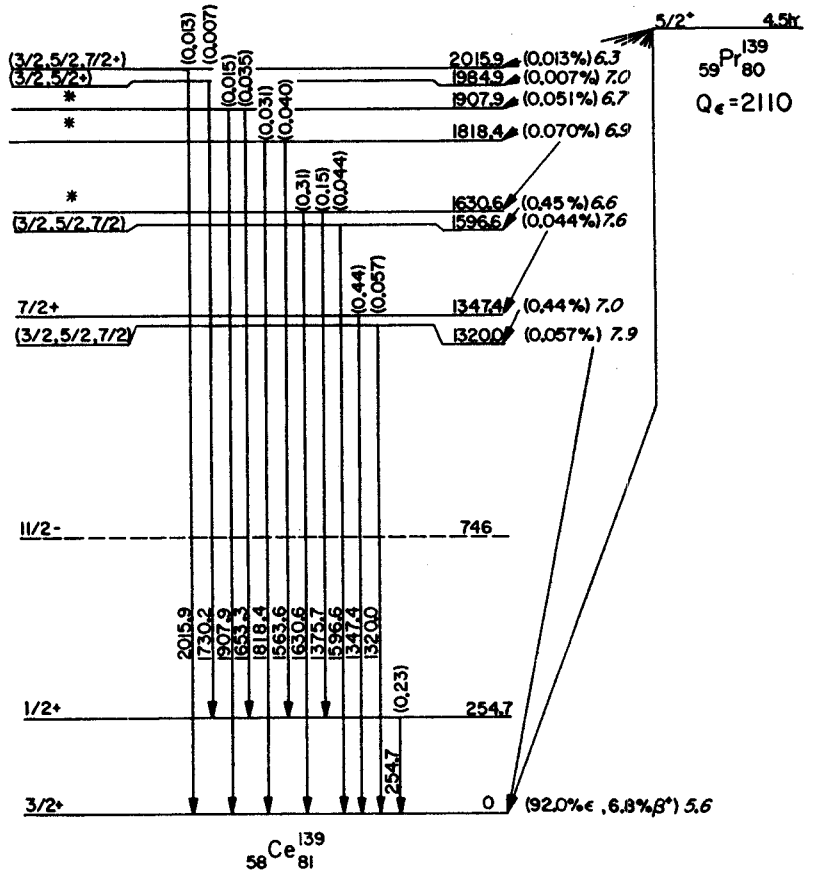

FIG. 3. Pr^{139} decay scheme. Energies are all given in keV and (total) transition intensities are given in percent of the Pr^{139} disintegrations. The β^+/ϵ ratio is a calculated value. The level at 746 keV is the well-known Ce^{139m}, but it is not populated in Pr^{139} decay. The three levels whose spins are designated by asterisks have been assigned $\frac{3}{2}+$ or $\frac{5}{2}+$, but the reader should consult the text for the details concerning these assignments.

recorded at times ranging 1–40 h after bombardment. This procedure was followed to check for underlying contaminant activities with different half-lives. None was observed.

In Table II, column 4, the ground-state γ-ray transitions from states that are primarily ϵ fed are clearly distinguished from the γ rays in cascade with the 254.7-keV γ by their larger anticoincidence/singles intensity ratios.

IV. DECAY SCHEME

The decay scheme that we were able to deduce from the foregoing measurements is shown in Fig. 3. Transition and excited-state energies are given in keV, the disintegration energy coming from the β^+ end point of 1090 ± 20 keV measured by Biryukov *et al.*[6] The β^+/ϵ ratio for decay to the Ce^{139} ground state is a calculated value, using Zweifel's method.[14] Experimental measurements of β^+/ϵ_K have varied widely,[2–6] and, as this is clearly an allowed transition, we have chosen the calculated value because any needed future adjustments could be made quite easily with respect to it. The other transition intensities, both for ϵ decay and for the (total) electromagnetic transitions are adjusted to this value and read in percent of the total Pr^{139} disintegrations. The log*ft* values (in italics on the right-hand sides of the levels) are based on a 4.5-h $t_{1/2}$.

The positions of the levels, with the exception of the 254.7- and 1984.9-keV levels, were indicated unambiguously by the enhancement of their respective ground-state transitions in the anticoincidence spectrum. The levels at 1630.6, 1818.4, and 1907.9 keV were confirmed by the 1375.7-, 1563-, and 1653.3-keV γ's that are in coincidence with the 254.7-keV γ. The adopted energies for these levels is a weighted average based on our relative confidence in the respective cascade and crossover transitions. The 254.7-keV level can, of course, be placed quite confidently on the basis of the coincidence behavior of the 254.7-keV γ. We observed no ground-state transition for the remaining level at 1984.9 keV, but the anticoincidence spectrum demonstrated clearly that the 1730.2-keV γ was in coincidence with a lower-energy γ ray, and the 254.7-keV γ is the only possibility—hence our rationale for placing this level. The 746.0-keV state is the well-characterized[15,16] Ce^{139m}, which, al-

[14] P. F. Zweifel, Phys. Rev. 107, 329 (1957).

[15] K. Kotajima and H. Morinaga, Nucl. Phys. 16, 231 (1960).

[16] R. E. Eppley, Wm. C. McHarris, D. B. Beery, and W. H. Kelly (to be published).

TABLE III. Ce^{139} level-scheme comparisons.

Present work		King, Neff, and Taylor[a]		de Frenne *et al.*[b]		$Ce^{140}(d,t)$[c]	
Energy (keV)	Assignment	Energy (keV)	Assignment	Energy (keV)	Assignment	Energy (keV)	Assignment
0	3/2+	0	3/2+	0	3/2+	0	3/2+
254.7	1/2+	254.7	(1/2)+	255.15	(1/2)+	250	1/2+
[746[d]	11/2−	745[d]	11/2−	746.0[d]	(11/2−)]	750	11/2−
1320.0	(3/2, 5/2, 7/2)	...	...	1320.0	(5/2, 7/2)	...	...
1347.4	7/2+	1347.4	(7/2+)	1346.8	(5/2, 7/2)	1340	7/2+
...	...	1575[e]	...	...	...	...	...
1596.6	(3/2, 5/2, 7/2)	1598	...	1595.6	(5/2, 7/2)	...	...
1630.6	(3/2, 5/2+)	1630.6	...	1630.7	(3/2, 5/2)	...	...
...	...	...	...	1729.8[e]	(5/2, 7/2)[e]	...	...
1818.4	(3/2, 5/2+)	1818	...	1818.0	(3/2, 5/2)	...	...
1907.9	(3/2, 5/2+)	1905	...	1907.0	(3/2, 5/2)	...	...
1984.9	(3/2, 5/2+)	...	...	...	...	...	...
2015.9	(3/2, 5/2, 7/2+)	...	...	2015.0	(5/2, 7/2)	...	...

[a] Reference 8.
[b] Reference 9.
[c] Reference 17.
[d] Ce^{139m}, which is not populated in the decay of Pr^{139}. This has been very well characterized as one of the $N=81$ $M4$ isomers; cf. Refs. 15 and 16.
[e] We consider these levels to have been placed incorrectly.

though not populated by Pr^{139} decay, is included in the decay scheme for completeness.

This decay scheme agrees in most essential features with the decay schemes proposed by King, Neff, and Taylor[9] and by de Frenne *et al.*,[9] but there are a few noteworthy differences. We compare our level placements with those of these groups in Table III; also included are the levels populated by the $Ce^{140}(d,t)Ce^{139}$ reaction.[17] Our anticoincidence data suggest that the 1730.2-keV γ is in coincidence with the 254.7-keV γ, so we have placed a level at 1984.9 keV and removed the one proposed by de Frenne *et al.* at 1729.8 keV. And, as we saw no evidence for the 1575-keV γ (probably from Pr^{142} decay) of King, Neff, and Taylor, in addition to which anticoincidence data indicated the 1320.0-keV γ to be a ground-state transition, we remove their 1575-keV level and place a level at 1320.0 keV, in agreement with de Frenne *et al.* Neither the 1984.9- nor the 2015.9-keV levels had been placed by King, Neff, and Taylor, although de Frenne *et al.* had placed the latter level.

V. DISCUSSION

In Ref. 10, we presented arguments to the effect that the ground state of Pr^{139} has a spin and parity $\frac{5}{2}+$ and that the major component of its wave function is a single $d_{5/2}$ proton outside the $(g_{7/2})^8$ subshell. Now, the Ce^{139} nucleus is one of a chain of odd-mass isotones from $_{52}Te_{81}^{133}$ to $_{64}Gd_{81}^{145}$, each of which has a metastable state that deexcites to the ground state via an $M4$ transition.[15,16] These closely related transitions have all been interpreted as $h_{11/2}\rightarrow d_{3/2}$ transitions, as have the corresponding isomeric transitions in the nearby $N=79$ isotones. And the ground-state spins of some of these, e.g., Nd^{141} and Ba^{137} (Refs. 18 and 19), have been measured to be $\frac{3}{2}$ by the atomic beam method. This, together with the smoothly varying energy differences between the isomeric states in the series and the smoothly varying reduced transition probabilities of the $M4$ transitions, strongly suggests that the Ce^{139} ground state is indeed $(d_{3/2})^{-1}$. The fact that 99% of the β decay populates this state directly with a logft of just 5.6 is consistent with the transformation of the $d_{5/2}$ proton into a $d_{3/2}$ neutron. Finally, population of the ground state by the (d,t) reaction[17] also corroborates the $\frac{3}{2}+$ assignment.

We observed no direct population ($\leq 0.01\%$) of the 254.7-keV state, and this is consistent with its being assigned $s_{1/2}$ from the (d,t) reaction. Also, there is a well-known[20] $s_{1/2}$ state at 281 keV in Ba^{137} and, although much less certain, such a state may exist[21] at 195 keV in Nd^{141}. Thus, the intermediate energy in Ce^{139} is consistent with apparent systematics. This $(s_{1/2})^{-1}$ state should differ from the $(d_{3/2})^{-1}$ ground state essentially only in the promotion of an $s_{1/2}$ neutron to the $d_{3/2}$ orbit, so the 254.7-keV γ should be an l-forbidden $M1$ and, as such, may have an observable half-life (a fraction of a nanosecond?) although its low intensity would make such an experiment a difficult one.

The only other state excited to any appreciable extent in the (d,t) reaction was a level at 1340 keV.

[17] R. H. Fulmer, A. L. McCarthy, and B. L. Cohen, Phys. Rev. 128, 1302 (1962).
[18] S. S. Alpert, B. Burdick, E. Lipworth, and R. Marrus, Bull. Am. Phys. Soc. 7, 239 (1962).
[19] I. Lindgren, in *Alpha-, Beta-, and Gamma-Ray Spectroscopy*, edited by K. Siegbahn (North-Holland Publishing Co., Amsterdam, 1965).
[20] M. A. Waggoner, Phys. Rev. 82, 906 (1951); 80, 489 (1950).
[21] I. Gratot, M. Le Pape, J. Olkowsky, and G. Ranc, Nucl. Phys. 13, 302 (1959).

Because of the nature of this reaction and the rather large spectroscopic factor for populating this state, one can probably assume that it contains most of the $g_{7/2}$ strength. The level we observed at 1347.4 keV corresponds to this state and its deexcitation solely to the $\frac{3}{2}+$ ground state is consistent with such an assignment. The rather large $\log ft=7.0$ for an allowed transition is easily explained even on simple shell-model terms by the fact that a $d_{5/2}$ proton is being converted to a $g_{7/2}$ neutron; however, the $g_{7/2}$ subshell in the parent is filled, so, in addition, a promotion of a neutron from $g_{7/2}$ to $d_{3/2}$ is required, thus slowing down the transition. There are a number of similar retardations now known.[22]

Assignments for the remaining states are more nebulous. The $\log ft$'s, ranging from 6.3 to 7.9 do not allow one to decide offhand between allowed and first-forbidden nonunique transitions, so spins for these states can be $\frac{3}{2}$, $\frac{5}{2}$, or $\frac{7}{2}$, with either even or odd parity. Owing to the apparent difficulty of constructing so many odd-parity states—it would require coupling the lower states to, say, a 3− vibrational state or the $h_{11/2}$ state to a 2+ vibrational state—most of the higher-lying states probably have even parity. Also, one would expect most allowed capture transitions in this nucleus to be somewhat retarded for reasons very similar to that causing the retardation of the transition to the $\frac{7}{2}+$ 1347.4-keV state.

The spin assignments can be narrowed down for the states that depopulate through the $\frac{1}{2}+$ 254.7-keV state. One has to be careful about making assignments based solely on the γ-ray branching ratios for the following reasons. The Ce^{139} nucleus lies intermediate between Ce^{138} and Ce^{140}, and, although Ce^{138} has a first excited state[23] at 790 keV that appears to be a 2+ quadrupole vibrational state, Ce^{140} has its first excited state[24] at 1596 keV, and this state decays by a nonenhanced $E2$ transition. Several calculations[25,26] on the properties of this Ce^{140} state indicate it to be complicated but essentially a two-quasiparticle state. Thus, because they may be either enhanced or not enhanced, in Ce^{139} one has to be particularly cautious with $E2$ transitions.

The $\frac{7}{2}+$ assignment is excluded for the states at 1630.6, 1818.4, and 1907.9 keV because of the γ-ray branchings from these states to the $\frac{1}{2}+$ 254.7-keV state. The intensities of the transitions from each to the $\frac{3}{2}+$ and $\frac{1}{2}+$ states differ at most by a factor of slightly more than 2. This suggests that the transitions in each pair have similar multipolarities, i.e., both $M1$'s ($+E2$'s) or one $E2$ with the other being largely $E2$ with a small admixture of $M1$. These would be consistent with the assignment of $\frac{3}{2}+$ or $\frac{5}{2}+$ to these three states. (The γ-ray branchings would also be consistent with all γ transitions being $E1$'s, implying $\frac{3}{2}-$ for the states. See our previous remarks, however, concerning the parities of the states.) One is tempted to try to use the core-coupling model to justify the $\frac{3}{2}+$ over the $\frac{5}{2}+$ assignment. However, the states and transitions can be explained almost equally well by a configuration that is primarily $s_{1/2}$ coupled to a 2+ core, primarily $d_{3/2}$ coupled to a 2+ core, or an intermediate mixture of both $s_{1/2}$ and $d_{3/2}$ coupled to the 2+ core. And, although tempting, at this point, it is not possible to make a clear distinction between $\frac{3}{2}+$ and $\frac{5}{2}+$ for the states.

The state at 1984.9 keV is tentatively assigned $\frac{3}{2}+$ or $\frac{5}{2}+$ on the basis of its single transition to the $\frac{1}{2}+$ 254.7-keV state. (The same remarks on parity apply as before.)

As of now, not much information can be gleaned from a comparison of the trends of states either in the Ce isotopes with $N<82$ or in the $N=81$ isotones because so little is known about states in these nuclides. The states in Ce^{139}, however, should prove useful in helping to interpret the properties of states in other nuclides in this region when more such states become known.

ACKNOWLEDGMENTS

We thank Dr. W. P. Johnson and H. Hilbert for their aid explaining the fine points and helping us operate the Michigan State University Cyclotron. We also thank Mrs. Carolee Merritt for helping with the computer programs and data analysis.

[22] For example, in Sn^{117}: D. B. Beery, G. Berzins, W. B. Chaffee, W. H. Kelly, and Wm. C. McHarris, Nucl. Phys. **A123**, 649 (1969).
[23] M. Fujioka, K. Hisatake, and K. Takahashi, Nucl. Phys. **60**, 294 (1964).
[24] S. Ofer and A. Schwarzschild, Phys. Rev. **116**, 725 (1959).
[25] W. M. Currie, Nucl. Phys. **48**, 561 (1963).
[26] M. Rho, Nucl. Phys. **65**, 497 (1965).

Reprinted from THE PHYSICAL REVIEW, Vol. 188, No. 4, 1851–1874, 20 December 1969
Printed in U. S. A.

Neutron-Deficient Members of the $A=139$ Decay Chain. I. 5.5-h Nd^{139m} and 30-min Nd^{139g}

D. B. BEERY* AND W. H. KELLY
Cyclotron Laboratory,† Department of Physics, Michigan State University, East Lansing, Michigan 48823
AND
WM. C. MCHARRIS
Department of Chemistry‡ and Cyclotron Laboratory,† Department of Physics, Michigan State University, East Lansing, Michigan 48823

(Received 17 March 1969)

We have studied the γ rays emitted following the decays of 5.5-h Nd^{139m} and 30-min Nd^{139g} with Ge(Li) and NaI(Tl) detectors in singles, coincidence, and anticoincidence configurations. Our study has indicated 51 γ rays accompanying Nd^{139m} decay and 21 that follow Nd^{139g} decay. Of these, 56 have been placed in decay schemes containing a total of 22 excited states. The decay scheme of $\frac{3}{2}+$ Nd^{139g} has much in parallel with those of similar nuclei in this region, and states are populated in Pr^{139} at 0 $(\frac{5}{2}+)$, 113.8 $(\frac{7}{2}+)$, 405.0 $(\frac{3}{2}+, \frac{1}{2}+)$, 589.2 $(\frac{5}{2}+)$, 916.8 $(\frac{1}{2}+, \frac{3}{2}+)$, 1074.4 $(\frac{1}{2}+, \frac{3}{2}+)$, 1311.8 $(\frac{1}{2}+, \frac{3}{2}+, \frac{5}{2}+)$, 1328.2 $(\frac{5}{2}+)$, 1405.5 $(\frac{1}{2}+, \frac{3}{2}+, \frac{5}{2}+)$, 1449.5 $(\frac{1}{2}+, \frac{3}{2}+, \frac{5}{2}+)$, and 1501.2 keV $(\frac{1}{2}+, \frac{3}{2}+)$. On the other hand, 11/2− Nd^{139m} decays only 12.7% via a 231.2-keV $M4$ isomeric transition and independently decays by electron capture to a set of almost completely different states in Pr^{139}. These are at 0 $(\frac{5}{2}+)$, 113.8 $(\frac{7}{2}+)$, 821.9 (11/2−), 828.1 $(\frac{7}{2}+, \frac{9}{2}+)$, 851.9 $(\frac{9}{2}+, \frac{7}{2}+)$, 1024.0 $(\frac{7}{2}+, \frac{9}{2}+, 11/2+)$, 1396.6 $(\frac{9}{2}, 11/2, 13/2)$, 1523.2, 1624.5 $(\frac{9}{2}-, 11/2-)$, 1834.1 $(\frac{9}{2}-, 11/2-)$, 1927.1 $(\frac{9}{2}-, 11/2-)$, 2048.8 $(\frac{9}{2}-, 11/2-)$, 2174.3 $(\frac{9}{2}-, 11/2-)$, and 2196.7 keV $(\frac{9}{2}-, 11/2-)$. Some 80.7% of its decay goes to the last six states, and we interpret them as being *three-quasiparticle* states. It appears that Nd^{139m} is one of a few nuclides whose intrinsic structure forces the preferred mode of decay to go into a three-quasiparticle multiplet, i.e.,

$$(\pi d_{5/2})^2(\nu d_{3/2})^{-2}(\nu h_{11/2})^{-1} \rightarrow (\pi d_{5/2})(\nu d_{3/2})^{-1}(\nu h_{11/2})^{-1}$$

The three-quasiparticle states are depopulated by numerous enhanced γ transitions between states in the multiplet and fewer, apparently highly hindered, transitions to lower states. Thus, the potential exists for extracting information about states near 2 MeV in this nucleus that normally is available only for states near the ground state.

I. INTRODUCTION

ONE of the most interesting regions of the nuclidic chart for current study is the region just below $N=82$, for here many systematic examples of rather extreme isomerism can be observed. The neutron-deficient side of the $A=139$ decay chain juts out into this region, and its members are well suited for probing the region because nuclei rather far removed from β stability are reached not too far below the closed shell. Thus, many interesting states should be populated by their decay, and these states should still be amenable to explanation in relatively straightforward shell-model terms—the number of nucleons making substantial contributions to a given configuration should not be so large as to be completely unmanageable.

$_{58}Ce_{81}^{139}$ is the first radioactive member on this side of the chain, and it decays directly to stable La^{139} with an electron-capture Q-value Q_ϵ of only 270 keV and a half-life of 140 days; it has a very simple decay scheme that has been known for a long time.[1] It does, however, have an interesting $h_{11/2}$ isomeric state (746 keV; $t_{1/2}=55$ sec), a member of the extensive $N=81$ series. The decay of the second radioactive member, 4.5-h $_{59}Pr_{80}^{139}$, to Ce^{139} is considerably more complex; we describe our results on this decay scheme in the following paper.[2]

$_{60}Nd_{79}^{139}$ is thrice removed from stable La^{139} and has a rather large amount of energy available for β decay ($Q_\epsilon=2.8$ MeV; cf. below). As in other $N=79$ odd-mass isotones, the $h_{11/2}$-$d_{3/2}$ (metastable-ground state) separation is fairly small, making the $M4$ isomeric transition quite slow. This means that here we are presented with two dissimilar isomers decaying almost independently, and because each can populate reasonably high-lying states in Pr^{139}, a wealth of information about many quite different states in this daughter nucleus is available from the study of these decays.

Nd^{139m} was first observed by Stover[3] in 1950 as part of an investigation of the products of bombardment of Pr^{141} with 40- and 50-MeV protons. Chemical identification was performed by ion exchange, and the mass number was established with reference to the granddaughter Ce^{139}. The half-life was measured to be 5.5±0.2 h.

---

* Present address: Manchester College, North Manchester, Ind. 46962.

† Work supported in part by the U. S. National Science Foundation.

‡ Work supported in part by the U. S. Atomic Energy Commission.

[1] M. L. Pool and N. L. Krisberg, Phys. Rev. 73, 1035 (1958).

[2] D. B. Beery, W. H. Kelly, and Wm. C. McHarris, following paper, Phys. Rev. 188, 1875 (1969).

[3] B. J. Stover, Phys. Rev. 81, 8 (1951).

Later studies[4,5] of conversion electron intensities and energy differences for a 231-keV transition accompanying this decay indicated it to be an $M4$ and to originate in Nd not Pr. Four neighboring odd-mass isobars with 79 neutrons were known[6] to have isomeric states involving an $\frac{1}{2}-\longrightarrow\frac{3}{2}+$ transition. From the trends in the isomeric level energies and in the reduced transition probablities, Gromov and his co-workers concluded that here we have a like pair of states[4] and that the 5.5-h activity was the $\frac{1}{2}-$ metastable state.

The $\frac{3}{2}+$ ground state was not seen so easily, and its half-life was only recently measured[7] to be 29.7 ± 0.5 min. For that experiment, it was produced by bombarding Pr^{141} with 30- and 33-MeV deuterons.

The only previous studies of Nd^{139m} decay[4,8] resulted in rather sketchy decay schemes containing serious disagreements. Because of this and the absence of any decay scheme for Nd^{139g}, we felt that this would make a good system for investigation. Our study has indicated the presence of 51 γ rays accompanying Nd^{139m} decay and 21 that follow Nd^{139g} decay. Of these γ rays, 56 have been placed in decay schemes containing a total of 22 excited states. Fourteen of these states have not been seen before.

The decay scheme of Nd^{139g} turns out to be unexceptional, having much in parallel with the decay scheme[9] of Nd^{141} and some other nuclei in this region below $N=82$. The low-spin states that it populates in Pr^{139} can be characterized reasonably well and follow expected systematics. On the other hand, the decay scheme of Nd^{139m} is anything but standard. This high-spin isomer decays only 12.7% by the 231.2-keV isomeric transition, the rest being by β^+ or electron capture (ϵ) to mostly high-spin high-lying states in Pr^{139}. Six of these, between 1624.5 and 2196.7 keV, are populated by decay that is less hindered ($\log ft$'s between 5.5 and 6.3) than the decay to an $h_{11/2}$ isomeric state at 821.9 keV in Pr^{139} ($\log ft=7.0$), which is almost certainly an *allowed* transition. This would seem to indicate that the transitions to these six states are also allowed, which would imply odd-parity states.

We interpret this as the configuration of Nd^{139m} being peculiarly suited for populating a multiplet of *three-quasiparticle* states. During the explanation we discuss the problem associated with multiple particle rearrangements in β and γ decay.

II. SOURCE PREPARATION

The 5.5-h Nd^{139m} activity was produced for most of our experiments by the relatively clean $(p, 3n)$ reaction on 100%-abundant Pr^{141}. Targets of 99.999% pure[10] Pr_2O_3 were bombarded typically for ≈1 h with ≈2 μA of 29-MeV protons from the Michigan State University sector-focused cyclotron. Sources were allowed to decay for about 5 h to let the 30-min Nd^{139g} produced by the bombardments reach transient equilibrium with Nd^{139m}. Experiments were then performed with the sources for approximately 20 h, until the Pr^{140} produced by the 3.3-day decay of Nd^{140} became a significant contaminant.

From crude excitation function studies of reactions following the bombardment of Pr^{141} with protons of various energies, we were able to distinguish the Nd^{139m+g} activities from weak-contaminant activities. Following each bombardment with 29-MeV protons, we were able to identify every contaminant peak observed in spectra recorded between 20 min and 40 h after the end of the bombardment. These weak contaminants, roughly in decreasing order of importance, were Pr^{140}, Pr^{139}, Ce^{139}, Nd^{141}, and Pr^{142}. It is significant that we did not produce any 22-min Nd^{138}, for its daughter, 2.1-h Pr^{138}, could prove a troublesome contaminant.

Nd^{139m} sources were also produced (somewhat serendipitously) following the bombardments of Nd^{142} with 36-MeV τ's (He^3 ions) and of Pr^{141} by 48- and 60-MeV τ's, all from the MSU cyclotron. These reactions were not so clean as the $(p, 3n)$ reaction on Pr^{141}, but they confirmed the relative intensities of the Nd^{139m} γ rays.

Most of our Nd^{139g} sources were produced by bombarding similar Pr_2O_3 tragets with 29-MeV protons for ≈45 sec. Experiments were carried out immediately upon concluding each of the bombardments, and the γ rays resulting specifically from Nd^{139g} decay were followed as their intensities dropped from their initial values to those when Nd^{139g} was in transient equilibrium with Nd^{139m}.

The relative intensities of all the Nd^{139g} γ rays we observed were confirmed by measurements of the activity produced by 48- and 60-MeV τ's on Pr^{141}. These reactions would produce Pm^{139}, which, were it a low-spin nucleus as anticipated, would populate Nd^{139g} by β decay much more strongly than Nd^{139m}. They did, in fact, yield Nd^{139g}/Nd^{139m} isomer ratios some 30 times as large as the $(p, 3n)$ reaction on Pr^{141}, but they yielded many more interfering short-lived activities as well.

III. EXPERIMENTAL RESULTS FOR Nd^{139m}

A. γ-Ray Singles Spectra

A 7-cm³ five-sided coaxial Ge(Li) detector manufactured[11] in this laboratory was employed to determine

[4] K. Ya. Gromov, A. S. Danagulyan, A. T. Strigachev, and V. S. Shpinel', Izv. Akad. Nauk SSSR, Ser. Fiz. 27, 1357 (1963).
[5] J. Gilat and W. J. Tretyl, University of California Lawrence Radiation Laboratory Report No. UCRL-17299, p. 20, 1967 (unpublished).
[6] C. M. Lederer, J. M. Hollander, and I. Perlman, in *Table of Isotopes* (John Wiley & Sons, New York, 1966), 6th ed.
[7] J. Lange, Kernforschungszentrum Karlsruhe Report No. KFK-519, p. 47, 1967 (unpublished); summarized in J. Lange, H. Münzel, and I. Leitl, Radiochimica Acta 8, 123 (1967).
[8] K. Ya. Gromov, A. S. Danagulyan, L. N. Nikityuk, V. V. Murav'eva, A. A. Sorokin, M. Z. Shtal', and V. S. Shpinel', Zh. Eksperim. i. Teor. Fiz. 47, 1644 (1964) [English Transl.: Soviet Phys.—JETP 20, 1104 (1965)].
[9] D. B. Beery, W. H. Kelly, and Wm. C. McHarris, Phys. Rev. 171, 1283 (1968).
[10] Obtained from Allied Chemical Corp., General Chemical Div., 800 Marion Ave., River Rouge, Mich. Targets of 99.9% Pr_2O_3 obtained from K & K Laboratories, Plainview, N. Y., were also used.
[11] This detector was manufactured by Dr. G. Berzins working with Dr. C. R. Gruhn, to both of whom we express our appreciation.

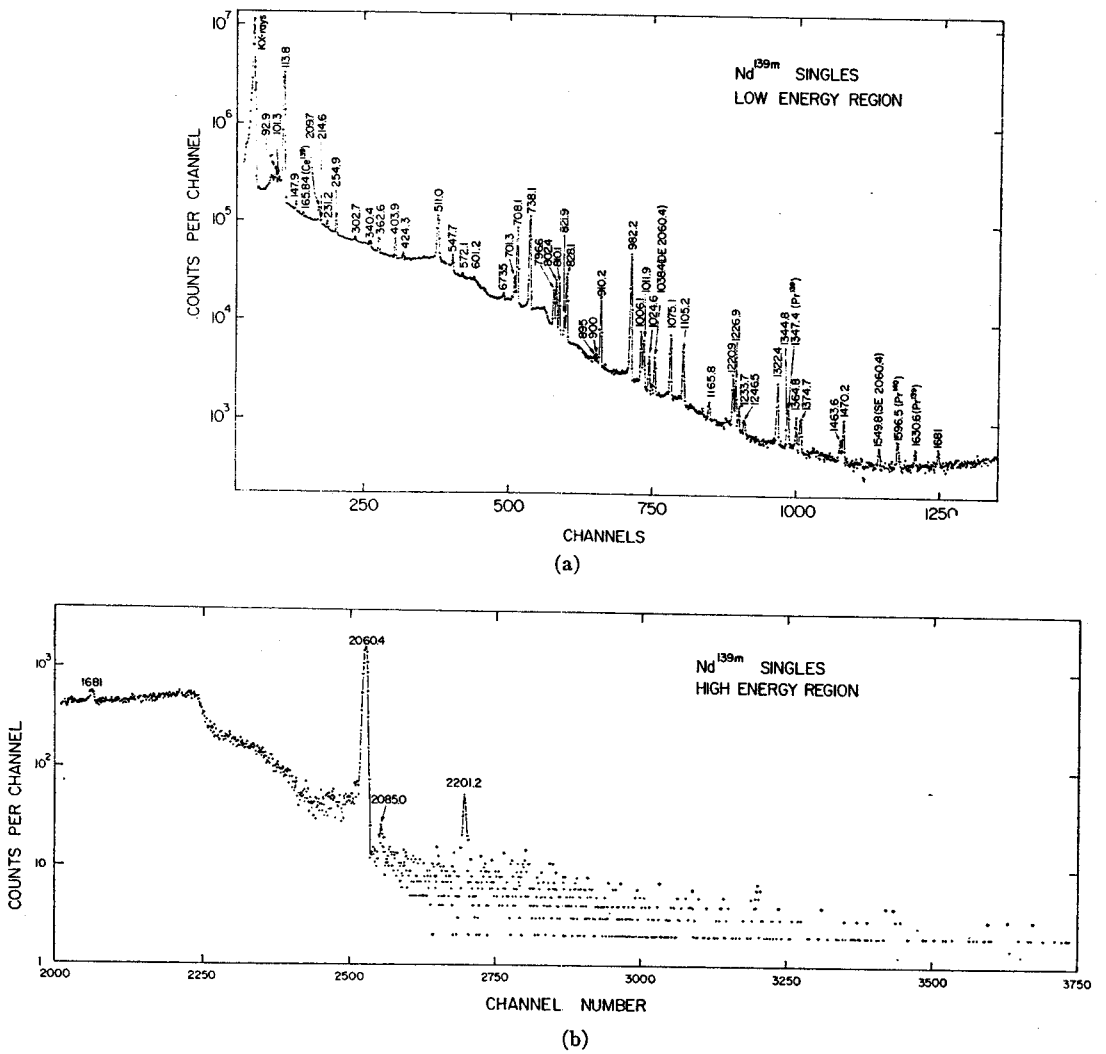

FIG. 1. (a) Nd^{139m} singles γ-ray spectrum taken with a 7-cm³ Ge(Li) detector—low-energy portion. This spectrum was accumulated for a 1-day period, using multiple bombardments to obtain optimum sources. Because of analyzer spillover, the portion of the spectrum below ≈ 120 keV was recorded for a shorter period of time and then normalized to the remainder of the spectrum. (b) Nd^{139m} singles γ-ray spectrum taken with a 7-cm³ Ge(Li) detector—high-energy portion. The events above 2300 keV come primarily from room background. From this spectrum an upper limit of 0.1% was placed on any transition with an energy greater than 2300 keV.

the energies and intensities of the Nd^{139m} γ rays. The wall thickness of the evacuated Al can enclosing the detector was 0.16 cm. Under typical operating conditions, a resolution of ≈ 2.5 keV full width at half-maximum (FWHM) for the 661.6-keV γ of Cs^{137} was obtained, using a room-temperature field-effect transistor (FET) preamplifier, a low-noise RC linear amplifier with pole-zero compensation, and a 4096-channel analyzer or analog-to-digital converter (ADC) coupled to a computer.

Energies of the prominent Nd^{139m} γ rays were measured by counting the Nd^{139m} sources simultaneously with several well-known calibration sources. To determine the energy calibration curve, we used a least-squares fit of the photopeak centroids of the calibration transitions to a quadratic equation after the background had been subtracted from under the peaks. The background correction for each peak was made by fitting a linear equation to several channels adjacent to both sides of the peak and then subtracting. The energies of the lower-intensity Nd^{139m} γ rays, which were obscured by the calibration standards, were then determined similarly by using the stronger Nd^{139m} γ rays as the standards. Some γ-ray singles spectra are shown in Figs. 1(a) and 1(b).

We used the spectrum shown in Fig. 1(b) to place an upper limit of 0.1% of the disintegrations of Nd^{139m} on any γ transition with an energy above 2300-keV. This would appear to rule out the 2350- and 2500-keV γ's proposed earlier[8,6] to have intensities ≈ 50 times as large as our upper limit. The events observed above 2300 keV in Fig. 1(b) come from long-lived room backgrounds that were not subtracted out.

The contaminant peaks seen in Fig. 1(a) accompany

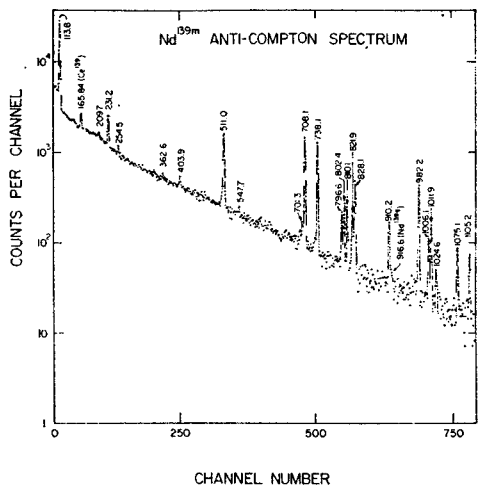

FIG. 2. Nd^{139m} anticoincidence spectrum recorded by the 7-cm³ Ge(Li) detector when placed inside the tunnel of an 8×8-in. NaI(Tl) split annulus, with a 3×3-in. NaI(Tl) detector at the other end of the tunnel. For details, see the text or Ref. 18. Characteristic of this type of spectrum is the noticeable absence of Compton edges. The 231.2-keV γ is the only γ ray enhanced over its singles intensity.

the reaction

$$Pr^{141}(p, 2n)Nd^{140} \xrightarrow{\epsilon} Pr^{140}$$

and Pr^{139} and Ce^{139} disintegrations following Nd^{139m+g} decay. Their energies, relative intensities, and intensity changes as functions of time were seen to be consistent with the properties of the associated decay schemes established in this study and elsewhere.[12–16,6]

A summary of the Nd^{139m} γ-ray energies and relative intensities is given in Table I. The energies assigned are mean values taken from a number of different measurements recorded at different times, different locations, with different system components, and with different parameters. Corresponding energy uncertainties are based on the reproducibilities of the Nd^{139m} energies from the calibration curves, the sizes of the Nd^{139m} photopeaks both before and after background subtraction, and the quoted errors on the standard energies.[17] The relative γ-ray intensities listed in Table I are also averages from a number of runs and were obtained using experimentally determined efficiency curves (cf. Ref. 9). Associated with these intensities are statistical uncertainties that include estimated uncertainties in the underlying backgrounds.

[12] J. D. King, N. Neff, and H. W. Taylor, Nucl. Phys. A99, 433 (1967).
[13] D. De Frenne, J. Demuynck, K. Heyde, E. Jacobs, M. Dorikens, and L. Dorikens-Vanpraet, Nucl. Phys. A106, 350 (1968).
[14] K. Histake, Y. Yoshida, K. Etoh, and T. Murata, Nucl. Phys. 56, 62 (19564).
[15] R. L. Graham and J. S. Geiger, Bull. Am. Phys. Soc. 11, 11 (1966).
[16] H. W. Baer, J. J. Reidy, and M. L. Wiedenbeck, Nucl. Phys. A113, 33 (1968).
[17] The 59.543±0.015-keV calibration line from Am^{241} was included with the standards listed in Table I of Ref. 9 and in Table I in D. B. Beery, G. Berzins, W. B. Chaffee, W. H. Kelly, and Wm. C. McHarris, Nucl. Phys. A123, 681 (1969).

B. γ-γ Coincidence Studies

Coincidence and anticoincidence experiments were performed using Ge(Li)-NaI(Tl) spectrometers. For our first experiment, in order to determine which γ rays appear in cascades and which come primarily from ϵ-fed

TABLE I. Energies and relative intensities of γ rays present in the decay of Nd^{139m}.

Measured γ-ray energy (keV)	Relative intensity
92.9±0.2	3.2±0.6
101.3±0.8	0.7±0.2
113.8±0.1	133±25
147.9±0.1	2.5±0.5
209.7±0.1	6.2±0.6
214.6±0.2	1.4±0.4
231.2±0.2	2.4±0.2
254.9±0.3	3.7±0.6
302.7±0.3	1.4±0.2
340.4±0.5	2.7±0.5
362.6±0.2	6.2±0.5
403.9±0.3	8.0±1.0
424.3±0.3	2.0±0.4
511.0(γ±)	3.2±2.8[a]
547.7±0.3	7.5±0.7
572.1±0.5	1.7±0.4
601.2±0.8	1.3±0.4
673.5±0.5	2.5±0.7
701.3±0.3	13.0±2.0
708.1±0.1	72.0±2.0
733.0±1.0[b]	1.0±0.6[b]
738.1±0.2	≡100
796.6±0.3	13.0±2.0
802.4±0.3	21.0±2.0
810.1±0.3	18.0±2.0
821.9±0.3	3.7±0.4
828.1±0.2	29.0±2.0
851.9±0.5[b]	1.4±0.4[b]
895.1±0.6	0.8±0.2
900.3±0.6	1.1±0.3
910.2±0.2	21.6±2.0
982.2±0.2	79.0±2.0
1006.1±0.2	9.5±0.7
1011.9±0.2	8.0±0.6
1024.6±0.3	3.6±0.4
1075.1±0.2	9.6±1.0
1105.2±0.2	7.4±0.4
1165.8±0.5	1.0±0.5
1220.9±0.3	5.0±0.5
1226.9±0.3	4.0±0.4
1233.7±0.5	0.8±0.4
1246.5±1.0	0.9±0.4
1322.4±0.3	7.0±0.9
1344.8±0.6	1.3±0.4
1364.8±0.6	1.7±0.6
1374.7±0.5	1.8±0.5
1463.6±0.5	1.0±0.3
1470.2±0.3	2.0±0.5
1680.7±0.8	0.8±0.2
2060.4±0.2	15.5±1.0
2085.0±0.5	0.1±0.05
2201.2±0.8	0.3±0.1

[a] Calculated from the decay scheme proposed later in the present study. Components of the observed annihilation photon intensity from Nd^{139g} and/or Pr^{139} decay always exceed the Nd^{139m} component.
[b] Seen in coincidence spectra only. The intensities given here are inferred from the completed decay scheme and the behavior of these photons in the coincidence spectra.

TABLE II. Relative intensities of photons in the decay of Nd^{139m} observed in coincidence experiments.

Energy (keV)	Relative intensity[a] Singles spectra	Anti-coincidence spectrum	113.8-keV γ-γ coinc. spectrum	113.8-keV γ-γ delayed coinc. spectrum	662-722 keV γ-γ coinc. spectrum	722-780 keV γ-γ coinc. spectrum
92.9	3.2	...	...	0.4	...	...
113.8	133.0	13	...	40	...	...
147.9	2.5	...	...	5	...	...
209.7	6.2	0.3	...	14	...	...
214.6	1.4	...	...	3	1.6	3.4
231.2	2.4	≡2.4[b]	...	<1.5	<1	<1
254.9	3.7	0.5	...	8.0	12	6.1
302.7	1.4	...	...	1.8	6.4	9.7
340.4	2.7	...	...	<0.6	<10	12
362.6	6.2	0.3	8	1.3	24	36
403.9	8.0	1.1	6	9.4	62	34
424.3	2.0	...	1	1.8	5.5	15
547.7	7.5	1.0	4	≡7.5	33	18
572.1	1.7	...	1	1.1	<4	16
601.2	1.3	...	2	<0.7	<6	<6
673.5	2.5	...	2	2.0	20	8
701.3	13	0.8	10	11	56	43
708.1	72	13	70	0.6	51	70
733	1.0	...	...	...	...	4
738.1	≡100	13	≡100	1.3	≡100	≡100
796.6	13	1.7	2	<1	18	48
802.4	21	2.3	14	18	98	60
810.1	18	2.4	17	<1	19	9.7
821.9	3.7	2.2	0.8	<1	<8	<8
828.1	29	5.7	3	0.9	35	103
851.9	1.4	0.4	...	<1	...	...
895.1	0.8	...	...	...	6	3
900.3	1.1	...	...	...	8	6
910.2	21.6	2.2	22	...	22	81
982.2	79	6.9	78	<1	285	461
1006.1	9.5	2.0	1	<1	11	40
1011.9	8.0	2.3	7	7.8	54	24
1024.6	3.6	0.5	4	<0.8	6.1	3
1075.1	9.6	1.8	9	<1	34	54
1105.2	7.4	1.4	4	6.6	43	27
1220.9	5.0	1.4	<1	<1	5.5	22
1226.9	4.0	0.6	2	4.7	21	12
1233.7	0.8	...	...	...	5	...
1322.4	7.0	1.6	5	<1	25	34
1344.8	1.3	...	0.8	<0.6	11	11
1364.8	1.7	...	1	0.9	10	6
1374.7	1.8	...	...	1.4	10	<8
2060.4	15.5	...	22	<5[d]	...	...
2085.0	0.1	...	0.2[c]	...	...	...

[a] All relative intensities from the coincidence runs are normalized with the aid of the singles spectra relative intensities listed here.

[b] This isomeric transition in Nd^{139} was the only transition seen which was not seen in coincidence with at least one other photon, thus it was used for normalization here.

[c] Only two counts observed.

[d] Limit placed on basis of absence of double escape peak and Compton background from the 2060.4-keV γ ray.

ground-state transitions, we employed an 8×8-in NaI(Tl) split annulus detector in an anticoincidence experiment with the 7-cm^3 Ge(Li) detector.[18] The Nd^{139m} source was inserted into the center of the annulus tunnel, which was then blocked by a 3×3-in. NaI(Tl) detector at one end and by the Ge(Li) detector at the other end. By including the 3×3-in. NaI(Tl) detector in anticoincidence with the Ge(Li) detector, the Compton edges from backscattering in the Ge(Li) detector were reduced over what they would have been with only the annulus in anticoincidence. The single-channel analyzers associated with the NaI(Tl) detectors were set to accept all γ rays above 80 keV. A resolving time (2τ) of ≈100 nsec was used, and the true-to-chance ratio was usually ≈100/1. The resulting spectrum is shown in Fig. 2.

The 231.2- and 821.9-keV γ-ray peaks seen here were enhanced in the anticoincidence experiments (relative to their singles intensities) far more than were any of the other Nd^{139m} transitions, as indicated in Table II. Thus, each of the other Nd^{139m} γ rays appeared to be involved in one or more coincidences with ≳80-keV photons. The following coincidence experiments elucidated most of these cascades.

A coincidence spectrum gated by the split annulus detector on the 113.8-keV γ is shown in Fig. 3. The γ-ray intensities seen in this experiment, normalized to

[18] R. L. Auble, D. B. Beery, G. Berzins, L. M. Beyer, R. C. Etherton, W. H. Kelly, and Wm. C. McHarris, Nucl. Instr. Methods **51**, 61 (1967).

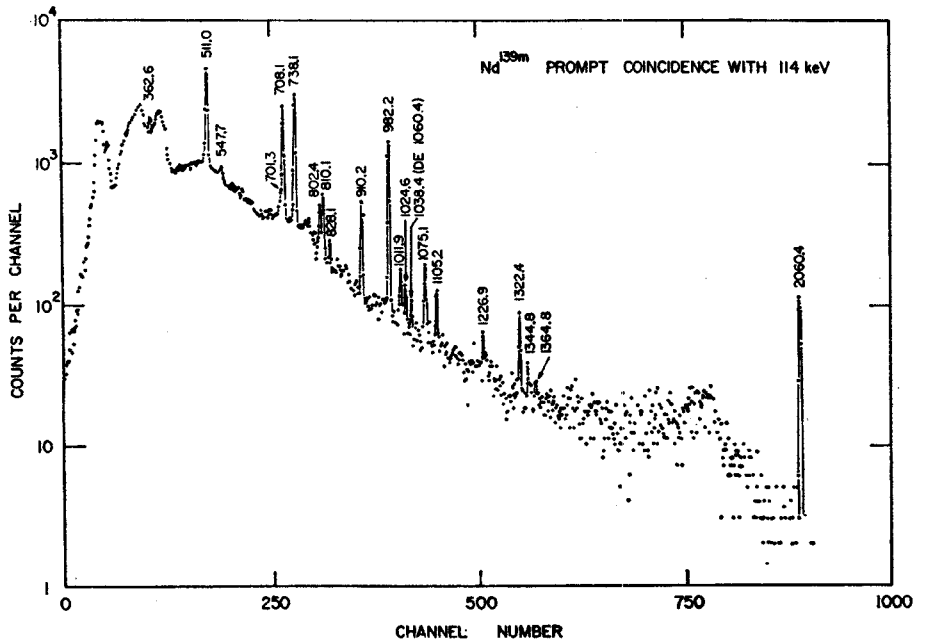

FIG. 3. Spectrum of Nd^{139m} γ rays in prompt coincidence with the 113.8-keV γ. The gate detector was the 8×8-in. NaI(Tl) split annulus, while the signal detector was the 7-cm^3 Ge(Li) detector. The results are listed in Table III.

TABLE III. Summary of γ-γ anticoincidence and coincidence experiment results.

Gate interval[a] (keV)	γ in gate[b] (keV)	γ's enhanced[c] (keV)	Figure No.
Anticoincidence	≈80–2500	231.2, 821.9[e]	2
110–118	113.8[d]	362.6, 601.2, 708.1,[e] 810.1, 910.2, 982.2, 1024.6, 1038*DE*, 1075.1, 1322.4, 1344.8, 2060.4, 2085.0	3
110–118 Delayed display spectrum	113.8[d]	147.9, 209.7, 214.6, 254.9, 302.7, 403.9, 424.3, 547.7, 572.1, 673.5, 701.3, 802.5, 1011.9, 1105.2, 1226.9, 1364.8, 1374.7	6
400–408	403.9	701.3	f
500–600	511.0, *547.7*	362.6	f
450–550	*511.0*, 547.7	...	f
680–720	673.5, 701.3, *708.1*[e], 733, 738.1	254.9, 302.7, 403.9, 673.5, 701.3, 802.5, 895.1, 900.3, 1011.9, 1105.2, 1226.9, 1233.7, 1364.8, 1374.7	4
720–760	701.3, 708.1[e], 733, *738.1*	214.6, 340.4, 362.6, 733, 982.2, 1075.1, 1322.4	5
790–840	796.6, 802:4, *810.1*, 821.9[e] *828.1*, 851.9	209.7, 302.7, 424.3, 572.1 796.6, 828.1, 910.2, 1006.1, 1220.9	f
840–900	*828.1*, 851.9, 895.1, 900.3, *910.2*	601.2, 810.1, 1024.6, 1165.8	f
950–1150	*982.2*, 1006.1, 1011.9, 1024.6, 1075.1, 1105.2, 1165.8	214.6, 340.4, 362.6, 851.9	f
1180–1300	1165.8, *1220.9* *1220.9*, 1233.7, 1246.5	821.9, 828.1	f
1900–2200	*2060.4*, 2085.0, 2201.2	113.8	f

[a] Prompt coincidence timing except where specified otherwise.
[b] Italicized γ energies carry the bulk of the γ intensity in the gates.
[c] That is, enhanced with respect to spectrum gated on adjacent regions. Conclusions summarized here are based on relative γ intensities in Table II, comparisons with results of other coincidence runs (to reduce gated background effects), and consideration of relative γ intensities within each run (to reduce effect of pulse heights on timing).
[d] Approximately $\frac{1}{3}$ of the population of the 113.8-keV state follows decay of the 821.9-keV state with a 40 nsec $t_{1/2}$.
[e] Delayed γ ray due to 40-nsec half-life of 821.9-keV state.
[f] These spectra can be seen in Ref. 19.

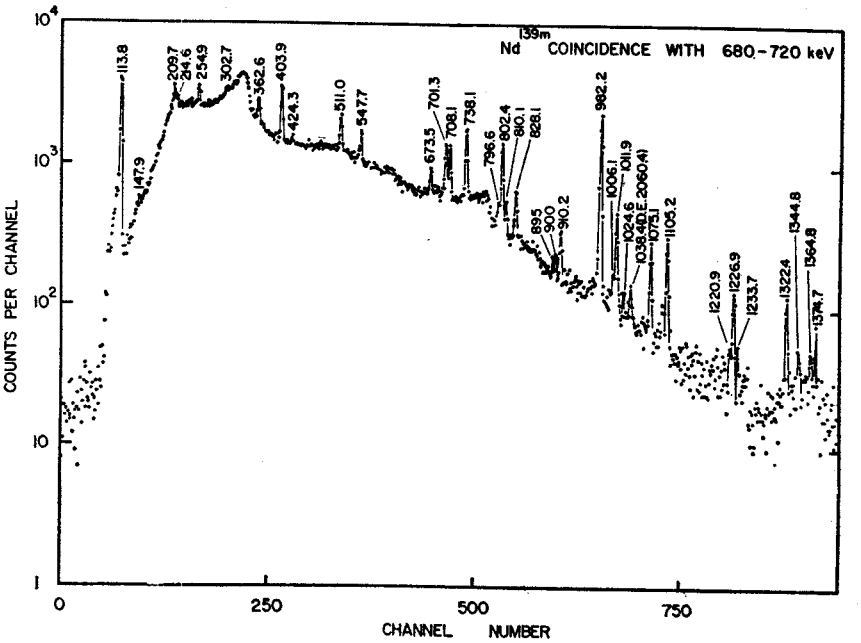

FIG. 4. Spectrum of Nd^{139m} γ rays in coincidence with the 680–720-keV energy interval. The gate signals came form the 8×8-in. NaI(Tl) split annulus.

100 for the 738.1-keV γ intensity, are listed in Table II. Here, four γ intensities are reduced by factors of about 10, viz., the 796.6-, 828.1-, 1006.1-, and 1220.9-keV γ's, whereas several other prominent peaks appear to be in coincidence with the intense 113.8-keV γ. These results are indicated in Table III.

In Figs. 4 and 5, we have the spectra resulting from gating this same spectrometer on two adjacent energy intervals, 680–720 and 720–760 keV. Because the resolution of the annulus in these experiments was only $\approx$13%, there was considerable overlap between these gated regions; however, as can be seen in Fig. 1(a) a single γ ray dominates each region, so a comparison of the intensities observed in coincidence with these adjacent gated regions was quite useful in constructing the decay scheme.

A comparison of the spectra recorded with adjacent coincidence gates also aided us in determining the effects of the underlying Compton backgrounds inevitably in the gates. In all we used 12 different gated

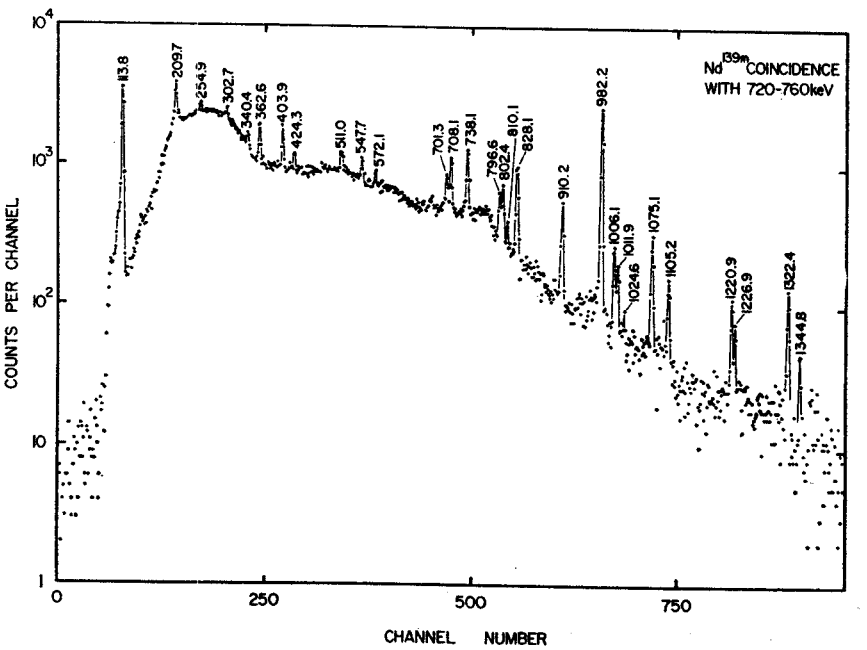

FIG. 5. Same as Fig. 4, except that the NaI(Tl) gate was set on the adjoining 720–760-keV energy interval.

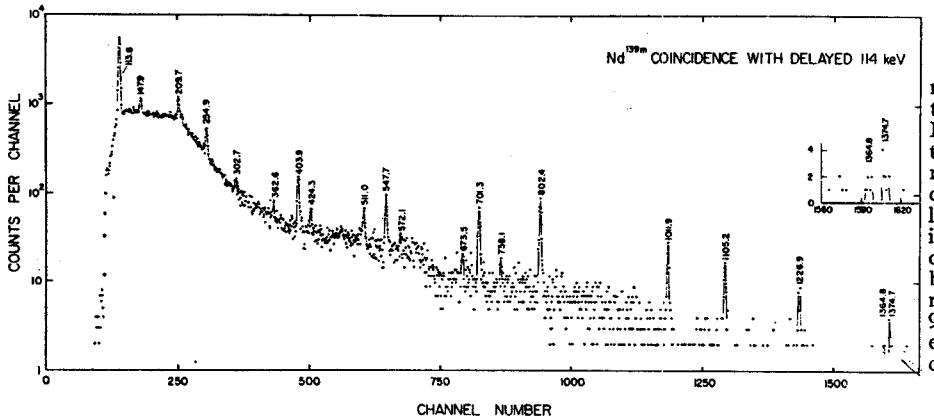

FIG. 6. Spectrum of Nd^{139m} γ rays in delayed coincidence with the 113.8-keV γ. A 3×3-in. NaI(Tl) scintillator was gated on the 113.8-keV γ and the timing resolution (2τ) of the coincidence circuit was ≈100 nsec, but a delay of ≈200 nsec was introduced into the Ge(Li) side of the circuit. Several peaks are enhanced by up to two orders of magnitude relative to the 708.1-, 738.1-, and 910.2-keV peaks, which were seen earlier to be in prompt coincidence with the 113.8-keV γ.

regions to obtain coincidence spectra[19] similar to those of Figs. 4 and 5. The results are summarized in Tables II and III.

C. Delayed Coincidence Experiments

It is possible that our single most useful coincidence experiment was a delayed coincidence experiment using a 3×3-in. scintillator and the Ge(Li) detector. The 3×3-in. NaI(Tl) scintillator was gated on the 113.8-keV γ, the coincidence timing resolution (2τ) was ≈100 nsec, and a delay of ≈200 nsec was added to the Ge(Li) side of the coincidence circuit. The resulting spectrum is shown in Fig. 6. Several peaks are enhanced up to 2 orders of magnitude relative to the 708.1-, 738.1-, and 910.2-keV peaks, which were seen earlier to be in prompt coincidence with the 113.8-keV γ. The intensities from this spectrum are listed in Table II. Later (Sec. IV A), we shall describe how this delayed coincidence spectrum confirms the placement of nine states in Pr^{139}.

The state responsible for the delays lies at 821.9 keV, and in order to measure its half-life, we used a fast-slow coincidence system with two 2×2-in. NaI(Tl) detectors and a time-to-amplitude converter (TAC). Now, from our prompt and delayed coincidence data we had no evidence for delays connected with states other than the 821.9-keV state. For this reason and because of leading-edge walk problems with lower-energy γ rays, we triggered the system with (prompt and delayed) pulses above 600 keV. The timing was chosen so that the prompt coincidence peak would be centered in the 512-channel analyzer used.

The time spectrum that remained following subtraction of the 17-counts/channel background is shown in Fig. 7. The resolution of the system was 3.3-nsec FWHM, and the timing calibration was made by inserting precisely measured pieces of delay cable into the circuit. No difficulties connected with channel widths or nonlinearities in the TAC were noted, so no corrections were made for these. The half-life calculated following a

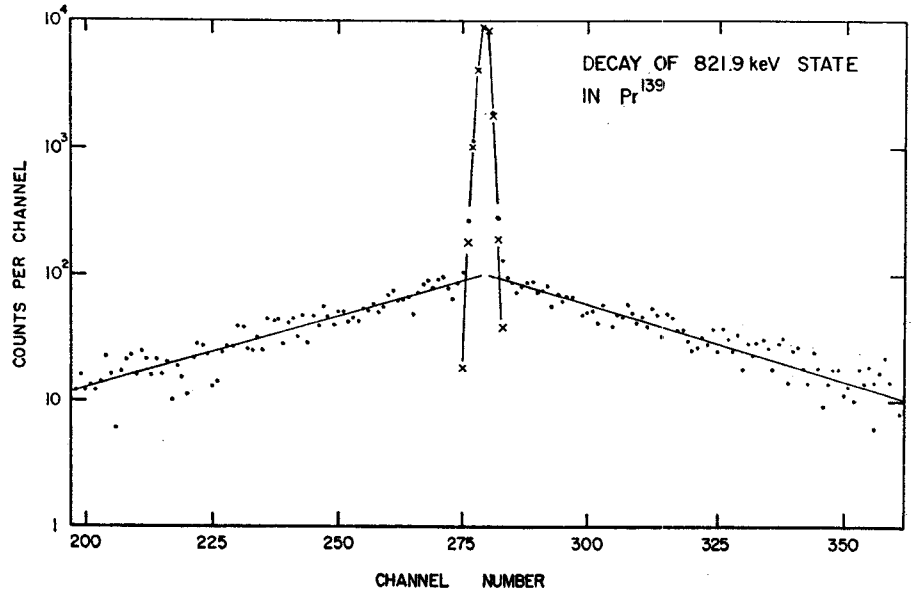

FIG. 7. Time-to-amplitude converter decay curve for the 821.9-keV state in Pr^{139}. The circuit used was symmetrical, with identical 2×2-in. NaI(Tl) detectors (gated on all pulses above 600 keV) starting and stopping a TAC. The calibration is 1.55 keV/channel, and the measured $t_{1/2}$ of the state is 40±2 nsec. Subtraction of the least-squared straight-line fit to the points produces the points indicated by x's, which show the resolution of the system to be 3.3-nsec FWHM.

[19] These are displayed in D. B. Beery, Ph.D. thesis, Michigan State University, 1969 (unpublished).

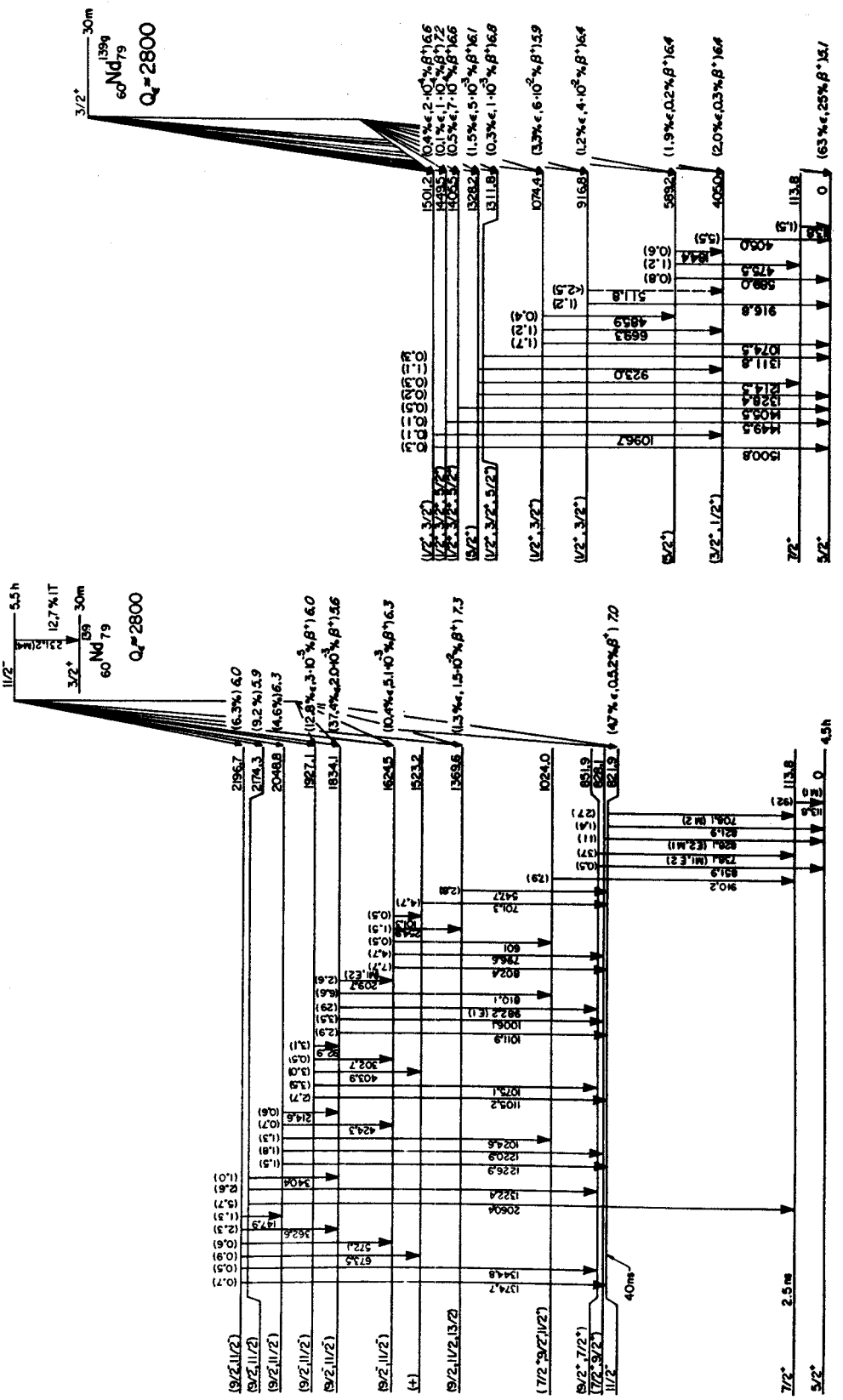

FIG. 8. Decay schemes of Nd^{139m} and Nd^{139g}. All energies are given in keV and (total) transition intensities are given in percent of the disintegrations of the respective parent. The β^+/ϵ ratios are calculated values and the log ft values (in italics on the right-hand sides of the levels) are calculated on the basis of 5.5-h and 30-min half-lives.

TABLE IV. Cascade energy relations for Nd^{139m} γ rays.

γ rays in sum	Sum	State energy adopted
821.9	821.9	821.9
113.8+708.1	821.9	
851.9	851.9	851.9
113.8+738.1	851.9	
802.4+821.9	1624.3	1624.5
796.6+828.1	1624.7	
601+910.2+113.8	1625	
254.9+547.7+821.9	1624.5	
101.3+701.3+821.9	1624.5	
1011.9+821.9	1833.8	1834.1
1006.1+828.1	1834.2	
982.2+851.9	1834.1	
810.1+910.2+113.8	1834.1	
209.7+802.4+821.9	1834.0	
1105.2+821.9	1927.1	1927.1
1075.1+851.9	1927.0	
403.9+701.3+821.9	1927.1	
302.7+(1624.5 state)	1927.2	
92.9+(1834.1 state)	1927.0	
1226.9+821.9	2048.8	2048.8
1220.9+828.1	2049.0	
1024.6+910.2+113.8	2048.6	
424.3+(1624.5 state)	2048.8	
214.6+(1834.1 state)	2048.7	
2060.4+113.8	2174.2	2174.3
1322.4+851.9	2174.3	
340.4+(1834.1 state)	2174.5	
1374.7+821.9	2196.6	2196.7
1344.8+851.9	2196.7	
673.5+701.3+821.9	2196.7	
572.1+(1624.5 state)	2196.6	
362.6+(1834.1 state)	2196.7	
147.9+(2048.8 state)	2196.7	

least-squares fit of a straight line to the logarithms of the data in Fig. 7 was 40±2 nsec. No evidence of decays with different half-lives was observed in this experiment. The ratio of the areas under the prompt peak and the delayed curves are consistent with our decay scheme and our interpretation that the 821.9-keV state decays with a 40-nsec half-life.

IV. Nd^{139m} DECAY SCHEME

We have constructed a decay scheme for Nd^{139m} from the results of our coincidence studies and the energy sums and relative intensities of the transitions. This decay scheme is shown in Fig. 8, together with the decay scheme for Nd^{139g}, which we shall discuss later. The striking difference between the two decay schemes is worthy of note with the 113.8-keV γ being the only common transition. All energies are given in keV, and the Q_ϵ is a calculated value.[20] Total transition intensities are given in units of percent per disintegration of the parent Nd ^{139m} parent. The β^+/ϵ ratios are also calculated values using the method of Zweifel.[21] In general, the energy sums of competing crossover and cascade transitions agree to within ±0.2 keV. Because there are so many coincident, cascading transitions in this nucleus, there are many checks as to the energies of most of the levels. The energy assigned for each level is therefore a weighted value based both on the transitions that feed into and out of that level. Both because there are an abnormally large number of γ-ray branchings in this nucleus and because our interpretation of the higher-lying states makes it essential that they be convincingly placed, we have presented the relevant sets of sums in Table IV, where it can be seen that the self-consistency is excellent.

A. 113.8-keV Level and Those That Are Depopulated through It

The large relative intensity of the 113.8-keV γ combined with its coincidence behavior lead us to place a first-excited state at 113.8 keV, in agreement with earlier studies.[8,5]

The isomeric state at 821.9 keV was first placed on the basis of several prompt-coincidence experiments having timing resolutions (2τ) of ≈100 nsec (see, e.g., Table III). It was then confirmed by the delayed coincidence experiment of Fig. 6, which suggested that seven levels above 821.9 keV are depopulated through the 821.9-keV state. The γ transitions presumed to originate from these levels were enhanced by roughly two orders of magnitude over their intensities in prompt coincidence experiments (cf. Table II), and the ratio of each intensity to that of, say, the 547.7-keV γ is within ≈20% of what it was in the singles spectra. Not only were the direct transitions from these levels to the 821.9-keV state enhanced, but so were a myriad of interconnecting transitions. (At γ-ray energies below 300 keV, quantitative comparisons of the delayed γ-ray intensities with our decay scheme were significantly less precise because the earlier crossovers of the lower-energy pulses artificially introduced enhancement factors of >2 into the delayed coincidence spectrum.) The energies of these seven Pr^{139} states, at 1369.6, 1523.2, 1624.5, 1834.1, 1927.1, 2048.8, and 2196.7 keV, were assigned from the weighted energy sums listed in Table IV.

B. 828.1-, 851.9-, 1024.0-, and 2174.3-keV States

These four states are suggested by energy sums and relative γ-ray intensities (cf. Table I), as well as by the prompt coincidence data (Tables II and III). The absence from Fig. 6 of all ten of the γ rays indicated in our decay scheme to feed the 828.1-, 851.9-, and 1024.0-keV states is consistent with our interpretation of the positions of these states.

The 828.1-keV state is also confirmed by the suppression of the 796.6-, 828.1-, 1006.1, and 1220.9-keV γ's in the prompt coincidence experiments gated on the 113.8-keV γ (see Fig. 3 and Table II).

C. Remaining γ Rays

The 12 very weak γ rays observed at 733, 895.1, 900.3 1165.8, 1233.7, 1249.9, 1364.8, 1463.6, 1470.2, 1681,

[20] J. H. E. Mattauch, W. Thiele, and A. H. Wapstra, Nucl. Phys. 67, 1 (1965); 67, 32 (1965); 67, 73 (1965).
[21] P. F. Zweifel, Phys. Rev. 107, 329 (1957).

TABLE V. Multipolarity of γ transitions.

Transition energy[a] (keV)	K-electron intensity[b]	γ-ray intensity[c]	Experimental α_K	Theoretical α_K				Multipolarity
				$E1$	$E2$	$E1$	$E3$	
209.7	25±14	6.2±0.6	9.7(−2)	3(−2)	1.2(−1)	1.3(−1)	4.6(−1)	$M1, E2$
						$M3$	$M4$	
231.2	≡1000	2.4±0.2	≡9.5[d]	...	...	2.4	9.5	$M4$[e]
				$E3$	$M2$	$E4$	$M3$	
708.1	152±8	72±2	≡1.74(−2)[d]	9.5(−3)	1.74(−2)	2.0(−2)	4.1(−2)	$M2$[e]
				$E1$	$E2$	$M1$	$E3$	
738.1	≈50±7	≡100	4(−3)	1.4(−3)	3.6(−3)	5.6(−3)	8.1(−3)	$M1, E2$
				$E1$	$E2$	$M1$	$E3$	
828.1	10±3	29±2	3(−3)	1.2(−3)	2.8(−3)	4.4(−3)	6.3(−3)	$E2, M1$
				$E1$	$E2$	$M1$	$E3$	
982.2	8±2	79±2	8(−4)	8.3(−4)	2.0(−3)	2.9(−3)	4.2(−3)	$E1$

[a] Energies from present study.
[b] Relative K-electron intensities from Ref. 8.
[c] Relative γ-ray intensities from present work.
[d] The theoretical value of Ref. 23 was used, as Ref. 4 and Ref. 8 agreed on a multipolarity for this transition based on measured K/L electron intensity ratios.
[e] See Refs. 4 and 8 for descriptions of two independent measurements of this multipolarity.

2085.0, and 2201.2 keV have not been definitely placed in the level scheme. These γ rays do not fit between any existing states and do not significantly change the interpretation of the level scheme or its comparison with other nuclei or with theoretical calculations. The sum of these γ-ray intensities amounts to only 1.5% of the observed Nd^{139m} γ-ray intensity. Some tentatively suggested placements follow.

The 733-keV γ was seen only in coincidence with the 738.1-keV γ. The energies of these two sum to 1471.2 keV, within the measured uncertainty of the 1470.2-keV γ, thus tentatively suggesting a level at 1584.0 keV.

Evidence involving poor statistics indicates that the 2085.0-keV γ is in coincidence with the 113.8-keV γ, whereas the 2201.2-keV γ is not. On these grounds alone, tentative states at 2198.8 and 2201.2 keV may be inferred.

In order to obtain a lower limit for the logft values of transitions to these "unplaced" states, we assumed that each unplaced state was fed directly by ϵ decay and deexcites entirely by the unplaced γ rays. It then followed that the corresponding logft values would all be larger than about 7.8.

The properties of a few of the remaining five very weak γ rays (1165.8, 1233.7, 1249.9, 1463.6, and 1681 keV) can be seen in Table II. We are not able to find a unique location from them in our decay scheme. The sum of their intensity is less than 0.7% of the total observed Nd^{139m} γ rays.

V. SPIN AND PARITY ASSIGNMENTS FROM Nd^{139m} DECAY

A. Electron Data and Multipolarities

We compared our γ intensities with the conversion-electron intensity data of Gromov *et al.*[8,22] in order to gain multipolarity information about some of the more-intense lower-energy transitions following Nd^{139m} decay. These comparisons and predicted multipolarities are listed in Table V and plotted in Fig. 9. We were not able to use the conclusions of Gromov *et al.* directly because their γ intensities were obtained with NaI(Tl) scintillators and differ markedly from our data. However, from K/L conversion intensity ratios, the 231.2- and 708.1-keV transitions have been established to be $M4$ and $M2$, respectively, by both sets of previous workers.[8,5] The theoretical conversion coefficients[23] for these transitions were then used as a basis for determining the remaining coefficients. At lower energies ($\lesssim$300 keV) it appeared that the coefficients were affected by absorption in the electron-counter window.

B. Ground and Metastable States of Nd^{139}

Here, at $N=79$, one ought to consider three-quasiparticle (hole) states, but to a reasonable first approximation the low-lying ones can be thought of as single-hole states, so there are some similarities with the $N=81$ nuclides. Among the latter, there are now seven known that have $d_{3/2}$ ground states and $h_{11/2}$ isomeric states connected by $M4$ isomeric transitions.[24] Also, the $N=79$ nuclei Te^{131}, Xe^{133}, Ba^{135}, and Ce^{137} (Refs. 25–28, respectively) have $\frac{3}{2}+$ ground states and $\frac{11}{2}-$ meta-

[22] K. Gromov, V. Kalinnikov, V. Kuznetsov, N. Lebedev, G. Musiol, E. Herrmann, Zh. Zhelev, B. Dzhelepov, and A. Kudryavtseva, Nucl. Phys. **73**, 65 (1965).

[23] L. A. Sliv and I. M. Band, in *Alpha-, Beta-, and Gamma-Ray Spectroscopy*, edited by K. Siegbahn (North-Holland Publishing Co., Amsterdam, 1965).

[24] R. E. Eppley, Wm. C. McHarris, D. B. Beery, and W. H. Kelly, The New Isomer Gd^{145m} and the $N=81$ $M4$ Transition Probabilities (to be published).

[25] L. M. Beyer, G. Berzins, and W. H. Kelly, Nucl. Phys. **A93**, 436 (1967); W. B. Walters, C. E. Bemis, and G. E. Gordon, Phys. Rev. **140**, B268 (1965).

[26] J. M. Ferguson, D. L. Love, and D. Sam, J. Inorg, Nucl. Chem. **24**, 1 (1962).

[27] S. Morinobu, T. Hirose, and K. Hisatake, Nucl. Phys. **61**, 613 (1965).

[28] R. B. Frankel, Ph.D. thesis, University of California, Berkeley, Lawrence Radiation Laboratory Report No. UCRL-11871, 1964 (unpublished); D. B. Beery, W. H. Kelly, and Wm. C. McHarris (to be published).

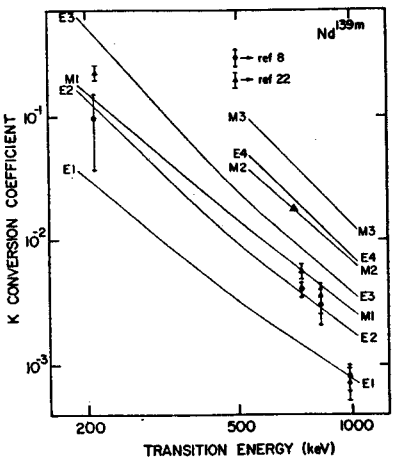

FIG. 9. A comparison of experimental and theoretical K-conversion coefficients for some of the γ transitions following Nd^{139m} decay. The lines are the theoretical values of Sliv and Band in Ref. 23. The data points were obtained by comparing the electron intensities of Gromov *et al.* (see Refs. 8, 22) with our γ-ray intensities, assuming the theoretical values of the 231.2- ($M4$) and 708.1-keV ($M2$) transitions to be correct for purposes of normalization.

stable states. Thus, when K-L conversion electron energy differences suggested that the 231.2-keV transition occurs in Nd rather than in Pr and the conversion line intensity confirmed that the transition was an $M4$, this indicated a similar $d_{3/2}$-$h_{11/2}$ isomer pair. We have plotted the energies of the $N=79$ and $N=81$ isomers in Fig. 10, including Nd^{139m} and a projection for Sm^{141m}.[29]

It is instructive to compare the reduced transition probability of the 231.2-keV γ with those of the other $M4$ γ rays, for these isomeric transitions should be among the best examples of true single-particle transitions. In Fig. 10, we have also plotted the squares of the radial matrix elements, $|M|^2$, of these transitions. These were calculated using Moszkowski's approximations for single-neutron transitions[30]

$$T_{SP}^{(ML)}=\frac{0.19(L+1)}{[(2L+1)!!]^2}|M|^2\left(\frac{\hbar\omega}{197\ \mathrm{MeV}}\right)^{2L+1}$$
$$\times[a \text{ in } 10^{-13}\ \mathrm{cm}]^{2L-1}\times S(j_i, L, j_f)\times 10^{21}\ \mathrm{sec}^{-1}.$$

Here, $T_{SP}^{(ML)}$ is the single-particle transition probability, L ($=4$ for $M4$'s) is the multipolarity, a ($=1.2\times 10^{-13}$ cm) is the effective nuclear radius, and $S(j_i, L, j_f)$ is a statistical factor (i.e., angular-momentum portion of the matrix element), which for $\frac{11}{2}\rightarrow\frac{3}{2}$ transitions has the value $\frac{15}{11}$.

The resulting values we obtained are consistently smaller than the approximation of a constant wave function,

$$|M|^2=[3/(L+2)]^2(\mu_n L)^2=14.6,$$

where μ_n is the magnetic moment of the neutron. This fact should not concern us, for $M4$ transitions are normally retarded over such estimates and one needs much more detailed information about the nuclear wave functions in order to make detailed comparisons meaningful. What is of more importance is the fact that the values of $|M|^2$ are not constant but show a definite trend in both the $N=79$ and $N=81$ nuclei. (It is unusual for $|M|^2$ not to be constant over such a series. For example, in the odd-mass neutron-deficient lead isotopes, $|M|^2$ was constant to the point that an apparent 15% discrepancy at Pb^{203} suggested that an unobserved transition was competing with the $M4$ isomeric transition. This competing transition was later discovered.[31])

Both because collective modes of the core would not be expected to contribute appreciably to a hexadecapole field and because the $h_{11/2}$ states cannot be mixed readily with other states in these nuclei, these $M4$ transitions should prove a more sensitive test of, say, $d_{5/2}$ and perhaps $s_{1/2}$ admixtures in the $d_{3/2}$ states than would normally be possible from electromagnetic transition rates. The fact that the $|M|^2$ values for the $N=79$ nuclei are consistently larger than those for the $N=81$ nuclei goes along with this, for the $N=79$ three-quasiparticle states would be expected to be much less pure, and only to a (good) first approximation can the transitions be characterized as proceeding from a pure $[(d_{3/2})^2 h_{11/2}]_{11/2-}$ to a pure $[(d_{3/2})^3]_{3/2+}$ configuration. A more complete analysis of these $M4$ transitions, using the occupation number formalism, is presently underway.[24]

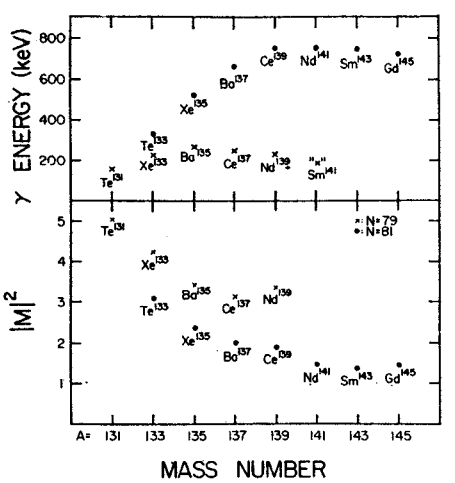

FIG. 10. Upper: Energies of the metastable states in the $N=79$ and $N=81$ isotones. (The Sm^{141} point is a predicted one.) Lower: Values of the squared radial matrix elements for the isomeric transitions in the same nuclei.

[29] R. Todd, R. E. Eppley, D. B. Beery, W. H. Kelly, and Wm. C. McHarris (unpublished).

[30] S. A. Moszkowski, in *Alpha-, Beta-, and Gamma-Ray Spectroscopy*, edited by K. Siegbahn (North-Holland Publishing Co., Amsterdam, 1965); S. A. Moszkowski, Phys. Rev. 89, 474 (1953).

[31] R. E. Doebler, Wm. C. McHarris, and C. R. Gruhn, Nucl. Phys. A120, 489 (1968).

C. Ground, 113.8-, and 821.9-keV States in Pr^{139}

The ground state of Pr^{139} is fed by the $d_{3/2}$ ground state of Nd^{139}. In our study of this decay (see below, Secs. VI, VII) we obtained a logft value of 5.1 for this transition, which suggests $\frac{1}{2}+$, $\frac{3}{2}+$, or $\frac{5}{2}+$ for the ground state of Pr^{139}. Any of these assignments could be consistent with the observed[2] 99% of Pr^{139} β-decay (log$ft=5.3$) to the $\frac{3}{2}$ ground state of Ce^{139}. The simple shell-model predictions by Kisslinger and Sorensen,[32] and systematics of odd-mass nuclei with odd proton numbers between 51 and 63 indicate $\frac{5}{2}+$ and $\frac{7}{2}+$ configurations for the two lowest levels of Pr^{139}. Sixteen nuclei in this region have ground state and first excited states well characterized,[6] and in every case the assignments are $\frac{5}{2}+$ and $\frac{7}{2}+$ or $\frac{7}{2}+$ and $\frac{5}{2}+$.

The measured K and L conversion electron intensities for the 113.8-keV transition and its 2.5-nsec half-life[33] are characteristic of the l-forbidden $M1$ transitions between $g_{7/2}$ and $d_{5/2}$ states. Sixteen of these also have been measured[6] in odd-proton nuclei between $Z=51$ and $Z=63$.

No direct β-population of the 113.8-keV state was observed from either the $\frac{3}{2}+$ or $\frac{1}{2}-$ states of Nd^{139}. This is consistent with a $\frac{7}{2}+$ assignment for this state. Our upper limit of 3% ϵ decay to it from Nd^{139m} places a lower limit for the logft at 7.6, although we really expect the logft to be appreciably higher. The ϵ decay from some of the $h_{11/2}$ Te and Sn isomers to $g_{7/2}$ states in their daughter nuclei has been observed,[34] and the logft's cluster around 9. For an estimated log$ft=9$ for decay to the 113.8-keV state in Pr^{139}, the corresponding ϵ decay is only 0.1%.

The above cumulative evidence rather strongly suggests $\frac{5}{2}+$ and $\frac{7}{2}+$ assignments for the ground and first excited states in Pr^{139}, which would imply $d_{5/2}$ and $(g_{7/2})^{-1}(d_{5/2})^2$ configurations.

The measured α_K (Table V) of the 708.1-keV transition indicated it to be an $M2$, and this, combined with our evidence of direct feeding of the 821.9-keV state by Nd^{139m}, suggests this state to be $\frac{11}{2}-$. Our measured 40-nsec $t_{1/2}$ is consistent with this assignment. We have not determined the amounts of admixing in the γ transitions, but Weisskopf single-particle estimates[35] for the $t_{1/2}$'s of a 708.1-keV pure $M2$ and an 821.9-keV pure $E3$ are 1.2×10^{-9} and 1.3×10^{-6} sec, respectively. Thus, the $M2$ (partial $t_{1/2}=42$ nsec) appears to be retarded over the single-particle estimate. This is not particularly surprising, however, as $M2$'s are customarily retarded. More interesting, the $E3$ (partial $t_{1/2}=600$ nsec) appears to be *enhanced* over the single-particle estimate, and $E3$'s also are most often retarded.[36] However, there are three other known enhanced $E3$'s, in La^{137}, Eu^{147}, and Eu^{149} (Refs. 37 and 38), all just below or above the $N=82$ shell. More will be said about this in Sec. IX in terms of possible octupole admixtures in the 821.9-keV state, but the dominant characteristics of this state warrant the assignment $h_{11/2}$. The logft of 7.0 for the ϵ population of this state is high but certainly within the realm of possibilities for an $\frac{11}{2}-\longrightarrow\frac{11}{2}-$ allowed transition. We shall see later (Sec. IX) that the reason for this is that a multiparticle rearrangement is necessary for Nd^{139m} to populate this state.

D. 828.1-, 851.9-, and 1024.0-keV States

The 828.1-keV γ appears to be of $E2$ and/or $M1$ multipolarity, which sets limits of $\frac{1}{2}+$ through $\frac{9}{2}+$ on the 828.1-keV state. This state is fed strongly by the 1624.5-, 1834.1-, and 2048.8-keV states, each of which is populated directly by $\frac{11}{2}-$ Nd^{139m}, so $\frac{1}{2}+$, $\frac{3}{2}+$, and possibly $\frac{5}{2}+$ can probably be eliminated. If the state were $\frac{9}{2}+$, one might expect some direct ϵ feeding (first forbidden); we see none, but our limits are not too precise on this—we mention it in anticipation of the problems that will arise concerning some of the higher-lying states. A $\frac{9}{2}+$ assignment would also suggest that the 828.1-keV transition be pure $E2$, but again the precision in α_K does not allow one to say concretely whether this transition does or does not contain some $M1$ character. We can place an upper limit of 0.27% (of Nd^{139m} disintegrations) on the missing 714.3-keV γ to the $\frac{7}{2}+$ 113.8-keV state. The absence of this transition is slightly surprising, considering either a $\frac{7}{2}+$ or $\frac{9}{2}+$ assignment, but, for example, a core-coupled configuration involving the $d_{5/2}$ ground state could result in either but would explain the absence of such a transition. We are left with both $\frac{7}{2}+$ and $\frac{9}{2}+$ as possible assignments.

Using the same approach with the 851.9-keV state, we obtain $\frac{9}{2}+$ as the probable assignment, with $\frac{7}{2}+$ as a somewhat less likely alternative. Again, the 738.1-keV γ appears to be $M1$ and/or $E2$, which sets limits of $\frac{3}{2}+$ through $\frac{11}{2}+$ for the state. This state is fed strongly by the 1834.1-, 1927.1-, 2174.3−, and 2196.7-keV states, each of which is populated directly by what looks like an allowed transition. In particular, the intense 982.2-keV γ from the 1834.1-keV state—the state with the strongest claim to being a high-spin $(\frac{9}{2},\frac{11}{2})$ odd-parity state—is characterized as an $E1$. This permits us to narrow the assignments down to $\frac{7}{2}+$, $\frac{9}{2}+$, and $\frac{11}{2}+$. $\frac{11}{2}+$ can be ruled out on the basis of the branching ratio of the 738.1- and 851.9-keV γ's, for it would force the 851.9-keV γ to be an $M3$, which has a predicted (single-particle estimate) $t_{1/2}$ of 1.0×10^{-6} sec, as compared with only 2.7×10^{-11} sec for a 738.1-keV $E2$. The

[32] L. S. Kisslinger and R. A. Sorensen, Kgl. Danske Videnskab. Selskab, Mat.-Fys. Medd. **32**, No. 9 (1960).
[33] A. A. Sorokin, Zh. Eksperim. i. Teor. Fiz. **47**, 1232 (1964) [English transl.: Soviet Phys.—JETP **20**, 833 (1965)].
[34] G. Berzins and W. H. Kelly, Nucl. Phys. **A92**, 65 (1967); L. M. Beyer, G. Berzins, and W. H. Kelly, *ibid.* **A93**, 436 (1967).
[35] A. H. Wapstra, G. J. Nijgh, and R. van Lieshout, in *Nuclear Spectroscopy Tables* (North-Holland Publishing Co., Amsterdam, 1959).
[36] C. F. Perdrisat, Rev. Mod. Phys. **38**, 41 (1966).
[37] J. R. Van Hise, G. Chilosi, and N. J. Stone, Phys. Rev. **161**, 1254 (1967).
[38] E. Yu. Berlovich, V. N. Klementyev, L. V. Krasnov, M. K. Kikitin, and I. Yurski, Nucl. Phys. **23**, 481 (1961).

TABLE VI. Weisskopf single-particle estimates for γ rays depopulating the high odd-parity states in Pr^{139}.

State energy (keV)	γ-ray energy (keV)	Relative intensity[a] (1%)	Single-particle estimate[b] for $t_{1/2}$ (sec) (corrected for conversion) $E1$	$M1$	$E2$
1624.5	101.3	6.5	1.1(−13)	1.6(−11)	3.8(−7)
	254.9	20	9.5(−15)	1.4(−12)	5.1(−9)
	601	6.5	7.8(−16)	1.1(−13)	7.6(−11)
	796.6	61	3.4(−16)	4.9(−14)	1.9(−11)
	802.4	≡100	3.3(−16)	4.8(−14)	1.8(−11)
1834.1	209.7	9.0	1.6(−14)	2.3(−12)	1.3(−8)
	810.1	23	3.2(−16)	4.7(−14)	1.7(−11)
	982.2	≡100	1.8(−16)	2.6(−14)	6.6(−12)
	1006.1	12	1.7(−16)	2.4(−14)	5.8(−12)
	1011.9	10	1.7(−16)	2.4(−14)	5.7(−12)
1927.1	92.9	89	8.2(−14)	1.2(−11)	3.3(−7)
	302.7	14	5.8(−15)	8.4(−13)	2.2(−9)
	403.9	86	2.5(−15)	3.7(−13)	5.4(−10)
	1075.1	≡100	1.4(−16)	2.0(−14)	4.2(−12)
	1105.2	77	1.3(−16)	1.8(−14)	3.6(−12)
2048.8	214.6	33	1.5(−14)	2.2(−12)	1.1(−8)
	424.3	39	2.2(−15)	3.2(−13)	4.3(−10)
	1024.6	72	1.6(−16)	2.3(−14)	5.3(−12)
	1220.9	≡100	9.5(−17)	1.4(−14)	2.2(−2)
	1226.9	83	9.3(−17)	1.3(−14)	2.2(−12)
2174.3	340.4	18	4.2(−15)	6.0(−13)	1.3(−9)
	1322.4	46	7.4(−17)	1.1(−14)	1.5(−12)
	2060.4	≡100	2.0(−17)	2.8(−15)	1.6(−13)
2196.7	147.9	57	3.7(−14)	5.4(−12)	5.9(−8)
	362.6	≡100	3.5(−15)	5.0(−13)	9.21(−10)
	572.1	26	9.1(−16)	1.3(−13)	9.7(−11)
	673.5	39	5.6(−16)	8.0(−14)	4.3(−11)
	1344.8	22	7.1(−17)	1.0(−14)	1.4(−12)
	1374.7	30	6.6(−17)	9.5(−15)	1.2(−12)

[a] The strongest γ ray from each level is arbitrarily given a relative intensity of 100% and the others are compared with this.

[b] Reference 29 as treated in Ref. 34.

branching ratio would also favor $\frac{9}{2}+$ ($M1$, $E2$ versus pure $E2$) over $\frac{7}{2}+$ (both $M1$, $E2$), but, as pointed out in connection with the 828.1-keV state, one has to know more about the internal structures of such states before other than gross decisions based on branching ratios can be made.

On the basis of the 910.2-keV γ to the $\frac{7}{2}+$ 113.8-keV state, a γ ray that is at least five times as intense as the unobserved 1024.0-keV ground-state γ ray, one can probably limit the spins of the 1024.0-keV state to a range of two units on either side of $\frac{7}{2}$. Because the state competes favorably for feeding from the 1624.5-, 1834.1-, and 2048.8-keV states, which again are fed directly by $\frac{11}{2}-$ Nd^{139m}, this range is biased toward the high-spin side of $\frac{7}{2}$. Finally, the lack of direct ϵ population (upper limit $\approx$0.4%) suggests even parity. Conclusion: $(\frac{5}{2}+)$, $\frac{7}{2}+$, $\frac{9}{2}+$, or $\frac{11}{2}+$ for this state.

E. High Odd-Parity States

The most intriguing aspect of this study is the population of (at least) six high-lying states in Pr^{139} by what appear to be allowed transitions from $\frac{11}{2}-$ Nd^{139m}. These six states, at 1624.5, 1834.1, 1927.1, 2048.8, 2174.3, and 2196.7 keV, are populated by ϵ decay with logft's that range from 5.6 to 6.3. This would seem to imply that these states have spins of $\frac{9}{2}$, $\frac{11}{2}$, or $\frac{13}{2}$, all with *odd* parity. Granted that logft values by themselves are not always reliable indicators of the degree of forbiddeness in β decay, still it is much more common for allowed transitions to be abnormally slow than for first-forbidden transitions to be abnormally rapid.[39] Also, the decay to the presumed $h_{11/2}$ 821.9-keV state should be, superficially at least, the most straightforward of the β-transitions from Nd^{139m}, and it has a logft of 7.0. Thus, these six high-lying states are favored for receiving population over the $h_{11/2}$ state. From this point of view, the ϵ decay to them is undoubtedly allowed. There are other indications, as well (to be described later), that they have odd parity. These six states also have other pecularities, among which are the large number of low-energy interconnecting γ transitions and the dearth of transitions to the low-lying states. In this section, we shall discuss these states somewhat phenomenologically, arriving only at estimates of the simplest external structures (i.e., spins and parities) consistent with our data, and will postpone the problems

[39] C. E. Gleit, C.-W. Tang, and C. D. Coryell, in *Nuclear Data Sheets*, compiled by K. Way *et al.* (U.S. Government Printing Office, National Academy of Sciences—National Research Council, Washington, D.C. 20418, 1963), NRC 5-5-109.

of detailed internal structure to Sec. IX, where it will be shown that they are three-quasiparticle states.

Now, although we have been perhaps overly conservative about drawing conclusions based on γ-ray branching ratios from the lower-lying states, the sheer number of competing γ rays from these high odd-parity states makes it a worthwhile endeavor to fathom at least whether or not useful information can be obtained by analyzing their various branchings. Consequently, we have assembled in Table VI the single-particle estimates for the $t_{1/2}$'s of all the γ rays originating from these states, assuming possible $E1$, $M1$, or $E2$ multipolarities. $M2$ and higher multipolarities were excluded on the basis of there being no likely mechanisms for enhancing them to the point that they could compete with the many possibilities for deexcitation by lower multipolarities. However, this tabulated information must be treated with circumspection, since the $E1$'s and $M1$'s could easily be retarded, as noted before; whereas, the $E2$'s could be either enhanced or not enhanced, depending on the collective or noncollective nature of the states involved. Also, because we expect some common internal structure among these states, differences between $M1$ and $E2$ transition rates may not be predictable; therefore, our most useful information will be expected to come from comparing transitions that lead to states not in the group of six.

Let us begin with the "prototype" state at 1834.1 keV. This state receives 37.4% of the ϵ decay, with $\log ft=5.6$, and the argument for its being $\frac{9}{2}-$, $\frac{11}{2}-$, or $\frac{13}{2}-$ is clearly stronger than for any of the other states. Of the five γ rays that deexite it, the intense 982.2-keV γ to the 851.9-keV state seems rather unambiguously to be an $E1$ (Table V, Fig. 9). This is additional evidence for odd parity, as we previously assigned the 851.9-keV state $\frac{9}{2}+$ or possibly $\frac{7}{2}+$. The $\frac{9}{2}+$ assignment would imply either $\frac{9}{2}-$ or $\frac{11}{2}-$ for the 1834.1-keV state, while the $\frac{7}{2}+$ assignment would limit it to $\frac{9}{2}-$.

At this point we can only check the consistency of the other γ rays with these assignments. The 1006.1-keV γ to the $(\frac{7}{2}+, \frac{9}{2}+)$ 828.1-keV state presumably is a parity-changing transition like the 982.2-keV γ, whereas the 1011.9-keV γ to the $\frac{11}{2}-$ 821.9-keV state is not. The simplest explanation is for the 1011.9-keV γ to be $M1$ and the 1006.1-keV γ to be $E1$. The pronounced difference in the rates of the 982.2- and 1006.1-keV "$E1$" γ's must be attributed to internal structures of the states. (We shall see later that there are strong implications that the transitions out of the high odd-parity multiplet are rather highly hindered, so small admixtures in the states involved could have strong effects on the transition rates.) Remembering that the latter is compatible with $\frac{7}{2}+$ for the 828.1-keV state, we are left with $\frac{9}{2}-$ and $\frac{11}{2}-$ for the 1834.1-keV state.

The relatively intense 810.1-keV γ would also appear to be an $E1$, allowing us to remove the $\frac{5}{2}+$ possibility for the 1024.0-keV state. The $M1$ and/or $E2$ assignment (Table V, Fig. 9) for the 209.7-keV γ adds nothing new, but we note that the 1624.5-keV state must be quite similar to the 1834.1-keV state for this transition to be so enhanced.

Arguments for the 1927.1-keV state, which receives 12.8% of the ϵ population, follow along similar lines. In particular, the 92.9-keV transition must be a collectively-enhanced $M1$ and/or $E2$, making the 1927.1- and 1834.1-keV states quite similar in origin. The 1105.2-keV γ to the 821.9-keV state may be $M1$, and the 1075.1-keV γ to the 851.9-keV state may be $E1$, all of which is consistent with $\frac{9}{2}-$ or $\frac{11}{2}-$ (equally probable) for the 1927.1-keV state. An educated guess for the 403.9-keV γ is $E1$, which would imply positive parity for the 1523.2-keV state.

The 2196.7-keV state also appears to be very closely related to the 1834.1-keV state, viz., the strong 362.6-keV γ. Arguments parallel those above, resulting in $\frac{9}{2}-$ or $\frac{11}{2}-$ as possible choices.

The 1624.5- and 2048.8-keV states are akin in that both favor depopulating to the 828.1- rather than the 851.9-keV state. In each case what would appear to be an $M1$ transition to the $\frac{11}{2}-$ 821.9-keV state competes most favorably with an apparent $E1$ to the 828.1-keV state. Arguments for odd parity are also weakest for these two states ($\log ft=6.3$ for ϵ decay to each), but the deexcitation pattern is no easier to interpret were we to assume high-spin even-parity states. Thus, we tentatively choose $\frac{9}{2}(-)$ or $\frac{11}{2}(-)$ as possible assignments. It is perhaps worth noting that, if our assignments are correct and the six "high odd-parity" states are indeed closely related, there seems to be an interesting gradation in properties, with the 1834.1-keV state standing toward the middle, being the only state directly connected to all the others by γ transitions. One example of this gradation is the strong transition between the 1927.1- and 1834.1-keV states, between the 1834.1- and 1624.5-keV states, and (less strong) between the 1624.5- and 1369.6-keV states—this contrasts with the weak transition between the 1927.1- and 1624.5-keV states and the absence of a transition (upper limit $\approx 0.2\%$) between the 1927.1- and 1369.6-keV states. (This sort of behavior ought to aid in sorting the states when shell-model calculations are done on our proposed three-quasiparticle configuration for these states.)

The 2174.3-keV state stands somewhat apart from the other five in that it is the only one to deexcite directly to the lowest states in Pr^{139} and to miss populating several of the other five with quite intense γ rays. Its large ϵ population ($\log ft=5.9$) does, however, indicate $\frac{9}{2}-$, $\frac{11}{2}-$, or $\frac{13}{2}-$. And its 2060.4-keV γ to the $\frac{7}{2}+$ 113.8-keV state, 1322.4-keV γ to the $(\frac{9}{2}+, \frac{7}{2}+)$ 851.9-keV state, and lack of a transition (1352.4-keV γ $\lesssim 0.3\%$) to the $\frac{11}{2}-$ 821.9-keV state favor the $\frac{9}{2}-$ assignment. The presence of the 2060.4-keV γ also implies, if it is a three-quasiparticle state, that this state includes some $\pi g_{7/2}$ character in its composition, thus being less "pure" than the other five.

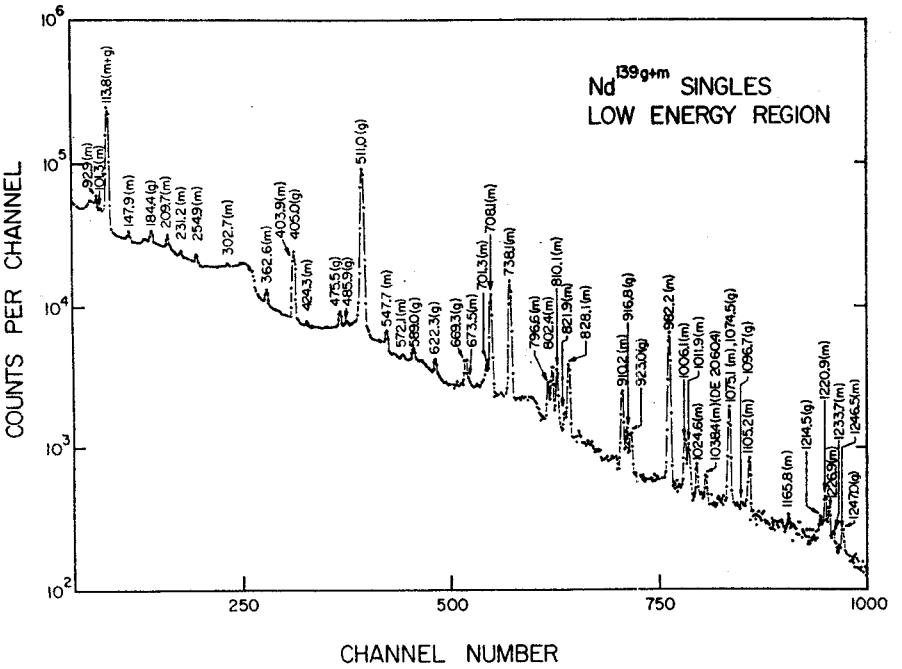

FIG. 11. (a) Nd^{139g+m} singles γ-ray spectrum taken with a 7-cm^3 Ge(Li) detector—low-energy portion. This spectrum is the sum of six $\approx$20-min runs taken $\approx$30 min after the end of 45-sec proton bombardments. In this way, the Nd^{139g} contribution was maximized both with respect to short-lived contaminants and with respect to Nd^{139m}. (b) Nd^{139g+m} singles γ-ray spectrum taken with a 7-cm^3 Ge(Li) detector—high-energy portion.

F. Remaining States

The only remaining states in Pr^{139} excited by Nd^{139m} ϵ decay that were known with enough assurance to be placed in the decay scheme are the 1369.6- and 1523.2-keV states. The 1369.6-keV state receives 1.3% of the ϵ decay, with $\log ft = 7.3$. Thus, one cannot decide between allowed and first-forbidden nonunique decay, and the assignment can be $\frac{9}{2}\pm$, $\frac{11}{2}\pm$, or $\frac{13}{2}\pm$. Even less can be said about the 1523.2-keV state which receives no direct population from Nd^{139m}. On the basis of the strength of the 101.3-keV γ from the 1624.5-keV state, a weak argument can be made for spins between $\frac{7}{2}$ and $\frac{13}{2}$ with perhaps even parity.

VI. EXPERIMENTAL RESULTS FOR Nd^{139g}

A. γ-Ray Singles Spectra

A γ-ray singles spectrum of Nd^{139g+m} taken with the 7-cm^3 Ge(Li) detector described in Sec. III A is shown in Figs. 11(a) and 11(b). This spectrum represents the sum of six runs taken $\approx$30 min after the end of $\approx$45-sec proton bombardments. The duration of each of these

runs was ≈20 min. Spectra were recorded periodically as the sources aged in order to identify activities with different half-lives and to follow the Ng^{139g} as it reached equilibrium with Nd^{139m}. Most of the γ-ray intensity, even this soon after the bombardments, originates from Nd^{139m} decay, for some 88% of Nd^{139g} β decay proceeds directly to the ground state of Pr^{139}.

A list of the energies and relative intensities of the γ rays identified with the decay of Nd^{139g} is given in Table VII. These were measured as described in Sec. III A except that the now well-determined Nd^{139m} γ ray energies were used as internal calibration standards. Of the 21 γ rays listed in Table VII, only the 405.0-keV γ has been reported previously.[7]

A basic cause of experimental difficulties encountered in the study of Nd^{139g} decay is that the annihilation photons are an order of magnitude more intense than any of the γ rays following its decay. This means that even the low activity of 5.5-h Nd^{139m} produced by our 45-sec bombardments significantly masks the 30-min Nd^{139g} γ rays shown in Figs. 11(a) and 11(b).

As mentioned briefly in Sec. II, an attempt was made to populate Nd^{139g} selectively apart from Nd^{139m} by using the

$$Pr^{141}(\tau, 5n)Pm^{139} \xrightarrow{\beta^+/\epsilon} Nd^{139g}$$

reaction. We expected that the ground state of Pm^{139} would be a $\frac{5}{2}+$ state and would populate $\frac{3}{2}+$ Nd^{139g} in preference to $\frac{11}{2}-$ Nd^{139m}, thus producing a cleaner spectrum. The attempt was a partial success because the Nd^{139g}/Nd^{139m} isomer ratio was indeed increased by an order of magnitude. However, the presence of many other short- and long-lived contaminants from competing reactions nullified any net advantage of this method for producing clean Nd^{139g} sources. One would need to use this reaction in conjunction with a rapid ion-exchange separation (not yet feasible but perhaps available within a few years) for it to be really clean. It did, however, verify the relative intensities of most of the Nd^{139g} γ rays. (The resulting spectra are displayed in Ref. 19.)

B. γ-γ Coincidence Studies

By analogy with the decay scheme[9] of $d_{3/2}$ Nd^{141}, we expected that a number of states would be present, which, upon receiving direct β population, would deexcite directly to the Pr^{139} ground state. For this reason we used the 8×8-in. NaI(Tl) split annulus[18] and a 3×3-in. NaI(Tl) detector in an anticoincidence experiment with the 7-cm³ Ge(Li) detector; the geometry was as described in Sec. III B. Again, the single-channel analyzer for the NaI(Tl) detectors was set so that the gate would be active for all γ rays above 100 keV. The resulting anticoincidence spectrum is shown in Fig. 12, and the resulting intensities of the Nd^{139g} γ rays (relative to 100 for the 738.1-keV Nd^{139m} γ ray) are listed in Table VIII. Seven states in Pr^{139} were indicated by these results.

TABLE VII. Energies and relative intensities of γ rays observed in Nd^{139g} spectra.

Measured γ-ray energy (keV)	Relative γ-ray intensity[a]
113.8±0.2	10.1±10[b]
184.4±0.4	4.2±0.4
405.0±0.4	36.4±3.0[c]
475.5±0.4	7.9±0.6
485.9±0.8	2.8±0.7
511.0($\gamma^{\pm}$)	360±50[d]
589.0±0.5	5.3±0.6[e]
622.3±0.3	6.4±1.0
669.3±0.5	8.3±2
916.8±0.4	8.5±0.6
923.0±0.4	6.9±0.8
1074.5±0.5	11.9±1
1096.7±1.0	0.9±0.4
1214.5±0.4	2.2±0.3
1247.0±1.0	0.6±0.3
1311.8±0.6	2.0±0.7
1328.4±0.6	1.1±0.3
1405.5±0.7	3.3±0.5
1449.5±0.7	0.8±0.3
1464.1±0.5	2.3±0.4
1500.8±0.8	2.0±0.5
1531.2±1.0	1.1±0.4

[a] Relative to 100 for the intensity of the 738.1-keV γ ray in Nd^{139m} ≈30 min after the end of ≈45-sec proton bombardments.

[b] Based on sum of γ intensity feeding 113.8-keV level as indicated in decay scheme (Fig. 8) because most of the 113.8-keV γ intensity originates from population by the 5.5-h Nd^{139m}, even 30 min after Nd^{139m+g} is produced.

[c] Result after the 403.9-keV component of the 403.9-, 405.0-keV doublet is subtracted out on the basis of the Nd^{139m} relative intensities (see Table I).

[d] Approximately 98% of the annihilation photons come from Nd^{139g} decay ≈30 min after the production of Nd^{139m+g}.

[e] From the decay scheme we can only place an upper limit of 16.1 on the intensity of a hypothetical 511.8-keV γ ray depopulating the 916.8-keV state.

In order to complement the anticoincidence data, a coincidence spectrum was obtained using the same apparatus. The gate from the NaI(Tl) detectors was open for γ rays above 350 keV. This "integral" coincidence spectrum is shown in Fig. 13(a), and the relative intensities derived from it are also included in Table VIII. As expected, they verify the results of the anticoincidence data.

The high intensity of the 405.0-keV γ suggests the presence of a state in Pr^{139} at this energy. Four energy sums also indicate possible γ-ray cascades involving this transition. To obtain evidence supporting these cascades, we gated the NaI(Tl) annulus detector on the 380–430-keV region and displayed the coincident spectrum seen by the 7-cm³ Ge(Li) detector. The resolving time (2τ) of the coincidence circuit was ≈100 nsec. This spectrum is shown in Fig. 13(b), and the relative intensities of the Nd^{139g} γ rays are included in Table VIII, where the ones that are thought to be in coincidence with the 405.0-keV γ are so indicated.

The same coincidence spectrometer was then gated on the 113.8-keV γ. The measured relative intensities from the resulting spectrum[19] are also listed in Table VIII. This experiment verified the energy-sum indication that the 113.8-keV γ is in cascade with the 475.5- and 1214.5-keV γ's.

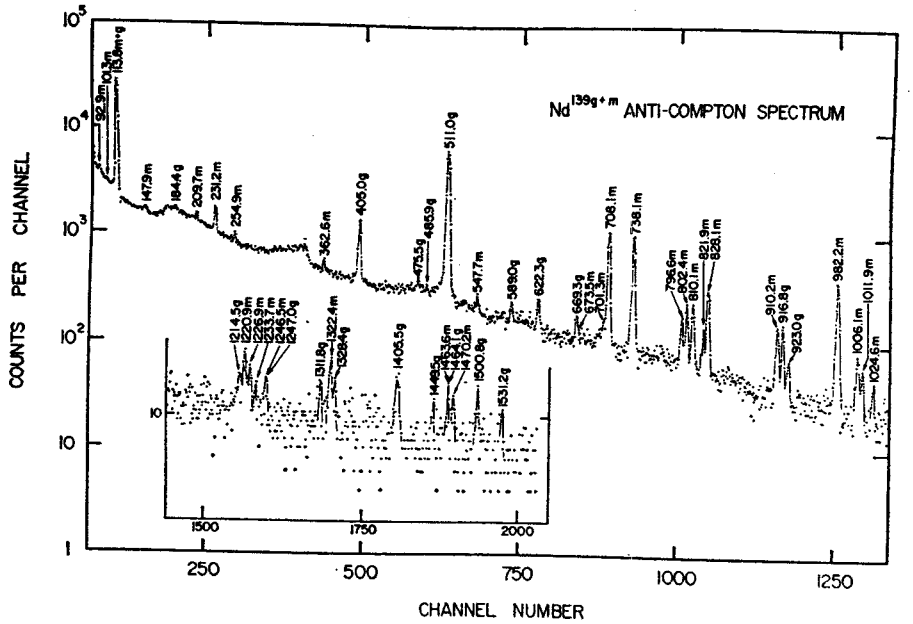

FIG. 12. Nd^{139g+m} anticoincidence spectrum. (cf. Fig. 2.)

Confirmations of several of the coincidences described above and new evidence for a 405.0–184.4-keV cascade were obtained with a 3×3-in. NaI(Tl) 7-cm³ Ge(Li) two-parameter (megachannel) spectrometer employing dual 4096-channel ADC's. These data are summarized in Table VIII. Following each coincident event, the channel numbers representing the photon energies were stored in a dedicated buffer in our SDS Sigma 7 computer. When the buffer filled, its contents were written on magnetic tape. We were then able to recover the coincidence information in slices in order to construct useful spectra. In Fig. 14(a), we show the integral Nd^{139g+m} coincidence spectrum obtained on the Ge(Li) side, and in Fig. 14(b) we show the results of gating on the 405-keV region of the NaI(Tl) side and displaying the resulting Ge(Li) spectrum.

TABLE VIII. Relative intensities of photons in the decay of Nd^{139g} observed in several γ-γ coincidence experiments.

		Relative intensity					
E_γ	Fig. 11 singles[a]	Fig. 12 anti-coincidence	Fig. 13 integral coincidence	Fig. 14 405-keV coincidence	Ref. 16 113.8-keV coincidence	Fig. 15a 2-*d* integral coincidence	Fig. 15b 2-*d* 405-keV coincidence
113.8	10.1	<24	...	...	...	<160	<231
184.4	4.2	<0.3	5.8[d]	...	...	4.8[d]	27[d]
405.0	36.4	<9.8	<49[d]	18	<17	35[d]	44
475.5	7.9	0.7	8.1[d]	5.2	11[d]	6.3[d]	...
485.9	2.8	0.5	2.7[d]	4.0[d]	<3	1.8[d]	24[d]
511.0[b]	360	120	304	127	360	78	287
(511.8?	<16.1?)	...	...	...	...	...	...
589.0	5.3	1.6	4.8	<9.8	<5	...	...
622.3	6.4	2.8	0.8	<8	<5	<2	...
669.3	8.3	1.8	1.4[d]	18[d]	<6	8[d]	61[d]
916.8	8.5	5.1[e]	0.3	1.9	<4	<1	...
923.0	6.9	1.0	0.8[d]	17[d]	<5	3[d]	41[d]
1074.5	11.9	8[e]	<1	<11	<13	<15	...
1096.7	0.9	<0.9	0.7[d]	2[d]	...	...	...
1214.5	2.2	0.5	<1	2	5	...	...
1247.0	0.6	<0.6	<0.6	<6.5	...	...	...
1311.8	2.0	0.8[e]	<0.3	<3	...	...	...
1328.4	1.1	0.5[e]	<0.3	<10	...	...	...
1405.5	3.3	2.3[e]	0.1	<3	...	...	...
1449.5	0.8	0.55[e]	0.1	<3	...	...	...
1464.1	2.3	<1.0	<0.6	<3	...	...	...
1500.8	2.0	1.2[e]	<0.2	<3	...	...	...
1531.2	1.1	0.4	<0.2	<3	...	...	...

[a] Intensities relative to 100 for the intensity of the 738.1-keV γ in Nd^{139m} ≈30 min after the end of 45-sec proton bombardments.

[b] Largely composed of annihilation photons, but an admixture of 511.8-keV γ's with an intensity of ≤16, using the scale of Table V, has not been ruled out. This possibility is discussed in Sec VII.

[e] Evidence seen here for primarily ϵ-fed ground-state transition.

[d] Evidence seen here for γ-γ coincidence event.

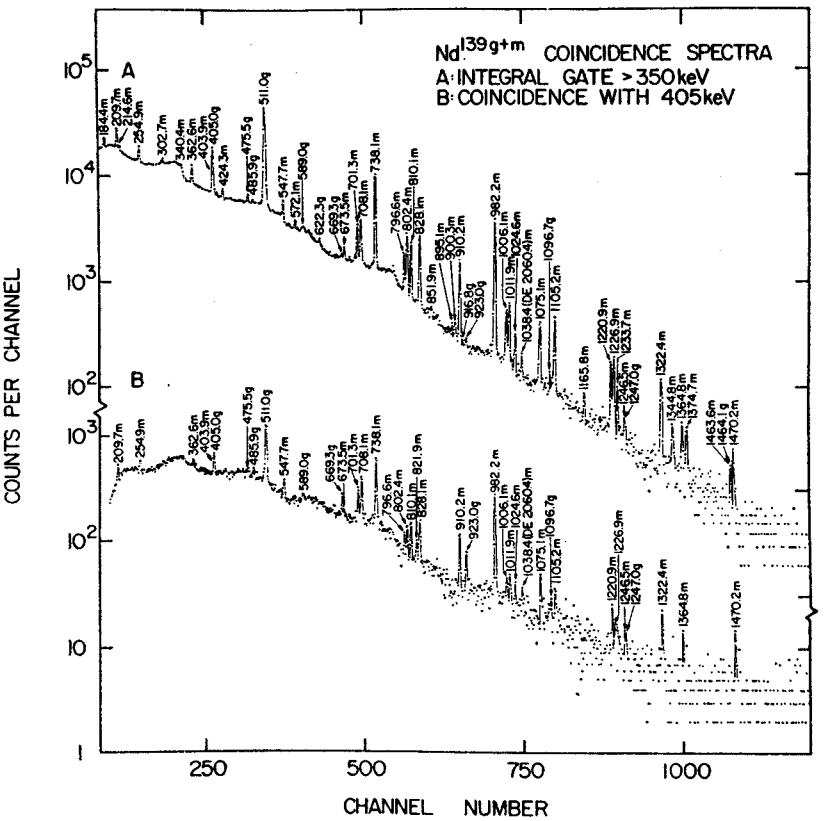

FIG. 13. (a) Nd^{139g+m} integral coincidence spectrum. This spectrum was recorded by a 7-cm³ Ge(Li) detector with the 8×8-in. NaI(Tl) split annulus set to accept all γ rays above 350 keV. (b) The annulus gate was set on the 405-keV energy region.

VII. Nd^{139g} DECAY SCHEME

The decay scheme for Nd^{139g} that we were able to deduce from our measurements was presented in Fig. 8 for comparison with the Nd^{139m} decay scheme. Again, all transition energies and excited state energies are given in keV and the β^+/ϵ ratios are calculated values.[21] All of the (total) transition intensities are given in percent of the Nd^{139g} disintegrations.

None of the ten excited states we propose has been reported previously in published Nd^{139g} decay-scheme studies. The only one of these states for which we also have evidence of population from Nd^{139m} decay (i.e., β decay) is the 113.8-keV state. The 113.8-keV γ was seen to have a 30-min decay component in addition to its dominant 5.5-h component. It was also observed to be in cascade with the 475.5- and 1214.5-keV γ's accompanying Nd^{139g} decay.

We mentioned earlier that the high intensity of the 405.0-keV γ indicates the probability of a state in Pr^{139} at 405.0 keV. This placement was confirmed by coincidences of four γ rays (five, if we include a tentative 511.8-keV γ) with the 405.0-keV γ. In the process of constructing the decay scheme, we assumed that the imbalance of γ-ray intensities leaving and entering the 405.0-keV state is removed entirely by β feeding of this state. However, we cannot rule the possibility that a 511.8-keV transition from a level at 916.8 keV to this state is present ($\leq 2.5\%$) but obscured by the intense annihilation photons.

Higher-lying states at 589.2, 1074.4, 1328.2, and 1501.2 keV are suggested by energy sums and relative photon intensities and confirmed by coincidence and anticoincidence information. The states at 916.8, 1311.8, 1405.5, and 1449.5 keV were placed on the basis of the enhancement (reduction) of the 916.8-, 1311.8-, 1405.5-, and 1449.5-keV γ's in anticoincidence (coincidence) experiments as seen in Figs. 12–14 and Table VIII.

The $Q_\epsilon = 2800$ keV is a calculated value,[20] which ought to be good to within several hundred keV. There have been several attempts to measure the β^+ end points, but at this time their precision is not particularly good. Several measurements of the (total) annihilation photon relative intensity component due to Nd^{139g} were used in order to calculate the 88% β branching to the ground state. In the $Nd^{139m+g} \rightarrow Pr^{139} \rightarrow Ce^{139}$ decay chain, Nd^{139g} accounts for $\approx 98\%$ of the annihilation photon intensity at ≈ 30 min after the 45-sec bombardments.

Four unplaced γ rays identified with Nd^{139g} decay were observed with energies (relative intensities) of 622.3 (6.4), 1247.0 (0.6), 1464.1 (2.3), and 1531.2 keV (1.1). The sum of these intensities yields 8.3% of the observed Nd^{139g} γ-ray intensity and 1.5% of the observed Nd^{139g} total disintegrations. Some properties of these γ rays can be deduced from Tables VII and VIII. The relatively strong 622.3-keV γ perhaps suggests placing a state at 622.3 keV; but, in view of the lack of any supporting evidence, we have omitted this from the decay scheme. The logft for population of such a state would be $\gtrsim 6.8$.

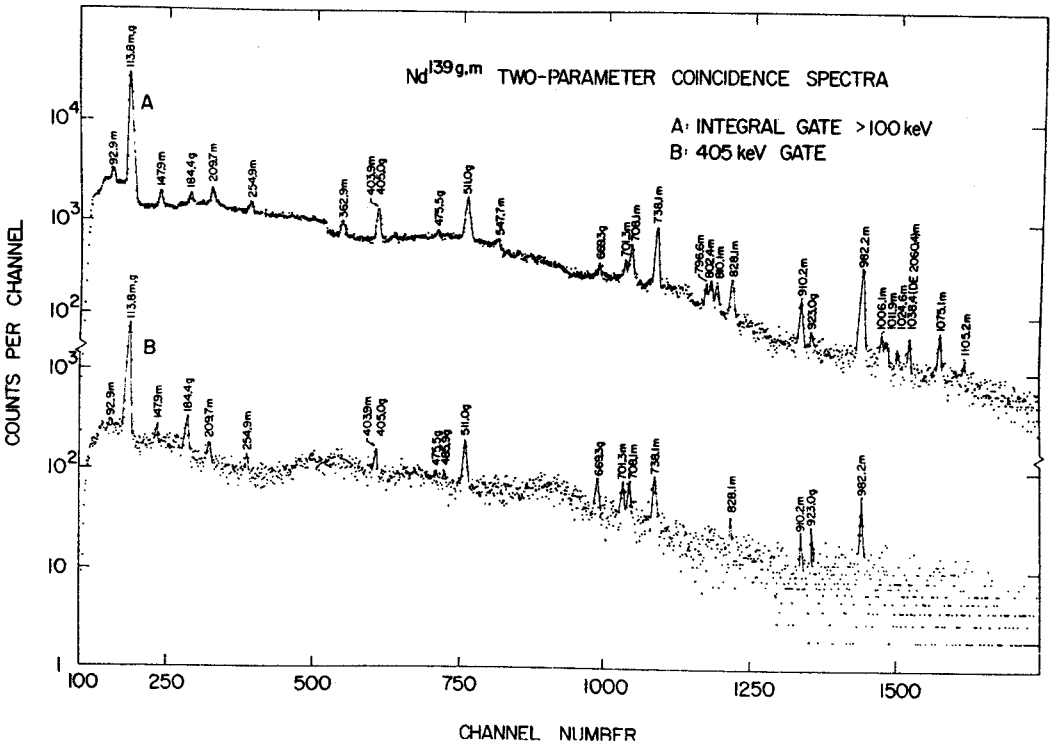

FIG. 14. Slices from two-dimensional (megachannel) γ-ray spectrum for Nd^{139g+m}. (A) Integral gate of all γ rays above 100 keV. (B) 405-keV gate. See the text for details.

VIII. SPIN AND PARITY ASSIGNMENTS FROM Nd^{139g} DECAY

Spin and parity assignments to the lowest two levels have been discussed in Sec. VI C in connection with the decay of Nd^{139m}. The 63% ϵ, 27% β^+ decay to the ground state is quite consistent with a $\pi d_{5/2} \rightarrow \nu d_{3/2}$ transition, and the $\log ft = 5.1$ is remarkably close to that found for the analogous transition in Nd^{141} decay[9] ($\log ft = 5.3$).

It is difficult to set a precise upper limit on direct β decay to the $\frac{7}{2}+$ 113.8-keV state because of the intense 113.8-keV γ-ray component from Nd^{139m} decay. Following the analogy with the much cleaner Nd^{141} decay, there we could place an upper limit of 0.03%, with $\log ft > 8.8$. For Nd^{139g} decay, of course, such precision is out of the question, but the fact that we see no indication of direct β population is clearly consistent with a $(d_{5/2})^2(g_{7/2})^{-1}$ configuration, as discussed before.

The remaining nine levels all are populated by β^+/ϵ decay from $\frac{3}{2}+$ Nd^{139g} with $\log ft$'s ranging from 5.6 to 7.2. These all fit quite nicely in the range expected for allowed decay, and, although one cannot rule out first-forbidden decay on the basis of these alone, we see no indication that we need postulate anything other than $\frac{1}{2}+$, $\frac{3}{2}+$, or $\frac{5}{2}+$ states as being populated directly by Nd^{139g}. Indeed, all the $\log ft$ values are actually slightly smaller than for the analogous transitions in Nd^{141} decay.[9] For some of the states, especially those exhibiting γ-ray branching, we can perhaps narrow the assignments further.

The states at 405.0 and 916.8 keV are tentatively assigned $\frac{1}{2}+$ or $\frac{3}{2}+$ because they both decay to the $\frac{5}{2}+$ ground state and miss the $\frac{7}{2}+$ 113.8-keV state. The 916.8-keV state may or may not decay also to the 405.0-keV state via the unobserved 511.8-keV transition, which just might have appreciable intensity. This fact is more concerned with the internal structure of (both) states than with their spin and parity—although the presence of the transition would lend further support to our assignments. Solely on the prediction of the shell model that the $s_{1/2}$ state ought to lie between the $h_{11/2}$ state and the $d_{5/2}$ and $g_{7/2}$ states, one is tempted to identify the 405.0-keV state with it. There is no supporting evidence, however, and one must ask why the $s_{1/2}$ state should be populated so easily here when it has not been seen in either Nd^{141} decay[9] or Ce^{143} decay[40] to the next heavier Pr isotopes, which otherwise show much the same single-particle state positions (within a few hundred keV). We shall also see that γ-ray branchings to this state tend to support the $\frac{3}{2}+$ rather than the $\frac{1}{2}+$ assignment.

Next we consider the states that decay through the $\frac{7}{2}+$ 113.8-keV state, namely, those at 589.2 and 1328.2 keV. The mere presence of the 475.5- and 1328.4-keV γ's rules out the $\frac{1}{2}+$ possibility for these states. We can tentatively narrow both assignments down to $\frac{5}{2}+$ with the aid of the γ-ray branchings.

For the 589.2-keV state, a $\frac{3}{2}+$ assignment would lead to single-particle estimates[35] of the relative intensities of the 589.0:475.5:184.4-keV γ's ($M1:E2:M1$, with possible $E2$ admixing in the $M1$'s) of 1:0.005:0.04. A $\frac{5}{2}+$ assignment (all $M1$'s) would lead to roughly 1:0.5:0.06. Although considerable $E2$ enhancement is

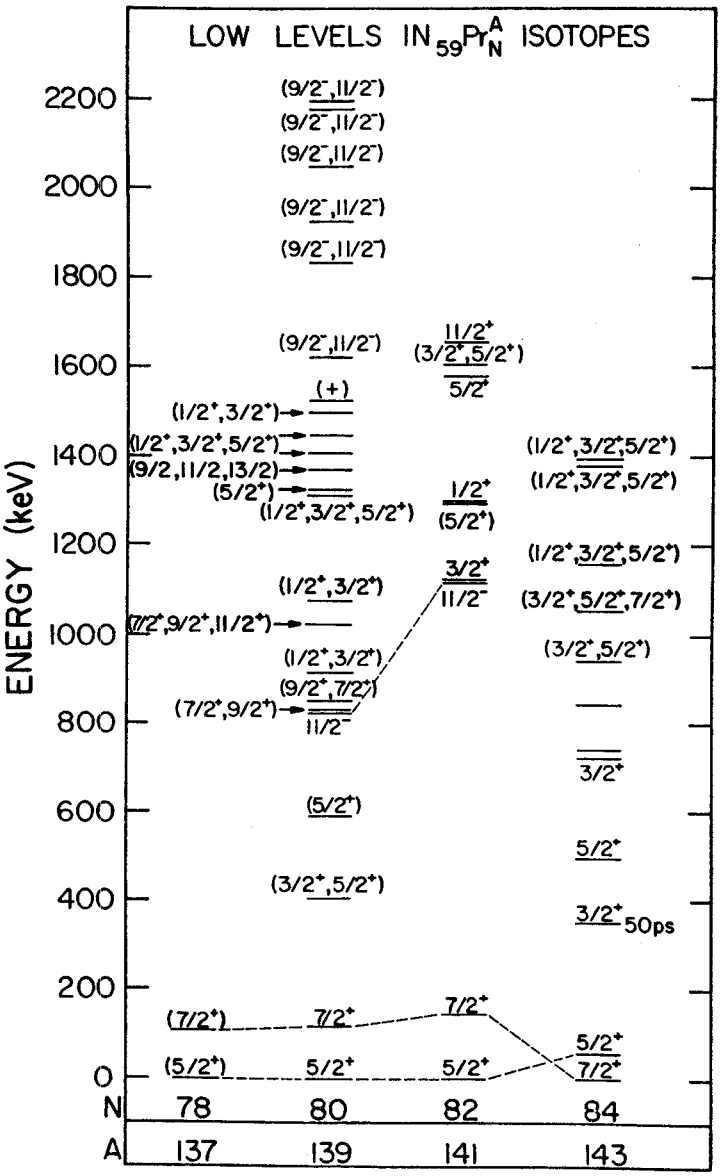

FIG. 15. Experimental levels in odd-mass Pr isotopes demonstrating the effects of changing neutron number on the positions of the states. Unambiguously related states are connected by the dashed lines. References: Pr^{137}, Ref. 22; Pr^{139}, this study; Pr^{141}, Refs. 9, 41, and 42; and Pr^{143}, Ref. 40.

to be expected (because of the softness of this nucleus to vibrations) and $M1$'s might be somewhat retarded, the latter ratio is clearly preferable when compared with the experimental ratio, 1:1.5:0.75. The 405.0- and 589.2-keV states may well be core-coupled states involving the $d_{5/2}$ ground state. That they lie so low is not too surprising, for Pr^{139} (two neutrons fewer than 82) should be somewhat analogous to Pr^{143} (two neutrons more than 82),[40] which, being again somewhat soft to vibrational excitations, appears to have core-coupled states at this same energy. A $\frac{5}{2}+$ assignment for the 589.2-keV state would exclude a $\frac{1}{2}+$ assignment for the 405.0-keV state.

Quite similar reasoning holds for the 1328.2-keV state, except that it lies high enough that one can deduce little about its internal makeup. The corresponding single-particle predictions for the relative intensities of the 1328.4:1214.5:923.0-keV γ's are 1:0.005:0.3 and 1:0.8:0.3 for $\frac{3}{2}+$ and $\frac{5}{2}+$ assignments, respectively. Although neither can be called a satisfactory fit (experimental ratios are 1:1.5:5.5), the latter is in the ball park. Considering the obvious enhancement of the γ rays to the 405.0-keV state from both the 1328.2- and 589.2-keV states, one is tempted to look for the 739.0-keV γ between the latter two. Unfortunately, the presence of the intense 738.1-keV γ from Nd^{139m} decay precludes our seeing it, and it could be as intense as 0.7% and have excaped detection.

The states at 1074.4 and 1501.2 keV are tentatively assigned $\frac{3}{2}+$ because they hit the ground state but miss the $\frac{7}{2}+$ 113.8-keV state in their depopulation. This is indeed tentative, however, and one must know more about the internal structure of these states before firm

[40] P. R. Gregory, L. Schellenberg, Z. Sujkowski, and M. W. Johns, Can. J. Phys. 46, 2797 (1968); K. P. Gopinathan, Phys. Rev. 139, B1467 (1965).

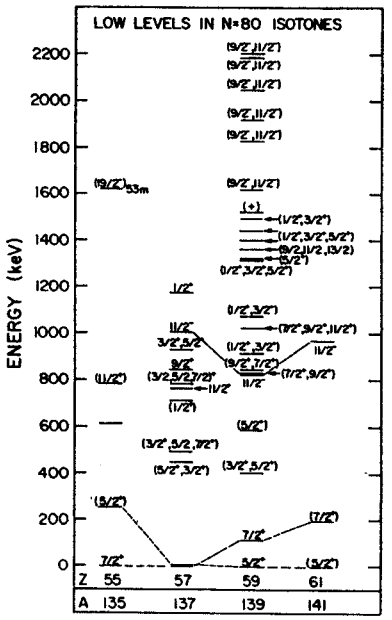

FIG. 16. Experimental levels in odd-mass $N=80$ isotones, demonstrating the effects of changing proton number on the positions of the states. Unambiguously related states are connected by the dashed lines. References: Cs^{135}, Ref. 43 and S. Thulin, Arkiv Fysik 9, 137 (1955); La^{137}, Ref. 28; Pr^{139}, this study; and Pm^{141}, Ref. 7 and R. Eppley, R. Todd, D. B. Beery, W. H. Kelly, and Wm. C. McHarris (unpublished).

assignments can be made. It would be quite possible, for example, to concoct a hypothetical $\frac{5}{2}+$ state consisting of a $d_{5/2}$ quasiparticle coupled to a 2+ phonon excitation that would clearly populate the ground state to the exclusion of the 113.8-keV state, straightforward multipolarity selection rules notwithstanding.

The remaining states, at 1311.8, 1405.5, and 1449.5 keV, which were placed on the basis of their ground-state transitions alone, might have their assignments narrowed down to $\frac{3}{2}+$ or $\frac{5}{2}+$; however, the population is quite weak for all three, with even parity even being somewhat in doubt, so we leave then as $\frac{1}{2}$, $\frac{3}{2}$, $\frac{5}{2}$ (+).

IX. DISCUSSION

A total of at least 23 states in Pr^{139}, practically none of which had been reported before, were observed from the combined decays of Nd^{139m} and Nd^{139g}. These states apparently can be classified in three quite distinct categories: (1) single-quasiparticle states, (2) single-quasiparticle states coupled to various vibrational configurations, and (3) three-quasiparticle states. Our conclusions can be most concrete about the states in the first category and, because of a rather unique feature in the β-decay properties of Nd^{139m}, the third category. As this is an experimental paper, our discussions that follow will remain empirical, but we indicate the directions, both experimental and theoretical, that might be taken for further elucidation of the properties of this most interesting nucleus.

A. Single-Particle States

Again, by "single-particle" states we mean merely those states with primarily single-quasiparticle amplitudes in their wave functions. These range from the more or less pure states near the ground to highly fractionated and complicated states at higher energies. When we speak of them in simple shell-model terms, this is not to imply that they are indeed pure shell-model states.

On the neutron-deficient side of $N=82$ in the lanthanide region, practically nothing has been done in the way of even qualitative calculations of the positions of nuclear states—even the pairing-plus-quadrupole force calculations of Kisslinger and Sorensen[32] give out at Nd^{141}. This means that we are forced to use empirical data for the mot part, although the sheer number of states excited in Pr^{139} in this study makes this more practicable than usual. Thus, in Figs. 15 and 16, respectively, we plot the known states in the light odd-mass Pr isotopes and in the odd-mass $N=79$ isotones. Here, we are beginning to get far enough from β stability that no scattering reactions have been done to excite states, so the number of states recorded is very much a function of Q_ϵ.

In Pr^{139} we probably see evidences of all the available single-proton states between $Z=50$ and $Z=82$. The most clearcut single-quasiparticle states are those at 0, 113.8, and 821.9 keV. The ground state undoubtedly consists primarily of a single $d_{5/2}$ proton outside a closed $g_{7/2}$ subshell, and the 113.8-keV state simply promotes a $g_{7/2}$ proton, resulting in $(d_{5/2})^2$ $(g_{7/2})^{-1}$. As mentioned previously, the retarded $M1$ transition between them is characteristic of the l-forbidden $M1$'s between $g_{7/2}$ and $d_{5/2}$ states in a wide variety of nuclei in this region. The relatively small spacing between the first two states is consistent with trends in both proton and neutron numbers in neighboring nuclei, for the $\frac{7}{2}+$ and $\frac{5}{2}+$ states cross over between Pr^{141} and Pr^{143} and also between La^{137} and Pr^{139}.

The 821.9-keV state shows evidence of being a single $h_{11/2}$ proton outside the closed $g_{7/2}$ subshell. As mentioned in Sec. V D, the $M2$ transition from this state to the 113.8-keV state is retarded, while the $E3$ to the ground state is enhanced over single-particle estimates. Van Hise, Chilosi, and Stone[37] suggest that a similarly enhanced $E3$ transition in La^{137} could be explained in terms of a coupling of the $d_{5/2}$ proton to a 3− octupole vibration, resulting in a nearby $\frac{11}{2}-$ state that could be mixed into this state. Superficially, one might ask why it is not also possible to admix a similar $\frac{11}{2}-$ state, this time based on the $g_{7/2}$ proton, into this state, thereby enhancing the $M2$ as well as the $E3$ transition. As it turns out, one cannot really test either hypothesis, for the positions of possible octupole states are unknown. With our above shell-model assignments, however, the $E3$ is the better single-particle transition, involving principally the deexcitation only of a proton from the $h_{11/2}$ to the $d_{5/2}$ orbit. The $M2$, conversely, involves breaking the $g_{7/2}$ subshell in addition, so its retardation follows even on these simple arguments.

The positions of the $d_{3/2}$ and $s_{1/2}$ states are not so clear, but they are probably fragmented and contribute to

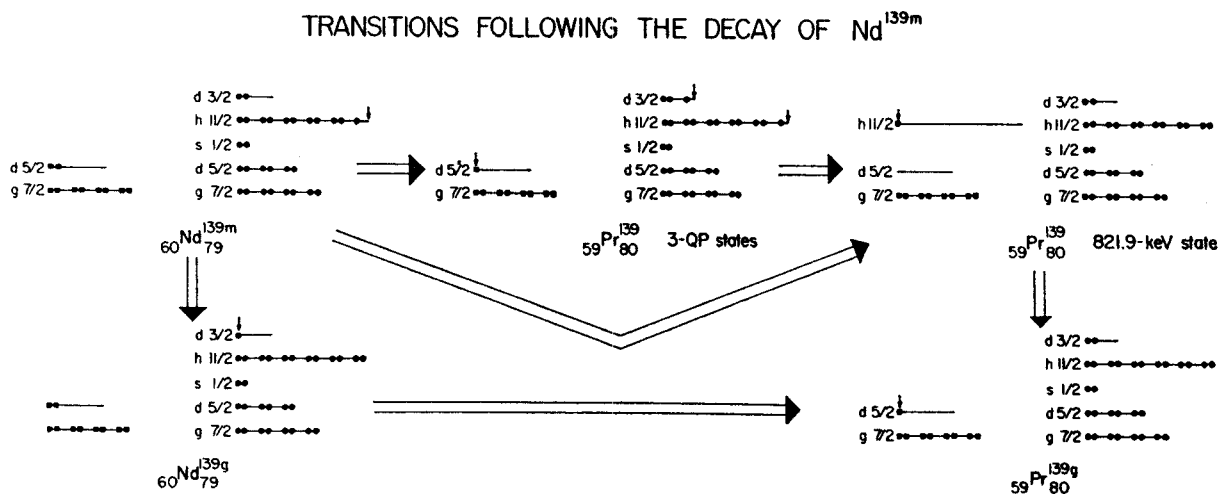

FIG. 17. Symbolic shell-model representations of some important transitions between Nd^{139} and Pr^{139} states. We have given a stylized picture of the proton (squares) and neutron (circles) states between 50 and 82 nucleons. The arrows point to the nucleons or holes of prime interest in each state.

several states above 1 MeV. The state at 405.0 keV (and at 589.2 keV, for that matter, if our spin assignments were incorrect) is not likely to be either of these single-particle states. In the more rigid Pr^{141}, other than the $g_{7/2}$ and $d_{5/2}$ states, there are no single-particle states below 1114 keV that were populated either by Nd^{141} decay[9] or by (τ, d)[41] or (d, τ)[42] scattering. Of the number of levels just above 1 MeV that were possible contenders, we were unable to identify specific levels with either the $d_{3/2}$ or $s_{1/2}$ states because of uncertainties connected with the vibrational character of that nucleus. Pr^{139} is much softer to deformations than Pr^{141}, and we thus expect many more low-lying states, but there is no reason to expect either the $d_{3/2}$ or $s_{1/2}$ states to drop drastically in energy, so they may be partly associated with a number of the higher levels.

B. Three-Quasiparticle States

In Sec. V E, we presented arguments to the effect that the six states at 1624.5, 1834.1, 1927.1, 2048.8, 2174.3, and 2196.7 keV appear to be high-spin odd-parity ($\frac{9}{2}-$ or $\frac{11}{2}-$) states. The only strightforward explanation we have found that will explain their enhanced ϵ population relative to the 821.9-keV state plus the many low-energy γ transitions among them and the dearth of direct transitions down to the ground or 113.8-keV states is that these six states are part of a three-quasiparticle multiplet having the configuration $(\pi d_{5/2})(\nu d_{3/2})^{-1}(\nu h_{11/2})^{-1}$. The particle transitions that we postulate are outlined in stylized form in Fig. 17.

In the extreme single-particle approximation, $_{60}Nd_{79}^{139g}$ can be represented as three $d_{3/2}$ neutron holes in the $N=82$ shell (i.e., a single neutron in the $d_{3/2}$ orbit) and eight $g_{7/2}$ (closed subshell) and two $d_{5/2}$ protons above $Z=50$. Owing to the isomeric properties discussed in Sec. V B, Nd^{139m} ought to differ only in the promotion of an $h_{11/2}$ neutron into the $d_{3/2}$ level, resulting in eleven $h_{11/2}$ and two $d_{3/2}$ neutrons. Now, there is nothing untoward about the decay of Nd^{139g} to the ground state of Pr^{139}, for the only change is the conversion of a $d_{5/2}$ proton into a $d_{3/2}$ neutron. This accounts for the low logft value of 5.1 for this transition.

The analogous transition from Nd^{139m}, i.e., $\pi d_{5/2} \rightarrow \nu d_{3/2}$, however, results in the three-particle configuration $(\pi d_{5/2})(\nu d_{3/2})^{-1}(\nu h_{11/2})^{-1}$. Hence, the apparent abnormally large population to these states is, in fact, the expected mode of decay. The 821.9-keV $\frac{11}{2}-$ state, on the other hand, should have the configuration $(\pi h_{11/2})(\nu d_{3/2})^2$, so decay to it would require converting one $d_{5/2}$ proton into an $h_{11/2}$ neutron, either in one step or perhaps through an intermediate $d_{3/2}$ neutron state, and a simultaneous promotion of the remaining $d_{5/2}$ proton to the $h_{11/2}$ state. The resulting relatively large logft of 7.0 is thus not unexpected.

Relatively few three-quasiparticle states are known, and these few are customarily produced by brute-force techniques (i.e., bombardments). Their recognition has hinged on an isomeric state now and then having a long half-life because of its high spin; for example, the nearby $\frac{19}{2}-$ isomer[43] at 1621 keV in Cs^{135} that could have either the same or a similar configuration as the states in Pr^{139}. It is worth noting that here we have somewhat unique mechanism for populating three-quasiparticle *multiplets* in a number of nuclei. The requirements are a high-spin nucleus, such as the $h_{11/2}$ isomers, and that it have sufficient decay energy to populate states above the pairing energy gap in its daughter nucleus. Additionally, the parent nucleus must be hung up with respect to decay by other modes; for example, an isomeric transition, if present, must be of sufficiently low energy to allow the ϵ decay to com-

[41] B. H. Wildenthal, R. L. Auble, E. Newman, and J. A. Nolen, Bull. Am. Phys. Soc. **13**, 1430 (1968).
[42] H. W. Baer and J. Bardwick, Bull. Am. Phys. Soc. **13**, 1430 (1968).
[43] L. B. Häller and B. Jung, Nucl. Phys. **52**, 524 (1964).

pete. Finally, the nucleus must have a relatively unique intrinsic configuration that forces the preferred decay path to be into the three-quasiparticle states. Such arrangements would appear to be present only for β^+/ϵ decay—further, they are likely to occur only below $N=82$. (Below $N=50$ the correct configuration occurs at Kr^{83} and Sr^{85}, but these are too close to β stability for populating high-lying states. Below $N=126$ the configuration is projected to occur around Pu^{211}, a region that is not even particle stable.)

Below $N=82$ the appropriate configurations can be found only at $N=79$ and $N=77$. On the neutron-rich side of $N=79$ there are, to be sure, some peculiar and complex decays of $\frac{11}{2}-$ isomers—e.g., Te^{131m} decays primarily to high-spin states at 1899 and 1980 keV[44]—but these cannot be pinned down as decay to three-particle states. On the neutron-deficient side, Ce^{137m} has a possible configuration, although it lacks the $d_{5/2}$ protons, so decay would be l forbidden ($\pi g_{7/2}\rightarrow\nu d_{3/2}$); however, its Q_ϵ is small enough to preclude such decay anyway.[45] This leaves Nd^{139m} as the nucleus closest to β-stability with the requisite properties. Other possible candidates in this region among currently known nuclei are $Sm^{141(m)}$ and $Nd^{137(m?)}$. These are now being investigated.

Although the above interpretation qualitatively explains most of the γ-ray branchings between members of the negative-parity multiplet, there are several places involving very highly hindered transitions where it runs into difficulties. We take this to mean that small admixtures in the states are very important in determining these transition rates. However, it is instructive to consider specifically one of the more extreme examples—the 1011.9-keV γ (2.9%) from the 1834.1-keV state to the $\frac{11}{2}-$ 821.9-keV state versus the unobserved (<0.5%) 1834.1-keV γ to the $\frac{5}{2}+$ ground state. With an $\frac{11}{2}-$ assignment for the 1834.1-keV state one would not expect to see the 1834.1-keV γ. However, with a $\frac{9}{2}-$ assignment, the arguments are not so clear. Single-particle estimates[35] for the $h_{1/2}$'s of the 1011.9- ($M1$) and 1834.1-keV ($M2$ or $E3$) γ's are 2.4×10^{-14} and 8×10^{-12} or 4×10^{-9} sec, respectively. According to our above description, the missing $M2$ or $E3$ would involve an apparently very simple $\nu d_{3/2}\rightarrow\nu h_{11/2}$ transition (the $M2$ would be l forbidden); there may also be some hindrance from uncoupling and recoupling the states. On the other hand, the observed 1011.9-keV $M1$ γ requires the simultaneous changes $\nu d_{3/2}\rightarrow\nu h_{11/2}$ and $\pi d_{5/2}\rightarrow\pi h_{11/2}$, each of which is doubly l forbidden. However, l forbiddeness loses much of its meaning in multiparticle transitions and would depend on the relative phases of the transforming states; also core polarization in multiparticle states tends to obviate the l selection rules.[46] Still, multiparticle γ decay is formally absolutely forbidden. Although there are known cases where such transitions take place at enhanced rates (e.g., the 63-keV $E1$ γ in Bk^{250} following Es^{254} α decay[47]), they are not common. When such involved rearrangements are compared, clearly the single-particle estimates lose all meaning, and minute admixtures could easily be the deciding factors.

In this multiplet of three-quasiparticle states, we thus have two different and potentially very rewarding sources of information: (1) The enhanced transitions between the various members of the multiplet should give information about the gross features of the states and should allow one to perform calculations on states at several MeV that normally can be done only near the ground state. (2) The very retarded transitions to states not in the multiplet should allow one to determine some of the admixtures in the states and also something more about the structures of many of the lower-lying states.

C. Vibrational States—the Remaining States

The term "quasiparticle" was used advisedly in the previous section, for the simple shell model becomes less and less of a good approximation for states at these energies. Thus, the states and the transition rates will need to be calculated from the occupation-number approach. When this is done, we expect that much more information will also be forthcoming about the remaining states in Pr^{139}, most of which are probably core-coupled vibrational states. At this time it would be especially interesting to know more about the nature of the 828.1- and 851.9-keV states, which receive considerable population from the three-quasiparticle states. Assuming that our interpretation of the latter is correct, the 828.1- and 851.9-keV states would seem to be constructed from the $d_{5/2}$ ground state coupled to a 2+ quadrupole vibration. That they receive so much population could be explained partly by their receiving it in default of other states being available (cf. the γ-ray branching discussion in the previous section) and perhaps partly by the fact that the three-quasiparticle states undoubtedly contain vibrational admixtures. After all, from one viewpoint three-quasiparticle states and single-quasiparticle-plus-core states are only extreme examples of the same thing.

ACKNOWLEDGMENTS

We are indebted to Dr. W. P. Johnson and H. Hilbert for aid in operating the Michigan State University Cyclotron. We thank R. Eppley for discussions about $M4$ isomers and for supplying us with his information on the $N=81$ isomers before publication. We also thank Dr. J. J. Kolata for his assistance and the use of his delayed-coincidence apparatus. Finally, we thank Dr. H. McManus for some very helpful discussions concerning the nature of three-quasiparticle states.

[44] L. M. Beyer, G. Berzins, and W. H. Kelly, Nucl. Phys. **A93**, 436 (1967).

[45] R. B. Frankel, Ph.D. thesis, University of California, Berkeley, Lawrence Radiation Laboratory Report No. UCRL-11871, 1964 (unpublished).

[46] M. Gmitro, J. Hendeković, and J. Sawicki, Phys. Rev. **169**, 983 (1968).

[47] Wm. C. McHarris, F. S. Stephens, F. Asaro, and I. Perlman, Phys. Rev. **144**, 1031 (1966).

NUCLEAR INSTRUMENTS AND METHODS 74 (1969) 309–314; © NORTH-HOLLAND PUBLISHING CO.

A HIGH PRECISION GONIOMETER FOR CHARGED PARTICLE SPECTROSCOPY*

K. M. THOMPSON† and C. R. GRUHN

Cyclotron Laboratory, Michigan State University, East Lansing, Michigan, U.S.A.

Received 4 July 1969

A high precision goniometer capable of positioning Ge(Li) charged particle detectors with a precision of ± 0.02° has been built. This device consists of a 4 ft radius, detector support which rotates outside of a central target vacuum chamber. The main features of the system are described and a summary of the tests to verify its operational capabilities is presented.

A description is also given of the installation of the unit on the beam line, illustrating the precautions which were taken to insure alignment. The performance of this apparatus in studying Ni(p,p′) reactions at 40 MeV is discussed.

1. Introduction

There have been two basic types of equipment designed and constructed to measure the angular distributions of differential cross sections in nuclear reactions. These two types are the vacuum pot design and the "spider" geometry. The first incorporates a vacuum chamber housing all of the detection instruments and targets. The second involves a central, target vacuum chamber with detectors viewing the target through ports in a sliding vacuum seal. At the Michigan State University Cyclotron Laboratory, MSUCL, there has recently been constructed a high precision goniometer of the latter type for charged particle spectroscopy.

This device was built to facilitate charged particle nuclear reaction studies in the energy range of 20–75 MeV. In particular the design was guided by the experimental requirements of inelastic proton scattering and ^{3}He induced reactions. Among the proposed experiments there were many which demanded the use of Ge(Li) charged particle detectors because of their energy resolving capabilities. These detectors have been successfully fabricated at MSUCL[1]) giving spectra, for example, with resolutions of 22 keV for 40 MeV protons[2]). A Ge(Li) package similar to the vertical cryostat design of Chasman[3]) was found to be most convenient.

Because of the large momentum transfer in ^{3}He induced reactions, high angular precision of the apparatus is required. The final specifications were arrived at through compromises concerning the following points: a typical expected beam geometry on target of 1 mm·mrad[4]), a periodicity in diffraction patterns of as small as 7.0° and a minimum of funds available for construction of the apparatus. These compromises yielded a system which is able to remotely position the detectors to ±0.02° relative to a reference direction and which allows the detectors to be placed at maximum radii of up to 4 ft from the targets. A final, basic feature of this system is that it is convenient to use.

Implementing all of the above mentioned features in a typical vacuum pot scattering chamber would necessitate a very large vacuum system. The chamber would be prohibitive in cost, and the necessary evacuation times along with the difficulty of reaching the interior points made this approach unacceptable for us. The "spider" geometry, on the other hand, avoids these problems since the rotating detector supports are outside of a small, central target vacuum chamber[5,6]).

2. Construction

The goniometer was designed for a modular construction. The mechanical as well as the electrical assemblies are composed of individual, easily removed sections. This design philosophy permits modifications to be easily incorporated into the total system to satisfy the requirements of a specific experiment.

This goniometer is composed of three basic units joined by one multiconductor cable. These units are a semi-portable goniometer drive and two control and power supply assemblies, one at the local station and one at the remote. These can be interconnected in either a retracted or an extended configuration allowing for the system to be easily moved from one location to another and to be conveniently tested.

2.1. Goniometer drive

The goniometer drive assembly is shown in fig. 1. This includes three, remotely controlled drive systems which position the target and the 4 ft radius main arm. These systems are rigidly fastened to an adjustable steel and aluminum base, fig. 1A. The four threaded steel

* Work supported in part by the National Science Foundation.

† In partial requirement for Ph.D. Thesis. Present address Argonne National Laboratory.

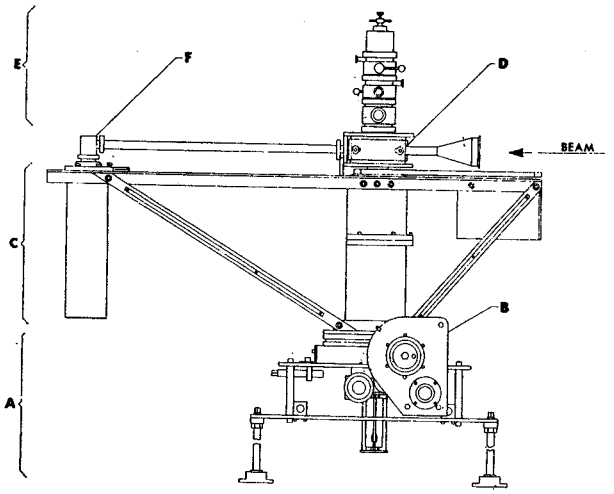

Fig. 1. A schematic of the goniometer drive unit. A–base, B–main arm gear box, C–detector positioning elements, D–target chamber, E–target lock, F–detector mount.

legs allow the goniometer to be adjusted so that the main arm is located between 3 and 12 inch below the scattering plane. These also permit alignment such that the main arm remains in a level plane during a complete revolution with its center of rotation intersecting the incident beam line. An *X-Y* stage is also incorporated to allow for a maximum of 1 inch of adjustment in the horizontal plane.

There are two rotating elements in this system which are used to position detectors with respect to the beam direction (fig. 1C). First, there is the 4 ft radius, remotely positioned, main arm. This element has a dual beam, counter balanced construction capable of supporting a maximum of 100 lbs at a radius of 4 ft. The dual beam design allows the Ge(Li) detector package along with its LN_2 dewar to be securely supported between the minimum and maximum radial positions.

This arm is driven by a Slo-Syn, SS1800-1005, bifilar stepping motor which is operated in both an ac synchronous mode with a speed of 72 rpm and in a dc stepping mode with 200 steps/revolution at a speed of 20 steps/sec. The motor is connected to the main arm through a 4:1 gear train (fig. 1B) and a 90:1 worm gear. This worm gear mechanism is a Bridgeport, 15 inch, rotary mill table. The resulting rotational velocities of the arm are 72°/min with the motor running in the ac mode and 6°/min for dc operation.

The angular position of the main arm is indicated by a vernier scale with a least count of 0.005° and a remote digital readout with a least count of 0.02°. The digital counter is driven by a pair of synchro motors which is connected directly to the Slo-Syn motor shaft.

The second detector positioning element is a $\frac{3}{4}$ inch thick aluminum arm located just above the main arm. This manually positioned element has a radius of 2 ft and is designed to support maximum loads of 50 lbs. The angular position is indicated relative to the main arm by a vernier scale with a least count of 0.1°.

The drive mechanisms for the target angle and target height are located below the rotary table. Both of these utilize a worm gear driven by a dual speed motor system. The position of the target is indicated on two remote digital readouts each of which is driven by a pair of synchro motors which is in turn connected to the drive motor shaft. The least count on the angle readout is 0.02° while on the height it is 0.2 mil. The gear train used for changing the angular position of the target results in an angular velocity of 432°/min in the fast mode and 36°/min in the slow mode. The target height can be varied at a speed of 1.80 or 0.072 inch/min. Below the target drive elements are located five microswitches which are activated by a cam on the end of the target shaft. Two of these switches define the target height limits of travel while the remaining define predetermined positions for three targets in the target holder.

Located just above the arms of the goniometer is the target vacuum chamber (fig. 1D) containing a 6 inch high target ladder designed to hold 2 inch wide target frames. The exact configuration of this chamber depends on the experimental needs. These determine, for example, what type of monitor port is incorporated. Also, the experiment dictates the geometry of beam entrance and exit ports used and the type of coupling needed between the detector and the target vacuum chamber.

The target chamber was designed to be easily modified by providing a replaceable section in the scattering plane. The first section constructed is 8 inch in diameter and has two fixed monitor ports at −45° and 135°, a slot for the scattered particles from −15° to 170°, and a single primary beam port. There is an O-ring seal around the outside of this slot which permits the use of a sliding vacuum seal as well as a thin foil window.

The sliding seal used on this chamber is similar to others[7,8]) and was designed to be used with Ge(Li) detectors in a windowless geometry. The seal strap is made of 10 mil stainless steel and is rotated using only the scattered beam port to transfer the torque between the main arm and the strap. The lubrication of this seal which provides a satisfactory operation is Dow Corning high vacuum silicon grease. A mixture of vacuum grease and oil with molybdenum disulfide powder was also tried but was rejected because it was less convenient to use.

A thin foil window of ½ mil Kapton[8]) has also been successfully used in place of the sliding seal on this chamber. Both of these options are used with an external beam dump located beyond the goniometer. As a result the particle beam must pass through either the foil window or the steel strap. In the latter case serious background radiation is produced and is, therefore, a limitation to the usefulness of this design.

In order to remove this limitation of the 8 inch chamber a 16 inch diameter section was fabricated[10]) with the following features. It includes a sliding seal with a similar construction as the first extending from 8° to 110°. This still allows angular distributions to be obtained, however, from 8° to 172° accomplished by rotating the chamber 180°. It also includes windowless exit and entrance ports for the primary beam along with two slots with removable thin foil windows of Kapton which are used with monitor counters.

A target transfer and hold lock (fig. 1E) is connected to the top of the chamber through a standard, 4 inch, Marman vacuum coupling. This lock consists of two vacuum valves and a small chamber containing a transfer mechanism. This assembly can be used to insert a target into the central chamber without breaking the chamber vacuum or, if necessary, without exposing the target to the atmosphere.

The detector carriage is shown in fig. 1F. The detector package and the LN_2 dewar are held by this support between the dual beams of the main arm. The radial position of the detector is fixed securely when the detector mount is tightened and the carriage is pinned to the main arm with ¼ inch, steel dowels. In addition to the single detector mount shown here, a dual mount has been made for holding two detectors side by side. The LN_2 dewar used with this latter system has a pot life of about 10 hour.

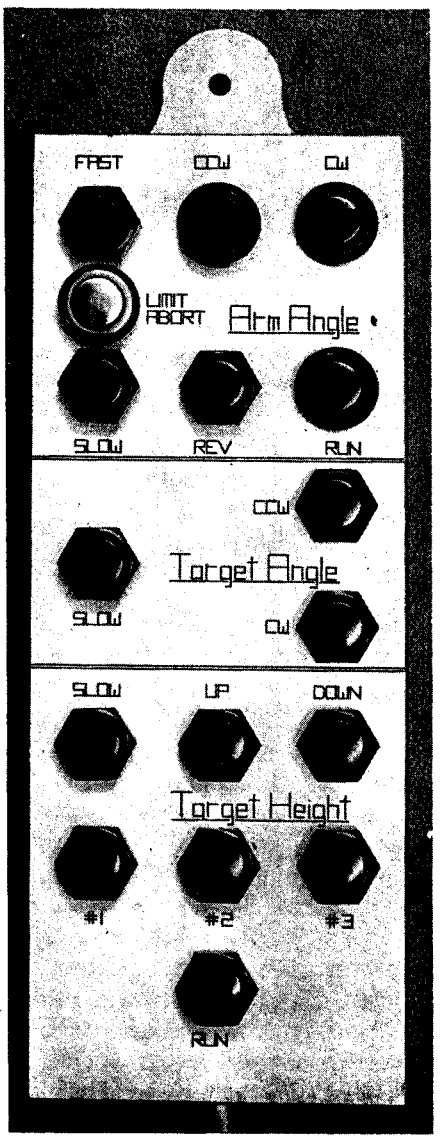

Fig. 2. Local control box.

2.2. Local electrical system

The local electrical system includes a portable control box connected to a power supply by 30 ft of multiconductor cable. The power supply along with the control relays are completely enclosed in a steel cabinet isolating the contact noise of the relays. The control box shown in fig. 2 contains all of the functions found on the remote control panel except the automatic angle increment feature of the main arm which is described below. In addition to these controls, however, there is a main arm limit override switch permitting the detector to be driven through zero degrees if necessary. This feature was incorporated only into the local control trying to minimize the possibility of an accident and not worrying about the slight inconvenience it might create. The mobility of this local control box greatly facilitates the alignment of the goniometer on the beam line.

2.3. Remote control panel

The remote control panel is shown in fig. 3. The controls on the panel are placed in three vertical groupings. The right hand section contains the controls and digital counter for the target angle. In the center is located the target height controls and counter. The three buttons located in a horizontal row are used for the automatic positioning of three targets in the target chamber. Any one of the targets may be selected by

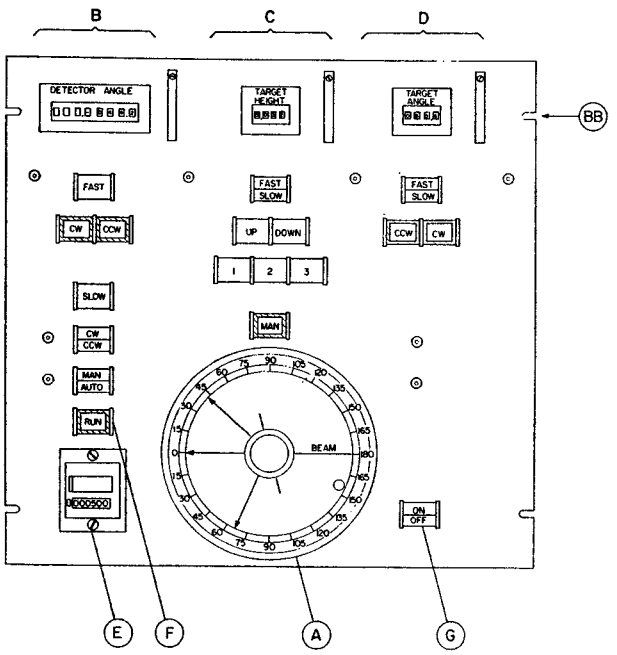

Fig. 3. The remote control panel.

pushing the corresponding button. In addition to this automatic feature there is a manual mode which permits, for example, a target uniformity scan.

The last group of controls on the left is for the main arm. The digital counter used for this readout is a dual-bank type[11]) which indicates the scattering angle of the detected particles increasing in either direction from 0°. At the bottom of this group is located a predetermined, electromagnetic digital counter. This counter is used to select the number of steps–0.01°/step–that the main arm is to be moved. In a typical experiment, for example, it is not uncommon to measure an angular distribution in equal angular steps. In such a case the size of the step is set on the preset counter and the motion is automatically completed when the run button is activated.

This remote control panel also contains a graphic display which shows the relative angular positions of the incident beam, the main arm, the target, and the manually positioned arm. This display is in the lower portion of the panel and is coupled to the digital readout system for both the main arm and target by a pair of small synchro motors.

3. Performance tests

After completion the assembled goniometer was subjected to a series of tests to determine its operational characteristics. Various positions of each of the three goniometer elements were measured by the corresponding digital readout system and simultaneously by a reference system which had an uncertainty less than that expected in the digital system.

There are two quantities which were used in these studies to indicate the characteristic errors of the readout system: δ and the backlash. The δ is defined by the equation:

$$\delta^2 = \sum_{i=1}^{N} (X_G - X_s)_i^2 / N,$$

where X_G is the measurement as determined by the goniometer readout system, X_s is the measurement in the reference system, and N is the total number of measurements involved. The backlash of a readout system is related to the differences of measurements of fixed positions when the element approaches these parts from opposite directions. These figures were obtained for each system operating under a variety of operating conditions.

The main arm was designed to measure scattering angles with a precision of 0.02°. To test this system it was necessary to find a reference of angular position to which digital readout of the main arm could be compared. The reference used was a set of points located around a central point which were defined with two transits and a steel tape measure. The transits were primarily used to determine straight lines between points. A K&E jig transit was also used to determine an accurate 90° angle ($\pm 0.003°$) between the lines of sight of the two scopes. The resulting total uncertainties were computed with standard techniques[12]) using estimates of the maximum standard errors for all of the procedures involved in the tests. The resulting uncertainties in the comparisons between the positions as measured by the two systems ranged between 0.002° and 0.007°.

The reference of angular position used to check the target angle readout was the main arm itself. A front surfaced mirror was placed in the target holder and an index mark fastened to the main arm was sighted through the mirror using a transit scope. Comparisons were then made between variations in the positions of the main arm and the corresponding positions of the target.

The reference for linear distances used to test the target height drive was a dial indicator capable of being read to 0.5 mil coupled to the slide on a vernier height gauge with a least count of 1 mil. The indicator tip contacted the top of the target shaft. The target height position as indicated by the digital readout was compared to the vernier gauge reading when the vernier slide had been adjusted to set the indicator to a

TABLE 1
Errors in the digital readouts for a typical setup.

	rms	Max	N
Main arm angle			
δ	0.012°	0.024°	77
Backlash	0.020°	0.062°	26
Target angle			
δ	0.3°	0.7°	66
Backlash	6.2°	6.7°	11
Target height			
δ	1 mil	2 mil	55
Backlash	11 mil	12 mil	16

reference point. The microswitches were also tested to determine how well a target could be repositioned in the automatic mode. It was found that this could be done with a standard error of 1 mil when a consistent direction of approach to the position is used.

A summary of the results of these tests are shown in table 1. These figures show what uncertainties might be expected in typical experimental setups. Maximum deviations which are the largest discrepancies observed during these tests, are shown along with the total number of measurements, N, involved in each rms value.

There are two additional aspects of the goniometer which effect precision to which the detectors can be positioned relative to the incident beam direction – the concentricity of the rotating elements and the flatness of rotation of the main arm. The concentricity was measured for each rotating element with respect to the other elements using a dial indicator. The total indicator fluctuations found in these tests ranged between 1 and 5 mil. This showed that the centers of rotation of the elements are all to within 2.5 mil of each other. The flatness of rotation of the main arm depends on how carefully the goniometer base and arm braces are adjusted when the system is aligned. It was found, however, that the arm can be adjusted to rotate in a level plane to ± 2 mil with little trouble.

4. Installation and use on the beam line

To utilize the precision of this goniometer to its fullest, it was necessary to install it with equal precision on the beam line of the sector focused cyclotron at MSU. The precision also depends on how well the incident beam geometry is determined. In the initial setup the beam direction and height at the center of the

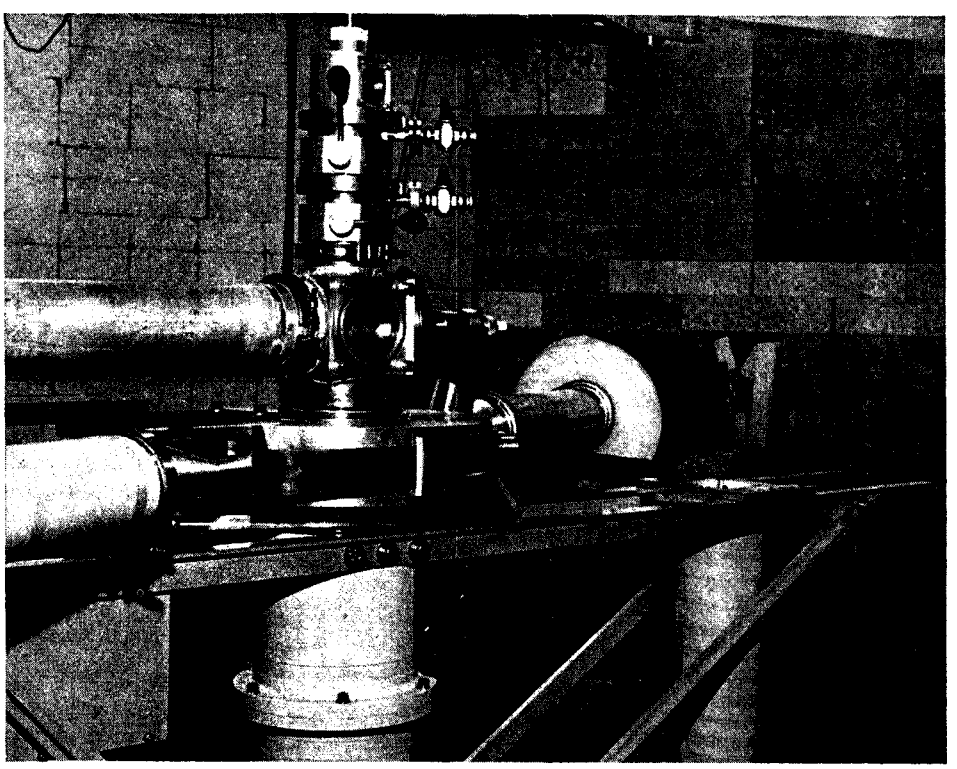

Fig. 4. The goniometer drive unit installed on the beam line.

goniometer were determined by taking beam burns at several locations in a region about this point. It was estimated that the beam direction was determined in this way with an uncertainty of $\pm 0.1°$. The goniometer was then adjusted such that the center of rotation intersected this beam line to ± 5 mil. The main arm was also at the designed height relative to the beam height to ± 2 mil and rotated in a level plane to ± 2 mil at the 4 ft radius.

The goniometer drive unit is shown in fig. 4 located on the beam line at MSUCL as viewed looking toward the beam dump located beyond the target chamber. It is shown here with the 16 inch target chamber with the sliding vacuum seal and a vacuum pumping system coupled to the target chamber just below the target lock. The beam dump is shielded by about 3 ft of concrete blocks and paraffin. This shielding was found to reduce the background of neutrons in the experimental area by a factor of about 10.

This experimental system has been successfully used for the measurement of inelastic proton scattering from the stable even nickel isotopes at 40 MeV. The alignment of the beam into the chamber was done in the following way. Two $\frac{1}{8}$ inch thick, tantalum, annular slits, $\frac{1}{2}$ inch and $\frac{1}{8}$ inch, in diameter were placed at a radius of 10 inch and at the center of rotation respectively. By adjusting the magnets in the external beam system, the beam current entering the beam dump through the smaller slit could be maximized. This method of setup permitted the adjustment of the incident beam so that it passed through the center of the goniometer.

The zero angle of the beam was determined in this experiment by using the kinematic cross-over of peaks[13]) of different target nuclei assuming the energy of the beam was determined by the beam analysis system. The carbon and oxygen contaminants in the nickel targets provided measurements throughout the experiment and resulted in the determination of the zero angle to better than $\pm 0.2°$ for all the detectors used.

The detector setup in this experiment involved two Ge(Li) counters separated by 20° and simultaneously used in conjunction with a $\frac{1}{2}$ mil Kapton window on the target chamber. Short evacuated couplings containing $\frac{1}{4}$ mil Mylar windows extended between the detector packages and the target chamber.

The $\frac{1}{16} \times \frac{1}{8}$ inch collimators on the detectors, located at a radii of 9.5 inch, permitted 3% statistics to be obtained in about one hour for states with differential cross sections of 2 mb/rad. Beam currents of up to

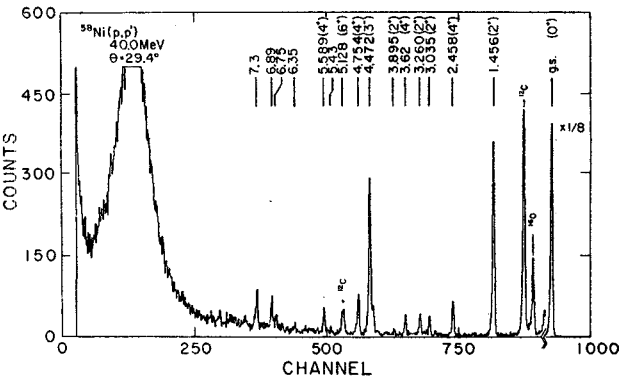

Fig. 5. A spectrum of inelastically scattered, 40 MeV protons from ^{58}Ni with $\theta_{Lab} = 29.4°$.

400 nA were used in this experiment, the maximum during any particular run being determined by what constitutes an acceptable pile up rate. With this setup the angular distributions for the four even nickel isotopes were obtained in 5° steps from 15° to 90° in a total of about 43 hour. A typical spectrum from this experiment is shown in fig. 5 plotted on a linear scale.

The authors express thanks to D. Rozof, G. Stork, N. Mercer, and the MSUCL machine shop staff for their help in the design, construction and assembly of the goniometer drive unit. The assistance of W. Johnson, R. deForest, and the staff of the electronics shop in the design and fabrication of the electrical control systems is acknowledged as is the help of A. Kaye in the procurement of the raw materials. Also appreciated are the many discussions with members of the professional staff and the graduate students and the willing assistance of the technical staff at MSUCL.

References

1) C. R. Gruhn, T. Kuo, B. Gottschalk, S. Kannenberg and N. Wall, Phys. Letters **24B** (1967) 266.
2) C. R. Gruhn, B.A.P.S. **13** (1968) 1363.
3) C. Chasman and R. A. Ristiney, Nucl. Instr. and Meth. **34** (1965) 250.
4) H. Blosser, to be published.
5) J. Cameron, Thesis (UCLA, 1967).
6) John H. Williams Lab. of Nucl. Phys. Ann. Report C00-126567 (1968) p. 170.
7) E. Feldl, C. Fetrow and C. F. Moore, Nucl. Instr. and Meth. **44** (1966) 98.
8) F. L. Borsay, Nucl. Instr. and Meth. **52** (1967) 338.
9) E. I. DuPont de Nemours, Wilmington, Del.
10) Designed and built by C. Maggiore and T. Kuo.
11) Durant, No. 4-4-Y-8831.
12) Y. Beers, *Theory of errors* (Addison-Wesley, 1962) p. 26.
13) B. M. Bardin and M. E. Rickey, Rev. Sci. Instr. **35** (1964) 886.

Reprinted from THE PHYSICAL REVIEW, Vol. 187, No. 4, 1246–1258, 20 November 1969
Printed in U. S. A.

Energy Dependence and Spectroscopy of the $^{16}O(p, d)^{15}O$ Reaction*

J. L. SNELGROVE† AND E. KASHY
Michigan State University, East Lansing, Michigan 48823

(Received 19 June 1969)

A systematic study of the extraction of spectroscopic factors for the (p, d) reaction on light nuclei and the difficulties encountered in obtaining reasonable distorted-wave Born approximation (DWBA) fits to the shapes of the angular distributions has been made. Deuteron spectra and angular distributions were measured for the $^{16}O(p, d)^{15}O$ reaction for 21.27-, 25.52-, 31.82-, 38.63-, and 45.34-MeV incident protons. The elastic scattering of protons from ^{16}O was measured over the same energy range and used to obtain proton optical-model parameters. Present results indicate that consistent spectroscopic information can be obtained from DWBA calculations when the deuterons in the exit channel have an energy greater than 20 MeV. Approximately 30% of the $1p_{3/2}$ strength appears to be missing from the 6.18-MeV, $\frac{3}{2}^-$ level of ^{15}O, and a large fraction of that strength appears in the 9.60- and 10.46-MeV levels. Small $2s$-$1d$ admixtures were observed in the ground state of ^{16}O, and excitation of a $\frac{1}{2}^+$ level is observed. This excitation is a possible candidate for a two-step excitation process.

I. INTRODUCTION

FOR a number of years the (p, d) reaction has proven to be a popular and valuable tool in nuclear spectroscopy. The selective way in which this reaction populates the levels of the residual nucleus provides information about these levels and about the ground state of the target nucleus, which can be compared to the predictions of various models which yield wave functions of nuclear states. The distorted-wave Born approximation (DWBA) theory of the direct reaction[1,2] has been widely used in the analysis of the (p, d) reaction to obtain spectroscopic information, which is usually given in terms of the spectroscopic factor. The meaningfulness of the spectroscopic factors, however, depends on the degree to which the DWBA calculation represents the actual reaction mechanism. In previous studies of (p, d) reactions on $1p$ shell[3–6] and $2s$-$1d$ shell[7,8] nuclei, difficulty was encountered in obtaining reasonable agreement between the experimental and DWBA angular distribution shapes when optical potentials which best described the elastic scattering were used in a standard DWBA calculation. The agreement was improved by the somewhat artificial means of adjusting optical potentials or using radial integration cutoffs, but in such cases one must be suspicious of the spectroscopic factors extracted. The present work was undertaken to study the use of the DWBA theory in the extraction of (p, d) spectroscopic factors for the light nuclei.

The nucleus ^{16}O was chosen for this study because its "closed" $1p$ shell nature and the numerous theoretical studies of its ground-state structure provided a basis for making predictions about the (p, d) spectroscopic factors to be expected, which could be used as a guide in evaluating the results of a given DWBA calculation. The strong dependence of the experimental peak of the $^{16}O(p, d)^{15}O$ $l_n=1$ angular distributions on the energy of the incident proton coupled with the availability of protons between 21 and 45 MeV made possible a test of energy dependence in the DWBA calculations. Similar studies have been made for the $^{40}Ca(d, p)^{41}Ca$ reaction[9] and for the $^{16}O(d, {}^3He)^{15}N$ and $^{40}Ca(d, {}^3He)^{39}K$ reactions.[10] Although the $^{16}O(p, d)^{15}O$ reaction has previously been studied with protons between 17 and 156 MeV,[7,11–16] it became clear as this study progressed that improved energy resolution made possible the extraction of additional spectroscopic information on the levels of ^{15}O, which is presented in some detail in this paper.

The elastic scattering of protons from ^{16}O was also studied at the various proton energies used in the (p, d) measurements in order to obtain optical-model parameters for use in the DWBA analysis. These data and parameters will be presented.

* Research supported by the National Science Foundation.
† Present address: Argonne National Laboratory, 9700 S. Cass Ave., Argonne, Ill. 60439.

[1] G. R. Satchler, Nucl. Phys. **55**, 1 (1964).
[2] R. H. Bassel, R. M. Drisko, and G. R. Satchler, Oak Ridge National Laboratory Report No. ORNL-3240, 1962 (unpublished); R. H. Bassel, R. M. Drisko, and G. R. Satchler, Oak Ridge National Laboratory Memorandum to the Users of the Code JULIE, 1966 (unpublished).
[3] L. A. Kull, Ph.D. thesis, Michigan State University, 1967 (unpublished).
[4] L. A. Kull, Phys. Rev. **163**, 1066 (1967).
[5] L. A. Kull and E. Kashy, Phys Rev. **167**, 963 (1968).
[6] R. L. Kozub, L. A. Kull, and E. Kashy, Nucl. Phys. **A99**, 540 (1967).
[7] R. L. Kozub, Ph.D. thesis, Michigan State University, 1967 (unpublished).
[8] R. L. Kozub, Phys. Rev. **172**, 1078 (1968).
[9] L. L. Lee, Jr., J. P. Schiffer, B. Zeidman, G. R. Satchler, R. M. Drisko, and R. H. Bassel, Phys. Rev. **136**, B971 (1964).
[10] J. C. Hiebert, E. Newman, and R. H. Bassel, Phys. Rev. **154**, 898 (1967).
[11] N. W. Chant, P. S. Fisher, and D. K. Scott, Nucl. Phys. **A99**, 669 (1967).
[12] G. G. Shute and R. E. Brown, University of Minnesota Linear Accelerator Laboratory Annual Progress Report No. 55, 1967 (unpublished).
[13] J. C. Legg, Phys. Rev. **129**, 272 (1963).
[14] J. K. P. Lee, S. K. Mark, P. M. Portner, and R. B. Moore, Nucl. Phys. **A106**, 357 (1967).
[15] D. Bachelier, M. Bernas, I. Brissand, C. Detraz, N. K. Ganguly, and P. Radvangi, Compt. Rend. **2**, 429 (1964).
[16] I. S. Towner, Nucl. Phys. (to be published).

II. EXPERIMENTAL APPARATUS AND METHODS

The proton beam of the Michigan State University sector-focused cyclotron was magnetically analyzed and focused on target at the center of a 36-in. scattering chamber. The energy, resolution, and divergence of the beam were determined from settings of the analysis system, which has been described elsewhere.[17]

The target was natural oxygen gas (99.76% ^{16}O) at approximately 30-cm Hg pressure contained in either a 3- or 5-in. cell with a 0.0005-in. Kapton[18] window. The detector used in the (p, p) experiments was a 0.25-in.-square, 0.50-in.-thick CsI(Tl) crystal mounted on the face of a photomultiplier tube. Most of the (p, d) data were obtained with commercial silicon detectors in a standard ΔE-E arrangement, using a Goulding system for particle identification, with a typical energy resolution of 110 keV for 45-MeV incident protons, a large fraction of which was attributable to kinematic broadening. In one experiment, particle identification was accomplished using a single counter with time-of-flight techniques, with a resolution of 60 keV for 32-MeV incident protons.

Angular distributions were taken in 5° steps from $\theta_{lab}=\sim 10°$ to 70° and in 7.5° steps from $\theta_{lab}=70°$ to 160°. Additional points were often taken between 10° and 20° to determine better the first peak of the angular distribution. Measurements were made on both sides of the beam to determine any zero correction to the digital readout of the scattering angle.

The energy spectra were analyzed on the Laboratory's Scientific Data Systems Sigma 7 computer to determine the mean energy and yield of each state seen. The energies were corrected for the energy lost in the gas and cell walls by the incident and scattered particles. The yields were corrected for background in all experiments, and in the (p, p) experiments corrections were made for analyzer dead time (typically $\leq 2\%$) and for counting losses due to reactions in the CsI(Tl) crystal ($\leq 2\%$). Differential cross sections were calculated using the geometrical corrections for gas-cell geometry given by Silverstein.[19] The total measurement uncertainty in the differential cross sections is estimated to be 3.6% at $\theta_{lab}\simeq 30°$. The error bars shown on all data represent the total uncertainty, i.e., the measurement uncertainty and the statistical uncertainty added in quadrature. A more detailed description of the experimental methods and the treatment of errors is contained in Ref. 20.

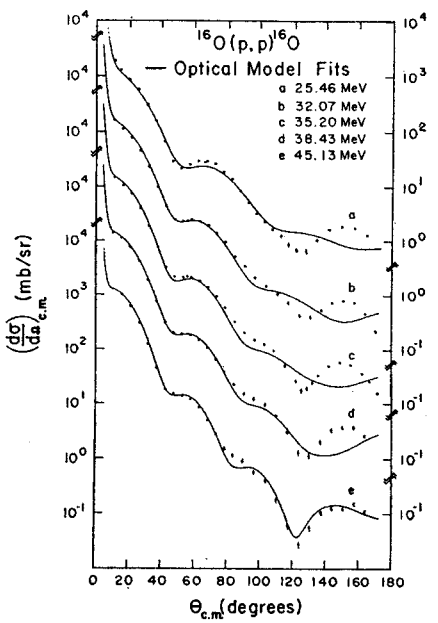

FIG. 1. Optical-model fits to the $^{16}O(p, p)^{16}O$ angular distributions using energy-dependent sets of parameters.

III. ELASTIC SCATTERING DATA AND OPTICAL-MODEL PARAMETERS

A. Proton Scattering

Differential cross sections for the elastic scattering of protons by ^{16}O were measured at incident energies of 25.46, 32.07, 35.10, 38.43, and 45.13 MeV over an angular range of 10° to 170° in the c.m. frame. After completing each angular distribution, measurement of the differential cross section at the position of the second maximum (50°–60°) over an energy range of ±300 keV around the bombarding energy showed that no sharp resonances existed. As a check on the efficiency of the counter system, differential cross sections for the elastic scattering of protons by protons were measured at several angles between 15° and 22° in the laboratory frame. These were compared to those measured by Johnston and Swenson[21] and were found to agree within the experimental errors. The $^{16}O(p, p)$ angular distributions are shown in Fig. 1. These data are in quantitative agreement with those of Cameron *et al.*[22,23] whose extensive study covered the energy range 23.4–46.1 MeV. They found that the behavior of the cross sections below 30 MeV indicated the existence of broad resonances in the p-^{16}O system. These resonances were too broad to have been detected during the search for sharp resonances within 300 keV of the original proton energy.

In the optical model of elastic scattering, it is assumed that the interaction of the two nuclei involved can be represented by scattering from a one-body complex

[17] G. H. Mackenzie, E. Kashy, M. M. Gordon, and H. G. Blosser, IEEE Trans. Nucl. Sci. NS-14, 450 (1967).
[18] E. I. Dupont de Nemours, Wilmington, Del.
[19] E. A. Silverstein, Nucl. Instr. Methods 4, 53 (1959).
[20] J. L. Snelgrove, Ph.D. thesis, Michigan State University, 1968 (unpublished).
[21] L. H. Johnston and D. A. Swenson, Phys. Rev. 111, 212 (1958).
[22] J. M. Cameron, University of California at Los Angeles Technical Report No. P-80, 1967 (unpublished).
[23] J. M. Cameron, J. R. Richardson, W. T. H. van Oers, and J. W. Verba, Phys. Rev. 167, 908 (1968).

TABLE I. Optical-model parameters describing proton elastic scattering from ^{16}O.

E_p(lab) (MeV)	V (MeV)	W_S (MeV)	W_D (MeV)	r_I (E)	a_I (F)	σ_R(expt)[a] (mb)	σ_R(theoret.) (mb)	χ^2/N
25.46	48.4	0.0	6.80	1.19	0.550	507	535	36.7
32.07	45 5	0.0	5.31	1.44	0.490	473	487	32.3
35.20	45.0	0.91	5.70	1.45	0.450	458	498	45.3
38.43	44.4	2.00	4.89	1.40	0.430	441	446	16.5
45.13	42.7	3.11	5.65	1.28	0.415	407	407	4.9

$r_{so}=r_R=1.12$ F, $a_{so}=a_R=0.69$ F, $r_c=1.15$ F, $V_{so}=7.0$ MeV

[a] Based on data found in Ref. 22.

potential having the form

$$V_{opt}(r)=V_c(r)-Vf(x)-i[W_S-4W_D(d/dx')]f(x')+V_{so}[(\hbar)^2/(m_\pi c)^2]r^{-1}[df(x)/dr](\boldsymbol{l}\cdot\boldsymbol{\sigma}),$$

where

$$V_c(r)=ZZ'e^2/r, \quad r\geq R_c$$
$$=ZZ'e^2[3-(r^2/R_c^2)]/2R_c, \quad r\leq R_c$$
$$R_c=r_cA^{1/3},$$

and

$$f(x)=(e^x+1)^{-1},$$

with

$$x=(r-r_RA^{1/3})/a_R,$$
$$x'=(r-r_IA^{1/3})/a_I.$$

V_c is the potential felt by a point charge Ze interacting with a uniformly charged sphere of radius R_c and charge $Z'e$.

Optical-model analyses were performed with the Perey search code GIBELUMP,[24] with the spin-orbit radius and diffuseness set equal to the corresponding real-well parameters. The initial calculations were constrained to give a single set of parameters which gave the best over-all fit to the five experimental angular distributions. However, owing to nonlocality effects not included in the optical potential, one expects the parameters to exhibit some energy dependence, so subsequent searches allowed the parameters to vary with the incident proton energy. The real radius and diffuseness tended not to vary and so were fixed. The angular distribution fits were found to be very insensitive to changes in V_{so}.

A value of 7.0 MeV for V_{so} was chosen on the basis of parameters found by Cameron[22] during preliminary analyses of elastic scattering[23] and polarization data.[25] Cameron[22] had also measured reaction cross-section data at incident proton energies appropriate to his work. Since these varied smoothly with energy, values of the reaction cross section σ_R for the incident proton energies of the present work were extracted by graphical interpolation. These were used as a guide in choosing between sets of optical parameters which gave essentially identical values of χ^2/N.

The final set of parameters is shown in Table I, and the corresponding fits are shown in Fig. 1. It was found that inclusion of a volume imaginary potential was necessary above 32.07 MeV, with its strength increasing with energy. This is probably due to the deeper penetration of the more highly energetic protons. The forward angle fits are improved, although the improvement is slight for the 25.46-MeV data. The back angle fits are very poor for all but the 45.13-MeV data. This behavior is consistent with that found by van Oers and Cameron[26] over the energy range of 23–53 MeV, by Barrett *et al.*[27] at 30.3 MeV, by Kim *et al.*[28] at 31.0 MeV, and by Fannon *et al.*[29] at 49.48 MeV. It has been found in other work[30] that the use of a spin-orbit radius parameter 10 to 15% smaller than the real radius parameter was helpful in obtaining fits to the back angle data. This was tried with no significant improvement. Thus, it appears that the optical model gives a poor description of proton elastic scattering from ^{16}O below 30 MeV where resonances occur, that between 30 and 40 MeV the description is good forward of 100° and that the

TABLE II. Deuteron optical parameters used in the DWBA analysis of the $^{16}O(p,d)^{15}O$ reaction.

E_d (MeV)	V (MeV)	r_R (F)	a_R (F)	W_D (MeV)	r_I (F)	a_I (F)
33.2	92.8	1.03	0.80	8.84	1.41	0.70
26.2	98.0	1.00	0.80	7.95	1.45	0.70
19.0	104.0	0.98	0.80	7.05	1.50	0.70
10.4	114.0	0.95	0.80	6.00	1.57	0.70
4.5	130.0	0.90	0.80	5.00	1.68	0.70

$r_{so}=r_R$, $a_{so}=a_R$, $V_{so}=7.57$ MeV, $r_{oc}=1.30$ F.

[24] Unpublished FORTRAN-IV computer code written by F. G. Perey and modified by R. M. Haybron at Oak Ridge National Laboratory.

[25] H. B. Eldridge, S. N. Bunker, J. M. Cameron, J. R. Richardson, and W. T. H. van Oers, Phys. Rev. **167**, 915 (1968).

[26] W. T. H. van Oers and J. M. Cameron, Bull. Am. Phys. Soc. **13**, 883 (1968).

[27] R. C. Barrett, A. D. Hill, and P. E. Hodgson, Nucl. Phys. **62**, 133 (1965).

[28] C. C. Kim. S. M. Bunch, D. W. Devins, and H. H. Forster, Nucl. Phys. **58**, 32 (1964).

[29] J. A. Fannon, E. J. Burge, D. A. Smith, and N. K. Ganguly, Nucl. Phys. **A97**, 263 (1967).

[30] M. P. Fricke, E. E. Gross, B. J. Morton, and A. Zucker, Phys. Rev. **156**, 1207 (1967).

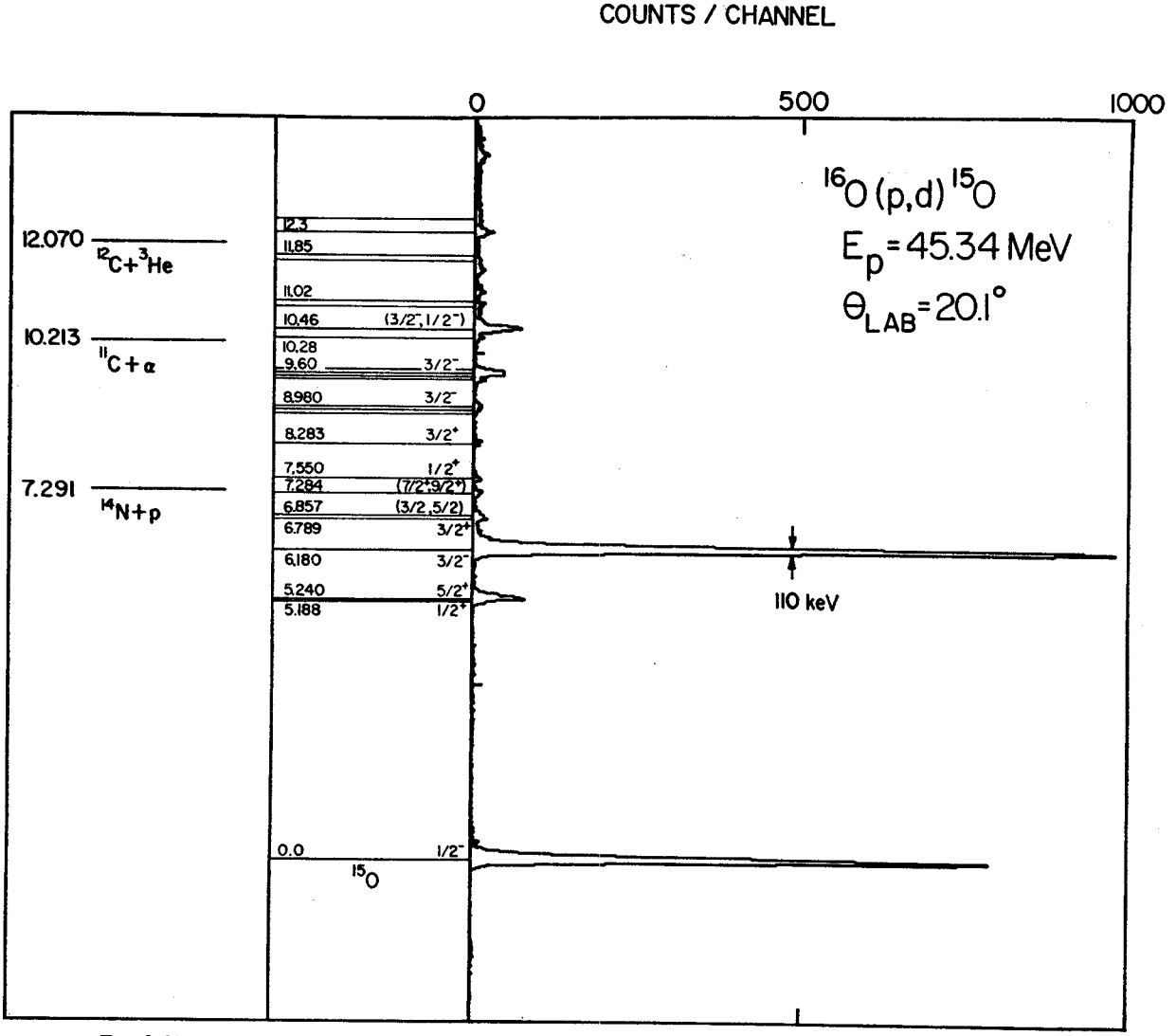

FIG. 2. Energy-level diagram of ^{15}O displayed beside a deuteron energy spectrum from the $^{16}O(p, d)^{15}O$ reaction for $E_p = 45.34$ MeV and $\theta_{lab} = 20.1°$.

optical model describes the scattering very well for incident protons above 40 MeV.

B. Deuteron Scattering

Since it is impossible to measure the elastic scattering of deuterons by the unstable nucleus ^{15}O, data for deuteron scattering by ^{16}O was used. Sets of optical-model parameters have been found for deuteron elastic scattering by ^{16}O for incident deuteron energies between 11.8 and 52 MeV.[31–37] Many studies have been done with lower energy deuterons, but the applicability of the optical model is questionable in these cases. The parameters used here are based on the 11.8-MeV parameters of Hodgson,[34] the 34.4-MeV parameters of Newman *et al.*,[36] and the 52-MeV parameters of Duelli *et al.*[37] Each of these studies used a derivative surface absorption and included spin-orbit effects. The various parameters were plotted with respect to deuteron energy and smooth curves weighted toward the 34.4-MeV parameters and away from the 16.8-MeV parameters were used to determine the parameters to be used in the (p, d) analyses. They are listed in Table II.

IV. EXPERIMENTAL RESULTS

In this section spectra and angular distributions are presented for the $^{16}O(p, d)^{15}O$ reaction. Some of the conclusions reached about possible spin and parity assignments are based upon the DWBA calculations discussed in the next section.

[31] W. Fitz, R. Jahr, and R. Santo, Nucl. Phys. A101, 449 (1967).
[32] Dai-Ca Nguyen, J. Phys. Soc. Japan 21, 2462 (1966).
[33] A. A. Cowley, G. Heymann, R. L. Keizer, and M. J. Scott, Nucl, Phys. 86, 363 (1966).
[34] P. E. Hodgson, Advan. Phys. 15, 329 (1966), quoted in Ref. 11.
[35] J. Testoni, S. Mayo, and P. E. Hodgson, Nucl. Phys. 50, 479 (1964).
[36] E. Newman, L. C. Becker, B. M. Preedom, and J. C. Hiebert, Nucl. Phys. A100, 225 (1967).
[37] B. Duelli, F. Hintenberger, G. Mairle, U. Schmidt-Rohr, P. Turek, and G. Wagner, Phys. Letters 23, 485 (1966).

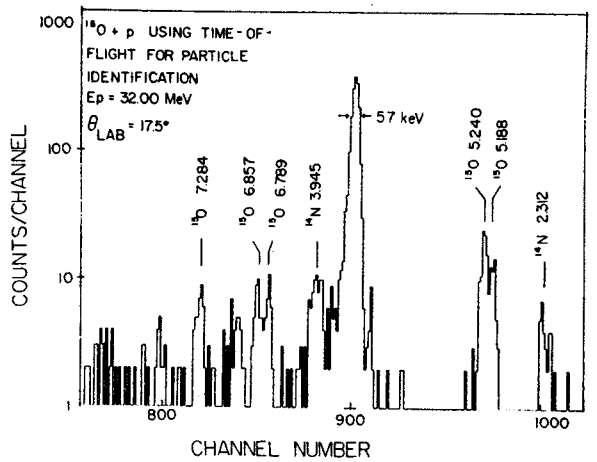

FIG. 3. Energy spectrum of reaction products at $\theta_{lab}=17.5°$ for 32.00-MeV protons incident on ^{16}O, obtained by use of time-of-flight techniques for particle identification.

A. Simple Model Predictions

Considered as a direct reaction, the (p, d) reaction involves the removal of a single neutron from the target nucleus, which is assumed to be in its ground state. The single-particle energies are given by Jolly[38] as 0.0, 27.0, 33.0, 44.0, and 45.0 MeV for the $1s_{1/2}$, $1p_{3/2}$, $1p_{1/2}$, $1d_{5/2}$, and $2s_{1/2}$ particles, respectively. Thus, for the low-lying levels one would expect either a $1p_{1/2}$ or a $1p_{3/2}$ neutron to be picked up; the pickup of a $1s_{1/2}$ neutron would be very unlikely owing to its strong binding. On this basis, one would expect the deuteron energy spectra to contain one $\frac{1}{2}^-$ peak, one $\frac{3}{2}^-$ peak, and no others.

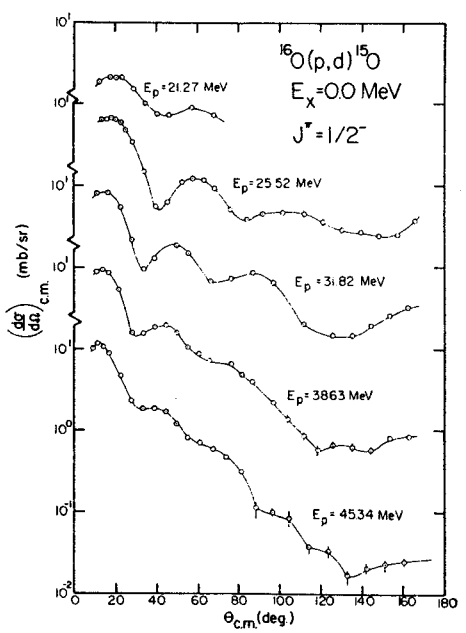

FIG. 4. Experimental deuteron angular distributions for the 0.0-MeV, $\frac{1}{2}^-$ level of ^{15}O from the ^{16}O$(p, d)^{15}$O reaction for incident proton energies between 21.27 and 45.34 MeV.

[38] H. P. Jolly, Phys. Letters 5, 289 (1963).

It is known, however, that the simple model is much too naive, even for the case of a "closed-shell" nucleus such as ^{16}O. One might consider the effects of low-lying deformed states in the closed-shell nucleus[39–42] when using that nucleus as a core. Brown and Shukla[43] have performed such calculations for ^{15}O and ^{15}N. They predict, in addition to the strong 0.0-MeV, $\frac{1}{2}^-$ and 6.18-MeV, $\frac{3}{2}^-$ levels, the existence of a $\frac{3}{2}^-$ level between 10.0 and 11.0 MeV of excitation and a $\frac{1}{2}^-$ level approximately 1.0 MeV lower. Bertsch[44] has predicted that core polarization could result in many highly fragmented states with excitation energies of approximately 20 MeV. Hence, core polarization can result in the sharing

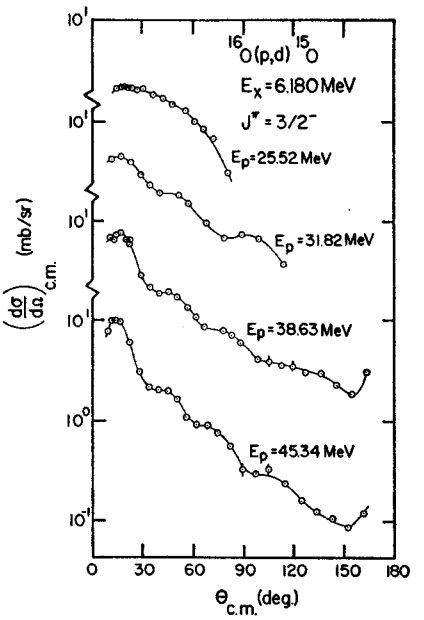

FIG. 5. Experimental deuteron angular distributions for the 6.180-MeV, $\frac{3}{2}^-$ level of ^{15}O from the ^{16}O$(p, d)^{15}$O reaction for incident proton energies between 25.52 and 45.34 MeV.

of the $1p_{1/2}$ and $1p_{3/2}$ strengths among several states. One would also expect the ^{16}O ground state to be more complex. Calculations have been performed[41] in which two-particle–two-hole and four-particle–four-hole admixtures have been considered. If such admixtures existed, one would expect to pickup some $1d_{5/2}$ and $2s_{1/2}$ neutrons, leading to positive parity levels in ^{15}O.

B. Energy Spectra

Figure 2 shows an energy-level diagram (including all known levels below 11 MeV) of the ^{15}O nucleus beside which has been placed a deuteron spectrum taken at a laboratory angle of 20.1° with 45.34-MeV incident

[39] H. Morinaga, Phys. Rev. 101, 254 (1956).
[40] T. Engeland, Nucl. Phys. 72, 68 (1965).
[41] G. E. Brown and A. M. Green, Nucl. Phys. 75, 401 (1966).
[42] G. E. Brown and A. M. Green, Nucl. Phys. 85, 87 (1966).
[43] G. E. Brown and A. P. Shukla, Princeton University Report No. PUC-937-268, 1967 (unpublished).
[44] G. F. Bertsch (private communication).

protons. All energies, spins, and parities for the levels below 9 MeV were taken from the γ-ray work of Warburton *et al.*,[45] those of the levels between 9 and 10 MeV from the work of Lambert and Durand,[46] and those of levels above 10 MeV from Lauritsen and Ajzenberg-Selove.[47] One immediately notices in Fig. 2 the presence of the two very strong peaks corresponding to $1p_{1/2}$ and $1p_{3/2}$ neutron pickup with all other states being much more weakly excited. Figure 3 shows a spectrum obtained using the time-of-flight system for mass identification in which the closely spaced levels near 5.2 and 6.8 MeV are partially resolved. The peaks corresponding to ^{14}N levels are due to ^{3}He particles from the $^{16}O(p,{}^{3}He)^{14}N$ reaction which reached the detector within the accepted time window. Other spectra showing comparable resolution were obtained with this method at laboratory angles between 12.4° and 30°.

C. Negative-Parity Levels

Below an excitation energy of 16.5 MeV, the existence of one $\frac{1}{2}^-$ and three $\frac{3}{2}^-$ levels have been confirmed.[45-47] Angular distributions measured for the 0.0-MeV, $\frac{1}{2}^-$ and 6.180-MeV, $\frac{3}{2}^-$ levels predicted by the simplest shell model are shown in Figs. 4 and 5. A first maximum between 10° and 20° in the c.m. frame is characteristic of $l_n=1$ pickup, with the angle at which the first maximum occurs decreasing as the incident proton energy increases. J dependence in this reaction exhibits itself in the generally steeper slope and more pronounced oscillation of the $J^\pi=\frac{1}{2}^-$ angular distributions.

The magnitude of the differential cross section at the first $l_n=1$ maximum, which is used in the extraction of spectroscopic factors, is shown as a function of the incident proton energy in Fig. 6. Included in this figure are points from other studies of the $^{16}O(p,d)^{15}O$ reaction between 18.5 and 100 MeV.[7,11-14] The dashed curves are drawn to accentuate the general trend of the data and indicate that the $\frac{3}{2}^-$ peak cross section becomes larger than the $\frac{1}{2}^-$ peak cross section at some point between 45 and 100 MeV. Data by Bachelier *et al.*[15] at 156 MeV, which are not shown, indicate that the peak cross sections drop to approximately 5.2 mb/sr and approximately 8.3 mb/sr for the 0.0- and 6.180-MeV levels, respectively.

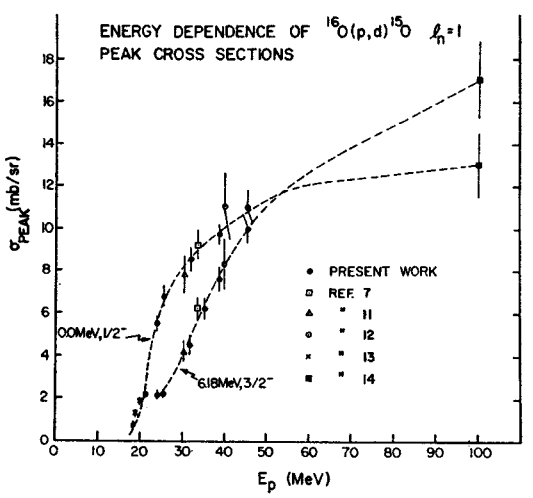

FIG. 6. Dependence of the $l_n=1$ peak cross section of the 0.0-MeV, $\frac{1}{2}^-$ and 6.180-MeV, $\frac{3}{2}^-$ levels of ^{15}O from the $^{16}O(p,d)^{15}O$ reaction on the incident proton energy.

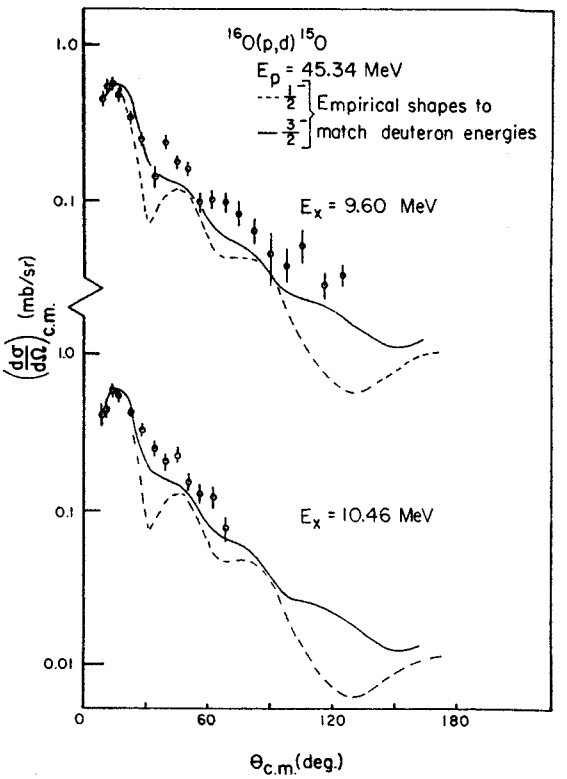

FIG. 7. Deuteron angular distributions for the 9.60- and 10.46-MeV levels of ^{15}O from the $^{16}O(p,d)^{15}O$ reaction for $E_p=45.34$ MeV.

Figure 2 shows the presence of two relatively strong deuteron groups corresponding to levels of higher excitation energy. The first group corresponds to the levels at 9.49, 9.53, 9.60, and 9.66 MeV, which have $J^\pi=\frac{5}{2}^-$, $\frac{1}{2}^+$, $\frac{3}{2}^-$, and $(\frac{7}{2},\frac{9}{2})^-$, respectively.[46] Careful examination of the energy spectra showed that all four levels were excited, but that approximately 70% of the yield was due to excitation of the 9.60-MeV, $\frac{3}{2}^-$ level. The other deuteron group comes from the excitation of the 10.46-MeV level, which was resolved from the 10.28-MeV level. Angular distributions for these levels are shown in Fig. 7. The angular distribution labeled 9.60 contains contributions from the other three close-lying levels. The curves represent empirical $l_n=1$ shapes corresponding to the Q values of the reactions leading to these states, obtained by graphical inter-

[45] E. K. Warburton, J. W. Olness, and D. E. Alburger, Phys. Rev. 140, B1202 (1965).
[46] M. Lambert and M. Durand, Phys. Letters 24B, 287 (1967).
[47] T. Lauritzen and F. Ajzenberg-Selove, in *Nuclear Data Sheets*, compiled by K. Way *et al.* (Printing and Publishing Office, National Academy of Sciences—National Research Council, Washington 25, D. C., 1962).

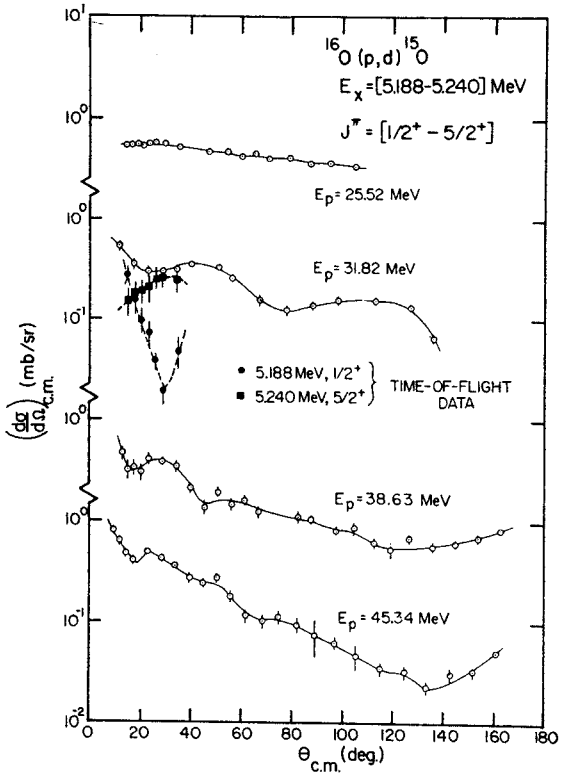

FIG. 8. Deuteron angular distributions for the 5.188–5.240 MeV doublet of ^{15}O from the ^{16}O$(p, d)^{15}$O reaction for incident proton energies between 25.52 and 45.34 MeV.

polation between the shapes of the 0.0 and 6.18 MeV angular distributions for 45.34- and 38.62-MeV incident protons. Both levels are seen to be $l_n=1$ in character, the assignment of $\frac{3}{2}^-$ to the 10.46-MeV level being preferred on the basis of shape. The angular distribution for the 9.60-MeV level does not disagree with the previous $\frac{3}{2}^-$ assignment for that level. Estimates of the $1p_{3/2}$ hole strength in these levels will be given in Sec. V, where spectroscopic factors will be discussed.

D. Positive-Parity Levels

As was noted previously, the only way in which a positive-parity level can be reached in ^{15}O by the direct pickup of a neutron from ^{16}O is for the ^{16}O ground state to contain an admixture of even-l neutrons. The most likely admixtures being $1d_{5/2}$ and $2s_{1/2}$ neutrons, one would look for $\frac{5}{2}^+$ and $\frac{1}{2}^+$ levels. The levels at 5.188, 7.550, 8.735, and 9.53 have previously been shown to be $\frac{1}{2}^+$. The level at 5.240 MeV has an assignment of $\frac{5}{2}^+$, and the $(\frac{3}{2}, \frac{5}{2})$ level at 6.857 MeV appears to be the mirror level of the 7.15 MeV, $\frac{5}{2}^+$ level in ^{15}N.

Examination of Figs. 2 and 3 shows that the 5.188–5.240-MeV doublet has considerable strength. Angular distributions for the unresolved doublet are shown in Fig. 8. The time-of-flight data taken with 32.0-MeV incident protons had sufficient resolution to allow a Gaussian peak shape analysis to be performed to separate the states. Using a nonlinear least-squares method, a skewed Gaussian was fitted to the single 6.18-MeV level to determine a peak shape. Then the areas and centroids of two Gaussians having this shape were adjusted, keeping a fixed separation corresponding to the known separation of the levels, until the fit to the 5.188–5.240-MeV group was judged best. The ratios of the areas were applied to the 31.82-MeV data to obtain partial angular distributions, also shown in Fig. 8. The large errors (approximately 30%) are due to the poor statistics of the data and the uncertainty in the ratios of the areas. The shape of the 5.188 MeV angular distribution is characteristic of $l_n=0$ pickup, whereas the occurrence of the first maximum near 30° for the 5.240-MeV angular distribution indicates an $l_n\geq 2$, consistent with the $\frac{5}{2}^+$ assignment. This disagrees with ^{16}O$(d, t)^{15}$O data quoted in Ref. 48, which showed no direct reaction pattern for the $\frac{1}{2}^+$ member of the doublet.

Excitations of the other $\frac{1}{2}^+$ and $\frac{5}{2}^+$ levels are very weak, with the exception of the 7.550 MeV, $\frac{1}{2}^+$ level, which does not exhibit the characteristics of $l_n=0$ pickup (Fig. 10). Wong[48] in a study of centroids and sums of direct reaction strengths with ^{16}O as a target, has found that central-force (e.g., Rosenfeld and Soper) calculations imply that most of the $1d_{5/2}$ strength is in the 5.24-MeV level, whereas calculations using realistic forces (e.g., Brueckner-Gamel-Thaler, Hamada-Johnston) imply that the dominant part of the $1d_{5/2}$ strength will be in a higher $\frac{5}{2}^+$ state. Thus, the present data tend to support the use of central forces.

Weak excitation of the $\frac{3}{2}^+$ levels at 6.789 and 8.283 MeV has been found, which could be due to the pickup of a $1d_{3/2}$ neutron. The shapes of the angular distributions (Fig. 10) are not inconsistent with such a pickup. An interesting angular distribution was measured for the level at 7.284 MeV, which had been assigned a spin of $\leq\frac{9}{2}$ and appears to be the mirror level of the 7.56-MeV,

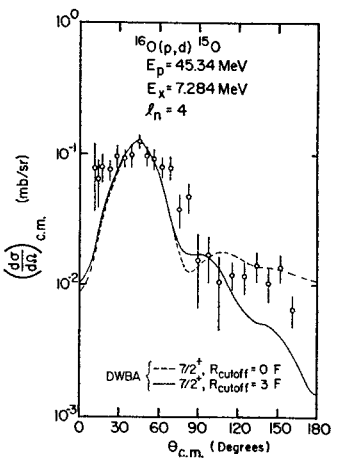

FIG. 9. Deuteron angular distribution and DWBA fit for the 7.284-MeV, $(\frac{7}{2}^+)$ level of ^{15}O from the ^{16}O$(p, d)^{15}$O reaction for E_p=45.34 MeV.

[48] S. S. M. Wong, Nucl. Phys. A120, 625 (1968).

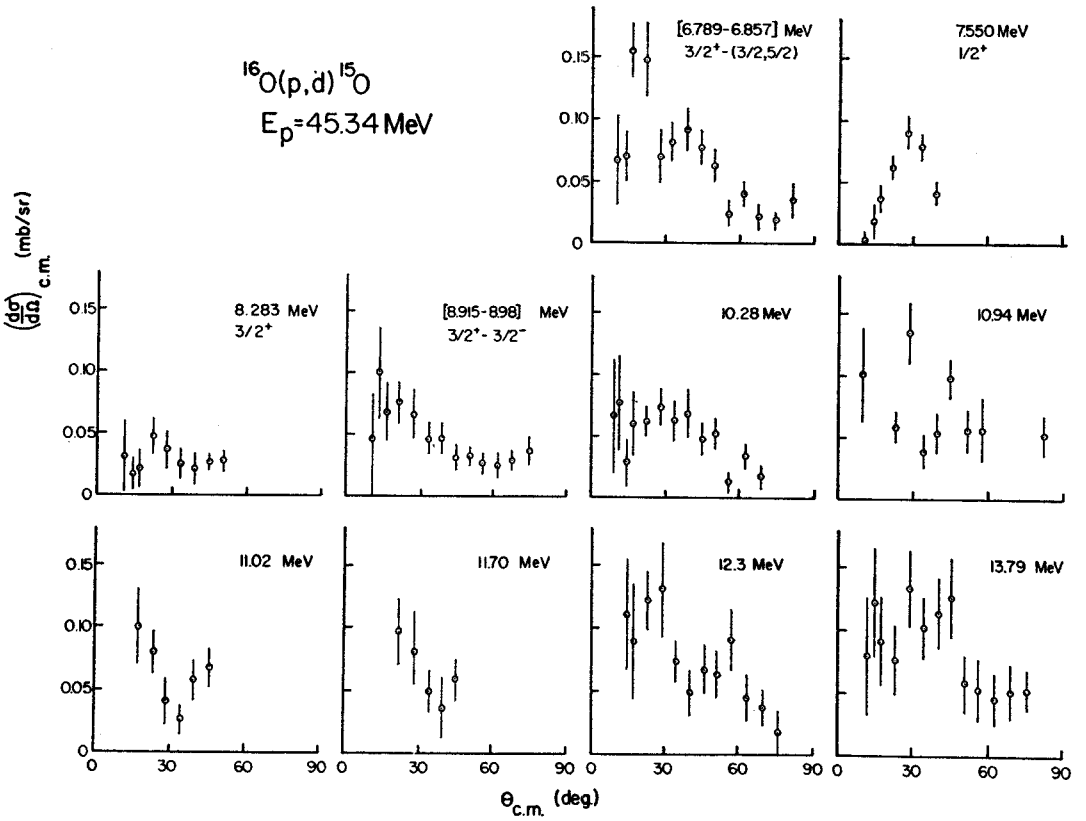

FIG. 10. Deuteron angular distributions for other levels excited in ^{15}O from the $^{16}O(p, d)^{15}O$ reaction at E_p=45.34 MeV.

$\frac{7}{2}^+$ level of ^{15}N. If it were excited by a direct reaction, it would correspond to the pickup of a $1g_{7/2}$ neutron. The angular distribution for this level obtained with 45.34-MeV incident protons is shown in Fig. 9. The calculated $l_n=4$ shape is somewhat similar to the data. An alternative and much more likely process for the excitation of this level is a two-step process in which the 6.13-MeV, 3^- level of ^{16}O is first excited, with the pickup of a $1p$ neutron (probably a $1p_{1/2}$ neutron) following. Evidence for such a process has been found in the $^{12}C(d, ^3He)^{11}B^*$ (6.67, $\frac{7}{2}^-$) reaction.[49] A $\frac{5}{2}^+$ level could also be excited by the pickup of a $1p_{3/2}$ neutron in a two-step process. The other angular distributions shown in Fig. 10 exhibit little character. However, the 12.30- and 13.79-MeV levels are quite strong (0.12 mb/sr).

V. DWBA ANALYSIS AND SPECTROSCOPIC FACTORS

Several observations about the $^{16}O(p, d)^{15}O$ spectroscopic factors were used in evaluating the results of a DWBA calculation. The simplest shell model predicts spectroscopic factors of 2 and 4 for the 0.0-MeV, $\frac{1}{2}^-$ and the 6.18-MeV, $\frac{3}{2}^-$ levels of ^{15}O, respectively, these being just the numbers of $1p_{1/2}$ and $1p_{3/2}$ neutrons available for pickup. If, however, some of the $1p$ strength lies in other ^{15}O levels of higher excitation, the spectroscopic factors for the 0.0- and 6.18-MeV levels will be reduced, but the sum of the $1p$ spectroscopic factors will still be 6. However, if the ground state of ^{16}O were to contain admixtures of neutrons from other shells, the total number of $1p$ neutrons available for pickup would be less than 6, and since the $1p_{1/2}$ neutrons are less strongly bound than the $1p_{3/2}$ neutrons, one expects the $1p_{1/2}$ subshell to be depleted more than the $1p_{3/2}$ subshell. Thus, one would expect the ratio of the summed $1p_{3/2}$ spectroscopic factors to the summed $1p_{1/2}$ spectroscopic factors to be greater than 2.

Extensive discussions of the DWBA theory may be found in the literature.[1,2,50] The standard calculation employs the local zero-range approximation in which local optical potentials are used and the interaction is assumed to take place at a point. The neglect of finite-range effects has been investigated by Austern *et al.*[51] and proved to be most important in reactions involving large momentum transfers. The inclusion of exact finite range and nonlocality calculations is difficult, but their effects are approximated by the local energy approximation[52,53] as a correction factor which multiplies the

[49] Y. Dupont and M. Chabre, Phys. Letters **26B**, 362 (1968).

[50] W. Tobocman, *Theory of Direct Nuclear Reactions* (Oxford University Press, New York, 1961).

[51] N. Austern, R. M. Drisko, E. C. Halbert, and G. R. Satchler, Phys. Rev. **133**, B3 (1964).

[52] P. J. A. Buttle and L. B. J. Goldfarb, Proc. Phys. Soc. (London) **83**, 701 (1964).

[53] C. M. Perey and F. G. Perey, Phys. Rev. **134**, B353 (1964).

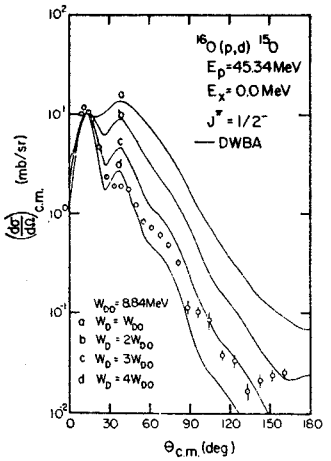

FIG. 11. DWBA fits to the $^{16}O(p, d)^{15}O$, E_p=45.34 MeV, E_x=0.0 MeV, $J^\pi=\frac{1}{2}^-$ angular distribution for different values of the deuteron imaginary-well depth.

zero-range radial form factor, lessening the contribution of the nuclear interior. A FORTRAN version of the Oak Ridge code JULIE[2] was used for all DWBA calculations.

The spectroscopic factor S is extracted from the data by application of the formula

$$S=\sigma_{\text{peak}}/2.25\sigma_{\text{JULIE}}$$

where σ_{peak} is the differential cross section at the characteristic forward peak of the angular distribution, a method successfully used in the past.[3,7] One might expect that the assumption of a direct reaction is more valid for forward angle scattering. It is also thought[54] that exchange terms, which were not included in the transition amplitude, are unimportant at forward angles, but that they might make noticeable contributions at the backward angles. Finally, the fit of the DWBA calculations to the data at forward angles, where most of the integrated cross section is contained, is usually best.

A. 0.0- and 6.18-MeV Levels

Initial DWBA calculations were made for 45.34-MeV incident protons using the optical-model parameters for the entrance and exit channels listed in Tables I and II. The parameters for the bound-state well were r_{0n}= 1.12 F, a_n=0.69 F, and λ=25. The geometric parameters are the same as those of the real proton well, and the value of the spin-orbit strength is the one normally used for nucleons. No lower integration cutoff was used in initial calculations. As can be seen in Fig. 11, the shape of the calculated angular distribution does not match the data. However, in studies of (p, d) reactions in $1p$ shell and $2s$-$1d$ shell nuclei, Kull[3] and Kozub[7] found that an increase in the imaginary-well depth W_D of the deuteron optical potential led to shapes which were in better agreement with the data. Figure 11 shows the results of such calculations in the present case. The shape does improve as W_D increases, but still is not well reproduced. The worst feature, in the present case, is that the magnitude of σ_{peak} decreases from 1.5 to 0.6 mb/sr as W_D increases from W_{D0} to $4W_{D0}$. These values give spectroscopic factors of 3.6 and 8.9, respectively, much too large for $1p_{1/2}$ pickup.

Siemssen *et al.*[55] also encountered the difficulty of reproducing the shape of the data from (d, p) reactions with $1p$ shell nuclei. He obtained reasonable fits by using a lower integration cutoff in the DWBA calculation. Following a similar procedure, W_D was kept at the value found from optical model calculations, and a series of DWBA calculations was made with different values of the lower integration cutoff radius (R_{cut}). The effect of the cutoff radius on σ_{peak} is shown in Fig. 12. Two maxima exist, one at R_{cut}=0 F and one at R_{cut}=3 F. For R_{cut}=0 F one gets a spectroscopic factor for the 0.0-MeV level of 3.2, whereas for R_{cut}=3 F it is 1.8, a much more acceptable value. For the 6.18-MeV level there is no appreciable difference in the spectroscopic factors for R_{cut}=0 F and R_{cut}=3 F. Figures 13 and 14 show the DWBA angular distributions for the ground and 6.18-MeV states. The shape for R_{cut}=3 F is better than for no cutoff but is still not very good. However, the first maximum is reasonably well reproduced, so the prescription of using the measured optical parameters with a lower integration cutoff of 3 F was adopted for all of the DWBA calculations.

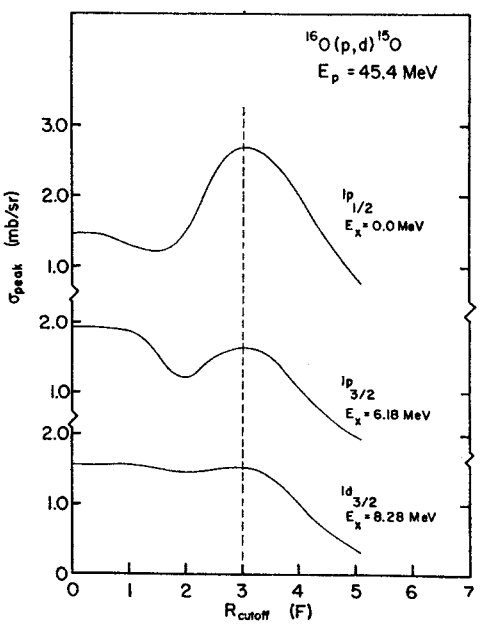

FIG. 12. Dependence of calculated l_n=1 and l_n=2 peak cross sections from the $^{16}O(p, d)^{15}O$ reaction for E_p=35.34 MeV on the value of the lower radial integration cutoff used in the DWBA calculation.

[54] N. Austern, in *Fast Neutron Physics*, edited by J. B. Marion and J. L. Fowler (Wiley-Interscience, Inc., New York, 1963), Vol. II.

[55] R. H. Siemssen, Bull. Am. Phys. Soc. 12, 479 (1967); J. P. Schiffer, G. C. Morrison, R. H. Siemssen, and B. Zeidman, Phys. Rev. 164, 1274 (1967).

Fixing the optical parameters and the integration limits left only the parameters of the bound-state well to be investigated. Since the value of 1.12 F for the radius parameter (r_{0n}) was somewhat smaller than that generally used, calculations were performed for $r_{0n}=1.25$ and 1.35 F. The shapes of the angular distributions were essentially unaltered, but σ_{peak} for the ground state rose from its value of 2.68 mb/sr for $r_{0n}=1.12$ F to 4.35 mb/sr for $r_{0n}=1.35$ F. This represents a lowering of the ground-state spectroscopic factor, the value being 1.51 for $r_{0n}=1.25$ F. This value of the spectroscopic factor is reasonable, but that for the 6.18-MeV, $\frac{3}{2}^-$ level seems much too small since the ratio of the $1p_{3/2}$ to the $1p_{1/2}$ spectroscopic factors is essentially unchanged by the change in r_{0n}. Owing to the lack of significant improvement in the shape and magnitude of the angular distributions with a higher value of r_{0n}, the value of r_{0n} was kept at 1.12 F for the subsequent calculations.

It has been noted that the inclusion of finite-range and nonlocality effects in the DWBA calculations tends to reduce the effect of the nuclear interior. Since this is also the effect of a lower integration cutoff a set of calculations including these effects was made. The code FANLFR2[56] was used to obtain the bound-state form factor which was then used by JULIE in the DWBA calculation. A range of 1.25 F was used with values of the nonlocality parameter β of 0.85 and 0.54 F for protons and deuterons, respectively. The angular distribution shapes were little improved from those calculated using the zero-range approximation with no radial integration cutoff, and a value of 3.0 was obtained for the ground-state spectroscopic factor. If one departs from the accepted value of the range given above and

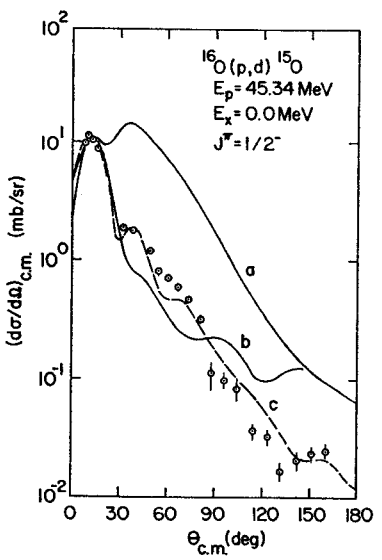

FIG. 13. DWBA fits to the $^{16}O(p,d)^{15}O$, $E_p=45.34$ MeV, $E_x=0.0$ MeV, $J^\pi=\frac{1}{2}^-$ angular distribution for different values of the lower radial integration cutoff of 0.0 for curve a, of 3.0 f for curve b and also using a modified form factor c.

[56] Oak Ridge computer code written by J. K. Dickens.

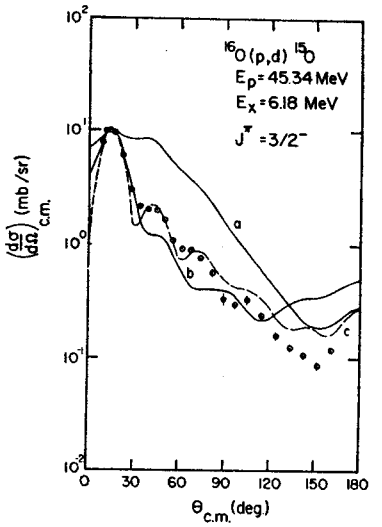

FIG. 14. DWBA fits to the $^{16}O(p,d)^{15}O$, $E_p=45.34$ MeV, $E_x=6.18$ MeV, $J^\pi=\frac{3}{2}^-$ angular distribution for different values of the lower radial integration cutoff of 0.0 for curve a, of 3.0 for curve b and also using a modified form factor c.

increases the value to approximately 2.4 F, the shapes of the calculated angular distributions are greatly improved, but the calculated cross sections are much too small, so these calculations were not used in the present work. Therefore, the use of finite range and nonlocality were abandoned. Recently, it has been pointed out[57] that by application of internal damping to the radial form factor one can get an angular distribution whose shape matches the data well, as shown in Figs. 13 and 14.

Having decided to use a lower integration cutoff with the normal deuteron optical-model parameters, calculations were performed for the 0.0-MeV, $\frac{1}{2}^-$ and 6.18-MeV, $\frac{3}{2}^-$ levels for incident proton energies of 25.52, 31.82, 38.62, and 45.34 MeV. The optical parameters used were those which described elastic scattering at the appropriate energy. The method used in choosing the four proton energies is illustrated in Fig. 15. For an incident proton energy E_p (e.g., 25.52 MeV) the deuterons leaving ^{15}O in the 0.0-MeV, $\frac{1}{2}^-$ state have the same energy in the c.m. frame as those leaving ^{15}O in the 6.18-MeV, $\frac{3}{2}^-$ state when the incident proton energy is E_p' (e.g., 31.82 MeV). Thus, for each pair of energies, reaction data having the same deuteron energies could be compared.

The results of these calculations for 45.34-MeV incident protons are represented by curve b of Figs. 13 and 14. Calculations for the 38.63- and 31.82-MeV protons give similar shapes, but the 25.52-MeV shape is significantly worse. The rather low deuteron energies for this latter case made the assumption of a direct reaction questionable. Spectroscopic factors and ratios of spectroscopic factors for the 0.0- and 6.18-MeV levels are given in Tables III and IV where the errors reflect

[57] B. M. Preedom, J. L. Snelgrove, and E. Kashy (to be published).

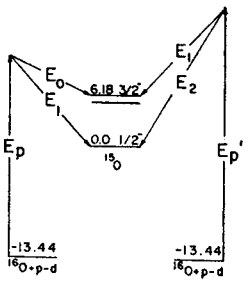

FIG. 15. Basis for the selection of incident proton energies for the $^{16}O(p, d)^{15}O$ experiments.

only the errors in the values of σ_{peak}. The extracted spectroscopic factor for the ground state is constant for the two higher bombarding energies, but it increases for lower values of the incident proton energy. The spectroscopic factor for the 6.18-MeV level rises as the energy of the incident protons decreases from 45 MeV. Table IV shows that the ratios of the spectroscopic factors for these levels is reasonably constant for incident proton energies greater than 30 MeV. The ratios given in the last column are based upon use of the proton energy scheme shown in Fig. 15 to reduce any Q-dependent effects. Only the ratios for the 45.34-MeV data remain unchanged. These data suggest that if reliable spectroscopic factors are to be extracted from the (p, d) reaction on light nuclei, the incident proton energy must be sufficient to produce deuterons having an energy greater than 20 MeV in the c.m. frame. Relative spectroscopic factors appear to be reliable even for lower incident proton energies or, conversely, for higher excitation energies. It is interesting to note here the similarity of the ratio of spectroscopic factors for the 6.18-MeV, $\frac{3}{2}^-$ and 0.0-MeV, $\frac{1}{2}^-$ transitions from the 45.34-MeV data to the ratio of the peak cross sections of these levels from the 100- and 156-MeV data, i.e., 1.3 and 1.6. A DWBA analysis of the 156-MeV $^{16}O(p, d)^{15}O$ data of Bachelier *et al.*[15] by Towner[16] results in spectroscopic factors of 1.70±0.25 and 1.90±0.8 for the 0.0- and 6.18-MeV states, respectively, indicating a serious problem in the form factor used in the analysis. On the other hand, the plane-wave analysis of that same data gave for the ratio of spectroscopic factors a value of 2.0.

TABLE III. Experimental spectroscopic factors for the 0.0- and the 6.18-MeV levels of ^{15}O from the $^{16}O(p, d)^{15}O$ reaction induced by 25.52–45.34-MeV protons.

E_x (MeV)	J^π	E (MeV)	σ_{expt} (mb/sr)	σ_{DWBA} (mb/sr)	S
0.0	$\frac{1}{2}^-$	25.52	6.8±0.5	0.94	3.2±0.2
		31.82	8.5±0.6	1.66	2.3±0.2
		38.63	9.7±0.5	2.38	1.8±0.1
		45.34	11.0±0.8	2.68	1.8±0.1
6.18	$\frac{3}{2}^-$	25.52	2.2±0.2	0.12	8.1±0.7
		31.82	4.5±0.5	0.57	3.4±0.4
		38.63	7.6±0.6	1.14	3.0±0.3
		45.34	10.0±0.7	1.72	2.6±0.2

It is possible to obtain better agreement between the DWBA calculations and the shapes of the experimental angular distributions. Chant *et al.*[11] freely adjusted the deuteron optical-model parameters to obtain the best fit to the ground-state angular distribution from their 30.3 MeV $^{16}O(p, d)^{15}O$ data. The imaginary-well depth was increased by a factor of approximately 3, with changes of 5–20% being made in the other parameters. The fit was very good for the ground-state angular distribution below 78° in the c.m. frame, where the data ended, but the 6.18-MeV fit was not as good. They did not calculate spectroscopic factors, so advisability of such a procedure could not be judged by that criterion. However, the calculations of the present work showed that an increase of the imaginary-well depth led to spectroscopic factors which were much too large.

A study similar to that of the present work has been made by Hiebert *et al.*[10] for proton pickup from ^{16}O. The $^{16}O(d, ^3He)^{15}N$ reaction was employed with an incident deuteron energy of 34.4 MeV. Satisfactory fits to the data were obtained using standard optical-model potentials. They found that the local finite-range form of the DWBA theory gave the most reliable spectroscopic factors. These values were 2.14 for the 0.0-MeV, $\frac{1}{2}^-$ level of ^{15}N and 3.72 for the 6.33-MeV, $\frac{3}{2}^-$ level. These differ slightly from the present values for neutron pickup from ^{16}O presented in Table III and probably reflect more the uncertainty in the extraction of spectroscopic factors than a dissimilarity of the proton and neutron configurations of the ^{16}O ground state.

TABLE IV. Ratios of experimental spectroscopic factors for the 0.0- and 6.18-MeV levels of ^{15}O from the $^{16}O(p, d)^{15}O$ reaction induced by 25.52–45.34-MeV protons.

E_p^+ (MeV)	E_p^- (MeV)	$\frac{S_{3/2}(E_p^+)}{S_{1/2}(E_p^+)}$	$\frac{S_{3/2}(E_p^+)}{S_{1/2}(E_p^-)}$
25.52	...	2.53±0.25	...
31.82	25.52	1.54±0.15	1.09±0.11
38.63	31.82	1.63±0.16	1.30±0.13
45.34	38.63	1.41±0.14	1.41±0.14

B. Spectroscopic Factors for Other ^{15}O Levels and the Ground State of ^{16}O

Using the criteria established in the previous section, DWBA calculations were performed for other levels in the 45.34-MeV data. The results are similar to those for the strong levels shown in the previous sections. Spectroscopic factors for these levels are given in Table V. Again, the errors quoted reflect only the errors in the experimental value of σ_{peak}. An estimate of the spectroscopic factors for the 5.188- and 5.240-MeV levels was obtained by adding together $2s_{1/2}$ and $1d_{5/2}$ DWBA angular distributions in varying combinations. The results are shown in Fig. 16. A combination of

TABLE V. Peak cross sections and spectroscopic factors for the levels observed in ^{15}O. The average cross section over the indicated angular range is given for weak levels having angular distributions showing no characteristic maximum. The uncertainties quoted in the spectroscopic factors represent only the uncertainties in σ_{peak}.

E_x (MeV)	J^π	l_n	σ_{peak} (mb/sr)	σ_{peak} (deg)	$S(p,d)$
0.0	$\frac{1}{2}^-$	1	11.0±0.8	12 ± 1	1.8±0.1
5.188	$\frac{1}{2}^+$	0			0.02±0.01
5.240	$\frac{5}{2}^+$	2			0.11±0.01
6.180	$\frac{3}{2}^-$	1	10.0±0.7	15 ± 1	2.6±0.2
6.789	$\frac{3}{2}^+$	2	0.08±0.03	20 ± 2	0.02±0.01
6.857	$(\frac{3}{2}, \frac{5}{2})$	2	0.08±0.03	20 ± 2	0.02±0.01
7.284	$(\frac{9}{2}^+, \frac{7}{2}^+)$	(4)	0.12±0.02	45 ± 3	≤0.03±0.01
7.550	$\frac{1}{2}^+$		0.08±0.03	30 ± 3	
8.283	$\frac{3}{2}^+$		0.05±0.02	24 ± 3	0.01±0.005
8.915	$\frac{3}{2}^+$				
8.980	$\frac{3}{2}^-$		0.08±0.04	21 ± 5	0.04±0.02
9.49	$\frac{5}{2}^-$				
9.53	$\frac{1}{2}^+$		0.57±0.05[a]	15 ± 1	
9.60	$\frac{3}{2}^-$	1	0.40±0.07[b]	15 ± 1	0.18±0.03
9.66	$(\frac{7}{2}, \frac{9}{2})^-$				
10.28			0.06±0.02	10− −46	
10.46	$(\frac{3}{2}^-, \frac{1}{2}^-)$	1	0.58±0.06	15 ± 1	0.28±0.03
10.94			0.08±0.03	10− −46	
11.02			0.06±0.02	18− −46	
11.70			0.06±0.02	24− −46	
12.30			0.12±0.05	24 ± 3	
13.79			0.12±0.05	9− −46	

[a] This number represents the combination of the four peaks between 9.49 and 9.66 MeV.

[b] This number represents the estimated contribution of the 9.60-MeV level alone.

$1d_{5/2}$ and $2s_{1/2}$ in the ratio 10 to 1 appears to give the best over-all fit. The spectroscopic factor for the 7.284-MeV, $\frac{7}{2}^+$ level assumes that its excitation is due only to a direct process, thus representing an upper limit.

It is interesting to determine the total $1p$ strength seen in the $^{16}O(p,d)^{15}O$ reaction at 45.34 MeV. By summing the spectroscopic factors for all of the $\frac{1}{2}^-$ and $\frac{3}{2}^-$ levels listed in Table V, we get

$$\sum S(1p_{1/2}) = 1.80, \qquad \sum S(1p_{3/2}) = 3.10,$$

hence

$$\sum S(1p) = 4.90.$$

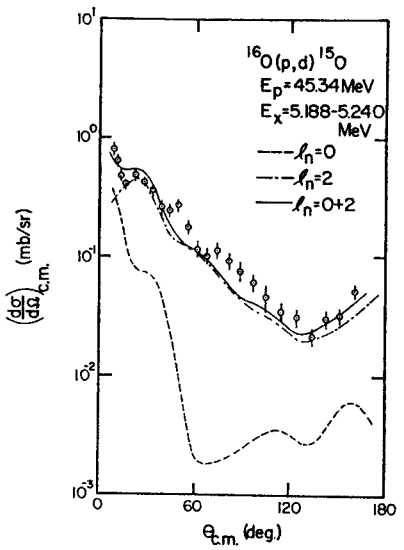

FIG. 16. DWBA fit to the $^{16}O(p,d)^{15}O$, E_p=45.34 MeV, E_x=5.188–5.240 MeV (doublet) angular distribution.

The relatively low value for the total $1p_{3/2}$ strength indicates the possibility of higher $\frac{3}{2}^-$ levels, as predicted by Bertsch.[44] The $\frac{3}{2}^-$ levels at 9.60 and 10.46 MeV might comprise the $\frac{3}{2}^-$ level predicted by Brown and Shukla[43] to be between 10 and 11 MeV. If it were at 10 MeV, they predict it would have a spectroscopic factor 3% of that of the 6.18-MeV level, whereas the observed value is 18%. An estimate of the $2s$-$1d$ admixtures in the ground state of ^{16}O is contained in the spectroscopic factors for the $\frac{1}{2}^+$, $\frac{5}{2}^+$, and $\frac{3}{2}^+$ levels:

$$\sum S(2s_{1/2}) = \sim 0.02, \qquad \sum S(1d_{5/2}) = 0.15,$$

$$\sum S(1d_{3/2}) = 0.04.$$

The present results can also be compared to those calculated from the ^{16}O ground-state wave function of Brown and Green.[41] This wave function has the form

$$|\,^{16}O_{gs}\rangle = 0.874\,|\,0p\text{-}0h\rangle + 0.469\,|\,2p\text{-}2h\rangle + 0.130\,|\,4p\text{-}4h\rangle,$$

where p is for particles and h is for holes. In the 2p-2h

and 4p-4h admixtures one can assume that on the average half of the particles and holes are neutrons, and half protons. Thus, the 0p-0h portion represents six $1p$ neutrons, and the 2p-2h and 4p-4h portions represent five and four $1p$ neutrons, respectively. One would then expect the summed $1p$ spectroscopic factor to be

$$\sum S(1p) = 6(0.874)^2 + 5(0.469)^2 + 4(0.130)^2 = 5.75$$

and

$$\sum S(\text{other}) = 0(0.874)^2 + 1(0.469)^2 + 4(0.130)^2 = 0.25.$$

The sum of the experimental $2s$-$1d$ spectroscopic factors agrees well with this prediction. It appears, then, that as much as 15% of the $1p$ strength could be in levels above 10.46 MeV.

VI. SUMMARY AND CONCLUSIONS

This work has provided valuable information about the use of DWBA calculations in the extraction of spectroscopic factors for the (p, d) reaction on light nuclei. While it is not possible to provide a definite guide for performing meaningful calculations, the effects of variations of certain parameters of the calculation was investigated. The most immediately obvious problem, the inability of a straightforward DWBA calculation to reproduce the shape of the angular distribution, was treated by the use of a lower integration cutoff rather than by changing the deuteron imaginary well depth, which resulted in too large values of the extracted spectroscopic factors. The 3-F cutoff used was a maximum in the σ_{peak}-versus-R_{cut} curve and is close to the value of $1.2A^{1/3}$ for ^{16}O and ^{15}O. In addition to improving the shape of the distribution, the value of the spectroscopic factor became more reasonable.

The radius parameter of the bound-state well (r_{0n}) offers a special problem since the value of the calculated peak cross section, and hence the spectroscopic factor, is a strong function of r_{0n}. One should be aware of this problem in any attempt to extract absolute spectroscopic factors; however, relative spectroscopic factors appear to depend much less strongly on r_{0n}. In the present work a value of r_{0n} equal to the real proton well radius gave reasonable spectroscopic factors.

It also was found that the energy dependence of the peak $l_n = 1$ cross sections for the two strongly excited levels of ^{15}O was not reproduced by the DWBA calculation for a deuteron energy in the c.m. frame of less than 20 MeV. Thus, if a (p, d) reaction on a light nucleus is to be performed at a single energy, the proton energy should be as high as practicable. The relative spectroscopic factors showed much less energy dependence than the absolute spectroscopic factors. The use of a method to eliminate some of the Q dependence in the relative spectroscopic factors did not result in any significant improvement and indicates that the problems involved are probably not in the deuteron channel. It may instead be that the high penetrability of the proton is not well accounted for in the DWBA calculation.

The spectroscopic factors extracted from the 45.34-MeV ^{16}O$(p, d)^{15}$O data indicate that about 30% of the $1p_{3/2}$ strength is missing from the 6.18-MeV, $\frac{3}{2}^-$ level. Approximately 12% of this missing strength is contained in the 9.60-MeV, $\frac{3}{2}^-$ and 10.46-MeV, $(\frac{3}{2}^-, \frac{1}{2}^-)$ levels, the latter assignment being made on the basis of the shape of the angular distribution. The 8.98-MeV, $\frac{3}{2}^-$ level contains less than 1% of the $1p_{3/2}$ strength. The remaining strength may reside in many highly fragmented states in the 20-MeV region of excitation.[44] Small $2s$-$1d$ admixtures and a possible $1g_{7/2}$ admixture were observed in the ground state of ^{16}O.

Finally, in view of the various problems in getting spectroscopic factors discussed here one comes to the rather interesting conclusion that the pickup experiment is indeed a better tool for finding out about ground-state admixture in the "unfilled shells" since information as to the occupation number in these shells, even with a 20–40% uncertainty is extremely useful, while the same uncertainty for occupation number of filled or partially filled shells makes such information relatively useless. Conversely, the (d, p) reaction then represents the tool which gives the quantitative measure of hole population for what are normally considered filled orbits.

ACKNOWLEDGMENTS

The authors gratefully acknowledge the assistance of B. M. Preedom and T. Arnette in the use of the optical-model and DWBA codes, and P. J. Plauger, C. Barrows, and B. Horning in acquiring and analyzing the data. We also thank all of the Laboratory staff for their help in building and maintaining the experimental apparatus and in running the cyclotron.

NUCLEAR SURFACE AND INELASTIC PROTON SCATTERING*

C. R. Gruhn, B. M. Preedom, and K. Thompson†
Department of Physics, Michigan State University, East Lansing, Michigan 48823
(Received 2 September 1969)

Comparisons of the electromagnetic and proton inelastic-scattering reduced transition probabilities for the even nickel isotopes are made. It is found that the values obtained for high multipole transitions in the inelastic scattering are extremely sensitive to the nuclear density distribution. This sensitivity is investigated for various phenomenological models of the nuclear density distribution.

We report in this Letter on the sensitivity of the analysis of proton inelastic scattering to phenomenological models of the nuclear density distribution. Proton inelastic scattering has often been analyzed using distorted-wave Born approximation (DWBA) calculations in terms of a "collective" model. The purpose of such analyses is to extract systematically the fractional amplitude of deformation β_L. The usual procedure is then to calculate the reduced transition probability $B(EL)$ after making simplifying assumptions on the nature of the nuclear density and charge distribution. The most common assumption is that of a uniform distribution. The resulting $B(EL)$'s for the first excited 2^+ states are then found to be in qualitative agreement with those deduced from electromagnetic measurements.[1,2] In recent years there has been great improvement in the resolution of electron inelastic-scattering experiments. These experiments have measured electromagnetic $B(EL)$'s for the higher multipole transitions. In this Letter we compare some results of recent electron-scattering and Coulomb-excitation measurements[3-5] with values of $B(EL)$ obtained from proton inelastic scattering from ^{58}Ni, ^{60}Ni, ^{62}Ni, and ^{64}Ni.[6] There are large discrepancies between the $B(EL)_{EM}$ and the $B(EL)_{p,p'}$ when one uses the standard method for obtaining the deformation[7] and then obtains the reduced transition probability using a nonuniform nuclear density distribution.[8] The density distributions we have studied are the usual phenomenological models, e.g., the Fermi distribution or the "wine bottle" distribution. These differences are shown to be quite sensitive to the tail of the assumed distribution.

The experimental measurements were carried out at the Michigan State University Cyclotron Laboratory using 40-MeV protons. The targets were self-supporting foils (~1 mg/cm^2) of separated Ni isotopes. The scattered protons were detected by Ge(Li) charged-particle detectors described elsewhere.[9] The angular distributions were measured using a goniometer[10] designed for use with the Ge(Li) detectors. The overall energy resolution was 0.1%.

A β_L was obtained for each inelastic transition by comparing the integrated differential cross section with the integrated DWBA (JULIE)[11] "collective"-model calculation. The DWBA calculations were made with the complete deformed optical potential and included Coulomb excitation for the $L=2$ and $L=3$ transitions.[6] The deformation was made using the standard prescription that the interaction depend only on the distance from the nuclear surface as described by Eq. (27) of Ref. 7. This is referred to as a "potential" deformation. The optical-model parameters used were those determined by Fricke.[12] The β_L's obtained in this experiment are consistent with those obtained by other reactions [(α,α'), (^{3}He, ^{3}He), and (d,d')][2].

Bassel et al.[7] present an alternative prescription for obtaining the deformation by defining the interaction in terms of equipotential surfaces which conserve volume. This method differs from the standard by an additional factor of r/R_0 in the form factor. The resulting deformation squared is reduced by a factor of approximately 1.4 for the $L=2$, 3, and 4 transitions. It should be pointed out that this latter method is more consistent with obtaining the deformation of the matter density. The results of using this deformation are discussed below.

The deformation parameter β_L is related[8] to the $B(EL)$ by

$$B(EL;0\rightarrow L)=e^2\left\{Z\frac{(2L+1)}{4\pi}\frac{\langle r^{2L-2}\rangle}{R^{L-2}}\right\}^2\beta_L^2, \quad (1)$$

where

$$\langle r^{2L-2}\rangle=\frac{\int r^{2L-2}\rho(\vec{r})d\vec{r}}{\int\rho(\vec{r})d\vec{r}}, \quad (2)$$

and R is the half-value radius.

In this expression the transition density $\rho(\vec{r})$ is taken to be of the same general form as the nuclear matter distribution. The nonuniform-den-

sity-distribution models used are

$$\rho_F/\rho_0 = \{1 + \exp[(r - R_{tr})/a_{tr}]\}^{-1} \text{ (Fermi)}, \quad (3)$$

and

$$\rho_w/\rho_0 = [1 + W(r/R_{tr})^2]\rho_F/\rho_0 \text{ (wine bottle)}. \quad (4)$$

Using the "potential" deformations, (p,p') $B(EL)$'s are compared with the electromagnetic $B(EL)$'s in Table I. It is seen that there is qualitative agreement with the uniform-density distribution using a radius equal to the Fermi "equivalent" uniform-charge-density[13] radius (column b). The striking result in Table I is that the nonuniform-density distributions (columns c and d) determined by electron elastic scattering[3-5] give (p,p') $B(EL)$'s which are most inconsistent with the electromagnetic $B(EL)$'s for the high multipolarity transitions. The disagreement is removed by making the density distributions less diffuse. When the diffuseness a_{tr} was adjusted to give agreement (see columns e and f) with the $B(EL)_{EM}$'s, both density distributions gave the same shape in the tail.

Bethe[14] points out that the asymptotic behavior of the density is given by an exponential tail where the decay constant α is given by

$$\alpha = (8M\epsilon)^{1/2}/\hbar = 0.44\epsilon^{1/2}\ \text{F}^{-1}, \quad (5)$$

where ϵ is the average state energy in MeV. We

Table I. Reduced transition probabilities $B(EL)$ in units of F^{2L}. The fractional errors of column a are the same as for columns b through f. [The errors are indicated below each $B(EL)$.]

Nucleus	E_x(MeV)	L	Electromagnetic B(EL)'s Ref. 1 Coul. Ex.	Ref. 4 (e,e')	Ref. 3 (e,e')	Inelastic Proton Model dependent B(EL)'s a	b	c	d	e	f
^{58}Ni	1.456	2	1050 101	946 16	1430 200	1030 47	1230	1720	1360	1190	1170
	3.035	2	102 4			94 6	112	156	124	108	106
	3.260	2	220 22			153 9	182	254	202	176	173
	4.472	3		26780 720	27200 3500	17400 800	24800	68600	39900	27400	27100
	2.468	4			145000 45000	99000 500	167000	1340000	513000	255000	255000
^{60}Ni	1.331	2	1397 115	1217 13	1790 220	1340 88	1600	2200	1730	1530	1500
	4.042	3		40500 992	30500 4800	21200 1400	30100	80700	47000	32800	32900
	2.502	4			270000 48600	121000 9000	200000	1600000	607000	303000	323000
^{62}Ni	1.169	2	1210 115	1263 16		1290 113	1530	2080	1590	1460	1420
	3.750	3		30240 778		22300 1950	21700	82600	44300	34000	33100
	2.334	4				107000 10000	181000	1300000	426000	261000	256000
^{64}Ni	1.344	2	1253 245			1070 180	1270	1710	1340	1210	1180
	3.560	3				27700 4500	39300	994000	56000	41500	41000
	2.608	4				95300 16000	161000	1100000	396000	226000	227000

[a] Assumes a uniform density distribution with $r_0 = 1.20$ F.

[b] Assumes a Fermi equivalent uniform-density distribution with $r_0 = 1.31$ F (see Ref. 12).

[c] Assumes a Fermi density distribution with $r_0 = 1.10$ F and $a = 0.566$ determined from elastic scattering (see Refs. 3, 4, and 12).

[d] Assumes a wine-bottle distribution with parameters determined by electron elastic scattering (see Ref. 5).

[e] Assumes a Fermi density distribution with $r_0^{tr} = 1.10$ F and $a^{tr} = 0.366$ F.

[f] Assumes a wine-bottle distribution (see d above) with all the parameters the same as in d except $a^{tr} = a_{ch_2} - 0.1$ F.

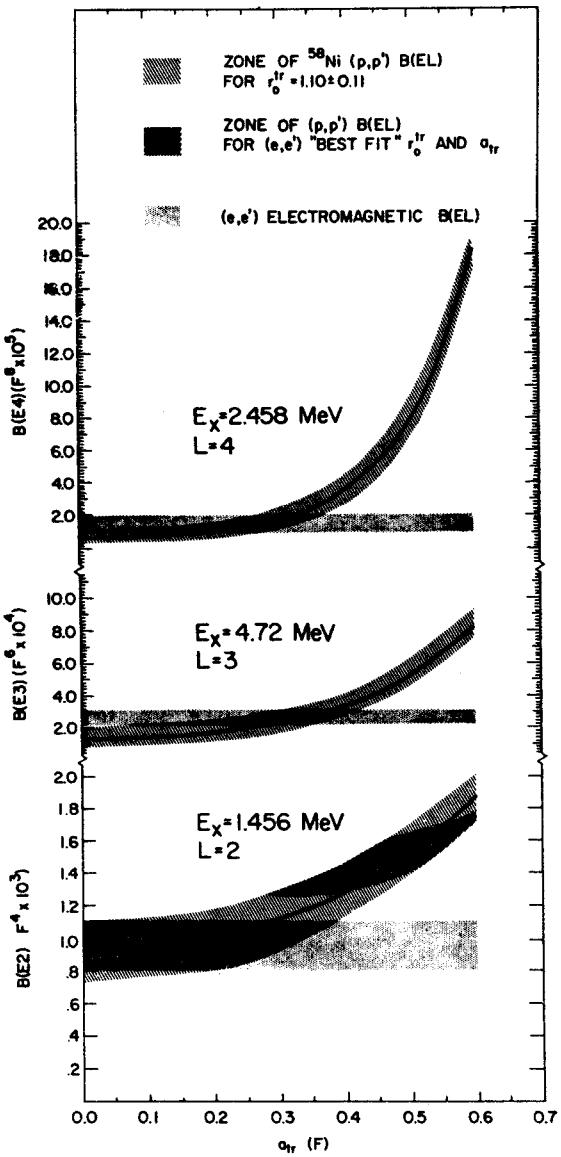

FIG. 1. The sensitivity of the $B(EL)_{(p,p')}$ results to the parameters of the transition density for ^{58}Ni. The electromagnetic $B(E2)$ and $B(E3)$ with an estimated 15% error on the model independence are taken from Ref. 4. The electromagnetic $B(E4)$ is taken from Ref. 3.

estimate the average state energy as follows:

$$\epsilon \simeq \tfrac{1}{2}[(\text{B.E.})_p + (\text{B.E.})_n] + \tfrac{2}{5}T_F, \qquad (6)$$

where, e.g., $(\text{B.E.})_p$ is the proton binding energy, and where we take the Fermi energy $T_F = 35.0$ MeV. For ^{58}Ni we calculate $\alpha = 2.2\ F^{-1}$, which is consistent with an average $\alpha = 2.1\ F^{-1}$ determined by the adjusted density distributions. A more detailed comparison on this point would require refitting the electron elastic-scattering data to a density distribution which has an exponential tail such as suggested by Bethe.[15]

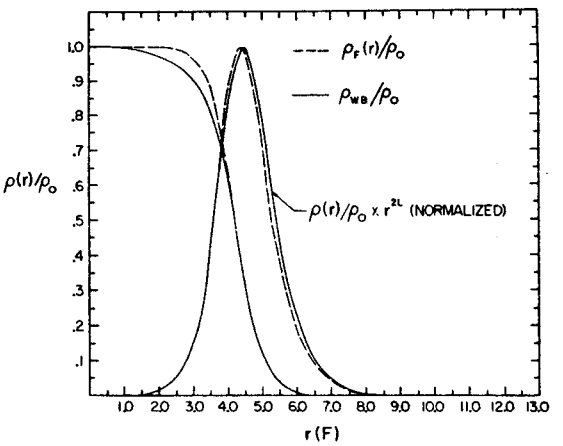

FIG. 2. The transition density distributions for ^{58}Ni used in the calculations of columns e and f of Table I. Also plotted is the product $[\rho(r)/\rho_0]r^{2L}$ (the integrand of $\langle r^4 \rangle$, i.e., $L = 3$).

Using the volume-conserving "matter" deformation, the (p,p') $B(EL)$'s of Table I are all reduced by a factor of 1.4. This factor is sufficient to bring the $B(EL)$'s calculated with the wine-bottle distribution (column d) into general agreement with the $B(EL)_{EM}$.

The sensitivity of the $B(EL)_{(p,p')}$ to the radius parameter R_{tr} ($R_{tr} = r_0^{tr} A^{1/3}$) and to the diffuseness a_{tr} in Eqs. (3) and (4) is indicated in Fig. 1. The zone for $B(EL)_{(p,p')}$ is drawn for values of $r_0^{tr} \pm 10\%$ and was calculated using the "potential" deformations. It is seen from the figure that if one requires agreement between $B(EL)_{EM}$ and $B(EL)_{(p,p')}$, then the diffuseness of the nuclear transition density must be smaller than that of the charge density for this range of transition radii. We also observe a discrepancy between the electromagnetic and (p,p') $B(EL)$'s for transition density parameters determined by electron inelastic-scattering data.[4] These parameters span a range of ambiguities as determined in the analysis of the inelastic electron data. It is important to note that this discrepancy is removed if one uses the "matter" deformation.

In Fig. 2, the integrand of $\langle r^5 \rangle$ (i.e., $L = 3$) and the density distributions are plotted as a function of radius. Note that the density distributions are nearly identical beyond the half-density radius. Since the integrand has its maximum value in the surface region, one would expect that the sharpness of this surface could have a large effect on the calculated $B(EL)$'s. The calculations are approximately 10 times more sensitive to the diffuseness parameter than to any of the other pa-

rameters for the $L=4$ transitions.

In summary, the relation between the β_L and $B(EL)$ is extremely sensitive to tha tail of the assumed transition density and comparisons between the (p,p') and electromagnetic $B(EL)$'s should be made with caution. In order to obtain more meaningful comparisons, it might prove worthwhile to reanalyze both the proton inelastic scattering and the electron inelastic scattering while requiring both analyses to be self consistent.

The authors would like to thank in particular Professor S. Austin for the discussions in which several of the ideas contained in this paper were introduced. The authors would also like to thank Professor H. McManus, Professor J. Borysowicz, and Professor E. Kashy for several helpful discussions.

---

*Work supported in part by the National Science Foundation.

†Present address: Argonne National Laboratory, Argonne, Ill. 60439.

[1]P. H. Stelson and L. Grodzins, Nucl. Data A1, 21 (1965).

[2]A. Bernstein, in Advances in Nuclear Physics, edited by M. Baranger and E. Vogt (Plenum Press, Inc., New York, to be published), Vol. III.

[3]H. Crannel, R. Helm, H. Kendall, J. Oesay, and M. Yearian, Phys. Rev. 123, 923 (1961).

[4]M. A. Duguay, C. K. Bockelman, T. H. Curtis, and R. A. Eisenstein, Phys. Rev. 163, 1259 (1967).

[5]J. R. Ficenec, W. P. Trower, J. Heisenberg, and I. Sick, Bull. Am. Phys. Soc. 14, 630 (1969).

[6]K. M. Thompson, thesis, Michigan State University (unpublished); K. M. Thompson, B. M. Preedom, and C. R. Gruhn, to be published.

[7]R. H. Bassel, G. R. Satchler, R. M. Drisko, and E. Rost, Phys. Rev. 128, 2693 (1962).

[8]A. M. Lane and E. D. Pendlebury, Nucl. Phys. 15, 39 (1960); L. W. Owen and G. R. Satchler, Nucl. Phys. 51, 155 (1964).

[9]C. R. Gruhn, T. Kuo, C. Maggiore, B. Preedom, L. Samuelson, and J. Chander, IEEE Trans. Nucl. Sci. 337 (1968).

[10]K. M. Thompson and C. R. Gruhn, to be published.

[11]All distorted-wave calculations use the FORTRAN-IV version of the distorted-wave code JULIE. R. H. Bassel, R. M. Drisko, and G. R. Satchler, Oak Ridge National Laboratory Report No. ORNL-3240, 1962 (unpublished), and "Oak Ridge National Laboratory Memorandum to the Users of the Code JULIE," 1966 (unpublished).

[12]M. P. Fricke, E. E. Gross, B. J. Morton, and A. Zucker, Phys. Rev. 156, 1207 (1967).

[13]L. R. B. Elton, Nuclear Sizes (Oxford University Press, New York, 1961).

[14]H. Bethe, Phys. Rev. 167, 879 (1968).

[15]H. Bethe and L. R. B. Elton, Phys. Rev. Letters 20, 745 (1968).

Reprinted from THE PHYSICAL REVIEW, Vol. 187, No. 4, 1259–1265, 20 November 1969
Printed in U. S. A.

$^{15}N(p, d)^{14}N$ Reaction at 39.8 MeV*

J. L. SNELGROVE† AND E. KASHY

Cyclotron Laboratory, Michigan State University, East Lansing, Michigan 48823

(Received 19 June 1969)

Energy spectra and angular distributions were obtained for the $^{15}N(p, p)^{15}N$ and $^{15}N(p, d)^{14}N$ reactions at 39.8 MeV. Spectroscopic factors were extracted for the levels in ^{14}N populated by $l_n=1$ pickup and were found to be in excellent agreement with intermediate-coupling predictions, which for this nucleus differ only slightly from j-j coupling. A width of 210±30 keV was measured for the $J^\pi=1^+$, $T=1$ level at 13.72 MeV. Angular distributions for other levels populated in the $^{15}N(p, d)^{14}N$ reaction are shown.

INTRODUCTION

THE availability of protons having energies greater than 30 MeV and high-resolution solid-state detectors in recent years has made possible the use of the (p, d) reaction for studying the spectroscopy of the light nuclei to relatively high excitation energies.[1–4] Some work has been done with 100- and 156-MeV protons,[5,6] although with poor enough resolution to limit studies to the strongly excited levels. In these studies spectroscopic factors have been extracted, mainly by comparison to distorted-wave Born-approximation (DWBA) calculations. Comparisons were then made to intermediate coupling shell-model predictions of the spectroscopic factors, such as those of Cohen and Kurath.[7] In the preceding paper,[4] the problem of extracting meaningful spectroscopic factors using DWBA calculations has been explored. The present paper uses the criteria developed there in an analysis of the $^{15}N(p, d)^{14}N$ reaction. This reaction has been studied previously by Bennett,[8] but the low proton energy (16.5–18.5 MeV) restricted the study to the 0.0-, 2.311-, and 3.945-MeV levels. The results of the present study are also compared to the predictions of Cohen and Kurath.[7]

EXPERIMENTAL PROCEDURE

A ^{15}N target, consisting of a 99% enriched ^{15}N gas maintained at a pressure of 29-cm Hg in a 3-in. cell with a 0.0005-in. Kapton[9] window, was bombarded with 39.89-MeV protons from the Michigan State University sector-focused cyclotron. Correcting for energy losses in the Kapton and gas gives a proton energy at the center of the cell of 39.84 MeV. The resulting deuterons were stopped in a $\Delta E-E$ counter telescope consisting of one 260- and two 2000-μ silicon surface barrier detectors. Mass identification was accomplished by multiplying the ΔE and E signals in a pulse multiplier designed by Miller and Radeka[10] to obtain a product pulse proportional to MZ^2. The elastic protons, which were not stopped by the detectors and thus produced product pulses smaller than those of protons which were stopped, were also detected. Angular distributions were measured between $\theta_{lab}=\sim10°$ and 142° with an over-all resolution of ~90 keV. The measurement uncertainty in the differential cross sections is estimated to be ~3.6% and was added in quadrature to the statistical uncertainty to obtain the total uncertainty represented by the error bars shown on all data points. A more detailed description of the experimental methods and the treatment of errors is contained in Ref. 11.

ELASTIC SCATTERING DATA AND OPTICAL-MODEL PARAMETERS

The $^{15}N(p, p)^{15}N$ angular distribution obtained is shown in Fig. 1 together with an optical-model fit performed with the Perey search code GIBELUMP.[12] An optical potential of the standard form was used, where W_S is a volume imaginary potential and W_D is a surface imaginary potential. The parameters (given in Table I) are similar to those for proton elastic scattering from ^{16}O at a comparable energy.[4]

For the analysis of the $^{15}N(p, d)^{14}N$ data, optical-model parameters for deuteron elastic scattering on ^{14}N at 32.8 MeV and lower were required. Very few data are

* Research supported by the National Science Foundation.

† Present address: Argonne National Laboratory, 9700 S. Cass Avenue, Argonne, Ill. 60439.

[1] L. A. Kull, Phys. Rev. **163**, 1066 (1967).

[2] L. A. Kull and E. Kashy, Phys. Rev. **167**, 963 (1968).

[3] R. L. Kozub, L. A. Kull, and E. Kashy, Nucl. Phys. **A99**, 540 (1967).

[4] J. L. Snelgrove and E. Kashy, preceeding paper, Phys. Rev. **187**, 1246 (1969).

[5] J. K. P. Lee, S. K. Mark, P. M. Portner, and R. B. Moore, Nucl. Phys. **A106**, 357 (1967).

[6] D. Bachelier, M. Bernas, I. Brissand, C. Detraz, N. K. Ganguly, and P. Radvangi, Compt. Rend. **2**, 429 (1964).

[7] S. Cohen and D. Kurath, Nucl. Phys. **73**, 1 (1965); **A101**, 1 (1967).

[8] E. F. Bennett, Phys. Rev. **122**, 595 (1961).

[9] E. I. Dupont de Nemours, Wilmington, Del.

[10] G. L. Miller and V. Radeka, Proceedings of the NAS Conference on Instrument Techniques in Nuclear Pulse Analysis, Monterey, California, 1963 (unpublished).

[11] J. L. Snelgrove, Ph.D. thesis, Michigan State University, 1968 (unpublished).

[12] Unpublished FORTRAN-IV computer code written by F. G. Perey and modified by R. M. Haybron at Oak Ridge National Laboratory.

TABLE I. Optical-model parameters used in the DWBA analysis of the $^{15}N(p, d)^{14}N$ reactions.

Outgoing particle	E (MeV)	V (MeV)	r_R, r_{so} (F)	a_R, a_{so} (F)	W_S (MeV)	W_D (MeV)	r_I (F)	a_I (F)	V_{so} (MeV)
p	39.84	43.9	1.13	0.66	4.54	2.93	1.42	0.48	8.0
d	32.9	93.5	1.02	0.80	0.0	8.70	1.41	0.70	7.57
d	24.8	98.5	1.00	0.80	0.0	7.80	1.46	0.70	7.57
d	17.2	106.0	0.97	0.80	0.0	6.80	1.52	0.70	7.57

available in the literature, and those which are available[13,14] correspond to lower deuteron energies and were analyzed using simplified forms of the optical-model potential. Thus, it was decided to use parameters derived from $^{16}O(d, d)^{16}O$ data, discussed in Ref. 4. Newman *et al.*[15] have shown that the variation of the parameters with Z and A is rather slow, so these parameters should be valid. Table I also lists the deuteron parameters used in the $^{15}N(p, d)^{14}N$ analyses.

EXPERIMENTAL RESULTS

The simplest shell-model configuration for the ^{15}N ground state is that of one $1p_{1/2}$ proton hole in a ^{16}O core. Thus, the neutron configuration should be similar to that of ^{16}O. The spin and parity of the ^{15}N ground state is $\frac{1}{2}^-$, so the pickup of a $1p_{1/2}$ neutron populates ^{14}N states having $J^\pi = 0^+, 1^+$, and the pickup of a $1p_{3/2}$ neutron leads to states having $J^\pi = 1^+, 2^+$. Based upon the simple shell model, using only $1p$ nucleons outside a filled $1s$ core, one can construct the ^{14}N configurations shown in Fig. 2. The isotopic spin quantum number T is good for all of the states shown, the particular combinations of the two terms of diagram (c) being necessary for this reason. The $T=1$ states are those in which a neutron could be transformed into a proton, or vice versa, without violating the Pauli principle. Of the ten possible levels, there are nine which could be reached by $1p$ pickup from ^{15}N, since excitation of the 3^+ level is forbidden by angular momentum conservation. The three other levels having configuration (b) are not populated by a direct pickup in the simplest model since they require the excitation of one of the protons in ^{15}N. Thus, one would expect to see six strong levels (one 0^+, $T=1$; two 1^+, $T=0$; one 1^+, $T=1$; one 2^+, $T=0$; and one 2^+, $T=1$).

There are over 50 known levels in ^{14}N between 0.0 and 14.0 MeV, 18 of which have been identified as 0^+, 1^+, or 2^+ (see Table II). The energies, spins, and parities are taken from Ref. 16 and the references therein, and are consistent with the present results

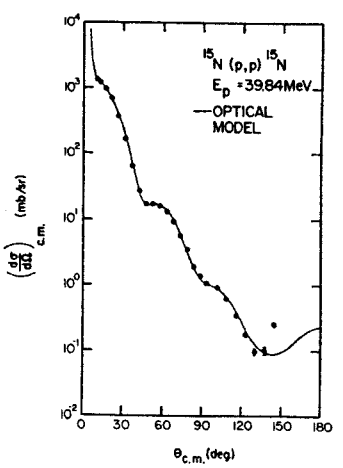

FIG. 1. Optical-model fit to the $^{15}N(p, p)^{15}N$ angular distribution.

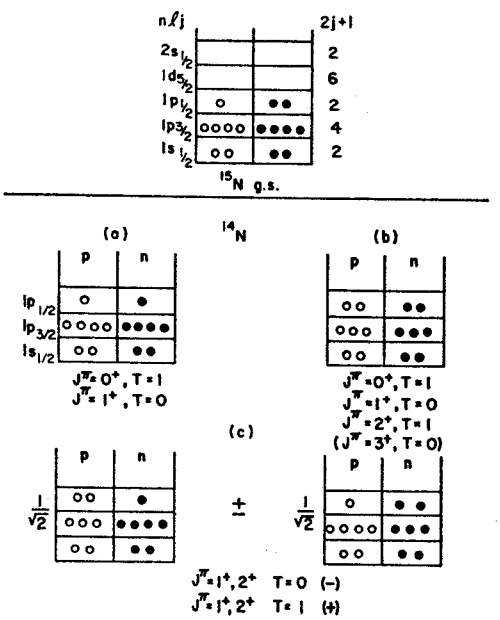

FIG. 2. Simple shell-model configurations of the ^{15}N ground state and the ^{14}N levels based only on $1s$-$1p$ nucleons.

[13] Dai-Ca Nguyen, J. Phys. Soc. Japan 21, 2462 (1966).
[14] J. L. Vidal, R. Bouche, C. Fayard, L. Feuvrais, M. Gaillard, P. Gaillard, M. Gouanere, M. Gusakow, G. H. Lamont, and J. R. Pizzi, J. Phys. (Paris), Coloq., No. 1, 128 (1966).
[15] E. Newman, L. C. Becker, B. M. Preedom, and J. C. Hiebert, Nucl. Phys. A100, 225 (1967).
[16] N. F. Mangelson, B. G. Harvey, and N. K. Glendenning, Nucl. Phys. A117, 161 (1968).

TABLE II. Peak cross sections and spectroscopic factors for the levels observed in ^{14}N. The average cross section over the indicated angular range is given for weak levels having angular distributions showing no characteristic maximum. The uncertainties quoted in the spectroscopic factors represent only the uncertainties in σ_{peak}.

E_x (MeV)	J^π	T	l_n	σ_{peak} (mb/sr)	θ_{peak} (deg)	$S(p,d)$
0.0	1^+	0	1	11.1±0.8	12 ± 1	1.27±0.09
2.311	0^+	1	1	3.4±0.2	14 ± 1	0.50±0.03
3.945	1^+	0	1	3.3±0.4	14 ± 1	0.60±0.07
4.910	0^-	0	0	0.06±0.02	12− −15	
5.104	2^-	0	2	0.22±0.06	18 ± 2	0.06±0.02
5.685	1^-	0	0	0.12±0.03	12− −15	
5.832	3^-	0	2	0.15±0.05	21 ± 3	0.04±0.01
6.21	1^+	0	1	0.15±0.04	15 ± 2	0.03±0.01
6.44	3^+	0		0.01±0.006	14− −34	
6.70				<0.01		
7.029	2^+	0	1	4.7±0.3	15 ± 1	1.02±0.07
7.40				0.02±0.01	18 ± 3	
7.60				<0.01		
7.97	2^-	0		0.05±0.02	15 ± 2	
8.060	1^-	1	0	0.06±0.03	12− −15	
8.617	0^+	1		0.02±0.01	21 ± 2	
8.906	3^-	1		0.04±0.02	12− −29	
8.963	5^+	0				
8.979	2^+	0		0.05±0.02	21 ± 2	
9.17	2^+	1	1	1.7±0.2	15 ± 1	0.49±0.06
9.388	2^-(?)	0	(3)	0.12±0.05	30 ± 3	0.05±0.02
9.508	2^-	1		0.06±0.02	9− −18	
9.702	1^+	0		0.01	9− −45	
10.096	(1^+)	0	1	0.10±0.03	16 ± 2	0.03±0.01
10.213	1^+	0		0.04±0.02	10− −22	
10.431	2^+	1	1	1.16±0.15	16 ± 1	0.39±0.05
10.85	(4^+)	0		<0.01		
11.06	1^+	0	1	0.09±0.03	16 ± 2	0.04±0.01
11.23	(3^-)	1				
11.299	2^-	0	(1)	0.05±0.03	15 ± 3	0.02±0.01
11.39	(1^+)	0		0.02±0.01	14− −24	
11.51	3^+	0		0.03±0.01	30 ± 3	
11.66				0.05±0.03	12 ± 3	
11.74	1^+					
11.80	(2^+)			0.03±0.02	12− −40	
11.97	2^+			~0.01	10− −30	
12.21	3^-					
12.29				0.01±0.01	14− −25	
12.52			(1)	0.32±0.05	24 ± 3	
12.61	3^+			0.06±0.03	11− −23	
12.80	4^+					
12.83	4^-			0.07±0.03	11− −30	
13.17	$(0^-, 1^-)$	0				
13.23				0.15±0.05	12− −15	
13.72	1^+	1	1	1.38±0.1	15 ± 1	0.81±0.06

except for the 9.388 level. An energy-level diagram of ^{14}N, displayed beside a deuteron energy spectrum obtained at $\theta_{lab}=19.9°$ for an incident proton energy of 39.84 MeV, is shown in Fig. 3. It is seen that many levels are excited; however, the strongly excited levels are seen to be either 0^+, 1^+, or 2^+.

Experimental angular distributions for the ten strongest levels exhibiting the characteristics of $l_n=1$ transfer, are shown in Figs. 4 and 5. J dependence is seen in the steeper slope of the 0^+ angular distribution ($p_{1/2}$ pickup) as compared to the 2^+ angular distributions ($p_{3/2}$ pickup). A Q-dependent effect is seen in the decreasing slopes of the 2^+ angular distributions with increasing excitation energy, as shown in Fig. 5. The slopes of the 0.0 MeV, 1^+ and the 2.311 MeV, 0^+ angular distributions shown in Fig. 4 are very nearly the same, indicating, on the basis of J dependence, that the ground state is populated mainly by $1p_{1/2}$ pickup, as one would expect from energy and model considerations. The other 1^+ angular distributions exhibit less steep slopes, indicating $1p_{3/2}$ pickup. The $^{15}N(p,d)^{14}N$ and $^{16}O(p,d)^{15}O$ $l_n=1$ angular distributions[4] are very similar.

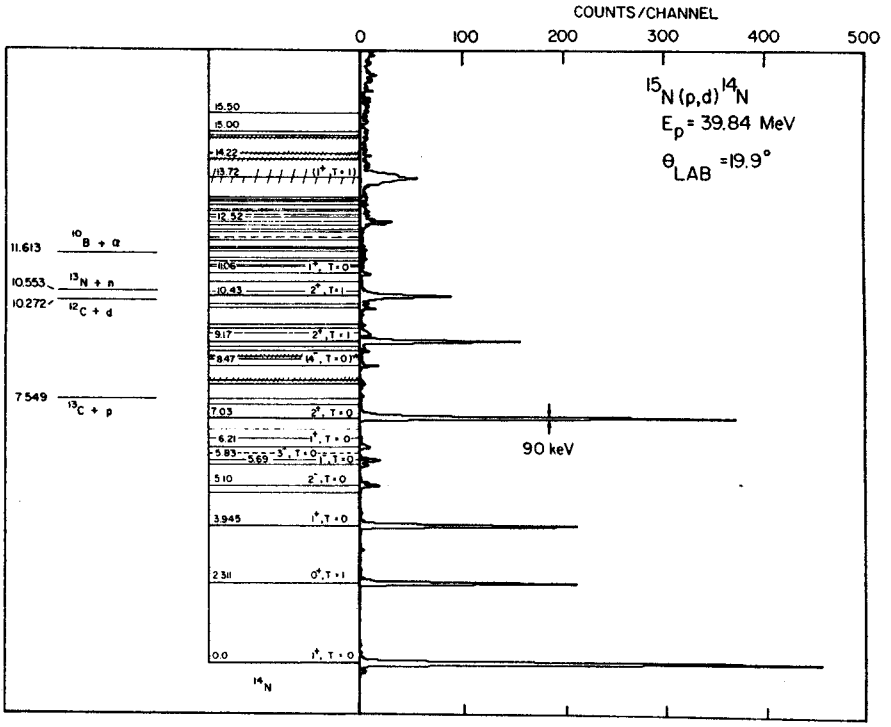

FIG. 3. Energy-level diagram of ^{14}N displayed beside a deuteron energy spectrum from the ^{15}N$(p, d)^{14}$N reaction for $E_p = 39.84$ MeV and $\theta_{lab} = 19.9°$.

The broad level at 13.72 MeV had been identified as a 1^+, $T=1$ level by Ball and Cerny[17] from a study of the ^{15}N$(^3$He, $\alpha)^{14}$N neutron pickup reaction. The present results confirm this assignment and yield a width for this level of 210±30 keV. Ball and Cerny also found almost equal excitation of the 9.17- and 10.43-MeV levels, as was found in the present work. Angular distributions for other levels excited are shown in Fig. 6. These levels are weakly excited, and their angular distributions do not contradict the assignments in Table II.

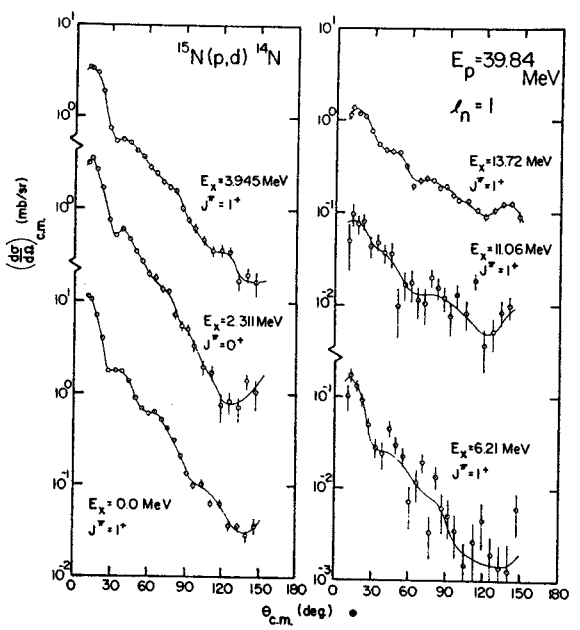

FIG. 4. Experimental deuteron angular distributions for the 0^+ and 1^+ levels of ^{14}N strongly excited in the ^{15}N$(p, d)^{14}$N reaction for $E_p = 39.84$ MeV. The solid lines are drawn to guide the eye.

[17] G. C. Ball and J. Cerny, Phys. Letters 21, 551 (1966).

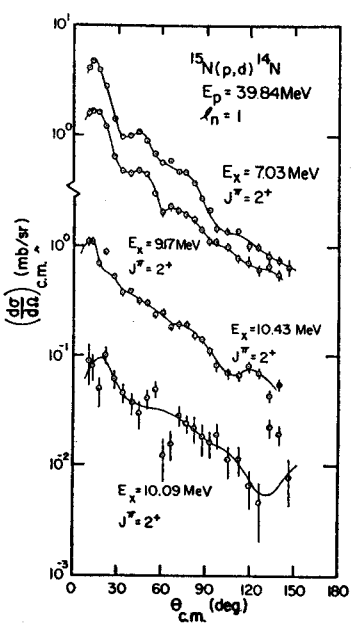

FIG. 5. Experimental deuteron angular distributions for the 2^+ levels of ^{14}N strongly excited in the ^{15}N$(p, d)^{14}$N reaction for $E_p = 39.84$ MeV. The solid lines are drawn to guide the eye.

The excitation of levels other than 0^+, 1^+, or 2^+ in the (p, d) reaction is an indication of admixtures in the ground state of ^{15}N, the most likely ones being $1d_{5/2}$ and $2s_{1/2}$, leading to excitation of 2^- or 3^- and 0^- or 1^- states, respectively. Most are very weakly excited. The level at 12.52 MeV had no previous assignment and is rather strongly excited, especially for a state with such a high excitation energy. Its angular distribution is most consistent with $1p$ pickup. The angular distribution of the 9.39-MeV level shows a rather broad maximum around 30° so that $l_n=3$ or possibly 4 might be preferred, which would disagree with the 2^- assignment for the state.

Levels assigned $J^\pi=3^+$ or 4^+ would require $1f$ neutron pickup in the direct reaction picture. The angular distributions for the 12.61- and 12.80-MeV levels may contain contributions from other close-lying levels. Again, the cross sections are small. The existence of a level between the 10.55- and 11.06-MeV levels has been reported at 10.71,[18] at 10.81,[16] and at 10.85 MeV.[19,20]

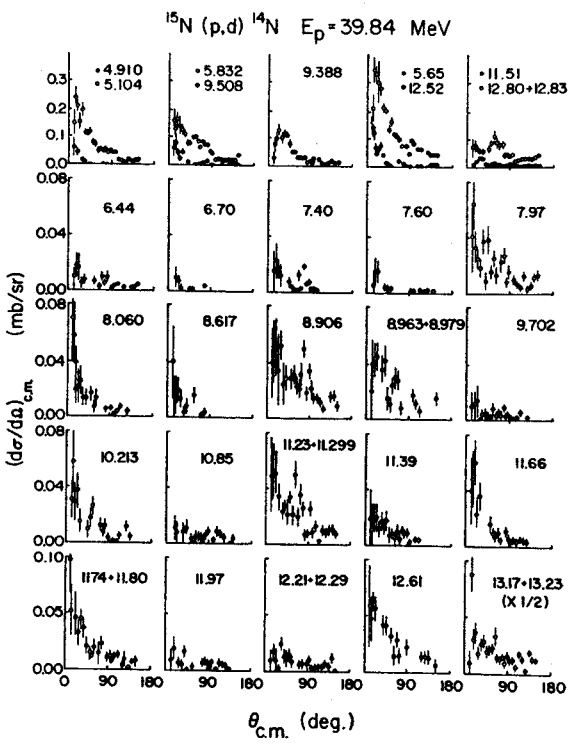

FIG. 6. Deuteron angular distributions for the ^{14}N levels not shown in Figs. 4 and 5 excited by the $^{15}N(p, d)^{14}N$ reaction for $E_p=39.84$ MeV.

[18] R. H. Pehl, E. Rivet, J. Cerny, and B. G. Harvey, Phys. Rev. 137, B114 (1965).
[19] B. G. Harvey, J. R. Merriwether, and J. Mahoney, Phys. Rev. 146, 712 (1966).
[20] R. H. Bassel, R. M. Drisko, and G. R. Satchler, Oak Ridge National Laboratory Report No. ORNL-3240, 1962 (unpublished); R. H. Bassel, R. M. Drisko, and G. R. Satchler, Oak Ridge National Laboratory Memorandum to the Users of the Code JULIE, 1966 (unpublished).

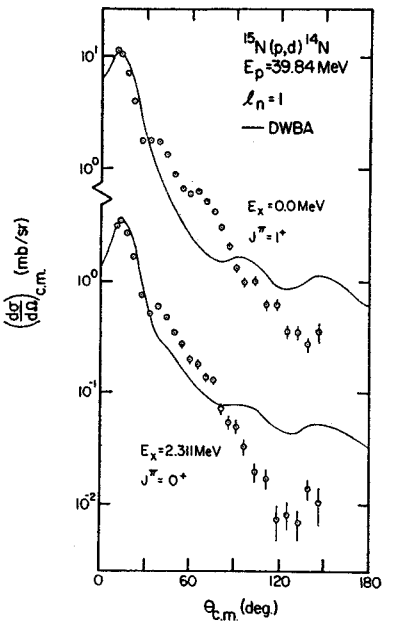

FIG. 7. DWBA calculations for the $^{15}N(p, d)^{14}N$, $E_p=39.84$ MeV, $E_x=0.0$- and 2.311-MeV angular distributions.

An assignment of $J^\pi=4^+$, $T=0$ has been made by Mangelson *et al.*[16] In the present work a very weakly excited level was found at 10.80 ± 0.05 MeV. The angular distribution is shown in Fig. 6. Several other levels were weakly excited, and their angular distributions are shown in Fig. 6. The peak cross sections, and where applicable, l_n values for all levels excited in the $^{15}N(p, d)^{14}N$ reactions are listed in Table II.

DWBA ANALYSES AND COMPARISON TO THEORY

The results of the study of the extraction of spectroscopic factors for the $^{16}O(p, d)^{15}O$ reaction have been applied in the present work. DWBA calculations were performed with the code JULIE[20] using a lower radial integration cutoff of 3 F and a bound-state well radius equal to the proton real-well radius. Figure 7 shows the results of the DWBA calculations for the first two $l_n=1$ levels, while Fig. 8 shows a calculation for one of the $l_n=2$ levels excited, representing a $1d_{3/2}$ admixture in the ^{15}N ground state. Spectroscopic factors were extracted by matching the experimental and calculated angular distributions at the characteristic first maximum. A discussion of this procedure is also given in Ref. 4. Table II contains a list of the spectroscopic factors extracted, the errors quoted reflecting only the error in the experimental peak cross section. The decision as to whether a 1^+ level was formed by $1p_{1/2}$ or $1p_{3/2}$ pickup was made on the basis of the shape of the angular distribution (J dependence) and on the predictions of Cohen and Kurath.[7] The total $1p$ strengths seen in this reaction are

$$\sum S(1p_{1/2})=1.77, \qquad \sum S(1p_{3/2})=3.41$$

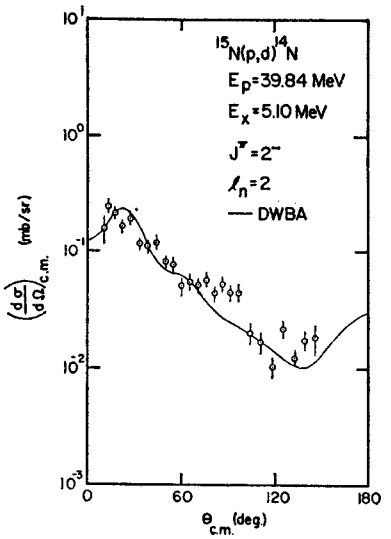

FIG. 8. DWBA calculation for the ^{15}N$(p, d)^{14}$N, $E_p=39.84$ MeV, $E_x=5.10$-MeV angular distributions.

giving $\sum S(1p)=5.18$. Thus we see approximately 10% more of the $1p_{3/2}$ strength than was observed in the ^{16}O$(p, d)^{15}$O reaction.[4] Excluding 0^- states, the amount of $2s$-$1d$ admixture in the ^{15}N ground state is given by $\sum S(2s-1d)=0.17$, again comparable to that found in the ^{16}O$(p, d)^{15}$O reaction. Hence we see about 90% of the total expected spectroscopic factor of 6.

The predictions of the intermediate coupling model of Cohen and Kurath[7] are given in Table III; they show six strong levels below 12.0 MeV, with three weak levels lying at higher excitation levels. Included in Table III are the spectroscopic factors expected in the jj-coupling limit. Pickup of a $1p_{1/2}$ neutron leads to states having configuration (a) in Fig. 2 whereas $1p_{3/2}$ pickup leads to states having configuration (c). It is seen that for the ^{15}N$(p, d)^{14}$N reaction the jj-coupling and intermediate-coupling descriptions are very similar.

A graphical comparison of the theoretical and experimental results is given in Fig. 9, where the lengths of the lines are proportional to the spectroscopic factors. The extensions of the theoretical lines represent the jj-coupling predictions. Seven strong levels were observed in the present experiment, all of which have angular distributions characteristic of $l_n=1$ pickup, whereas the Cohen and Kurath calculations predict only six levels. It appears that the $1p$ strength in the 2^+, $T=1$ level predicted to be at 9.524 MeV is shared by the 2^+, $T=1$ level at 10.43 MeV, a conclusion also reached by Ball and Cerny from their ^{15}N$(^3$He, $\alpha)^{14}$N work.[17] The mixing of these levels is supported by the values of the $M1$ transition strengths of the (9.17-MeV–0.0-MeV) and (10.43-MeV–0.0-MeV) transitions. Warburton and Pinkston[21] indicate that a single 2^+, $T=1$ level having a $(1s)^4(1p)^{10}$ configuration is allowed in the 10-MeV region (the one predicted by both jj coupling and intermediate coupling). A 2^+, $T=1$ level having a $(1s)^4(1p)^8(1s)(1d)$ configuration is expected in the same region. The predictions for the relative $M1$ strengths for ground-state transitions from these levels are 12 and 0, respectively. Since the observed $M1$ strengths for the 9.17- and 10.43-MeV ground-state transitions are 4.1 and 5.5, respectively, Warburton and Pinkston[21] suggest that these two levels are mixtures of the two configurations. The ratio of the $(1s)^4(1p)^{10}$ components of the two levels is given by the ratio of the $M1$ strengths and can be obtained from the present work as the ratio of the $1p$ spectroscopic factors for these levels. These ratios are

$$[(1s)^4(1p)^{10}, (9.17\text{ MeV})]/[(1s)^4(1p)^{10}, 10.43\text{ MeV})] = 0.75$$

from the $M1$ strengths, while from the present (p, d) experiment we get

$$[(1s)^4(1p)^{10}, (9.17\text{ MeV})]/[(1s)^4(1p)^{10}, (10.43\text{ MeV})] = 1.25\pm0.15.$$

Thus, both the work of Warburton and Pinkston[21] and the present work suggest strong mixing of the two levels, but disagree somewhat about the division of $1p$ strength between them. The sum of the spectroscopic factors for the 9.17- and 10.43-MeV levels is slightly less than that predicted for the 9.524-MeV level, but the over-all

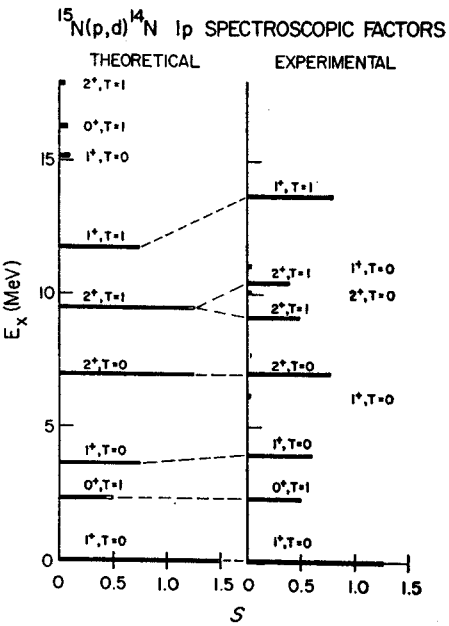

FIG. 9. Theoretical and experimental $l_n=1$ spectroscopic factors for the ^{15}N$(p, d)^{14}$N reaction.

[21] E. K. Warburton and W. T. Pinkston, Phys. Rev. 118, 733 (1960).

TABLE III. Intermediate-coupling predictions of coefficients of fractional parentage and spectroscopic factors for $1p$ neutron pickup from ^{15}N. Also included are the spectroscopic factors predicted in jj coupling.

E (calc.) (MeV)	(J^π, T)	nlj	CFP	$\sum_i CFP^2$	S	S_{jj}
0.0	$(1^+, 0)$	$1p_{3/2}$	0.0542			
		$1p_{1/2}$	−0.3601	0.1326	1.459	1.500
2.690	$(0^+, 1)$	$1p_{1/2}$	0.3376	0.1140	0.418	0.500
3.616	$(1^+, 0)$	$1p_{3/2}$	0.2434			
		$1p_{1/2}$	0.0642	0.0633	0.696	0.750
6.991	$(2^+, 0)$	$1p_{3/2}$	−0.3371	0.1136	1.250	1.250
9.524	$(2^+, 1)$	$1p_{3/2}$	−0.5704	0.3255	1.192	1.250
11.783	$(1^+, 1)$	$1p_{3/2}$	−0.4523			
		$1p_{1/2}$	0.000	0.2046	0.750	0.750
15.238	$(1^+, 0)$	$1p_{3/2}$	−0.0776			
		$1p_{1/2}$	−0.0505	0.0086	0.095	0.000
16.323	$(0^+, 1)$	$1p_{1/2}$	0.1497	0.0224	0.082	0.000
17.879	$(2^+, 1)$	$1p_{3/2}$	−0.1246	0.0155	0.057	0.000

agreement is good. These data thus support the 2^+, $T=1$ assignments for the 9.17- and 10.43-MeV levels. The several weakly excited $l_n=1$ levels observed in the present experiment probably result from small admixtures of the wave functions of the strong levels having the same J^π and T. No levels of measurable strength were observed above 13.72 MeV. The three weak levels predicted by Cohen and Kurath probably appear at much higher excitation energies and may be mixed with other levels. The strongest of these levels would be expected to have a peak cross section of only 50 μb/sr, and since the levels are well above the particle threshold and therefore expected to be broad, there would be little hope for being able to separate them from the background. The excellent over-all agreement of the Cohen and Kurath intermediate-coupling predictions and the experimental spectroscopic factors is further evidence for the validity of this model for $1p$-shell nuclei.

ACKNOWLEDGMENTS

The authors are indebted to P. J. Plauger and B. Horning for their assistance in acquiring and analyzing the data.

NUCLEAR INSTRUMENTS AND METHODS 82 (1970) 304–306; © NORTH-HOLLAND PUBLISHING CO.

AN ENERGY CALIBRATION METHOD FOR BEAM ANALYZER-MAGNETIC SPECTROGRAPH COMBINATIONS

G. F. TRENTELMAN and E. KASHY*

Cyclotron Laboratory, Department of Physics, Michigan State University, East Lansing, Michigan, U.S.A.

Received 9 February 1970

A method of energy calibration for beam analyzer-magnetic spectrograph combinations is described which promises highly accurate results for beam energies equivalent to 20–100 MeV protons.

Energy calibrations of magnetic spectrographs and accelerator beam transport systems in combination may be achieved with a sensitive null method utilizing different reaction products from a beam induced nuclear reaction. When two different reaction products (or a reaction product and a scattered particle) with different formation Q-values are observed at a known laboratory scattering angle, there exists a unique beam energy for which the magnetic rigidities of the two particles will be identical at that angle. If such particles are observed with a magnetic spectrograph they will appear as two superimposed peaks having the same radius of curvature for any value of the spectrograph field. The value of this beam energy is therefore established to the limit of accuracy that the centroids of these peaks are superimposed, that the laboratory scattering angle is known, and that the Q-value of the reaction is known. Effects due to the variation of cross section with scattering angle and to target thickness can be taken into account and made to add only a minor contribution to the uncertainty. The established beam energy then determines the magnetic rigidity (or $B\rho$ value) for the spectrograph at a specific radius of curvature and field setting. A series of judiciously chosen reactions each requiring a different beam energy

* Supported in part by the National Science Foundation.

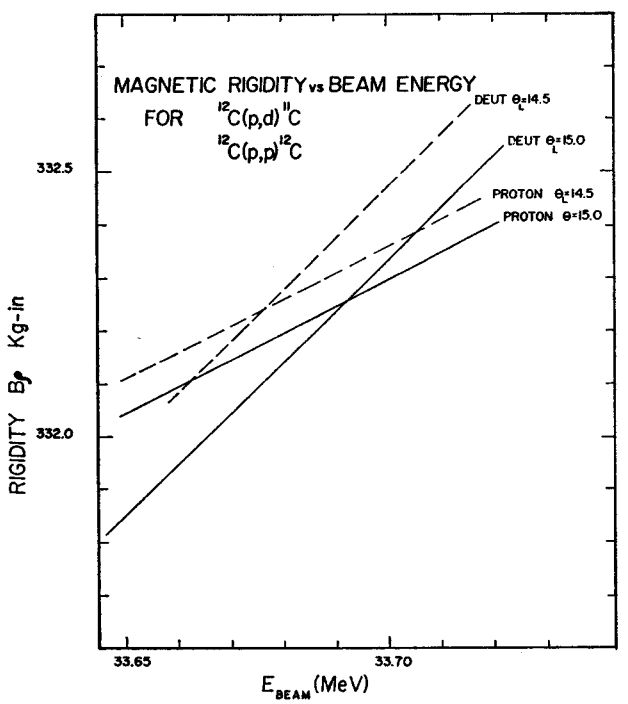

Fig. 1. Magnetic rigidity of outgoing particles for $^{12}C(p,p)^{12}C$ and $^{12}C(p,d)^{11}C$ reactions at $\theta_{lab} = 14.5°$ and 15.0° as functions of incident beam energy.

TABLE 1a
Some useful reactions for calibration in momentum matching method.

Reaction	Ex (residual nucleus) (MeV ± keV)	Q value (MeV ± keV)
$^{12}C(p,p)^{12}C$	0.0	0.0
$^{12}C(p,p)^{12}C^*$	4.4398 ± 0.3[5])	−4.4398 ± 0.3
$^{16}O(p,p)^{16}O$	0.0	0.0
$^{16}O(p,p)^{16}O^*$	6.1305 ± 0.4[6])	−6.1305 ± 0.4
$^{12}C(p,d)^{11}C$	0.0	−16.4953 ± 1.1[1])
$^{16}O(p,d)^{15}O$	0.0	−13.4434 ± 1.2[1])
$^{16}O(p,d)^{15}O^*$	6.180 ± 4.0[7])	−19.6234 ± 4.0
$^{12}C(d,d)^{12}C$	0.0	0.0
$^{12}C(d,d)^{12}C^*$	4.4398 ± 0.3	−4.4398 ± 0.3
$^{16}O(d,d)^{16}O$	0.0	0.0
$^{16}O(d,d)^{16}O^*$	6.1305 ± 0.4	−6.1305 ± 0.4
$^{12}C(d,t)^{11}C$	0.0	−12.4624 ± 1.1[1])
$^{16}O(d,t)^{15}O$	0.0	−9.4105 ± 1.3[1])
$^{16}O(d,t)^{15}O^*$	6.1800 ± 4.0	−15.5905 ± 4.0
$^{15}N(p,p)^{15}N$	0.0	0.0
$^{15}N(p,d)^{14}N$	0.0	−8.6102 ± 0.8[1])
$^{15}N(p,d)^{14}N^*$	2.3128 ± 0.06[8])	−10.9230 ± 0.8

TABLE 1b
Possible reaction pairs for momentum match energy calibrations. Calculations are for $\theta_{lab} = 15.0°$.

Reaction 1	Excitation energy 1 (MeV ± keV)	Reaction 2	Excitation energy 2 (MeV ± keV)	Beam energy[a] (MeV ± keV)	Beam particle	Magnetic rigidity of outgoing particles (kG·in)
$^{12}C(p,d)^{12}C$	0.0	$^{12}C(p,d)^{11}C$	0.0	33.691 ± 2.2	p	332.256
$^{12}C(p,p)^{12}C^*$	4.4398 ± 0.3	$^{12}C(p,d)^{11}C$	0.0	29.009 ± 2.2	p	282.884
$^{16}O(p,p)^{16}O$	0.0	$^{16}O(p,d)^{15}O$	0.0	27.336 ± 2.5	p	299.009
$^{16}O(p,p)^{16}O$	0.0	$^{16}O(p,d)^{15}O^*$	6.180 ± 4.0	40.106 ± 8.0	p	363.381
$^{16}O(p,p)^{16}O^*$	6.1305 ± 0.4	$^{16}O(p,d)^{15}O$	0.0	20.981 ± 2.5	p	219.312
$^{16}O(p,p)^{16}O^*$	6.1305 ± 0.4	$^{16}O(p,d)^{15}O^*$	6.180 ± 4.0	33.607 ± 8.0	p	299.600
$^{12}C(d,d)^{12}C$	0.0	$^{12}C(d,t)^{11}C$	0.0	38.502 ± 3.0	d	498.783
$^{12}C(d,d)^{12}C^*$	4.4398 ± 0.3	$^{12}C(d,t)^{11}C$	0.0	29.203 ± 3.0	d	398.802
$^{16}O(d,d)^{16}O$	0.0	$^{16}O(d,t)^{15}O$	0.0	28.867 ± 4.0	d	431.974
$^{16}O(d,d)^{16}O^*$	6.1305 ± 0.4	$^{16}O(d,t)^{15}O$	0.0	16.283 ± 4.0	d	254.009
$^{16}O(d,d)^{16}O$	0.0	$^{16}O(d,t)^{15}O^*$	6.180 ± 4.0	48.096 ± 12.0	d	558.980
$^{16}O(d,d)^{16}O^*$	6.1305 ± 0.4	$^{16}O(d,t)^{16}O^*$	6.180 ± 4.0	35.232 ± 12.0	d	433.230
$^{15}N(p,p)^{15}N$	0.0	$^{15}N(p,d)^{14}N$	0.0	17.446 ± 1.6	p	238.220
$^{15}N(p,p)^{15}N$	0.0	$^{15}N(p,d)^{14}N^*$	2.3128	22.174 ± 1.6	p	268.898

[a] Error reflect uncertainty in the masses.

and each being observed at many points in the focal plane of a spectrograph would simultaneously calibrate both the spectrograph and the beam analysis system. A sample pair of reactions for this method is $^{12}C(p,p)^{12}C$ and $^{12}C(p,d)^{11}C$, with the (p,d) Q-value $= -16.4953 \pm 0.0011$ MeV[1]). As seen in fig. 1, the proton and deuteron rigidity curves coincide for $\theta_{lab} = 15.0°$ at $E_{beam} = 33.691$ MeV and $B\rho_p = B\rho_d = 332.256$ kG·in. The other pair of curves showing the situation at $\theta_{lab} = 14.5°$ indicate how the beam energy at the cross over point depends on the laboratory scattering angle. Interestingly enough, fig. 1 also shows that the $B\rho$ value of the cross over point is relatively insensitive to θ_{lab}. Therefore, the spectrograph calibration is insensitive to the scattering angle. The simultaneous detection and identification of the protons and deuterons required can be achieved for example by detecting them with a position sensitive detector in which the energy losses of the two particles are different. Some expected uncertainties for this method using the example of the $^{12}C(p,d)$ and $^{12}C(p,p)$ reactions and a spectrograph of $\Delta D/\Delta\rho$ dispersion = 2.5 (ΔD being the particle motion along the focal plane for a corresponding $\Delta\rho$) operating at 10 kG are given below.

$\Delta E_{beam}/\Delta(D_p - D_d) = 43$ keV/mm, $\Delta(D_p - D_d)$ = error in centroid separation;

$\Delta E_{beam}/\Delta\theta_{lab} = 30$ keV/degree = uncertainty in lab detection angle at 15°;

$\Delta E_{beam}/\Delta Q = 2.0$ keV/keV, ΔQ = uncertainty in (p,d) Q-value.

Using the split-pole spectrograph[2]) at the Michigan State University Cyclotron Laboratory with a 300 μm position sensitive silicon surface barrier detector, we have obtained peak widths of 0.4 mm fwhm[3]) for deuterons so that a $\Delta(D_p - D_d)$ value of 0.06 mm is not unreasonable. If lab scattering angles are accurate to 0.05°, and 1.1 keV is used as the uncertainty in (p,d) Q-values, a total uncertainty of 4 keV at the beam energy of 33.691 MeV determination should be feasible. Tables 1a and 1b list a series of calculations using targets of ^{12}C, ^{15}N and ^{16}O. The combinations of (p,d) and (p,p) reactions on light nuclei are particularly appropriate for this method since their cross sections are larger, their $B\rho$ curves cross steeply, and their Q values are generally well known. The combination of the (d,d) and (d,t) reactions, while less favorable on each of these counts, does provide calibration points at much higher rigidities i.e. corresponding approximately to 100 MeV protons and should prove extremely valuable. The use of ^{15}N target in this method looks particularly promising since the (p,d) Q-value of -8.6102 ± 0.0008 MeV[1]) connects two stable residual nuclei and may therefore be more reliable. Finally, the reactions are such that the calibration energies provided lie from a region well above that where (p,n) calibration points are available and overlap the region where

that method of calibration can be used. Thus, this procedure, coupled with a magnet recycling method[4]) should provide an accurate, reproducible energy calibration.

References

[1]) C. Maples, G. W. Goth and J. Cerny, Nuclear reaction Q-values, UCRL-16964 (1966).

[2]) J. E. Spencer and H. A. Enge, Nucl. Instr. and Meth. **49**, no. 2 (1967).

[3]) R. K. Jolly, G. F. Trentelman and E. Kashy, to be published.

[4]) J. L. Snelgrove and E. Kashy, Nucl. Instr. and Meth. **52**, no. 1 (1967).

[5]) C. Chasman, K. W. Jones, R. A. Ristinen and D. E. Alburger, Phys. Rev. **159** (1967) 830.

[6]) J. B. Marion, University of Maryland Technical Report no. ORO-2098-58.

[7]) E. K. Warburton, J. W. Olness and D. E. Alburger, Phys. Rev. **140** (1965) B1202.

[8]) F. Ajzenberg-Selove, Energy levels of light nuclei: $A = 14$, LAP-82, to be published in Nucl. Phys.

NUCLEAR INSTRUMENTS AND METHODS 83 (1970) 267–271; © NORTH-HOLLAND PUBLISHING CO.

ANALYSIS OF ISOCHRONOUS CYCLOTRONS WITH SEPARATED HARD-EDGE MAGNETS*

M. M. GORDON

Cyclotron Laboratory, Michigan State University, East Lansing, Michigan 48823, U.S.A.

Received 27 February 1970

The orbit properties of isochronous cyclotrons with separated magnets are analyzed on the basis of the hard-edge approximation. This analysis extends previous work by treating magnets having a quite general shape. This treatment results in a generalized expression for the field index. A computer program ("Spyring Code") is described which uses this analysis to calculate orbit properties for a given magnet geometry. Results are presented for a 600 MeV cyclotron having a symmetric six sector geometry with a radially decreasing magnet fraction. These results demonstrate that this type of magnet geometry produces greater vertical focusing than a comparable design with a constant magnet fraction.

1. Introduction

This paper presents an analysis, based on the hard-edge approximation, of isochronous cyclotrons with separated magnet sectors having a quite general shape. This type of accelerator was first analyzed by Roberts and Salzman who assumed in addition that the equilibrium orbits were approximately circular[1]). G. Schatz has recently provided an exact analysis for the special case where the field within the magnets is homogeneous[2]). In a previous paper, we presented an extensive discussion of isochronous cyclotrons with magnets having constant angular width and no spiral[3]). The present paper removes such restrictions, and therefore represents a generalization of these preceding analyses.

If (r,θ) are the polar coordinates relative to the machine center, then the shape of a sector magnet is given by the functions $\theta_1(r)$ and $\theta_2(r)$ which specify the position of the two magnet boundaries; to be specific, we assume: $\theta_2 > \theta_1$. These functions may have any desired form, except that for a cyclotron having N sectors, they must satisfy: $(\theta_2 - \theta_1) < 2\pi/N$. The magnet geometry can be characterized alternatively by the "magnet fraction" $f(r)$ and the "spiral function" $\theta_0(r)$ given by

$$f(r) = (\theta_2 - \theta_1)N/2\pi, \tag{1a}$$

$$\theta_0(r) = (\theta_2 + \theta_1)/2, \tag{1b}$$

where $f(r) < 1$, and $\theta_0(r)$ may be changed by an arbitrary additive constant. If $\theta_0(r)$ increases (or decreases) monotonically with radius, then the magnets have "spiral", while if $\theta_0(r)$ is constant, then the magnet geometry is symmetric. If $f(r)$ and $r(\mathrm{d}\theta_0/\mathrm{d}r)$ are both constants, then we have a type of "scaling" orbit geometry in which all the focusing properties depend only on $\beta = v/c$ for different ions or for different final energies of a given ion[4]).

* This work was supported by the National Science Foundation.

The "hard-edge" approximation, as it is used here, actually consists of two separate assumptions. The equilibrium orbit is assumed to consist of a single circular arc within each magnet joined smoothly to a straight line segment between each pair of adjacent magnets. Thus, in addition to requiring that the magnetic field drops abruptly to zero at both edges of the magnet, it is also assumed that the magnetic field is constant along the orbit within each magnet.

2. Orbit geometry

As shown by G. Schatz[2]), each equilibrium orbit can be inscribed in a regular N-sided polygon whose center coincides with the machine center and whose sides coincide with the straight sections of this orbit; each equilibrium orbit therefore has the same symmetry properties as its circumscribing polygon. This conclusion holds quite generally for the hard-edge approximation assumptions given above, and is independent of the magnet shape. In particular, if the particle enters the magnet at $(r,\theta) = (R_1,\theta_1)$ and exits from the magnet at (R_2,θ_2), then $R_1 = R_2 = R$. In determining the orbit properties, we shall use R as the independent variable rather than the particle energy E.

The geometry of an equilibrium orbit for one half of

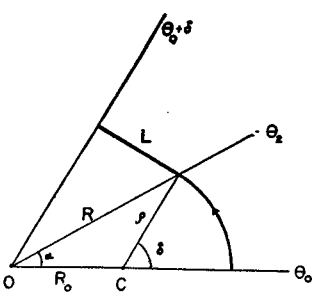

Fig. 1. Equilibrium orbit geometry for one half of a sector, from $\theta = \theta_0$ to $\theta = \theta_0 + \delta$.

a sector is shown in fig. 1. The angle $\alpha(R)$ is defined by

$$\alpha(R) = (\theta_2 - \theta_1)/2 = f(R)\delta, \tag{2}$$

where $\delta = \pi/N$. The circular arc segment of the equilibrium orbit has radius of curvature ρ and center of curvature at the point C whose coordinates are $(r,\theta) = (R_0,\theta_0)$ relative to the machine center at the point O; the straight line portion of the equilibrium orbit has length $2L$ per sector. Considering the geometry of fig. 1, the values of ρ, R_0, and L can be expressed in terms of R and α as follows:

$$L = R\sin(\delta - \alpha) = R_0 \sin\delta, \tag{3a}$$

$$\rho \sin\delta = R\sin\alpha. \tag{3b}$$

The spiral function $\theta_0(R)$ does not enter into these relations, and serves only to locate one equilibrium orbit relative to another.

It is convenient to introduce the parameters $b(R)$ and $a(R)$ given by

$$b(R) = R_0/\rho = \sin(\delta - \alpha)/\sin\alpha, \tag{4a}$$

$$a(R) = L/\rho\delta = b(\sin\delta)/\delta. \tag{4b}$$

The total arc length S of the equilibrium orbit can then be writen as $S = 2\pi\rho(1+a)$. Since the isochronism condition requires that the rotation period T_0 be a constant independent of R, we can write

$$v = S/T_0 = \rho(1+a)\omega_0, \tag{5}$$

where $\omega_0 = 2\pi/T_0$, and $v = v(R)$ is the constant speed of the particle in the equilibrium orbit.

For a particle of charge q and rest mass m_0, the following dynamical relation holds: $m_0 v\gamma = qB\rho$, where γ is the relativistic mass factor and $B(R)$ is the constant magnetic field strength along the orbit within the magnet. This relation together with the isochronism condition above then yields

$$B(R) = (m_0\omega_0/q)(1+a)\gamma. \tag{6}$$

It should be noted that all of the orbit properties derived in this section depend only on $f(r)$; that is, they are independent of (df/dr) as well as $\theta_0(r)$.

3. Field index

The properties of the linear oscillations of particles displaced from the equilibrium orbit are determined by the field index $k = (\rho/B)(\partial B/\partial x)$, where $(\partial B/\partial x)$ is the component of the field gradient along the outward normal to the equilibrium orbit. In order to evaluate k within the magnet, consider the point P in fig. 2 which is located at a distance $(\rho + dx)$ from the point C, the center of curvature of the equilibrium orbit, and let ϕ be the angle between the line CP and the line from the machine center at O which passes through C along the

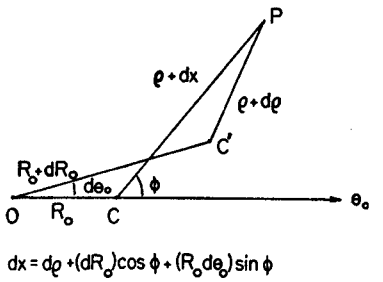

Fig. 2. Geometric diagram required for the field index derivation.

$\theta = \theta_0$ axis; according to this definition, ϕ has the limiting values $\phi = \pm\delta$ respectively at the two magnet boundaries $\theta = \theta_{2/1} = \theta_0 \pm \alpha$. The point P lies on another equilibrium orbit whose radius of curvature is $(\rho + d\rho)$ and whose center of curvature is at the point C′ having the coordinates $(r,\theta) = (R_0 + dR_0, \theta_0 + d\theta_0)$, as shown in fig. 2. If the field along this equilibrium orbit is $(B + dB)$, then the field index within the magnet is given by $k(\phi) = (\rho/B)(dB/dx)$.

The relation between the various differentials can be obtained by considering the two triangles shown in fig. 2: OCQ and QPC′, where Q is the intersection point of the lines CP and OC′. This geometry yields the following value for dx to first order:

$$dx = d\rho + (dR_0)\cos\phi + R_0(d\theta_0)\sin\phi. \tag{7}$$

Furthermore, differentiation of eqs. (5) and (6) leads to the following result:

$$(dB)/B = (\beta\gamma)^2(d\rho)/\rho + \gamma^2(d\omega)/\omega, \tag{8}$$

where $\omega = (1+a)\omega_0$. Since R has been chosen as the independent variable, we now write

$$k(\phi) = k_0/\lambda(\phi), \tag{9}$$

where $k_0 = (R/B)(dB/dR)$ and $\lambda(\phi) = (R/\rho)(dx/dR)$. Upon using the expressions (7) and (8) above and evaluating the various derivatives, we then obtain

$$k_0 = (\beta\gamma)^2\rho' - \gamma^2 A\alpha', \tag{10a}$$

$$\lambda = \rho' + b(R_0')\cos\varphi + b(\theta_0')\sin\varphi, \tag{10b}$$

with the following definitions:

$$t_1 = R(d\theta_1/dR),\ t_2 = R(d\theta_2/dR); \tag{11a}$$

$$\alpha' = R(d\alpha/dR) = (t_2 - t_1)/2; \tag{11b}$$

$$\theta_0' = R(d\theta_0/dR) = (t_2 + t_1)/2; \tag{11c}$$

$$\rho' = 1 + (\alpha')\cot\alpha; \tag{11d}$$

$$R_0' = 1 - (\alpha')\cot(\delta - \alpha); \tag{11e}$$

$$A = (\sin\delta/\sin\alpha)^2[(1+a)\delta]^{-1}; \tag{11f}$$

and with b given by eq. (4a). When $\alpha' = \theta_0' = 0$, this expression for $k(\phi)$ reduces to the one previously ob-

tained[3]). Moreover, on taking the limit $(1/N)\to 0$, we then obtain

$$k\to f(\beta\gamma)^2 - R(\mathrm{d}f/\mathrm{d}R), \tag{12}$$

which agrees with the result found by Roberts and Salzman[1]).

If x and z represent the horizontal and vertical displacements from the equilibrium orbit, and if y stands for either x or z, then the differential equation for the linear motion is

$$(\mathrm{d}^2y/\mathrm{d}\phi^2) + K_y(\phi)y = 0, \tag{13}$$

where $K_x(\phi) = 1 + k(\phi)$ and $K_z(\phi) = -k(\phi)$ and where ϕ ranges from $-\delta$ to $+\delta$. This differential equation can be integrated numerically so as to yield the transfer matrix for the x or z motion through the magnet.

In conformity with the hard-edge approximation, the boundary conditions at the two magnet edges can be derived from the corresponding field indices $k_1(\phi)$ and $k_2(\phi)$ which are given by[1-3]):

$$k_{1/2}(\phi) = -\tan(\delta - \alpha \pm \zeta_{1/2})\Delta(\phi \pm \delta), \tag{14}$$

where Δ is the Dirac delta function, and where

$$\tan\zeta_{2/1} = t_{2/1} = \theta_0' \pm \alpha', \tag{14a}$$

with $t_{2/1}$ defined by (11a). These field indices, together with $k(\phi)$ within the magnet, are all functions of R in general; however, when $\alpha' = 0$ and θ_0' is a constant, then k_1 and k_2 are both constants, and $k(\phi)$ depends only on $\beta = v/c$ – this is the scaling geometry mentioned in sec. 1.

4. Spyring code

A computer program, named "Spyring Code", has been developed which uses the analysis presented in the preceding sections to calculate all the important orbit properties associated with a given magnet geometry[5]). The input to this program consists of the following: the number of sectors N; a table of values for the magnet boundary angles θ_1 and θ_2 versus the radius r, which may be expressed in arbitrary units; the charge and mass of the ion to be considered. In addition, any two of the following four parameters must be specified: the length scale factor r_0 which converts the given r values to those of the full scale magnet; the orbital frequency $\nu_0 = \omega_0/2\pi$; the kinetic energy $E = E^*$ at $r = r^*$; the field strength $B = B^*$ at $r = r^*$, where r^* is any one of the given r values. For each R corresponding to a given r value, this program produces the following output data: the geometric properties of the equilibrium orbit; the kinetic energy E; the field strength B; the frequencies ν_x and ν_z of the linear oscillations. It also provides tables of the horizontal and vertical width functions, W_x and W_z, as a function of the arc length along the equilibrium orbit; these dimensionless width functions, which were discussed at length in a previous paper[3]), are each obtained from the formula: $W = (m_0\omega_0\beta/p)^{\frac{1}{2}}$, where p is the momentum and where β here is a quantity derived from the transfer matrix as defined by Courant and Snyder[6]).

Although the Spyring Code is quite capable of handling spiral magnet geometries, we shall omit examples of such designs here since the power of spiral to increase the vertical focusing is well known[4]). We shall instead consider a symmetric $(\theta_0 = 0)$ magnet geometry in which the magnet fraction f decreases with radius. This type of design, which has not been considered before, produces greater vertical focusing than would be obtained from a comparable design having a fixed f value. This magnet design with decreasing f value has, however, an obvious disadvantage in that the field strength within the magnet must increase faster than γ, and the resultant field gradients may pose a difficult design problem.

For the $N = 6$ geometry with constant $f = \frac{1}{3}$ (i.e., $\alpha = 10°$), the value of ν_z decreases from 1.46 to 1.00 when the proton energy increases from $E = 0$ to 420 MeV. In order to extend this design so as to reach 600 MeV while maintaining $\nu_z > 1$, the type of magnet shape shown in fig. 3 was investigated. Here, the magnet edge has a "bend" at a certain radius value, and then continues along a straight line; this particular magnet shape was chosen for its simplicity – any similar shape would work equally well. First, the

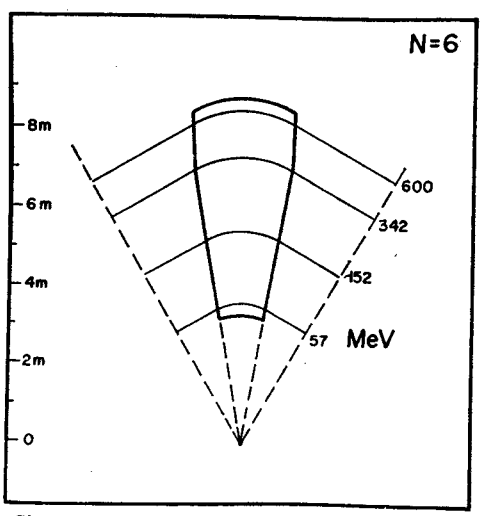

Fig. 3. Six sector magnet geometry with decreasing magnet fraction. Equilibrium orbits are shown for: 57, 152, 342 and 600 MeV, corresponding to the orbital frequency: $\nu_0 = 4.568$ MHz. Length scale at left is in meters; see table 1.

TABLE 1
Orbit data for magnet geometry shown in fig. 3.

		Proton				$E \to 0$	
R (m)	2α (deg)	E (MeV)	B (kG)	ν_x	ν_z	ν_x^0	ν_z^0
0.00	20.0	0	8.6	1.07	1.46	1.07	1.46
6.38	20.0	247	10.9	1.38	1.23	1.07	1.46
6.98	20.0	323	11.6	1.48	1.13	1.07	1.46
7.10	20.0	342	11.8	1.53	1.16	1.08	1.49
7.22	19.7	360	12.1	1.57	1.21	1.09	1.55
7.33	19.5	379	12.4	1.60	1.20	1.10	1.56
7.64	18.8	435	13.4	1.69	1.18	1.10	1.60
7.89	18.3	490	14.3	1.78	1.14	1.10	1.64
8.11	17.9	545	15.2	1.88	1.10	1.10	1.68
8.31	17.6	600	16.0	1.98	1.05	1.10	1.70

position of the bend was established at a radius value where $\nu_z \approx 1.1$; then, the value of α at the "final" radius was adjusted so that $\nu_z > 1$ out to 600 MeV. This process required several iterations with the Spyring Code, and in each case, the radius scale and the orbital frequency were determined by setting $E = 600$ MeV and $B = 16$ kG at the final radius value. The final magnet geometry is the one depicted in fig. 3; the "bend" occurs at $R = 7.10$ m, and the value of α decreases from 10° at this point to a final value of 8.8° at $R = 8.31$ m.

Table 1 presents a selection of the Spyring Code

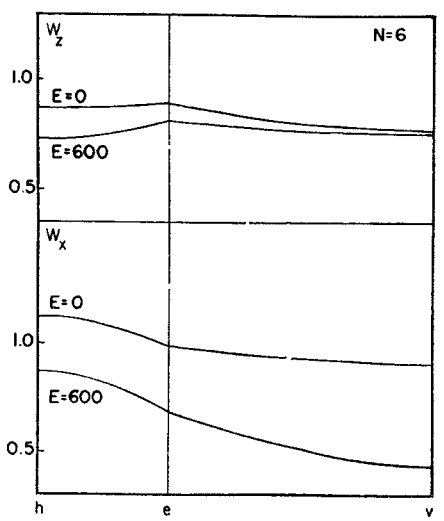

Fig. 4. Plots of width functions versus arc length at $E = 0$ and 600 MeV for magnet geometry shown in fig. 3. The arc length scale runs from center of magnet (h) to magnet edge (e) and thence to center of valley (v); the two sections of this scale are not commensurate.

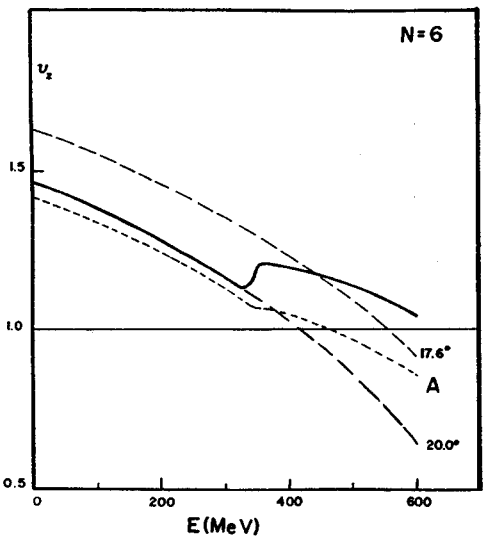

Fig. 5. Plots of vertical focusing frequency ν_z versus proton energy E. The solid curve pertains to the magnet geometry of fig. 3 and table 1. The dashed curve (labelled "A") was derived from the $[(1/N) \to 0]$-approximation formula for this magnet geometry. The two broken curves are for magnets having constant angular widths of 20° (bottom) and 17.6° (top).

output data for this magnet geometry (with the numbers rounded off to three digits). In addition to R (in meters) and the angular width 2α (in degrees), the table provides values of E (in MeV), B (in kG), ν_x and ν_z for the 600 MeV proton case; the last two columns give the values for ν_x^0 and ν_z^0 which are the focusing frequencies obtained for any nonrelativistic $(E \to 0)$ ion in this magnet geometry. With an appropriate set of pole-face coils to produce the necessary field changes, the same magnet geometry can be used for lower energy protons or for heavier ions; in all such cases, the value of ν_x or ν_z at a given R value will fall between the corresponding pair of values given in this table.

Another part of the output data was used to produce the plots shown in fig. 4 of the width functions W_x and W_z at $E = 0$ and 600 MeV; the curves for these two energy values bracket those for the intermediate energies which are omitted. These width functions have arbitrary units since only their variation with energy and position is significant. Since these functions are symmetric, their variation is shown for only one half of a sector[3]).

5. Discussion

One of the most interesting features of the data presented in table 1 is the relatively sharp increase in ν_z which occurs just beyond the "bend" ($R = 7.10$ m). This phenomenon, which has been observed to

occur in several different cases, implies that for a given f value, the value of ν_z is increased when $(\mathrm{d}f/\mathrm{d}r) < 0$. Fig. 5 displays curves of ν_z versus E which help to reveal the nature of this phenomenon. In addition to the solid curve which pertains to the magnet geometry under consideration (fig. 3), two broken curves are shown for magnets having constant angular widths of 20° and 17.6°. The 20° magnet curve, which coincides with the solid curve below 323 MeV, diverges abruptly from the solid curve between 323 and 360 MeV where the "bend" occurs (cf. table 1). Furthermore, the 17.6° magnet curve falls to a value of $\nu_z = 0.92$ at 600 MeV which is 13% lower than the value found in table 1 at this energy; since the equilibrium orbits are identical for these two magnet geometries at 600 MeV, this result clearly demonstrates the significant effect of $(\mathrm{d}f/\mathrm{d}r) < 0$. The dashed curve (labelled "A") in fig. 5 was obtained from the $[(1/N) \to 0]$-approximation formula: $\nu_z = [(1/f) - \gamma^2]^{\frac{1}{2}}$ using the f values for the magnet under consideration (fig. 3); as can be seen, this simple formula is reasonably accurate only where f is constant. The $[(1/N) \to 0]$-approximation formula implies that when $(\mathrm{d}f/\mathrm{d}r) < 0$, the resultant additional edge focusing is completely cancelled by the added defocusing produced within the magnet [cf. eq. (12)]; however, the results of fig. 5 show that this cancellation is quite imperfect for the case considered here. It should be noted that the value of $(\mathrm{d}f/\mathrm{d}r)$ has a relatively insignificant effect on the value of ν_x.

Since the results obtained from the Spyring Code are based on the restrictive assumptions of the hard-edge approximation discussed in sec. 1, these results should be at least partially discounted when applied to real magnets. When, for example, the magnet profile of the SIN (Zurich) cyclotron was inserted, the Spyring Code yielded $\nu_z = 1.40$ to 1.21 over the energy range from 80 to 550 MeV, whereas the actual values are $\nu_z = 0.94$ to 0.75 for this energy range[7]). Such poor agreement should not be surprising, however, since the isogauss contour lines for the SIN magnet do not match closely enough those required for the validity of the hard-edge approximation.

For a given average field value and a given maximum field value, a hard-edge magnet will produce the greatest vertical focusing. For example, the following simple "soft-edge" field:

$$B = B_0(1 + \cos N\theta), \tag{15}$$

yields $\nu_z \approx 0.7$ at $E = 0$. A hard-edge magnet with the same average field (B_0) and the same maximum field ($2B_0$) would have a constant magnet fraction $f = 0.5$, and in this case, a value of $\nu_z \approx 1.0$ would be obtained for $E = 0$. For those cyclotrons where a hard-edge magnet design is considered both desirable and feasible, the Spyring Code provides the means for investigating very quickly the orbit properties of a wide variety of possible magnet geometries.

I wish to acknowledge my indebtedness to D. A. Johnson for expertly performing all the computer work, including the programming.

References

1) A. Roberts and F. Salzman, Report No. At(30-1)-875 (University of Rochester, Aug. 1956) unpublished.
2) G. Schatz, Nucl. Instr. and Meth. **72** (1969) 29; see also, E. M. Moroz and M. S. Rabinovich, Proc. 1956 CERN Symp., vol. I (CERN, Geneva, 1956) p. 547.
3) M. M. Gordon, Ann. Phys. **50** (1968) 571.
4) K. Symon, D. Kerst, L. Jones, L. Laslett and K. Terwilliger, Phys. Rev. **103** (1956) 1837.
5) An outline of this program and a Fortran listing can be obtained by writing to the author.
6) E. D. Courant and H. S. Snyder, Ann. Phys. **3** (1958) 1.
7) W. Joho and H. Braun, ETH Report (Zurich, April 1966); W. Joho, SIN Report TM-11-07 (Zurich, Febr. 1970) unpublished.

Reprinted from THE PHYSICAL REVIEW C, Vol. 1, No. 3, 1118–1125, March 1970
Printed in U. S. A.

Level Structure in ^{145}Eu†

E. NEWMAN, K. S. TOTH, R. L. AUBLE, R. M. GAEDKE,* AND M. F. ROCHE‡
Oak Ridge National Laboratory, Oak Ridge, Tennessee 37830
AND
B. H. WILDENTHAL
Michigan State University, East Lansing, Michigan 48823
(Received 31 October 1969)

Levels in ^{145}Eu were investigated by the ^{144}Sm(^{3}He, d) reaction and by the decay of 25-min ^{145}Gd. At the ^{3}He energy used, i.e., 40.33 MeV, the angular distributions for the stripping reaction were found to be highly structured. This fact permitted reliable assignments of transferred orbital angular momenta to the residual levels. Singles γ-ray spectra for the decay of ^{145}Gd were measured with a 20-cm^3 Ge(Li) detector. The two sets of experimental data were then used to propose the following sequence of ^{145}Eu levels: 0 ($\frac{5}{2}^+$), 330.1 ($\frac{7}{2}^+$), 716 ($^-\frac{1}{2}$), 808.4 ($\frac{1}{2}^+$), 1041.9 ($\frac{3}{2}^+$), 1599.9 ($\frac{7}{2}^+$), 1757.9 ($\frac{3}{2}^+$), 1844.7 ($\frac{3}{2}$, $\frac{5}{2}^+$), 1880.6 ($\frac{1}{2}$, $\frac{3}{2}^+$), 2112.0 ($\frac{3}{2}$, $\frac{5}{2}^+$), and a ($\frac{1}{2}^+$), ($\frac{3}{2}$, $\frac{5}{2}^+$) doublet at ~2480 keV. The salient features of this level scheme are that (1) the (^{3}He, d) reaction predominantly populates the first five energy levels, and (2) the decay from ^{145}Gd ($\frac{1}{2}^+$) proceeds mainly to the levels at 1757.9 and 1880.6 keV and not to the single-particle states at 808.4 and 1041.9 keV. The present results were compared with experimental systematics available for $N=82$ isotones and with the implications of a recent shell-model calculation for nuclei in this region.

I. INTRODUCTION

THE nuclei with a closed shell of 82 neutrons are of particular interest since their low-lying level structure should arise mainly from proton excitations. The assumption of a doubly magic $N=82$, $Z=50$ core for these nuclei makes possible a variety of detailed microscopic calculations of the properties of their energy levels.[1,2] In the present study, levels in ^{145}Eu were investigated by the ^{144}Sm(^{3}He, d) reaction and by the decay of 25-min ^{145}Gd. The results were then compared with experimental systematics available for $N=82$ isotones and with the implications of a recent shell-model calculation[3] for nuclei in the same region.

II. γ RAYS IN ^{145}Gd DECAY

A radioactive source that contained ^{145}Gd was produced by bombarding 5 mg of Sm_2O_3 (enriched in ^{144}Sm to 95.1%) with helium ions accelerated in the ORIC. The bombarding energy (~45 MeV) was selected so as to correspond to the peak of the (α, $3n$) excitation function. Since the highly enriched samarium oxide powder was spread over a 2-cm^2 area, ^{145}Gd was the main rare-earth product. Chemical separations were not made.

γ-ray spectra were measured with a 20-cm^3 coaxial Ge(Li) detector connected via a field-effect-transistor preamplifier and an amplifier to a 1600-channel analyzer. Measurements were begun within 5 min after the end of bombardment. The relative photopeak efficiency of the detector system was determined prior to the spectral measurements with the use of standard ^{182}Ta, ^{207}Bi, and ^{226}Ra sources.

A portion of the γ-ray spectra (0.71–1.89 MeV) measured during the first hour of decay time is shown in Fig. 1. All peaks that are identified by energy only are assigned to ^{145}Gd decay. Note that the 721-keV transition in ^{145}Gd due to the 80-sec isomeric state[4] was also observed. This peak, prominent during the first few minutes of counting, was later overwhelmed by Compton distributions due to the higher-energy γ rays seen in Fig. 1. In Fig. 2, we display another spectrum taken during the second hour of counting with a higher amplifier gain. This spectrum shows the doublets at ~950 and ~1070 keV partially resolved. The 894.1-keV γ ray due to the decay[5] of the daughter nuclide ^{145}Eu (5.9 day) is more intense in Fig. 2 than in Fig. 1.

Table I summarizes the γ-ray data for ^{145}Gd. Transition energies are based on the energies of γ rays observed in the standard sources listed above and on the energies of the annihilation radiation and the 894.1-keV transition in ^{145}Sm. The energy values listed in Table I are estimated to be accurate to within ±1 keV. Relative intensities are based on a value of 100 for the 1757.9-keV γ-ray intensity. The absolute intensities given in column 3 were determined by assuming no direct decay to the ^{145}Eu ground state and by taking the sum of intensities for all ground-state transitions in ^{145}Eu to be equal to 100%. (See Sec. IV for the discussion of

† Research sponsored by the U.S. Atomic Energy Commission under contract with Union Carbide Corporation.
* Present address: Trinity University, San Antonio, Tex.
‡ Present address: Argonne National Laboratory, Argonne, Ill.
[1] R. J. Lombard, Nucl. Phys. **A117**, 365 (1968); M. Rho, *ibid.* **65**, 497 (1965); L. S. Kisslinger and R. A. Sorensen, Kgl. Danke Videnskab. Selskab, Mat.-Phys. Medd. **32**, No. 9 (1960).
[2] K. S. Toth, E. Newman, B. H. Wildenthal, R. L. Auble, R. M. Gaedke, and M. F. Roche, in *International Conference on Radioactivity in Nuclear Spectroscopy: Techniques and Applications* (Gordon and Breach Science Publishers, Inc., New York, to be published).
[3] B. H. Wildenthal, Phys. Rev. Letters **22**, 1118 (1969).
[4] G. Jansen, H. Morinaga, and C. Signorini, Nucl. Phys. **A128**, 247 (1969).
[5] I. Adam, K. S. Toth, and M. F. Roche, Nucl. Phys. **A121**, 289 (1968).

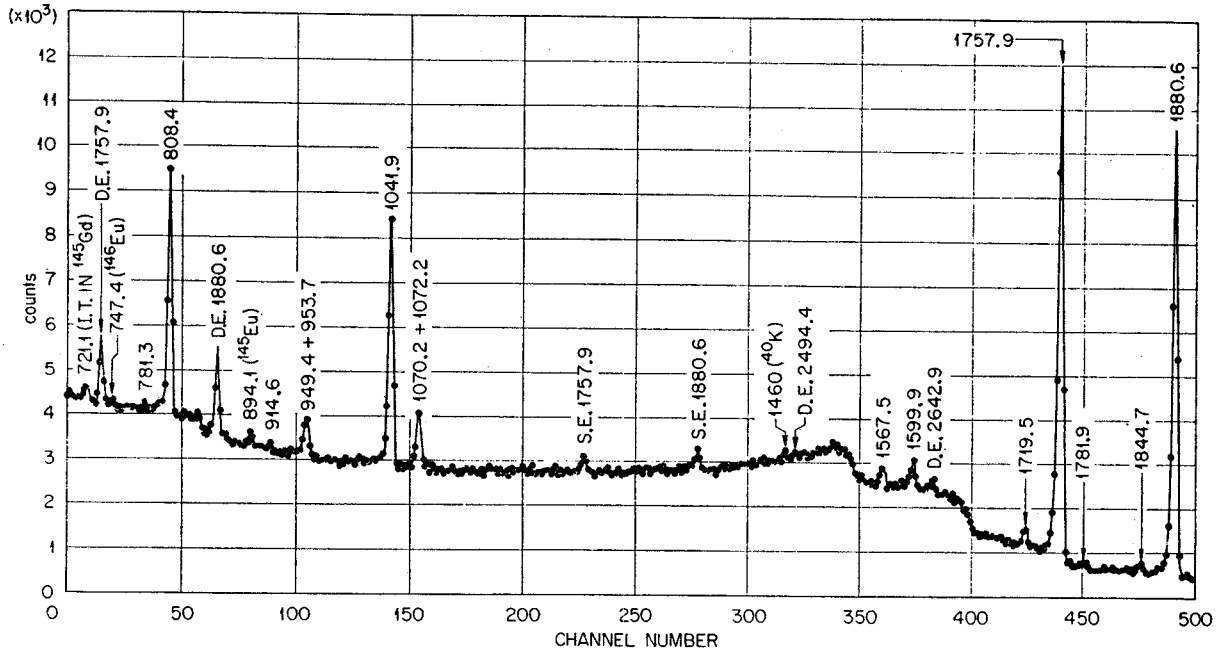

FIG 1. Portion of the ^{145}Gd γ-ray spectrum (0.71–1.89 MeV) measured during the first hour of decay. Peaks identified by energy only are assigned to ^{145}Gd decay.

the ^{145}Gd decay scheme.) The assumption of no direct decay to the ground state was based on the following evidence: Within the experimental uncertainties, the 25-min component of the annihilation radiation was found to be twice as intense as the 1757.9-keV γ ray. This means that the ^{145}Gd positron intensity on our relative-intensity basis is $\sim$100. Grover[6] measured the intensity ratio $[\beta^+/(K \text{ x rays})]$ to be 0.6, which gives a relative K-x-ray intensity of $\sim$167. The intensity sum ($\beta^+ + K$ x ray) of 267 is, within error limits, equal to 270, the relative-intensity sum for transitions that proceed to the ^{145}Eu ground state. It would appear, therefore, that there is little or no direct ^{145}Gd decay to the ground state.

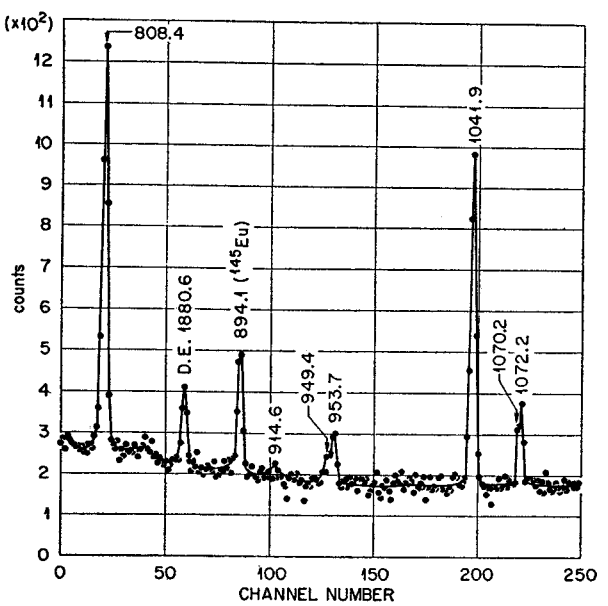

FIG. 2. Portion of the ^{145}Gd γ-ray spectrum (0.80–1.08 MeV) taken with a higher amplifier gain during the second hour of decay. Peaks identified by energy only are assigned to ^{145}Gd decay.

III. PROTON LEVELS IN ^{145}Eu

The single-particle levels in ^{145}Eu were investigated by using the (^{3}He, d) proton stripping reaction on a target of ^{144}Sm. At the incident energy used (40.33 MeV), the differential cross sections are markedly oscillatory with unique angular patterns,[7] thus permitting reliable assignment of the transferred orbital angular momentum to the various residual levels. From these results, a knowledge of the sequence of shell-model orbitals in the region, the appropriate distorted-wave (DW) calculations, the spins, and the configurations of many of the observed levels could be deduced.

The ^{144}Sm target was an enriched (94.5%) rolled metallic foil of 460-μg/cm^2 areal density. The deuteron spectra were recorded with photographic emulsions located in the focal plane of the broad-range magnetic spectrograph. The energy resolution was about 35 keV, attributable mainly to target thickness. A deuteron

[6] J. R. Grover, Phys. Rev. **116**, 406 (1959).
[7] B. H. Wildenthal, E. Newman, and R. L. Auble, Phys. Letters **27B**, 628 (1968).

TABLE I. γ rays in ^{145}Eu.

Energy (keV)	Relative intensity[a]	Absolute intensity[b]
330.1	7.9	2.9
781.3	0.8	0.3
808.4	25.5	9.4
914.6	0.7	0.3
949.4	1.5	0.5
953.7[c]	3.0	1.1
1041.9	27.3	10.1
1070.2	2.5	0.9
1072.2	4.5	1.7
1567.5	2.6	1.0
1599.9	5.0	1.8
1719.5[c]	3.0	1.1
1757.9	100	37.0
1781.9	1.8	0.7
1844.7	1.2	0.4
1880.6	98	36.3
2202.8[c]	1.8	0.7
2494.3	3.9	1.4
2642.9[c]	6.6	2.4
2663.2	0.9	0.3
2674.0	0.6	0.2
2837.7	2.5	0.9

[a] Based on a value of 100 for the 1757.9-keV γ-ray intensity.
[b] Calculated by assuming no direct decay to the ^{145}Eu ground state.
[c] Not placed in decay scheme.

spectrum at 21° (L) is shown in Fig. 3. The peaks are identified by the energies obtained from the spectrograph calibration, and the errors for these determinations are also indicated. Differential cross sections for the various states were measured between 5° and 36° in the laboratory system. The absolute cross sections are based on the ^{3}He elastic scattering yield between 36° and 40° (L) as measured in the spectrograph. The absolute cross sections are then determined by assuming that the observed elastic scattering cross section is equal to that calculated by the optical model. The parameters used in the optical-model calculation are based on those found by Gibson *et al.*[8] It is believed that the absolute cross sections obtained in this way are accurate to better than 20%. The angular distributions are presented in Fig. 4. The errors shown are the statistical uncertainty only and do not reflect the absolute uncertainty discussed above. The curves associated with each distribution are the results of a DW calculation (JULIE) assuming the orbital angular momentum transfer noted on the figure. The curves were calculated using the separation-energy prescription. The bound-state wave function was calculated using a nuclear radius parameter $r_0 = 1.24$ F, a spin-orbit term with a radius parameter[9] $r_{so} = 1.14$ F, and strength $\lambda = 20$. The distorted waves in the entrance and exit channels were calculated from the parameters of Ref. 8 and from an optical-model analysis of 34.4-MeV deuteron elastic scattering,[10] respectively. The curve labeled as the sum of two values of the transferred angular momentum was arrived at by summing, incoherently, the appropriately weighted single-l-transfer calculations. The group requiring this summation was assumed to arise from the excitation of two levels whose spacing was less than the experimental resolution.

In Table II, we present the spectroscopic information derived from the analysis discussed above. Although the orbital angular momentum for a level is determined by experiment, the total angular momentum is not. For the present study, this, in principle, leads to uncertainty in allocating the observed $l=2$ levels between $J=\frac{3}{2}$ and $\frac{5}{2}$. In fact, however, the J assignment can be made with a reasonable degree of certainty from a knowledge of the sequence of shell-model orbitals. Since the ground state is $\frac{5}{2}^+$, the strongly excited $l=2$ level at 1042 keV is probably $\frac{3}{2}^+$ since a $\frac{5}{2}^+$ assignment would imply a total $d_{5/2}$ spectroscopic factor in excess of unity and an empty $d_{5/2}$ orbital is untenable for the wave function of the ^{144}Sm ground state.[7] The $l=2$ levels above 1042 keV have been assumed to be $\frac{3}{2}^+$ for the purpose of calculating spectroscopic factors. It is seen that the first five observed levels contain the major portion of the single-particle strength for the single-particle orbits that are being filled between $Z=50$ and $Z=82$.

TABLE II. Level parameters derived from the ^{144}Sm(^{3}He, d)^{145}Eu reaction.

^{145}Eu level (keV)	l transfer	J^π	C^2S
g.s.	2	$5/2^+$	0.33
329	4	$7/2^+$	0.17
716	5	$11/2^-$	0.82
809	0	$1/2^+$	0.98
1042	2	$3/2^+$	1.01
1599	4	$7/2^+$	0.02
1757	2	$3/2^+$	0.02
1843	2	$3/2^+$	0.10
2108	2	$3/2^+$	0.04
2480[a]	2	$3/2^+$	0.04
	0	$1/2^+$	0.02

[a] Unresolved doublet.

[8] E. F. Gibson, B. W. Ridley, J. J. Kraushaar, M. E. Rickey, and R. H. Bassel, Phys. Rev. **155**, 1194 (1967).

[9] E. Newman and B. H. Wildenthal, Bull. Am. Phys. Soc. **13**, 1463 (1968).

[10] E. Newman, L. C. Becker, B. M. Preedom, and J. C. Hiebert, Nucl. Phys. **A100**, 225 (1967).

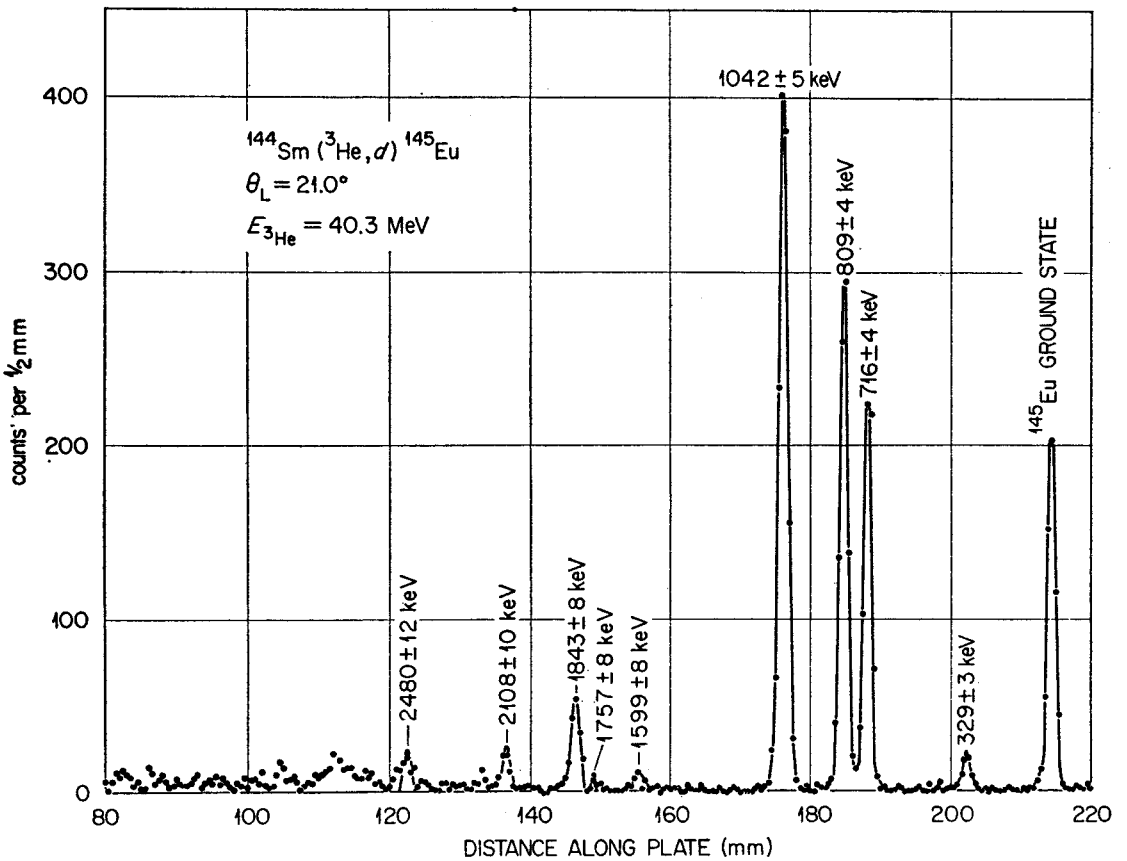

FIG. 3. Deuteron spectrum recorded at 21° (L) from the ^{144}Sm(^{3}He, d)^{145}Eu reaction.

IV. DISCUSSION

The ^{145}Eu level scheme based on the two sets of data is shown in Fig. 5. Note that the 1880.6-keV state was not excited by the (^{3}He, d) reaction, while the high-spin $\frac{11}{2}^-$ 716-keV state was not observed in the decay study. The 2494.3-keV state shown in the decay scheme is proposed as being the $\frac{1}{2}^+$ member of the doublet observed in the stripping reaction at ~2480 keV. Levels above 2.5 MeV are tentatively proposed on the basis of sums and differences of transition energies. Previous information on the low-lying states of ^{145}Eu has been summarized in a recent nuclear data sheets compilation[11] that showed only excited states at 330, 809, 1760, and 1882 keV.

Because of uncertainties in the measured photon intensities and the fact that not all of the observed γ rays were included in the decay scheme, percentages of direct decay were determined only for the states most strongly populated in decay, i.e., those at 808.4, 1041.9, 1757.9, and 1880.6 keV. Logft values based on these decay rates were calculated by using a decay energy[6] of 5.3 MeV and the curves of Moszkowski[12] in a slightly modified version.[13]

The salient features of the experimentally determined ^{145}Eu level scheme are (1) the (^{3}He, d) reaction predominantly populates the first five energy levels, (2) the level density between 1 and 2 MeV is much lower than for the lighter odd-mass $N=82$ nuclei (see, e.g., Refs. 14 and 15), (3) the $\frac{5}{2}^+$ ground state is not appreciably fed by the direct decay of ^{145}Gd, and (4) the ^{145}Gd decay, in contrast to the stripping results, populates mainly the levels at 1757.9 and 1880.6 keV.

Let us turn our attention first to items 1 and 2. The (^{3}He, d) results for the first five levels of ^{145}Eu are consistent with those of similar experiments on lighter $N=82$ nuclei,[7] and the entire set of phenomena can be understood in the following theoretical framework: The 82 neutrons, together with 50 of the protons, form

[11] L. W. Chiao and M. J. Martin, in *Nuclear Data Sheets*, compiled by K. Way *et al.* (Printing and Publishing Office, National Academy of Sciences—National Research Council, Washington, D.C. 20025, 1967), NRC B2-1-81 (for $A=145$).

[12] S. Moszkowski, Phys. Rev. **82**, 35 (1951).

[13] G. J. Nijgh, A. H. Wapstra, and R. Van Lieshout, in *Nuclear Spectroscopy Tables* (North-Holland Publishing Co., Amsterdam, 1959), Chap. 5, Sec. 4, pp. 58–65.

[14] D. DeFrenne, K. Heyde, L. Dorikens-Vanpraet, M. Dorikens, and J. Demuynck, Nucl. Phys. **A110**, 273 (1968).

[15] D. B. Beery, W. H. Kelly, and W. C. McHarris, Phys. Rev. **171**, 1284 (1968).

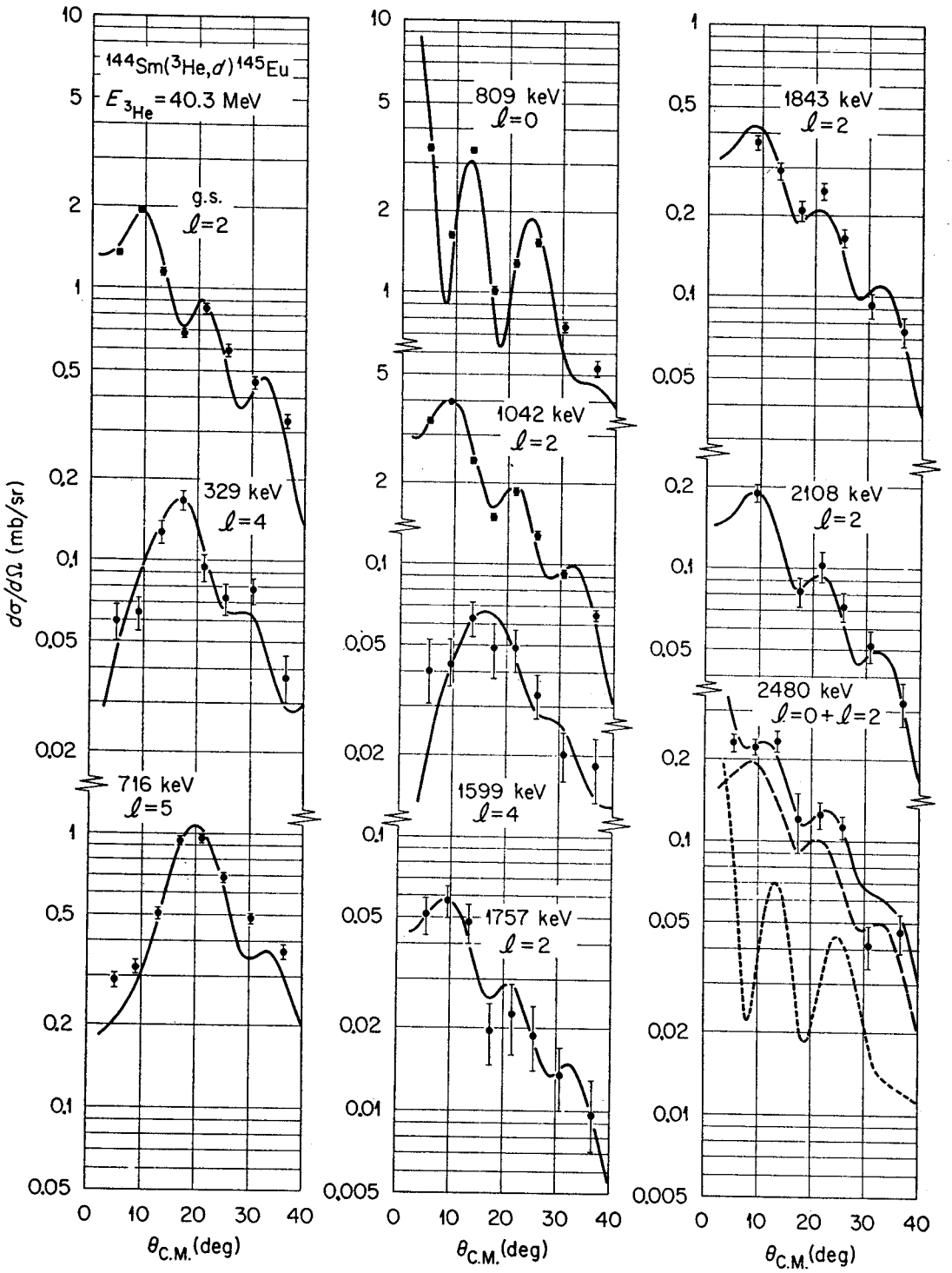

FIG. 4. Differential cross sections for the various states populated in the ^{144}Sm(^{3}He, d)^{145}Eu reaction. Curves associated with each angular distribution are the result of a DW calculation assuming the orbital angular momentum transfer shown in the figure.

major closed shells and can be neglected in considering the structural details of the low-lying energy levels. The protons in excess of 50 occupy the "*sdgh*" major shell, composed of five single-particle orbits, of which the $1g_{7/2}$ and $2d_{5/2}$ energies lie significantly lower than do those of the $1h_{11/2}$, $2d_{3/2}$, and $3s_{1/2}$ orbits. Thus, the active protons in the ground states of even $N=82$ nuclei ($Z=52$–64) tend to occupy $1g_{7/2}$ and $2d_{5/2}$ orbits. Proton stripping reactions on these targets do show $l=2$ and $l=4$ transitions to low-lying states of $J^\pi=\frac{5}{2}^+$ and $\frac{7}{2}^+$.

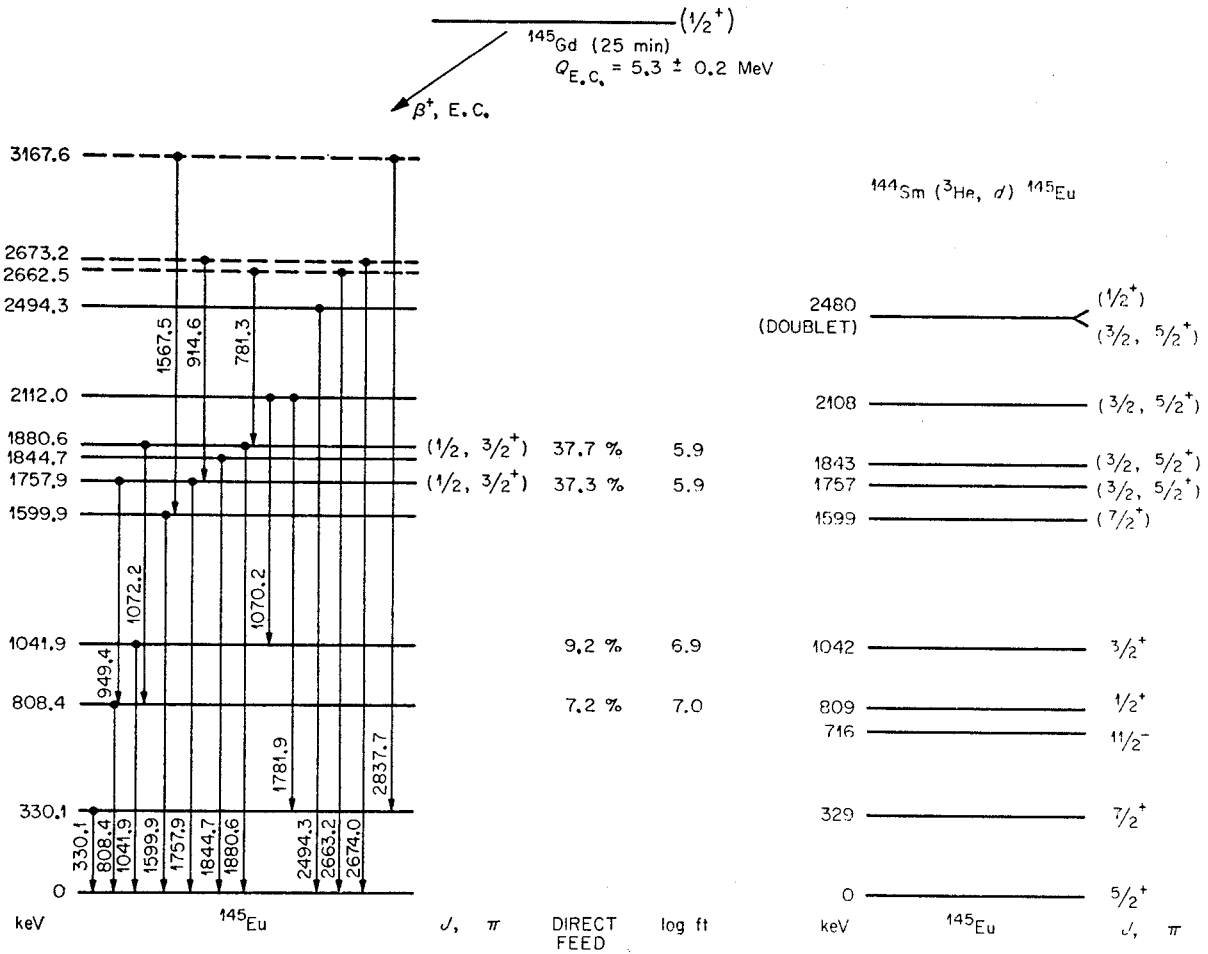

FIG. 5. Europium-145 level scheme based on experimental data obtained from the study of (1) the decay of ^{145}Gd and (2) the ^{144}Sm(^{3}He, d)^{145}Eu reaction.

Similarly, $l=5$, 0, and 2 transitions populate higher excited states of $J^\pi=\frac{11}{2}^-$, $\frac{1}{2}^+$, and $\frac{3}{2}^+$, respectively. The spectroscopic factors for the transitions to the two lowest states should be reduced in proportion to the occupancy of these orbits in the target ground state, while the transitions to the higher three states should proceed with almost the maximum limit of intensity, reflecting the vacancy of these orbits in the target ground state. The systematics of the single-particle centroids in the odd-mass isotones determined via (^{3}He, d) reaction experiments are presented in Fig. 6. These states can be understood as the coupling of the unpaired proton in one of the five "*sdgh*" orbits with the 0^+ ground state of the target nucleus. It is clear from Fig. 6 that the results for ^{145}Eu follow the trends established in the lighter nuclei.

The details of Fig. 6 agree with the results of a shell-model calculation[3] based on the ideas of the preceding paragraph. The basis space of the model encompasses four classes of configurations for the Z' active protons (those in excess of 50). For the odd-A nuclei these are type (1), in which all particles occupy the $1g_{7/2}$ and $2d_{5/2}$ subshell, and all but one are $J=0$ coupled pairs; type (2), in which one particle occupies either the $3s_{1/2}$ or $2d_{3/2}$ orbit and is coupled to a completely paired mixture of $d_{5/2}$ and $g_{7/2}$ protons; type (3), where a $g_{7/2}$ or $d_{5/2}$ particle is coupled to a mixture of $d_{5/2}$ and $g_{7/2}$ particles that include at least one broken pair; and type (4), involving *both* at least one broken pair in the $\frac{7}{2}-\frac{5}{2}$ space *and* the elevation of a single particle into the $\frac{1}{2}-\frac{3}{2}$ space. Thus, the $g_{7/2}$ and $d_{5/2}$ orbits are treated as a subshell, and the model considers all states in that subshell together with one-particle excitations into the higher two positive-parity orbits. Two-particle excitations into these higher orbits have, for the present, been excluded. This appears to be a good approximation for most of the $N=82$ chain. However, such configurations may be expected to become important as the $g_{7/2}$–$d_{5/2}$ space closes out, as it does for the nuclei of present interest, ^{144}Sm, ^{145}Eu, and ^{145}Gd. Excitations into the $1h_{11/2}$ orbit have not yet been included in the calculation. There seems no reason, however, not to extrapolate the model systematics for the positive-parity orbits to help understand the behavior of the $1h_{11/2}$ single-particle state.

In the lighter odd-mass $N=82$ isotones, as observed

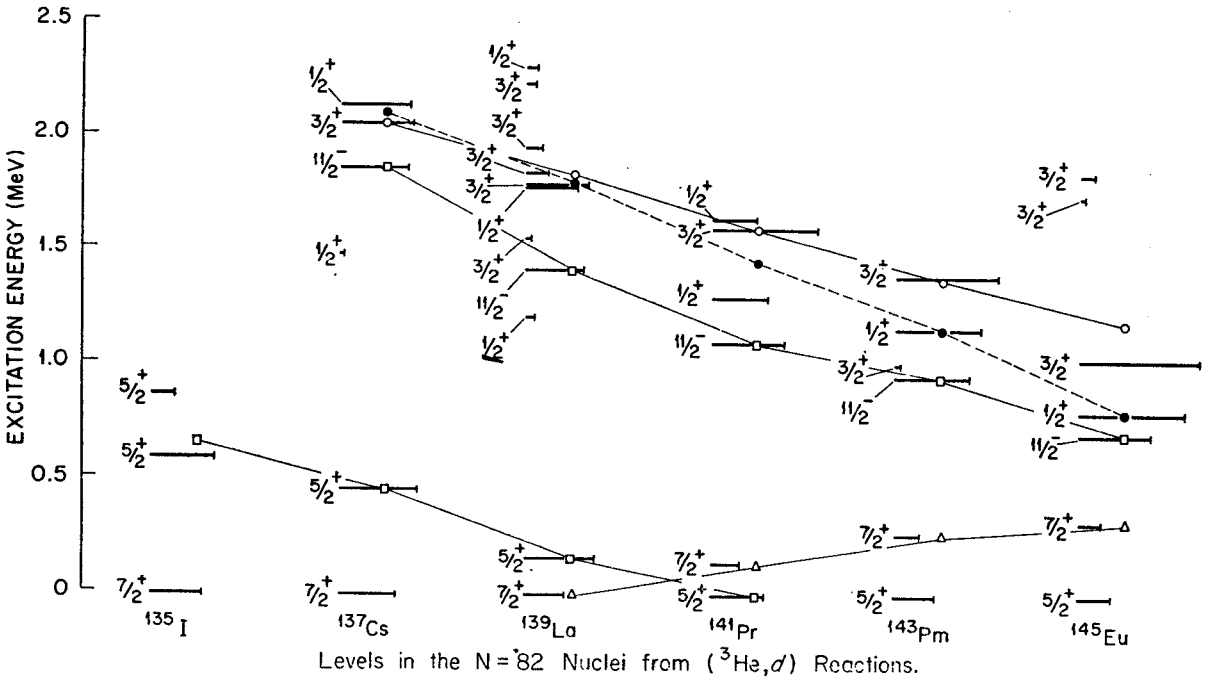

FIG. 6. Systematics of the single-particle centroids in odd-mass $N=82$ isotones as determined via (^{3}He, d) reactions.

experimentally, the shell-model calculation just described predicts the occurrence of many levels between 1- and 2-MeV excitation. It indicates that their wave functions have the character of either type (2) or type (3). States of type (4) lie above 2 MeV. That is to say, states between 1 and 2 MeV involve *either* elevation to a higher single-particle orbit *or* the breaking of a $J=0$ pair in the $g_{7/2}$–$d_{5/2}$ space.

In the model space just described, ^{145}Eu is essentially a "one-hole" nucleus. Specifically, it is no longer possible to construct type-(3) states. Single-particle states of type (2) have, in fact, moved below 1-MeV excitation (see the trend in Fig. 6). Thus, the model spectrum between 1 and 2 MeV becomes vacant. The model spectrum of ^{145}Eu is compared to our composite experimental spectrum in Fig 7. We note that the measured and predicted energies of the first four positive-parity states are in good agreement and that the stripping reaction labels them as the single-particle states. Between 1 and 2 MeV, the experimental level density is indeed reduced in comparison to lighter nuclei. There is, however, a multiplet of levels between 1.6 and 1.9 MeV that seems too far removed from the closest model states at ~2.2 MeV to justify it being associated with them. The higher model states arise from the type-(4) configurations previously mentioned. Thus, the model results appear successful in accounting for the simple "single-particle" states and the general decrease in the density of the higher excited states. There is, however, experimental evidence for the existence of states below 2 MeV whose origins appear to lie outside the model basis.

The third important feature of the experimental results, the absence of observable direct decay to the ^{145}Eu ($\frac{5}{2}^+$) ground state, is at variance with what occurs[13,14] in the ostensibly similar decays of ^{141}Nd ($\frac{3}{2}^+$) and ^{143}Sm ($\frac{3}{2}^+$) to ^{141}Pr and ^{143}Pm, respectively. In each of the latter cases, the transition to the $\frac{5}{2}^+$ ground state of the residual nucleus dominates the decay with a logft value of ~5. The nature of these decays is easily interpreted. The decaying state can be pictured as a $2d_{3/2}$ neutron hole. The active protons in the state, arranged in $J=0$ coupled pairs, primarily occupy the g-d subshell; but, as experiment shows[7] and BCS theory implies, small admixtures of $J=0$ proton pairs in the $1h_{11/2}$, $2d_{3/2}$, and $3s_{1/2}$ orbits are also present. The β decay could then proceed via an allowed transition $\pi d_{5/2} \rightarrow \nu d_{3/2}$ leaving a $d_{5/2}$ proton coupled to the remaining proton core. For the case of ^{145}Eu, on the other hand, the $\frac{1}{2}^+$ and $\frac{3}{2}^+$ states at 808.4 and 1041.9 keV are significantly fed in the direct decay of ^{145}Gd but not the $\frac{5}{2}^+$ ground and the $\frac{7}{2}^+$ first excited states. Therefore, on the basis of β-decay selection rules, it appears that the spin of the parent cannot be $\geq\frac{3}{2}^+$. Thus, a spin of $\frac{1}{2}^+$ is the only assignment compatible with the experimental data.

The simplest representation of the ^{145}Gd ground state, under the assumption of $J=\frac{1}{2}^+$, would then be a $3s_{1/2}$ neutron hole coupled to a 14-proton state in which the $g_{7/2}$ and $d_{5/2}$ orbits are predominantly occupied. Now, however, insofar as the β-decay process is concerned, the $d_{5/2}$ protons are essentially inactivated because of the $\Delta J=2$ barrier. The transition must, therefore, proceed via the decay of one of a pair of $s_{1/2}$ (or with less probability $d_{3/2}$) protons that are mixed into the domi-

nant $g_{7/2}$–$d_{5/2}$ proton structure. The transition rate would then be expected to be slower than for the $A=141$ and $A=143$ cases. This retardation is indeed observed.

The proposed assignment of $J^\pi=\frac{1}{2}^+$ to the ground state of ^{145}Gd does not resolve all of the problems posed by the experimental decay data. As noted in Fig. 5, the levels at 1757.9 and 1880.6 keV are populated with significantly more intensity than are the single-particle levels at 808.4 and 1041.9 keV. Since the 1757.9- and 1880.6-keV levels are reached via the β^+ decay, their spins are $\frac{1}{2}$ or $\frac{3}{2}$ with our assumption of $\frac{1}{2}^+$ for the ^{145}Gd ground state. The 1757.9-keV level is also characterized by an $l=2$ (^{3}He, d) angular distribution; it must have $J^\pi=\frac{3}{2}^+$. It should be recalled that the states between 1600 and 2000 keV were those that apparently could not be accounted for by the shell-model calculation.

We emphasize that it is the ^{145}Eu single-particle states that are expected to be fed most strongly by decay from the ^{145}Gd ground state. It is generally assumed that the ground states of the even-mass $N=82$ isotones with Z and $Z+2$ protons are related to each other by the simple addition of a zero-coupled pair of protons in the "*sdgh*" space. The single-particle states of the $Z+1$ system would then be reached either by adding a proton to the Z proton ground state or by annihilating one from the $Z+2$ ground state. For the lighter $N=82$ nuclei, this assumption accounts for the observed phenomena. Failure of the ^{145}Gd decay (i.e., the annihilation of a proton in the $Z'=14$ ground state) to populate the same levels a does the (^{3}He, d) reaction (i.e., the addition of a proton to the $Z'=12$ ground state) strongly suggests that the $Z'=14$ ground state is not related to the $Z'=12$ ground state in the same fashion that the $Z'=12$ ground state is related to that of $Z'=10$, etc. The $Z'=14$ ground state seems to have more overlap with the active core of the ^{145}Eu states at 1600–2000-keV excitation. We have suggested that these states in ^{145}Eu involve the occupation of the $h_{11/2}$, $d_{3/2}$, and $s_{1/2}$ orbits to a qualitatively greater extent than do the lower known levels of ^{145}Eu. Thus, one is led to speculate that the lowest-energy configuration of 14 active protons also involves this qualitatively greater amount of excitation into these orbits than do the ground and low excited states of the lighter numbers of the chain.

To go beyond these qualitative speculations, it will be necessary to have more experimental information, particularly about the $Z'=14$ system. In addition, detailed theoretical studies of the behavior in the vicinity of the transition from the $1g_{7/2}$–$2d_{5/2}$ region to the $1h_{11/2}$–$3s_{1/2}$ region is also highly desirable.

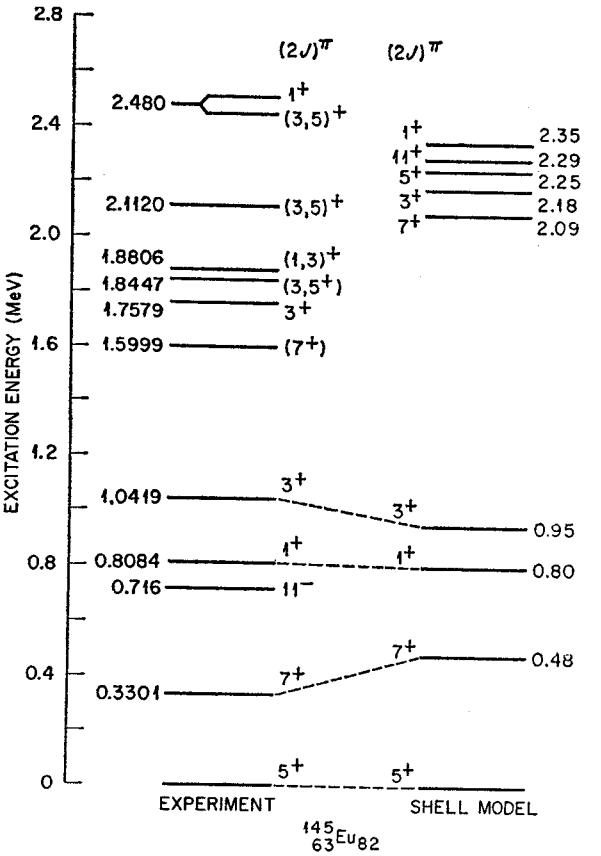

FIG. 7. Composite experimental level scheme for ^{145}Eu compared with the results of the shell-model calculation.

ACKNOWLEDGMENTS

Two of us (B.H.W. and R.L.A.) wish to thank the Oak Ridge Associated Universities for the support of an Atomic Energy Commission Special Postdoctoral Fellowship. The authors wish to thank Ruby Shelton for scanning the nuclear emulsions and the cyclotron crew for their help in performing the bombardments.

EFFECT OF CORE POLARIZATION IN THE REACTION ^{209}Bi$(p,p')^{209}$Bi(1.61 MeV) AT 39.5 MeV*

W. Benenson, S. M. Austin,† and P. J. Locard‡
Cyclotron Laboratory and Physics Department, Michigan State University, East Lansing, Michigan 48823

and

F. Petrovich and J. R. Borysowicz
Physics Department, Michigan State University, East Lansing, Michigan 48823

and

H. McManus§
Theoretical Physics Department, Oxford University, Oxford, England
(Received 1 December 1969)

The cross section for the $1h_{9/2}$-$1i_{13/2}$ single-proton transition in the reaction ^{209}Bi$(p,p')^{209}$Bi* at 39.5 MeV has been measured. It is shown that most of the observed cross section is due to admixtures of the state formed by coupling the valence proton of ^{209}Bi to the highly collective 3^- state of ^{208}Pb at 2.614 MeV. An estimate of core polarization, based on the work of Kuo and Brown, grossly underestimates the $L=3$ component of the cross section.

In ^{209}Bi there are two low-lying $\frac{13}{2}^+$ states of very different character. The 1.609-MeV level lies near the expected position of a single proton outside a closed ^{208}Pb core and shows up strongly in ^{208}Pb$(^3$He$,d)^{209}$Bi.[1] Some $(^3$He$,d)$ strength is observed in the $\frac{13}{2}^+$ state at 2.602 MeV. Both of these states decay to the ground state by strong $E3$ transitions.[2,3] In the simplest picture the ground state is a $1h_{9/2}$ proton outside a closed ^{208}Pb core, and the 1.609-MeV state is a $1i_{13/2}$ proton outside the same core, whereas the 2.602-MeV state is a member of a weak-coupling septet formed by coupling the $1h_{9/2}$ single particle to the strongly collective 3^- state of ^{208}Pb at 2.614 MeV. A perturbation calculation by Mottelson[4] has shown that the two $\frac{13}{2}^+$ states are mixed. The admixture of the 2.602-MeV state into the 1.609-MeV state is $\epsilon^2 = 4.8\times10^{-2}$. In this calculation the coupling matrix element was estimated from the γ decay of the 3^- state of ^{208}Pb. The mixing of the states accounts for the observed $(^3$He$,d)$ strengths.

In this Letter new experimental data on the 1.609-MeV, $\frac{13}{2}^+$ state in ^{209}Bi are presented. The differential cross section for the excitation of this level in the (p,p') reaction was obtained using 39.5-MeV protons from the Michigan State University cyclotron and a self-supporting Bi foil. The scattered particles were detected in a lithium-drifted germanium detector in a side-entry configuration. The energy resolution was typically about 50 keV overall, and the peak-to-valley ratio was over 2000 to 1. Figure 1, a spectrum obtained at 35°, illustrates the difficulties of seeing the relatively weak single-particle states, which are shown underlined.

Recent progress has been made in understanding the (p,p') reaction in terms of "realistic forces." The main features of the differential cross sections for several transitions in the reactions ^{12}C(p,p') and ^{40}Ca(p,p') at incident energies from 25 to 55 MeV can be reproduced in local distorted wave calculations using Kallio-Kolltveit (K-K) force[5] as the projectile-target interaction with an approximate treatment of antisymmetrization.[6,7] The K-K force is a good approximation to the central part of the shell-model reaction matrix. This same approach has been successful in describing the inelastic proton scattering from low-lying states in ^{50}Ti, ^{89}Y, and ^{90}Zr.[7,8] Core polarization, which is important in these transitions, has been estimated by including 2p-1h (two-particle, one-hole) or 3p-1h components, whichever is appropriate, in the target wave functions. These components are calculated using first-order perturbation theory, and only those states formed by coupling the valence nucleon to particle-hole excitations of the core with energies up to $2\hbar\omega$ are considered. This is essentially the approach first used by Horie and Arima to calculate effective charges.[9] The same picture is used by Kuo and Brown in their work on the bound state problem.[10]

Kuo has suggested[11] that the particle-hole treatment of core polarization may not be adequate when there is the possibility of contributions from highly collective phonons of the core. This appears to be the case for this transition. Because of this we calculate the cross section in two ways: (1) including only 2p-1h components

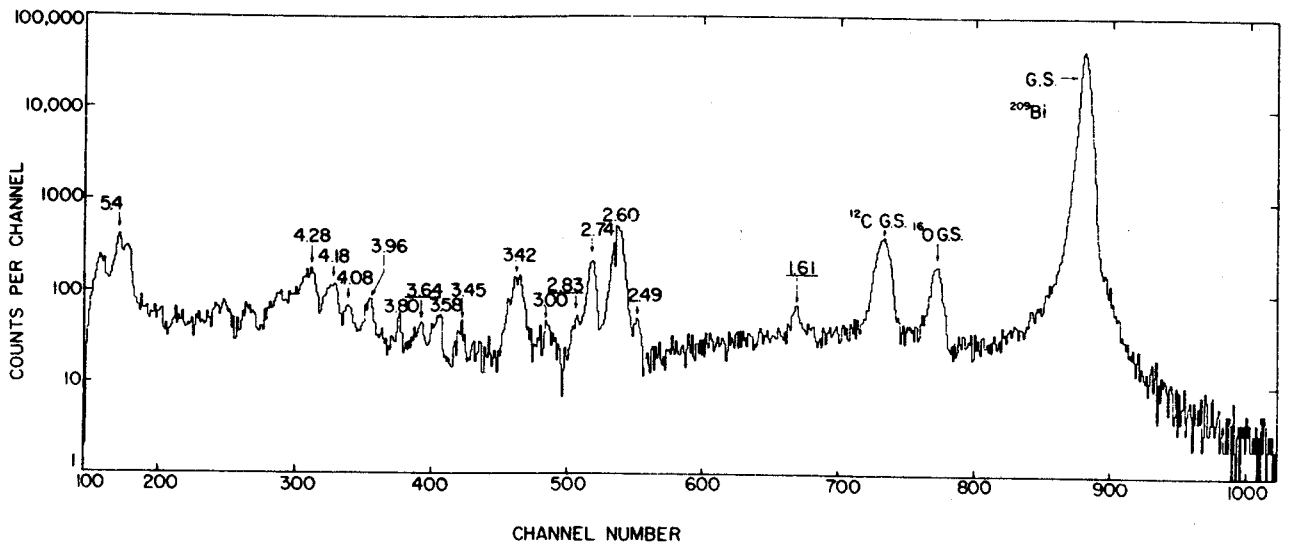

FIG. 1. Spectrum of protons from the reaction ^{209}Bi$(p,p')^{209}$Bi taken at 35° in the lab. The resolution is about 45 keV. The peaks shown underlined are single-particle states in ^{209}Bi.

in the wave functions, (2) replacing the components with p-h coupled to angular momentum $J_c = 3$ by components which contain the 3^- core state of ^{208}Pb. In the latter calculation we use the macroscopic vibrational model to describe the core. The procedure is essentially that described by Mottelson in Ref. 4. The calculation could have been kept completely microscopic by using the random-phase approximation vector of Gillet to describe the 3^- state in ^{208}Pb.[12]

The wave functions which contain only the 2p-1h admixtures will be designated Set I. They are defined as follows:

$$|jm\rangle' = |jm\rangle + \sum A_{j'}(j'(\mathrm{ph})J_c)|[j'(\mathrm{ph})J_c]jm\rangle, \quad (1)$$

where the sum is over j' and phJ_c and

$$A_{j'}(j'(\mathrm{ph})J_c) = -(\Delta E)^{-1}\langle[j'(\mathrm{ph})J_c]j|G|j\rangle. \quad (2)$$

Here $|jm\rangle$ specifies the state of the valence proton in the presence of a closed core. The quantity (ph)J_c refers to a particle-hole state of the core with angular momentum J_c and excitation energy ΔE. This is coupled to a valence proton in the state j' to give j. G denotes the coupling interaction which is taken to be the K-K force. Particle-hole pairs are formed from the shells shown in Table I. Harmonic-oscillator wave functions have been used, and the energy denominators were taken in part from experiment[13] and in part from the Nilsson scheme at zero deformation. The size parameter $\hbar\omega$ is 6.8 MeV.

The wave functions used in the second calculation will be designated Set II. They are the same as Set I except for the replacement

$$\sum_{\mathrm{ph}} A_j(j'(\mathrm{ph})J_c = 3)\,|[j'(\mathrm{ph})J_c = 3]jm\rangle \rightarrow B_j(j')|j' \otimes 3^-; jm\rangle, \quad (3)$$

$$B_j(j') = (E_j - E_{j'} - \hbar\omega_3)^{-1}\langle j' \otimes 3^-; j|V|j\rangle, \quad (4)$$

$$\langle j' \otimes 3^-; j|V|j\rangle \sim \langle k\rangle(\hbar\omega_3/2C_3)^{1/2}\langle j'\|Y_c\|j\rangle, \quad (5)$$

$$V = -k(r)\sum_{LM}\alpha_{LM}Y_{LM}(\hat{r}). \quad (6)$$

Equations (3)-(6) are the usual expressions encountered when the macroscopic vibrational model is used in the treatment of particle-vibrational coupling. The quantity $k(r) = RdU(r)/dr$, where $U(r)$ is the single-particle potential seen by the extra-core proton, R specifies the nuclear radius, $\langle k\rangle$ denotes a radial integral, $\hbar\omega_3$ is the ex-

Table I. Particle and hole orbitals used in microscopic calculation. The absence of total angular-momentum subscript indicates that both $j = l \pm \frac{1}{2}$ orbits are included.

Particles		Holes	
Protons	Neutrons	Protons	Neutrons
$1h_{9/2}$	$1i_{11/2}$	$1d$	$1f$
$2f$	$2g$	$2s$	$2p$
$3p$	$3d$	$1f$	$1g$
$1i$	$4s$	$2p$	$2d$
$2g$	$1j$	$1g$	$3s$
$3d$	$2h$	$2d$	$1h$
$4s$	$3f_{7/2}$	$3s$	$2f$
$1j_{15/2}$		$1h_{11/2}$	$3p$
$2h_{11/2}$			$1i_{13/2}$

citation energy of the 3^- phonon of ^{208}Pb, and C_3 gives a measure of the core stiffness to this lowest octupole vibration. Reference 4 gives $\langle k \rangle = 60$ MeV and $C_3 = 649$ MeV. Analyses of the reaction $^{208}\mathrm{Pb}(p, p')^{208}\mathrm{Pb}$ give $\beta_3 \sim 0.13$ for this state[14] which is the only state with a large value of β in ^{208}Pb. The relation $\beta_3 = 7^{1/2}(\hbar\omega_3/2C_3)^{1/2}$ implies $C_3 = 543$ MeV which is smaller than the value from Ref. 4 and corresponds to an admixture $\epsilon^2 = 5.5\times10^{-2}$ of the 2.602-MeV, $\frac{13}{2}^+$ state in the 1.609-MeV, $\frac{13}{2}^+$ state. The smaller value of C_3 was used in this work.

The cross section for this transition has 20 components each designated by (LSJ) referring to orbital, spin, and total angular momentum transfer. Details for calculating the cross section from the wave functions being considered in this work are given in Ref. 8. In this work, as a matter of convenience, we have used a pseudopotential for the projectile-target interaction which is known to give results consistent with those obtained using the K-K force and treating antisymmetrization approximately. The 2p-1h components of the cross section have been included only in the $S=0$ terms in the cross section because it is only in these components that they add coherently. In using wave function Set II the components of the wave functions defined by Eqs. (3)-(6) contribute only to the $(LSJ) = (303)$ component of the cross section. The remaining 19 components are the same in Sets I and II.

Figure 2 shows the total differential cross sections obtained with wave function Set I and Set II. The (303) components are also shown for both cases. The differential cross section (II) gives a good fit to the experimental data. The (303) (II) component is dominant at forward angles. The enhancement due to core polarization, i.e., ratio of integrated cross sections with and without core polarization, of (303) (II) is about 200. Because of this large enhancement the valence contribution to (303) (II) is small. Considering only this component and neglecting the valence contribution, the data place an upper limit on $\epsilon^2 = 10^{-1}$. Wave function Set II gives $B(E3) = 2.4 \times 10^{-2} e^2$ b^3 which is slightly larger than the experimental values $(1.3\text{-}2.0)\times10^{-2} e^2$ b^3,[2,3] obtained from Coulomb excitation measurements.

The particle-hole model fails to reproduce the effect of the 3^- phonon of ^{208}Pb. The enhancement of (303) (I) is about 13 which is an order of magnitude smaller than the value obtained for (303) (II). This model predicts that many components make important contributions to the total differential cross section. In particular, (303) (I) is comparable in magnitude with (112) which involves the lowest allowed L and J transfers. As the lowest J transfer is highly favored in γ transitions, the particle-hole model predicts that the 1.609-MeV, $\frac{13}{2}^+$ state will decay to the ground state predominantly by an $M2$ transition which is in contradiction to experiment. In a previous analysis of the reaction $^{89}\mathrm{Y}(p, p')^{89}\mathrm{Y}$(0.908 MeV),[8] which involves a single proton going from the $2p_{1/2}$ to the $1g_{9/2}$ level, the particle-hole model gave a good fit to the experimental angular distribution and predicted appreciable contributions from both the (314) and (505) components. Here the levels are known to be connected by an $M4$ γ transition.[15] In this case there are no strongly collective core states contributing because ^{88}Sr has no strong low-lying 5^- state.

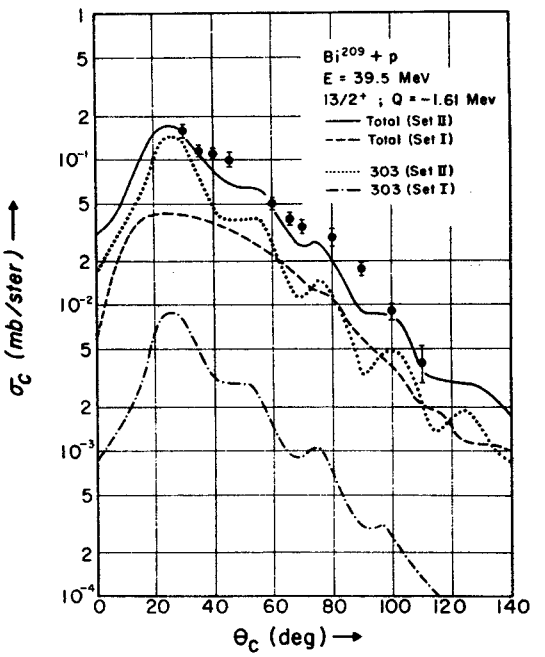

FIG. 2. The experimental data compared with the theoretical results obtained with both sets of wave functions. The total differential cross sections and the (303) component are shown for both cases.

It is concluded that highly collective core phonons can play an extremely important part in the core polarization process, and that care must be exercised in applying the uncorrelated particle-hole model for core polarization.

The authors are indebted to Dr. C. N. Davids, Dr. R. A. Paddock, Mr. I. D. Proctor, and Mr. S. Fox for their help in taking the data. This experiment would not have been possible without the germanium detector fabricated by Professor C. R. Gruhn and Mr. T. Kuo. Thanks are due to

Mr. R. Trilling for providing the program which was used to calculate the two-body matrix elements and to Dr. J. Schiffer for interesting conversations.

---

*Work supported in part by the National Science Foundation and the U. S. Atomic Energy Commission.

†Alfred P. Sloan Fellow.

‡Present address: Centre d'Etudes Nucléaires de Grenoble, Grenoble, France.

§Permanent address: Michigan State University, East Lansing, Mich.

[1]R. Woods, P. D. Barnes, E. R. Flynn, and G. J. Igo, Phys. Rev. Letters 19, 453 (1967); J. S. Lilley and N. Stein, Phys. Rev. Letters 19, 709 (1967); C. Ellegaard and P. Vedelsby, Phys. Letters 26B, 155 (1968).

[2]J. S. Lilley and W. R. Phillips, in John H. Williams Laboratory of Nuclear Physics, University of Minnesota, Annual Report No. COO 1265-67, 1968 (unpublished), p. 123.

[3]J. W. Hertel, D. G. Fleming, J. P. Schiffer, and H. E. Gove, Phys. Rev. Letters 23, 488 (1969).

[4]B. R. Mottelson, J. Phys. Soc. Japan Suppl. 24, 96 (1968).

[5]A. Kallio and K. Kolltveit, Nucl. Phys. 53, 87 (1964).

[6]F. Petrovich, H. McManus, V. A. Madsen, and J. Atkinson, Phys. Rev. Letters 22, 895 (1969).

[7]F. Petrovich, thesis, Michigan State University (unpublished).

[8]F. Petrovich, H. McManus, and J. R. Borysowicz, to be published.

[9]H. Horie and A. Arima, Phys. Rev. 99, 778 (1955).

[10]T. T. S. Kuo and G. E. Brown, Nucl. Phys. 85, 40 (1966), A92, 481 (1967), A114, 241 (1968); T. T. S. Kuo, Nucl. Phys. A90, 199 (1967), A103, 71 (1967).

[11]T. T. S. Kuo, Phys. Letters 26B, 63 (1967).

[12]V. Gillet, A. M. Green, and E. A. Sanderson, Nucl. Phys. 88, 321 (1966).

[13]D. A. Bromley and J. Weneser, Comments Nucl. Particle Phys. 11, 151 (1968).

[14]G. R. Satchler, R. H. Bassel, and R. M. Drisko, Phys. Letters 5, 256 (1963); T. Stovall and N. M. Hintz, Phys. Rev. 135, B330 (1964); M. P. Fricke and G. R. Satchler, Phys. Rev. 139, B567 (1965); A. Scott and M. P. Fricke, Phys. Letters 20, 654 (1966); J. Saudinos, G. Vallois, O. Beer, M. Gendrot, and P. Lopato, Phys. Letters 22, 492 (1966).

[15]M. Goldhaber and A. W. Sunyar, Phys. Rev. 83, 906 (1951).

INTERNATIONAL CONFERENCE
ON PROPERTIES
OF NUCLEAR STATES

MONTREAL, CANADA
AUGUST 25-30, 1969

CONFÉRENCE INTERNATIONALE
SUR LES PROPRIÉTÉS
DES ÉTATS NUCLÉAIRES

MONTRÉAL, CANADA
25-30 AOÛT 1969

THREE-QUASIPARTICLE MULTIPLETS IN NUCLEI BELOW $N = 82$

D. B. Beery*, R. Muthukrishnan, and W. H. Kelly, Cyclotron Laboratory†, Department of Physics, and Wm. C. McHarris, Department of Chemistry‡ and Cyclotron Laboratory†, Department of Physics, Michigan State University, East Lansing, Michigan 48823, U.S.A.

The ε decay of Nd^{139m} has been found to populate a multiplet of high-lying, odd-parity states in Pr^{139} (figure below), which we have interpreted as three-quasiparticle states [Phys. Rev. Lett. 22, 1191 (1969)]. The two Nd^{139} isomers follow the trend of $N = 79$ isomers, and the decay of Nd^{139g} [Beery, Kelly, and McHarris, to be publ.] is straightforward and similar to the decay of many nuclei in this region, proceeding mostly to the Pr^{139} ground state. Because of the small amount of energy for the $M4$ isomeric transition, only 12.7% of Nd^{139m} decay proceeds by this path, and 80.7% of its decay goes to the six states between 1624.5 and 2196.7 keV in Pr^{139}. This contrasts with only about 5% going to the $h_{11/2}$ state at 821.9 keV. This can be explained, however, even with the simplest use of the shell model. The $3/2^+$ ground state of Nd^{139} can be pictured as three neutron holes below $N = 82$, i.e., $(\nu d_{3/2})^{-3}$, and ten protons above $Z = 50$, i.e., $(\pi g_{7/2})^8(\pi d_{5/2})^2$. Its β^+/ε decay then involves converting one of the $d_{5/2}$ protons into a $d_{3/2}$ neutron, resulting in $\pi d_{5/2}$, the ground state of Pr^{139}. From the reduced transition probability of the $M4$ transition, Nd^{139m} appears to differ from Nd^{139g} only in the promotion of an $h_{11/2}$ neutron to the $d_{3/2}$ orbit, so its configuration can be written as $(\pi d_{5/2})^2(\nu d_{3/2})^{-2} \times (\nu h_{11/2})^{-1}$. The same ε decay transition, $\pi d_{5/2} \rightarrow \nu d_{3/2}$, produces the three-particle states, $(\pi d_{5/2})(\nu d_{3/2})^{-1}(\nu h_{11/2})^{-1}$. On the other hand, to reach the $h_{11/2}$ state at 821.9 keV in Pr^{139} would require transforming a $d_{5/2}$ proton into an $h_{11/2}$ neutron, either directly or through an intermediate $d_{3/2}$ state, and the simultaneous promotion of the remaining $d_{5/2}$ proton into an $h_{11/2}$ state. The large number of enhanced transitions between members of the three-quasiparticle multiplet should provide a handle on the major components of their wave functions, while the retarded transitions to lower-lying states should indicate some of the impurities. Calculations are presently underway to determine the composition of the states. (The configuration, $(\pi d_{5/2}) \times (\nu d_{3/2})^{-1}(\nu h_{11/2})^{-1}$ can produce four each of $9/2^-$ and $11/2^-$ states.) We predict that a number of nuclei in the region below $N = 82$ should have configurations that will direct their ε decay into similar three-quasiparticle multiplets. Preliminary results on Sm^{141m} indicate that it indeed does possess similar decay properties [R. E. Eppley, R. R. Todd, D. B. Beery, W. H. Kelly, and Wm. C. McHarris, in progress], and one can also hypothesize that the abrupt change in decay properties of Gd^{145} [M. F. Roche, K. S. Toth, and R. M. Gaedke, Bull. Am. Phys. Soc. 14, 20 (1969); Eppley, McHarris, and Kelly, to be publ.] from the lower $N = 81$ isotones represents a forced decay to three-particle states.

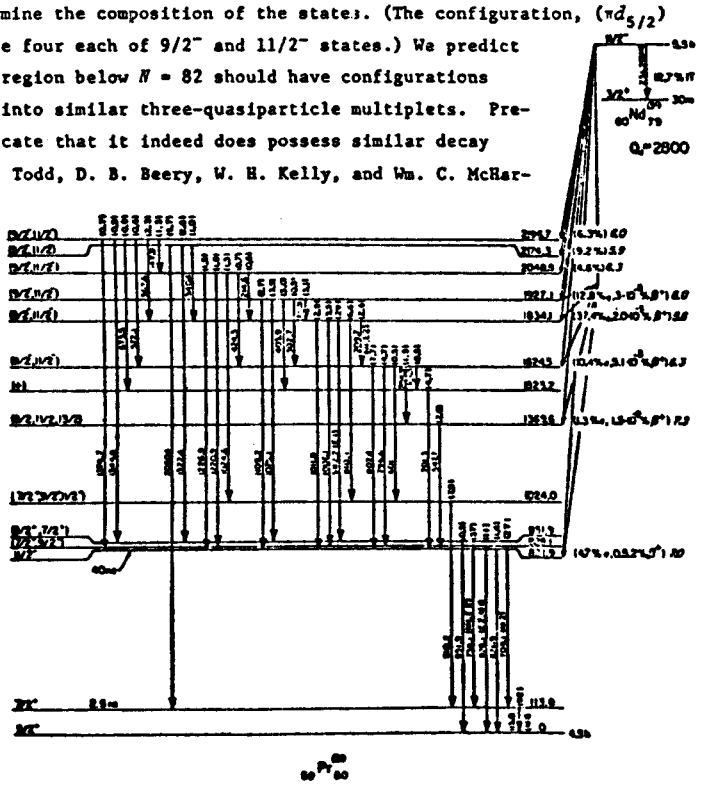

*Present address: Manchester College, North Manchester, Indiana

Supported in part by the †U.S.N.S.F. and the ‡U.S.A.E.C.

The Michigan State University Cyclotron Computer Facility*

W. Benenson, R.A. deForest, R.F. Au, D.L. Bayer, and W.E. Merritt
Cyclotron Laboratory, Michigan State University
East Lansing, Michigan 48823

Abstract

The Michigan State University Cyclotron Computer facility consists of a Scientific Data Systems Sigma-7 computer with a laboratory designed multi-purpose interface. The operating system is a time-sharing supervisor called JANUS which permits safe real-time operation. The computer is available to the laboratory staff 24 hours a day, and it is often serving as many as six users simultaneously. FORTRAN jobs including compiling can be run anytime and have an effective memory of 128k locations. On-line use of the computer is mainly particle identification or one to four parameter pulse height analysis.

---

*Work supported in part by the U.S. National Science Foundation.

Paper contributed to the International Conference on Radioactivity in Nuclear Spectroscopy -- 11-15 August 1969

A NaI(Tl) Split Annulus for Coincidence, Anticoincidence, Triple Coincidence, and Pair Spectrometry

W. H. Kelly

Cyclotron Laboratory,* Department of Physics

and

Wm. C. McHarris

Department of Chemistry†

and

Cyclotron Laboratory,* Department of Physics

Michigan State University

East Lansing, Michigan 48823

---

*Work supported in part by the U. S. National Science Foundation.
†Work supported in part by the U. S. Atomic Energy Commission.

During the last three years we have been using an 8"×8"-in. NaI(Tl) split annulus more or less routinely as a counterpart to Ge(Li) detectors in various coincidence and anticoincidence configurations.[1] Its most common use has been for Compton suppression (external, collimated source) and simple anticoincidence experiments (internal source), most often with the insertion of an additional 3"×3"-in. NaI(Tl) detector at the end of its tunnel opposite the Ge(Li) detector in order to reduce Compton edges further. In fact, we have found it advisable to perform such experiments at the very outset of study of a new decay scheme so as to pinpoint immediately any delayed transitions or primarily β-fed ground-state transitions. The split feature of the annulus has made it very useful for other, more exotic experiments as well. Among these have been triple coincidence experiments involving short-lived nuclides or weak transitions, made possible only because of the high efficiency of the annulus. It has also been used as part of an efficient pair spectrometer for obtaining β^+ feedings and/or double-escape spectra, and it has been used to enhance the background reduction of a "Compton" or "duode" spectrometer.[2] As examples of its use in coincidence and triple coincidence experiments are straightforward and already appear in the literature,[1,3] here we concentrate on examples of experiments in anticoincidence and pair spectrometry which are selected to illustrate both the advantages and the pitfalls inherent in the use of such a system.

In fig. 1 we show singles and anticoincidence (internal source) spectra of γ-rays from the decay of 2.6-h Nd^{141}. In this decay[4] a level

at 1126.8 keV in Pr^{141} is depopulated by the 1126.8-keV γ directly to the ground state and also by the 981.3-keV γ, which is in coincidence with the 145.4-keV γ. Arbitrarily setting the intensity of the 1126.8-keV γ to be 100 in both spectra, one finds that the 145.4-keV γ drops from 30.3 in the singles spectrum to 11.1 in the anticoincidence spectrum, while the 981.3-keV γ drops from 3.0 to 1.1. Yet the background, especially under the 981.3-keV γ, has dropped even further. This can be explained partly because the Compton distributions, especially toward the edges, stand a somewhat greater chance of being rejected than do the (presumably isotropic) photopeaks. Additionally, Compton distributions originating from γ-rays in cascade can be rejected also because of that fact, although the degree to which this aids in revealing weak peaks depends intimately on the decay scheme in question. The weak 981.3-keV γ, although in a cascade itself, rides on a much more intense Compton background, a considerable portion of which also results from cascades, so the net result is an enhancement of the γ-ray over the background.

Although one normally gets the best results in Compton suppression by using external, collimated sources, the foregoing shows that with internal sources one also finds enhancement of photopeaks, even those in cascades, over the background. (Also, the use of an internal source plus the additional 3×3-in. NaI(Tl) detector affords the better reduction of Compton *edges*, unless one can collimate the γ-rays from an external source through a 3×3-in. annulus.) This is most important when one is studying short-lived activities, which require many bombardments to accumulate spectra with good statistics. In such cases a single anticoin-

cidence spectrum often can produce reasonable suppression and at the same time yields information about which transitions are in cascades. As an example of the latter, the enhancement in the anticoincidence spectrum of the 1126.8-keV γ (non cascade) over the 1147.1-keV γ (cascade) should be noted.

In fig. 2 we show an example of the use of the annulus as part of a pair spectrometer used to determine β^+ feedings from Bi^{205} to the 703.4- and 987.5-keV states in Pb^{205}. Any β^+ feeding from such a heavy nucleus is expected to be very weak, and determining it requires a very efficient counting system plus a long counting time. Using a relatively hot internal source, the spectrum in fig. 2 took 90 hours to collect. The Bi^{205} decay scheme, however, is very complex,[5] so the analysis of this spectrum is not straightforward. First, it should be noted that it is not so clean as a usual pair spectrum. This comes about because the low-energy background is much stronger than either the higher-energy γ-rays that could produce pairs or the very weak β^+ feedings to the 703.4- and 987.5-keV states. In the Bi^{205} spectrum, in particular, there is a very strong, complex background underlying the weak 511-keV $\gamma\pm$, so one has to correct for this by taking comparison spectra with the gate of one half of the annulus set on either side of the 511-keV peak. One also has to worry about summing of lower-energy γ-rays into and out of the 511-keV gate. For chance summing this can be compensated for by careful control of the source strength. Finally, because high-energy γ-rays that can produce pairs feed both the 703.4- and 987.5-keV levels, the full decay scheme has to be relatively well known and corrections must be made for the enhancement of the

of the 703.4- and 987.5-keV γ's because of these feedings. After making all the corrections that are presently possible, we found that the β^+ feeding to the 703.4-keV state was 0.05% and that to the 987.5-keV state was approximately an order of magnitude smaller.

We wish to thank not only Dwight Beery and Ken Kosanke, whose results we quote, but also all the other students whose exploration and exploitation of the possibilities of the annulus have usually brought exciting, even exhilarating results.

References:

[1]R. L. Auble, D. B. Beery, G. Berzins, L. M. Beyer, R. C. Etherton, W. H. Kelly, and Wm. C. McHarris, Nucl. Instr. Methods 51, 61 (1967).

[2]C. R. Gruhn, J. V. Kane, W. H. Kelly, T. Kuo, and G. Berzins, Nucl. Instr. Methods 54, 268 (1967).

[3]G. Berzins and W. H. Kelly, Nucl. Phys. A92, 65 (1967); R. C. Etherton, L. M. Beyer, W. H. Kelly, and D. J. Horen, Phys. Rev. 168, 1249 (1968); D. B. Beery, W. H. Kelly, and Wm. C. McHarris, Phys. Rev., in press (1969).

[4]D. B. Beery, W. H. Kelly, and Wm. C. McHarris, Phys. Rev. 171, 1283 (1968).

[5]S. H. Vegors, Jr., R. L. Heath, and D. G. Proctor, Nucl. Phys. 48, 230 (1963); K. L. Kosanke and Wm. C. McHarris, in progress.

Figure Captions:

Fig. 1 Singles and anticoincidence γ-ray spectrum from 2.6-h Nd^{141}. The Ge(Li) detector was a 7-cm^3 5-sided coaxial detector manufactured at MSU. For the anticoincidence spectrum it was placed inside an 8×8-in. NaI(Tl) split annulus. The source was placed inside the annulus between the Ge(Li) detector and an additional 3×3-in. NaI(Tl) detector. These spectra were taken by D. B. Beery.

Fig. 2 Pair spectrum from Bi^{205} showing the 703.4- and 987.5-keV γ's resulting from weak β^+ feedings to these respective levels in Pb^{205}. This spectrum was taken by K. L. Kosanke.

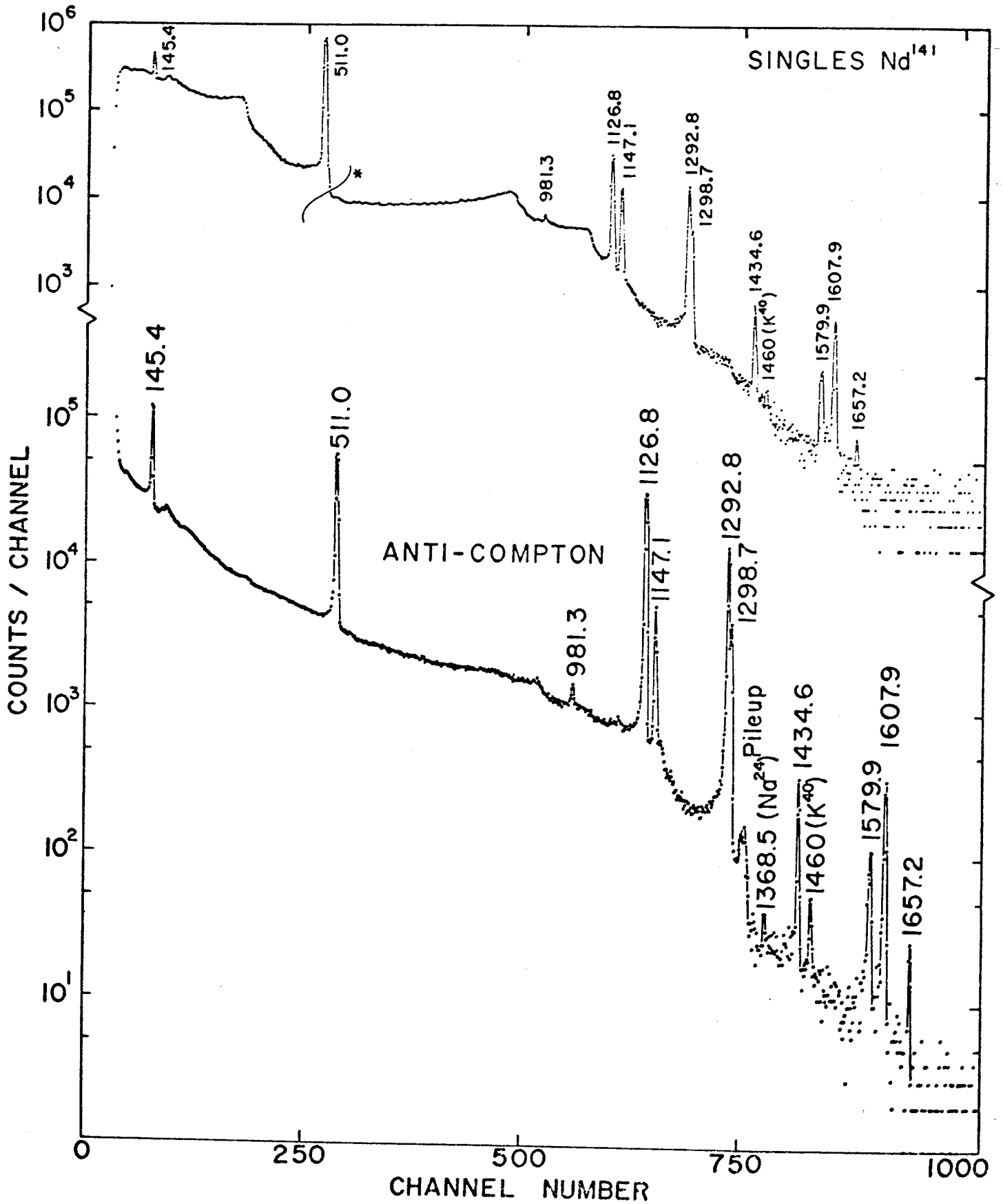
SINGLES Nd141
ANTI-COMPTON
COUNTS / CHANNEL
CHANNEL NUMBER
145.4
511.0
981.3
1126.8
1147.1
1292.8
1298.7
1434.6
1460(K40)
1579.9
1607.9
1657.2
1368.5 (Nd24) Pileup
0
250
500
750
1000

Bi^{203} TRIPLE COINCIDENCE
511 keV-511 keV-ANY
USING SPLIT NaI ANNULUS (GATES)
AND Ge (Li) (DISPLAY)
2606.9 DE
2535.2 DE
1903.5 DE
1861.9 DE
813.3
1776.0 DE
1764.5 DE
703.4
1614.5 DE
570.9
1551.0 DE
260.6 AND 262.9
264.2
1152
COUNTS PER CHANNEL
CHANNEL NUMBER
0
250
500
750
1000
10^4
10^3
10^2
10^1
1

Invited Paper to be given before the
International Conference on Radioactivity in Nuclear Spectroscopy
11-15 August 1969

Data Acquisition from Simultaneous Experiments Using the MSU Sigma-7 Computer*

Wm. C. McHarris, R. F. Au, D. L. Bayer, W. Benenson,
R. A. DeForest, W. H. Kelly, and W. E. Merritt

Michigan State University
East Lansing, Michigan 48823

*Work supported in part by the U. S. National Science Foundation.

The large size of the nuclear spectroscopy group at Michigan State University and the relative ease and efficiency with which experiments can be performed using the MSU Sector-Focused Cyclotron make it imperative that simultaneous data acquisition and analysis be possible. The Sigma-7 computer at the MSU Cyclotron Laboratory forms the basis of a flexible real-time, time-sharing system that meets the requirements for performing simultaneous spectroscopic experiments or spectroscopic experiments simultaneously with nuclear scattering experiments, all the while allowing data analyses to be performed.

The computer consists of 32*K* of 32-bit core memory plus a 1.5-megabyte (8 bits = 1 byte) RAD (rapid access disk) for file storage and a 3.0-megabyte RAD for memory swapping during computation. [During this fall a 5.3-megabyte RAD (transfer rate ≈ 3 megabytes/sec) will be added for memory swapping and both current RAD's (transfer rate ≈ 0.19 megabytes/sec) will be used for file storage.] It has standard peripherals such as teletypes (with and without paper tape), card reader, card punch, 600 lines/sec line printer, two 9-track magnetic tape units, and a CalComp plotter. A large general-purpose interface[1] built in this laboratory connects it to two scope displays -- a Fairchild 737A live-display scope and a Tektronix 611 storage scope -- and to the various nuclear instrumentation of the laboratory. This includes four Northern Scientific 13-bit ADC's plus coincidence and routing circuitry and a Nuclear Data 160 analyzer that can dump its memory directly into the computer. Computer control of the cyclotron itself is partially operational and is expected to be completed during the fall of 1969.

At the heart of the flexibility of the system is the time-sharing software, which was written in this laboratory.[2] This system, called JANUS, permits the simultaneous execution of a set of programs, called "tasks," and performs the swapping in and out of memory which increases the effective size of the computer enormously. Perhaps a list of the currently implemented tasks will give the best idea of the versatility of the system. They can be divided into two classes -- 1) those primarily for real-time use of the system and 2) the monitors for controlling batch programs:

1) *Real-time tasks*

1. POLYPHEMUS Single-parameter data recording from up to four 13-bit ADC's with print, plot, punch, and MOIRAE (see below) analysis. Either whole-word or half-word channels.

2. GEORGE On-line two-dimensional data acquisition and simultaneous display.

3. EVENT Megachannel, multidimensional data collection. Reads ADC's singles, dual coincidence, etc., and lists data on magnetic tape for later analysis.

4. HYDRA External particle identification of up to eight spectra using analog particle identifiers.

5. TOOTSIE Internal on-line data acquisition for digital particle identification. Uses up to four ADC's and can collect many simultaneous spectra.

6. NDDUMP The Nuclear Data analyzer is dumped into the computer and four 1024-channel CPUNCH (compressed binary punch) decks are produced.

7. NDPLOT A set of CPUNCH decks can be read, plotted in various

linear and logarithmic formats, using the CalComp plotter, and listed.

8. PDPTAPE Block binary paper tapes from the PDP-9 computer also in the laboratory are read and converted into CPUNCH decks.

9. MOIRAE Live-scope data analysis program. Discussed below.

10. COPY Any card deck can be copied.

11. LIST Any card deck can be listed on the line printer.

12. CALC Live-display scope can be used as a desk calculator.

13. SPACEWAR Game played with switches on the live-display scope.

14. TOUR Gives visitors a tour of the laboratory on the live-display scope, explaining the construction of the cyclotron, sector-focusing, etc.

2) *Monitors*

A. JBCM The JANUS basic control monitor, similar to the SDS BCM. Ties up peripherals not essential for real-time use so as to insure faster output of the single program being run under it.

B. JFCM The JANUS file control monitor. Handles up to four programs at once and stores others for later processing. It can be used to "swallow" large calculations such as the DWBA code JULIE so that batch processing can proceed at the same time.

C. JPCM A JANUS file control monitor used to initiate subtasks for cyclotron control.

D. ABS-DEBUG Used to debug new tasks for JANUS.

E. SYSGEN Used to generate a new JANUS system tape.

Multiple "copies" of a number of the tasks can coexist, e.g., several

different TOOTSIE's could be assigned to different sets of ADC's, so the number of simultaneous program possibilities is enormous. Clearly, the number and kinds of peripherals put a practical limit on what programs can be run together, and if too many programs are running at once, the "overhead" time involved in monitoring and memory swapping becomes great enough to lead to diminishing returns. However, there have been numerous occasions in our laboratory when one might have witnessed such scenes as the following. (Each user of the computer is his own operator.)

1. A two-dimensional, "megachannel" Ge(Li)-Ge(Li) coincidence experiment on γ-rays from Pb^{200} decay is entering its third day under the task EVENT. The storage scope was used to set up this experiment, but, once the experiment was running, this scope was given over to other programs. The scope is brought back to EVENT periodically to check on how things are progressing, but a separate one-dimensional analyzer and several scalers are the only continuous monitors. The 21-h Pb^{200} is replenished every few days by a $Tl^{203}(p,4n)Pb^{200}$ bombardment using the proton beam of the cyclotron. The task EVENT does get stopped several times per day when the tape unit being used is needed for another program, but the tapes are protected by automatic ends-of-file, and if the ADC's, amplifiers, etc., are not altered, EVENT can easily pick up where it left off.

2. The group operating the cyclotron for the night sets up the task TOOTSIE to collect the (p,d) and (p,t) spectra simultaneously from a single bombardment of Ne^{20} with 40-MeV protons. They use the storage scope to set gates for the digital identification of deuteron and triton pulses from the ΔE and E counters. Because generating displays is one of the most time-

consuming operations for the central processor (that is why a storage scope was selected as the second display unit), they find it necessary to terminate (usually politely) the game of SPACEWAR that was proceeding on the live-display scope. Otherwise, they may have to wait five or ten seconds for each update of their own display, which can be annoying when one is setting up. (Incoming data always have the highest priority, so there is no danger of losing these because of other tasks, but displays have much lower priority, even when part of on-line tasks such as TOOTSIE or POLYPHEMUS, so the human element is left to control them.) Once their gates are set in the two-dimensional mode, ΔE vs $\Delta E+E$, they then monitor the progress of their experiments by periodic updatings of one-dimensional displays on the storage scope. From time to time they punch (CPUNCH) out their accumulated spectra and plot them (all part of TOOTSIE). In the event that the card punch or plotter is in use, the spectra go into a buffer memory to await the availability of the proper device.

3. A student brings in previously collected spectra of γ-rays from Bi^{204} decay. He uses the task MOIRAE to analyze them for energies and intensities. This is done with the live-display scope, using switches to select input information as described below.

4. Several other students have been following the decay of Sm^{141}, using the PDP-9 computer as an analyzer. They bring in some output paper tapes in block binary form, feed them into the Sigma-7, using the task PDP-TAPE, and receive CPUNCH decks in return.

5. One of us is completing a paper on the decay of Gd^{149} and needs "fresh" plots of his spectra for the draftsman. He cleans the India

ink pens for the CalComp plotter, and, using the task NDPLOT, proceeds to run off a number of spectra from CPUNCH decks.

6. Three FORTRAN programs are being run under the task JFCM. Running continually throughout the night is the DWBA code JULIE, being used to calculate ten cases for inelastic proton scattering from some of the Ni isotopes. Through memory swapping, the Sigma-7 can handle programs requiring as much as 128*K* words of memory. Although programs such as JULIE run much more slowly than they would on a larger computer, we have found it no great inconvenience to load a deck in the evening and pick up the printout the next morning.

Running more sporatically are the two other programs. The program TASK RECOVERY is being used to sort spectra from the tapes that resulted from a previous megachannel spectrum of Bi^{205} γ-rays taken with the task EVENT. And the spectrum-analysis program SAMPO,[3] which one of us brought back from Berkeley, is being modified, debugged, and tested as a complementary program to the task MOIRAE.

More detailed information about the programs of most interest to nuclear spectroscopists follows, together with some specific examples of their use:

The task EVENT and the FORTRAN program EVENT RECOVERY. The task EVENT, when used in a two-dimensional mode, accepts the input from two of the 13-bit ADC's. This means that two-dimensional spectra as large as 8192 ×8192 can be run, but we usually find, say, 1024×2048 or 4096×4096 to be more than adequate. When a coincidence event is detected, its x and y ad-

dresses are listed in the two halves of a single computer word, which is fed into a dedicated buffer memory. There are two of these buffers, each with a capacity of 240 words. When one buffer fills, the listing is shifted to the other, while the contents of the first one are written on magnetic tape. The upper limit on the counting rate is set by the speed with which data can be written on the tape, and this is approximately 3000 words/sec. A standard 2400-ft tape completely filled will hold some 1.1 million events.

Most of our Ge(Li)-Ge(Li) spectra, especially of longer-lived activities, are taken with the detectors placed at an angle of 90° to each other and with shielding inserted between them to minimize Compton coincidences. For shorter-lived activities, however, when it is often necessary to collect a full spectrum by repeated bombardments during one night, one needs the most efficient counting geometry possible. For these we place the detectors 180° to each other with little or no shielding between them. Offsetting the source from the central axis helps to reduce $\gamma^{\pm}$ coincidences, but the Compton edges can sometimes be quite large when this geometry is used. Thus, although these spectra are reduced in quality from the 90° spectra, they are still quite valuable.

The program EVENT RECOVERY is used to scan the tapes and to assemble one-dimensional spectrum "slices" from various gates. Gates can be set on either the x or the y side, and one has the option of setting gates by themselves or of setting gates having selected background gates on either side. For the latter, the program subtracts the background according to the weighted size of the background gates. When a single gate is used, sorting through a 2400-ft tape takes approximately 10 min, depending, of course, on

the particular spectrum and on what else the computer is doing at the same time. Up to about five gates can be sorted simultaneously with relatively little increase in time, perhaps a total of 15 min for sorting one tape. When more than five gates are sorted simultaneously, the memory swapping involved starts slowing down the process markedly, so, although the program can accept an indefinite number of gates, rarely do we use more than five at a time.

The data analysis task MOIRAE. Most of our spectrum analysis is done using this task. Up to 25 spectra can be introduced into the computer by cards, tape, or a data acquisition task. They can then be called up on the live-display scope and manipulated by a set of 32 switches. Some of the switches control the display of the spectrum, such as linear or log display, expansion of vertical and/or horizontal axes, shifting portions of a spectrum from left to right, etc. The others control various routines used to determine the centroids and intensities of the peaks displayed. Some typical spectrum analyses are shown in the following figures.

Fig. 1 shows a portion of the γ-ray spectrum from the decay of Bi^{204} with the background fit to a second-order polynomial. The switches are used to move the tall pointer to the positions of points in the spectrum to be used in calculating the background. Up to 50 points can be used, and the background can be fit up to the ninth degree. The shorter lines show the points that have been accepted. Alternatively, one can select up to 25 pairs of points enclosing regions of up to 512 spectrum points (total) for calculating the background.

Fig. 2 shows the same spectrum, this time with the background

fit to a third-order polynomial. In this and the previous figure, the region of background fit is about as large as one can use and expect to get reasonable results with a low-order polynomial.

Fig. 3 shows a fifth-order fit to the same spectrum. Note that the region of background fit is almost doubled from the previous figures.

Fig. 4 is a display of the data of fig. 3 with the (fifth-order) background subtracted. To obtain the areas of these peaks, one then selects the peak limits with the large pointer and chooses to calculate the peak position either by the full peak or that portion of the peak higher than one-third peak (meaning higher than one-third peak defined within the limits selected). The task then finds the centroid, the area, the sum of raw data plus background, and the square root of that sum.

In fig. 5 we see the above fifth-order background fit with more of the spectrum included for perspective. The fit in question was to a Compton edge.

Once one is satisfied with the display on the scope, he can punch, plot, or print out any information contained on it. After accumulating all the analyses he desires, he can have the computer calculate a calibration curve if he chooses, by making a least-squares fit to an nth degree polynomial. Or he can calculate his peak energies by a similar least-squares fit to a previously generated calibration curve. In each case all the statistical quantities, such as standard deviation of each peak energy from the curve, are also calculated.

Although MOIRAE has proven to be a very satisfactory task, we are continually improving it. For example, it is now in the process of being

modified to add a Gaussian fit with exponential tails to determine the peak area. MOIRAE, however, has proven to be the biggest bottleneck in our work, simply because of the amount of time involved in sitting if front of the scope performing fits. For this reason we are starting to perform some of our analyses with the program SAMPO,[3] which searches out peaks on its own. We hope that it will shortly be able to perform much of the more routine analysis and that MOIRAE will be reserved for quality control and for fits to more complicated regions that require on the spot inspections. We are also updating the data analysis programs on the PDP-9 to make them more or less comparable to MOIRAE.

The task TOOTSIE. Most of the particle identification from scattering reactions performed in the laboratory is now done by TOOTSIE, but, because of its extreme flexibility, this task is also of interest to spectroscopists. In fig. 6 we show a set-up for collecting tritons from the (p,t) reaction on a Pr^{141} target. It is a plot of ΔE vs $\Delta E+E$, and we are looking at a slice in the xy plane. The tritons lie in the region between the two curves, each of which was generated by a fifth-order fit to points like those still showing on the upper curve. The tritons can thus be separated digitally from the deuterons and protons, which lie below and to the left. The order of fit can be changed at will, and TOOTSIE can collect multiple spectra, such as (p,d) and (p,t), simultaneously. TOOTSIE also offers numerous other modes of identification, such as those including time as a second or third co-ordinate. This makes it a potentially powerful tool for the spectroscopist performing on-line experiments.

Acknowledgments:

The successful implementation of such a complex system has naturally required the efforts and co-operation of almost everyone in the Cyclotron Laboratory. In particular, however, we thank Carolee Merritt for her aid in preparing and running the programs and Greg Giesler and Dwight Beery for their long hours of work on the spectroscopic programs. And repeated thanks should be given to J. O. Kopf and P. J. Plauger, who originated and wrote JANUS.

References:

[1]J. V. Kane, Physics Today, vol. 19, no. 7, p. 59 (July 1966); T. H. Close, D. V. Hirst, J. V. Kane, C. Y. Kao, J. Kateley, W. A. Shunk, and M. E. Williams, Ark. Fys. 36, 553 (1967).

[2]J. O. Kopf, Ph. D. Thesis, Michigan State University (1968); J. O. Kopf and P. J. Plauger, Bull. Am. Phys. Soc. 13, 700 (1968); P. J. Plauger and J. O. Kopf, Bull. Am. Phys. Soc. 13, 701 (1968).

[3]Written by J. Routti, whom we thank for its availability.

Figure Captions:

Fig. 1 Portion of Bi^{204} γ-ray spectrum with second-order background fit. The analyses in figs. 1-5 were performed by J. B. Cross.

Fig. 2 Same as fig. 1, with third-order fit.

Fig. 3 Same as fig. 1, with fifth-order fit.

Fig. 4 Fig. 3 with background subtracted.

Fig. 5 Larger portion of Bi^{204} γ-ray spectrum showing the fifth-order background fit in better perspective.

Fig. 6 ΔE vs $\Delta E+E$ display of particles resulting from a proton bombardment of a Pr^{141} target. The tritons lie between the two curves drawn by the task TOOTSIE. From an experiment of R. W. Goles.

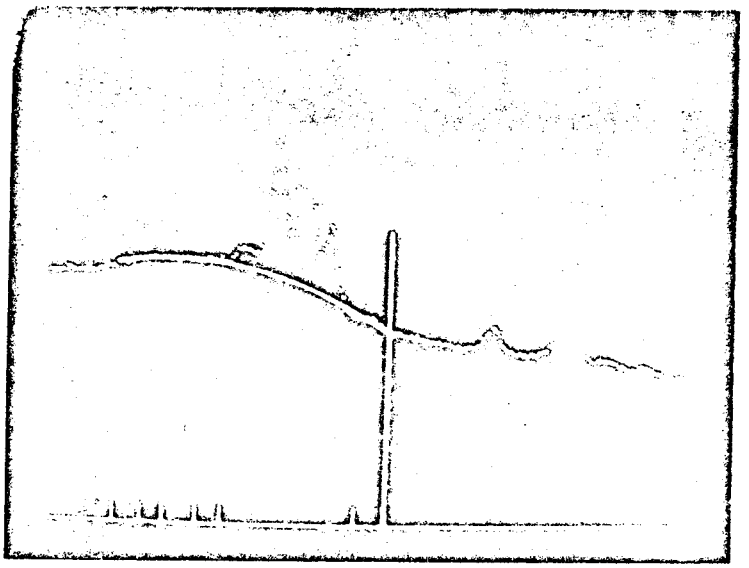

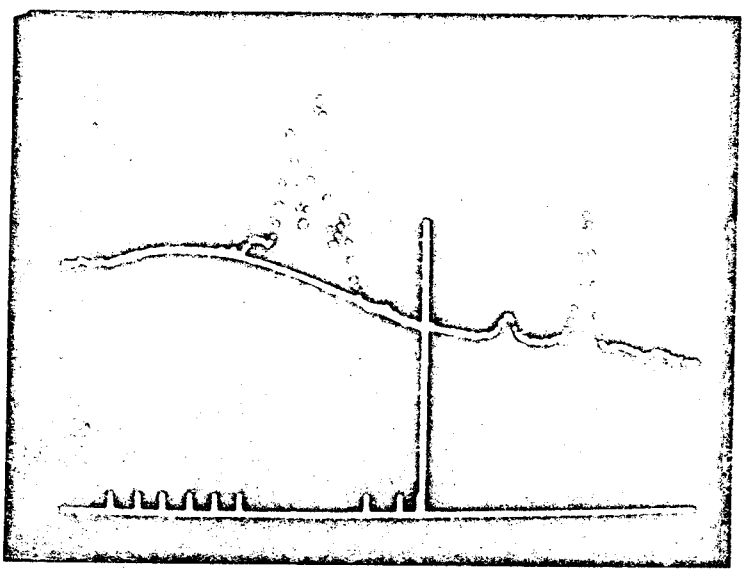

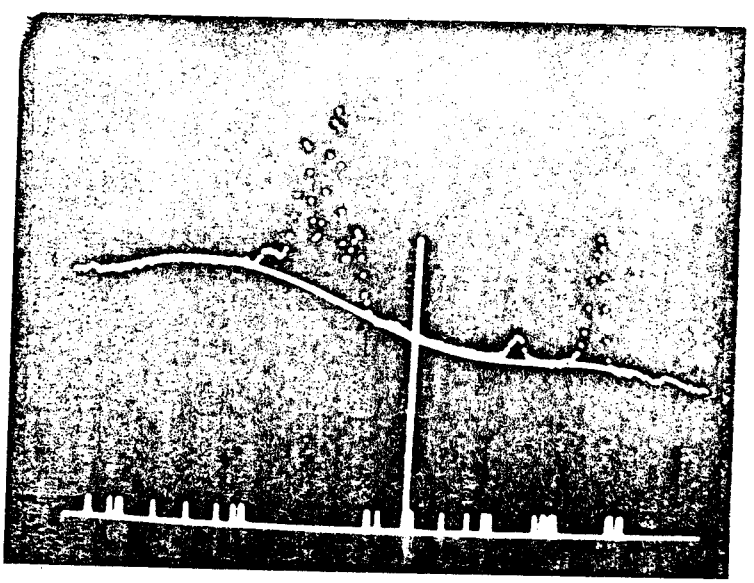

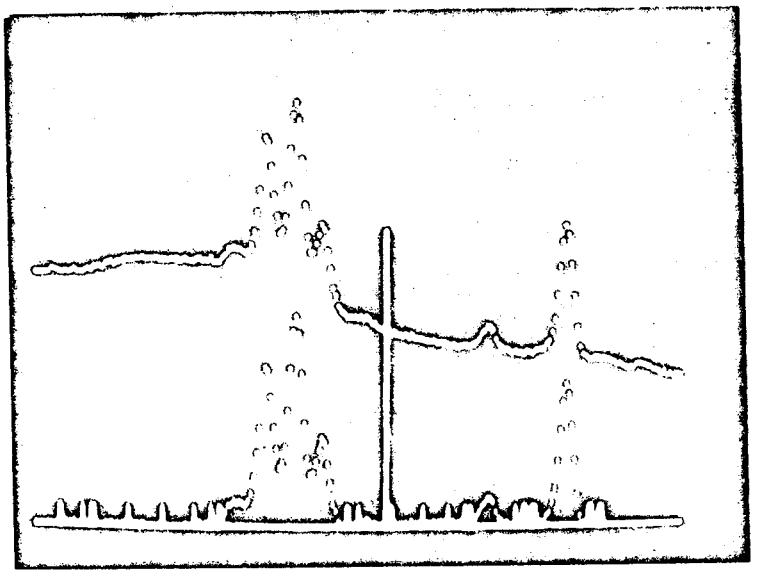

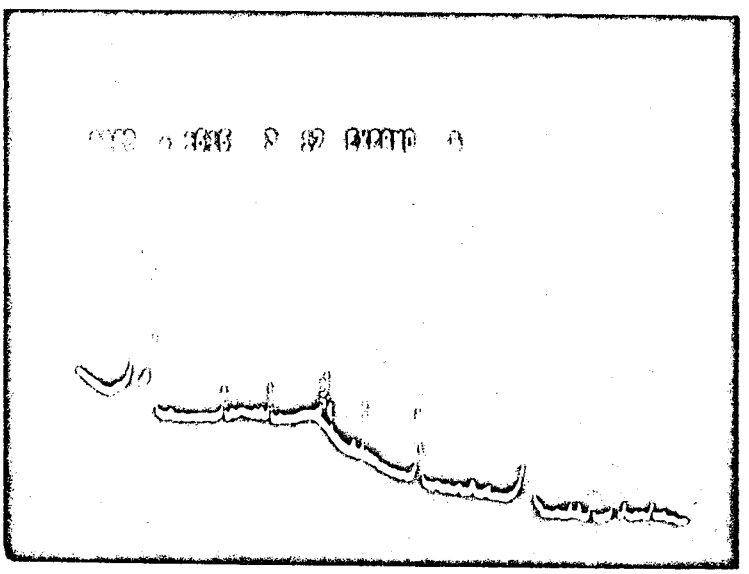

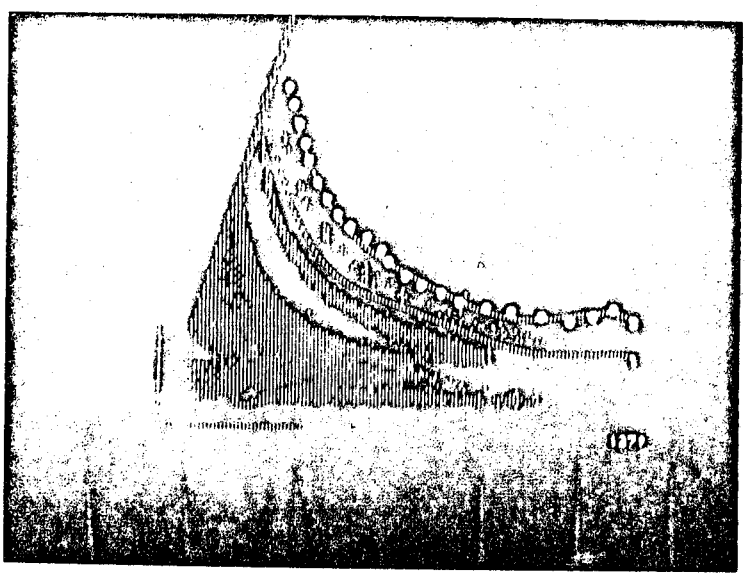

Optimization of the Cyclotron Central Region for the Nuclear Physics User*

H. G. Blosser
Cyclotron Laboratory and Department of Physics
Michigan State University
East Lansing, Michigan 48823, USA

ABSTRACT

Beam requirements for high quality nuclear physics experiments are reviewed along with features of central region arrangements for preferentially transmitting particles satisfying the requirements. With such a central region, phase widths of 1.5° can be achieved and such phase widths in conjunction with good stablizing circuits lead to highly monochromatic beams. (External beam energy spread 0.04% fwhm at MSU.) Such systems also give 100% extraction efficiency and high transmission thru external analysis systems. (Total transmission of 20% at MSU for 1 in 6000 energy resolution and emittance of less than 1 mm-mr.)

1. INTRODUCTION

Modern nulcear physics is a science of detail in which significant experiments are concerned in almost every case with careful determination of the individual properties of particular nuclear quantum states. Such experiments require very monochromatic beams in order to separate close lying quantum states, with good collimation in order to precisely study spatial details of the states. Desired beam currents are generally modest—usually in the range 50-500 nA on target—the limitation on current coming in most cases from the data processing system. Frequently the nuclear characteristics of greatest interest are rare phenomena and the cleanness of the setup is of great importance in separating the desired results from background phenomena.

Relative to these nuclear physics requirements, the cyclotron in its normal condition is a very intense, rather imprecise beam source. This mismatch is generally corrected by means of a beam analysis system which transmits a precisely defined subsection of the beam to the user. The remaining beam (typically

*Supported by the National Science Foundation.

90-99% of the total) is stopped and in so doing intense radiation and residual activity are produced along with intense thermal heating, all of which lead to substantial problems. Moreover these problems are all in principle unneccessary—the external analysis system is selecting a certain volume in phase space which (as a result of the character of the equations of motion) must have uniquely originated in a corresponding phase space volume at the center of the cyclotron and therefore the function of the external analysis system could have been accomplished by an equivalent phase space selection in the center of the cyclotron, but with the problems of radiation and residual activity eliminated and the problems of thermal heating greatly reduced. While such a central region system in principle exists, none such has yet been totally realized in practice, although great progress has been made. The situation is reviewed in this paper.

2. SYSTEM REQUIREMENTS

In nearly every case energy resolution is the primary factor determining the accelerator requirements for a given nuclear experiment. The nuclear physics itself gives no universal criterion for adequate resolution since the separation of nuclear quantum states rapidly approaches zero as the excitation of the nucleus is increased, with heavy nuclei far from closed shells as the most severe case. The accelerator is, however, never the sole factor in determining the energy resolution of an experiment—energy loss and straggling in the target and energy resolution of detectors are other very important effects and the accelerator system is therefore completely adequate whenever its contribution to the resolution is small compared to other factors. This is still a complicated criterion with many variations depending on the conditions of particular experiments. At our laboratory for example most physics users at present specify 1 in 3000 for the beam energy spread, a few ask for 1 in 6000 and on rare occasions 1 in 10,000 is used.

Emmitance requirements generally follow from the energy requirement via the combination of slit size and useful aperture of the analysis system or, for light targets, from kinematic broadening due to the combination of the spot size on target and the finite angular spread of the beam and detector. The emittance in the scattering plane (normally the radial plane) contributes linearly to the energy spread whereas the perpendicular emittance (axial) gives a quadratic contribution—hence

an axial emittance substantially larger than the radial emittance is usually acceptable. Tha actual value of the emittance necessary for given resolution is determined by the physical size of the analysis system and the scattering chamber. We have for example at MSU an unusually compact analysis system[1] (magnets weighing only 7 tons)—1 in 6000 resolution with this system requires 0.5 mm entrance and exit slits and for lowest aberrations the divergence is limited to 2 milli-radians (mr), therefore yielding 1 mm-mr for the required emittance. If this system were twice as large in all dimensions and with all fields reduced to 1/2, it would have exactly the same resolution with 1.0 mm slits and 2 mr divergence and therefore an emittance 2 times larger could be allowed. (The larger analysis system would of course be more expensive and would require more space—ergo for specified energy resolution a cyclotron with good emittance can work with a smaller analysis system and thus achieve a significant cost savings.) In a similar fashion the size of the scattering chamber fixes the target-detector distance and therefore the target spot-size and divergence required to reduce kinematic broadening to a specified level. In the MSU setup, which is fairly typical, these various factors lead to requirements of 1 mm-mr and 3 to 5 mm-mr for the radial and axial emittances respectively in a normal high-resolution experiment.

The final beam property to discuss is the duty-cycle, a parameter frequently misunderstood (and even more frequently weighed with exagerrated importance). As is well known, an isochronous cyclotron normally produces a continuous train of nano-second pulses separated in time by about 50 nanoseconds. Therefore to slow equipment the cyclotron appears to yield a continuous beam (100% macro-duty-cycle) whereas to fast equipment it appears to yield a sharply pulsed beam (1-3% micro-duty-cycle). For fixed experimental requirements (specified pileup probability, true to accidental ratio, etc.) the duty-cycle then in a complicated way determines the running time required to obtain a given result. The complexity arises from the fact that the quantity of significance, the running time, is an involved mixture of the characteristics of the accelerator and the detection system with wide variations in the characteristics of the latter quantity depending on the experiment. The present highest resolution detection system for example consists of a magnetic spectrograph with photographic plates, an arrangement whose performance is completely independent of duty cycle. Running time for such

an arrangement is determined entirely by the accelerator luminosity. Less well recognized is the fact that the wide class of direct reaction spectroscpic experiments [(p,d), (d,p), (p,t), (^{3}He,d)...etc.] is independent of a cyclotron type micro-duty-cycle since the counting rate is controlled by the data processing time for an event, a time interval of order tens of microseconds. (Very sharp beam microstructure can often in fact be a positive advantage in such experiments, the timing information allowing particle identification in a single detector in lieu of the conventional two detector dE/dx, E system and thereby yielding improved energy resolution due to decreased surface loss and dead layer effects.) A good duty cycle is of most benefit for the various multi-final particle experiments such as (p,2p), (p,p'γ) etc. Even for such experiments as these the detector is however also of key importance. At present, for example, the best resolution for both γ rays and high energy protons, is obtained with Germinaium detectors—these detectors have a charge collection time of about 10 ns and therefore the advantage of a true DC beam relative to cyclotron pulsing is of order 5 to 1 rather than the 50-1 or 100-1 which the acceleration duty cycle alone would imply. (A further consequence of this property of Germanium detectors is the fact that for such experiments a cyclotron with very short, sub-nanosecond pulses is completely equivalent to a machine with normal 2-3 nanosecond pulses or to a possible "flat-topped" machine with 8-10 nanosecond pulses, since the Germanium charge collection time in every case makes it impossible to separate two events from the same cyclotron pulse.) The class of experiments for which long duty cycle is of greatest advantage reduces then to experiments studying multi-particle final states using fast detectors—certainly an important class of experiments but nevertheless a small part of contemporary nuclear experimentation. In summary then, good duty cycle is an important and valuable attribute but in most experiments of much less importance than energy resolution. Since the cyclotron involves a fundamental conflict between duty cycle and energy spread it is in most circumstances best to favor energy resolution. (Leaving the choice of good duty cycle or high energy resolution as a free option for each user is of course the obvious ideal solution.)

3. DESIGN CONSIDERATIONS

3.1 Energy Spread

Since the acceleration in a cyclotron comes solely from the rf system[2], the energy spread in the beam must come from some variation in the relationship of the beam to the rf. In actual fact, the energy spread of a cyclotron beam is dominatly a result of three effects, namely: (a) time fluctuations in the amplitude of the dee voltage, usually called "rf ripple", (b) the fact that all particles do not cross the accelerating gaps at the same time, the distribution of the particles relative to the rf being referred to as the "phase width" of the beam, and (c) time fluctuations in either the rf frequency or the magnetic field either of which will produce a "phase shift" of the beam relative to the rf and hence a change in acceleration. The first and last of these factors, the stabilization of the rf voltage, the rf frequency and the magnetic field are engineering problems whereas restriction of the beam phase width is an orbit dynamics problem. As regards the engineering problems—modern techniques readily allow the stabilization of magnetic fields to levels of 1 part in 100,000 and of rf frequencies to 1 part in 1,000,000 (using an MOPA system). With such stabilization the contribution to the beam energy spread from factor (c) above is negligible. Stabilization of the rf voltage has proved much more difficult. Levels of 2 to 6 in 10,000 have been achieved in our lab after long effort[3,4]—1 in 10,000 is believed possible. Even at these levels the rf voltage is still the dominant factor in the beam energy spread when a good phase selection system is in use and our engineering colleagues are hence accordingly urged to press on further with their already highly productive efforts on voltage stabilization.

Finally let me consider the problem of limiting the phase width of the beam or "phase selection" as it is usually called. Phase selection via the phase dependence of the electric focussing forces was suggested a number of years ago by Hagedoorn[5] and extensively studied[6]. To my knowledge there have however as yet been no experimental studies of the performance of such systems. Recently at MSU we have installed a very effective radial motion phase selection system—since this system has not been discussed elsewhere I will describe it in some detail here.

The essential feature of the system is a phase dependent centering error the origin of which can be qualitatively understood from Fig. 1. Our cyclotron like most recent cyclotrons

FIGURE 1

has the puller extended à la W.I.B. Smith[7] in order to place the ions initially at a positive phase. The most intense beam group crosses the source to puller gap effectively at zero phase and enters the south dee. Due to the puller offset the south dee on the first turn is essentially 180° in length and so the particles also leave this dee at zero phase as indicated by the "2" on the right of Fig. 1. But now the flight path to the north dee entry at "3" is only about 45° and so particles enter this dee at a time when the voltage is rapidly changing. Since this gap is increasing the energy by about 40%, there is a large shift in the effective orbit center and due to the rapidly changing voltage this shift has a strong phase depencence thus producing a phase dependent centering shift. At later gaps such as 5,7, etc., the shift is alternately decreased and increased but since the energy increase on gap 5,7, etc., is 20%, 12%,...etc., the large shift at gap 3 is never compensated. A following slit system arranged to require centering will then act as a phase selecting system.

The phenomenon is depicted quantitatively in Figs. 2 and 3 which show results of numerical orbit tracking. For these

FIGURES 2 & 3

figures a "central" ray and six "displaced" rays have been tracked, the displaced rays differing from the central ray in that they leave the ion source in successive two degree steps earlier and later than the central ray. In Fig. 2 the phase difference between the central ray and the displaced rays is plotted vs. turn number. The difference in starting time is seen to result in an almost exactly identical difference in phase showing that a structured central region has essentially no phase grouping. Fig. 3 is similar to Fig. 2 except that the radius difference between the displaced rays and the central rays is plotted rather than the phase difference. In marked contrast with the phase difference the radius difference is sharply structured, the structure repeating periodically with the precessional frequency in the manner characteristic of a

centering error. For phase selection a slit placed at the antinode of this spacing modulation will clearly be the most effective, i.e. in the vicinity of turn 28 for the rays shown here.

We have not as yet however looked at the complete problem—a real source has both a finite size and a finite divergence and all of the rays shown in Figs. 2 and 3 originated at the center of the source moving straight ahead. A study of rays displaced in initial position from the rays of Figs. 2 and 3 so as to represent the finite source aperture produced results essentially identical to Fig. 2 and 3 and so no figures showing these results are included herein. In contrast a study of rays initially diverging from the source showed marked differences—these results are shown in Figs. 4 and 5. The most

FIGURES 4 & 5

important new phenomenon is the strong phase shift which occurs on the first half turn for the ray whose initial divergence carries it to the inside of the turn. The shorter path length causes this ray to be displaced in phase by about 4° for the maximum divergence case selected. The phenomenon is also strongly non-linear as can be seen from the inset in Fig. 4 which gives the phase shift $\Delta\phi$ vs. the divergence angle $\Delta\theta$. Another important feature to notice in Fig. 5 is the fact that rays of given phase come to a focus in the vicinity of turn 23 and are thoroughly scrambled near trun 28, i.e. the effective centering error is phase shifted relative to that for rays leaving the source with no divergence, and an additional slit will hence be necessary for best phase selection.

Experimental data showing the performance of such a system is given in Fig. 6 which is a plot of gamma ray intensity vs.

FIGURE 6

time for the beam on the internal probe of the cyclotron. The two curves are with 0.5 mm slits on the 18th and 28th turns "in" and "out" (in our cyclotron these slits are controlled by a console switch and can be inserted or removed in about 1 sec). With the slits "in" the pulse width is 0.2 ns fwhm corresponding to 1.4 rf degrees. With the slits down the phase width is 3.4 ns fwhm corresponding to 23 rf degrees. Using the phase slits and adjusting the field or frequency so that the phase group is on the average on the top of the rf wave, the contribution

to the energy spread from the phase width is reduced to about 1 part in 14,000. With improved rf amplitude control beams of 1 in 10,000, energy precision should hence be attainable.

3.2 Emittance

Comparing the desired emittance values (section 2) with the natural characteristics of the cyclotron we immediately note that the emittance requirement should be easy to achieve, at least in principle, since the specification is essentially identical to the measured emittance of a cyclotron ion source (after correcting for the energy difference between the cyclotron external beam and the DC acceleration used in the source studies). Fig. 7 and Table 1, for example, show source geometry and a

FIGURE 7

summary of the most recent emittance data from the MSU source testing facilities.[8] Since the data are taken at 35 keV the inferred emittances at 40 MeV for a 3 amp arc would be about 0.9 mm-mr radially and 3.0 mm-mr axially for 90% transmission. These values are adequate for energy resolutions of up to 1 in 10,000 even with a relatively compact analyzing system.

The DC source emittance data lead to an interesting speculation as to the origin of the 10-50 mm-mr radial emittance observed in many cyclotrons. It seems unlikely that the ion source emittance is significantly different from machine to machine since the studies of both Mallory[9] and Cluxton[8] show no strong geometry effect. In the acceleration process the radial phase space area should be essentially preserved due to Liouville's theorem and the generally weak coupling of the radial motion to either the axial or longitudinal motion. Also, the typical cyclotron is a highly linear device over distances of the order of turn widths and it is therefore unlikely that the phase space area of a well centered beam will be enlarged by non-linear mixing of filled and unfilled regions. The dominant phenomenon producing the emittance enlargement appears in fact to be a combination of the mixing of radial phase space regions in multi-turn extraction combined with an experimental inability to distinguish between emittance and dispersion. Figs. 8 and 9 show results of a computer study illustrating the phenomenon. Central

FIGURES 8 & 9

rays have been tracked from the ion source thru the cyclotron and deflector and out into the fringe field for various initial

phases and rf voltages. Points are labelled to indicate the initial τ_o (minus signs omitted). The dominant feature of these results is very strong dispersion— for a given turn the position of the final point varies smoothly up and down the r, P_r line in very direct relation to the final energy. Fig. 9 shows this even more directly, the results from Fig. 8 being replotted as Energy vs. a coordinate S giving the position along the dispersion line. Note from the Figs. that when an energy difference sufficient to permit an additional turn builds up, a distinct shift in the location of trajectories occurs. Multi-turn extraction hence will be expected to yield a larger emittance than single turn extraction even for a very well centered beam such as in these calculations (design ray centered to $\pm$0.2 mm).

Results of experimental studies of the external beam distribution are shown in Fig. 10. The results agree very closely

FIGURE 10

with the behaviour expected from the computer studies, namely that the total length of the distribution is dominantly a result of dispersion (in this case the energy spread being almost entirely a result of rf voltage ripple). Using computer results to separate the emittance and dispersion, one obtains the results shown at the right of the figure. The resulting radial emittance value is 0.7 mm-mr which is in reasonable agreement with the 0.9 mm-mr expected from the DC source stuides. Corresponding experiments on the axial emittance give a measured value of 5.0 mm-mr which is likewise in reasonable agreement with the figure of 3.0 expected from the DC studies. The cyclotron beam is thus inferred to be inherently very well collimated but with energy and radial position varying slowly in time in accord with the rf voltage ripple.

To further test the validity of the dispersion-emittance separation two additional tests were made. In the first of these the rf ripple was doubled by reducing the gain of the rf voltage feedback loop and the data of Fig. 10 were remeasured. The length of the distribution (along the dispersion curve) increased by $\sim$80% without detectable change in the width (perpendicular to the dispersion curve) as the analysis would predict. In the second test the beam analysis system was set up for 1 in 6000 resolution and the beam reaching the target was measured as a function of the aperture of a radial slit located at the edge

of the cyclotron at the position of the emittance measurements. Results of this experiment are shown in Fig. 11. One sees that

FIGURE 11

the beam satisfying the 1 in 6000 energy requirement comes entirely from the center 6 mm of the beam at the fringe field location in excellent agreement with the expectation from Figs. 8 and 10.

While similar calculations or experiments for other cyclotrons are not available, the basic nature of the phenomena make it likely that these results are widely valid, namely that the external beam of any cyclotron is in fact a very small pencil of essentially the same phase space area as observed in source studies and moving in time on a nanosecond scale for the phase distribution and a milli-second scale for rf voltage or magnetic field variations. As these time variations are removed the spatial size of the external beam shrinks and approaches the value expected from ion source studies.

3.2 Duty-Cycle

For experiments with high energy resolution a cyclotron has inherently a low microscopic duty-cycle. The origin of this pheonomenon can be understood by looking at Fig. 12 which shows

FIGURE 12

final energy for central rays leaving the ion source at initial rf times (τ_o) as indicated on the horizontal axis. The curves are parabolic in form, the energy maximum at τ_o=-23° corresponding to the ray which is on the average exactly centered on the rf wave. When the maximum radius particles reach the deflector, they are sliced off—particles earlier and later make an additional revolution and are then themselves sliced off, etc. The total resulting energy distribution vs. time for the extracted beam is then as shown i.e. a central parabolic section and successive sawtoothed satellites. If this beam is fed to a beam analysis system set for 1 in 6,000 (and with the system tuned for maximum transmission) the beam transmitted will be that corresponding to the shaded areas on the upper energy band in the figure. Immediately one notes that nearly all of the shaded area ($\sim$5/6) comes from the parabolic section of the distribution. Hence after energy analysis the beam will be sharply pulsed even though the phase distribution in the cyclotron may have been very broad. If the effect of rf ripple is included the curves in Fig. 12

move up and down in time while the energy selection band stays fixed—this will then give an apparent smearing out in a beam time distribution taken over an extended time, but this is in fact a false indication of duty cycle improvement—any position of the energy distribution curve relative to the energy acceptance bite other than that indicated for the upper band of the fig. in fact gives even sharper pulsing and lower duty cycle than the case shown. (Schematically this can be understood by thinking of the energy acceptance interval as shifted say to the lower band in Fig. 12—the pulses are clearly sharper and the duty cycle lower but because the pulses occur at a different time relative to the rf, a time-of-flight spectrum as normally taken will be broadened and thus falsely indicate an improved duty cycle.)

Results of an experimental study of the beam time distribution following energy analysis are shown in Fig. 13. As in

FIGURE 13

Fig. 6 curves are shown with the phase selection slits both "in" and "out" but now the two distributions are essentially identical thus confirming that the beam analysis system transmits essentially the same particles as the phase slits. This result is also confirmed by observations of the transmitted beam current. Beam actually reaching the target is essentially independent of the slits up or down condition. Using the slits thus removes beam which would eventually be lost but before it has received enough energy to produce radiation or radioactivity.

4. CONCLUSIONS

Carefully stablized cyclotrons and external analysis systems can furnish precise particle beams well matched to the needs of contemporary nuclear physics experiments. If the cyclotron central region is carefully arranged most of the beam which fails to satisfy the analysis requirements can be removed in the central region. Using such a system (and with good stabilizing circuits on the magnet and rf) the MSU cyclotron has produced beams with energy spread of 0.04% fwhm and with the external analysis system set for 1 in 6000 resolution, 20% of the beam leaving the cyclotron central region is transmitted all the way to the user's scattering chamber 30 meters away. The system also easily gives 100% transmission thru the cyclotron and 100% extraction efficiency. Activation problems are therefore minimized.

I am indebted to M. M. Gordon for many helpful discussion, to D. A. Johnson for carrying out the computer work and to R. St.Onge and W. P. Johnson for planning and setting up the time-of-flight apparatus.

REFERENCES

1) G. H. Mackenzie, E. Kashy, M. M. Gordon and H. G. Blosser, IEEE Trans. on Nucl. Sci. NS-14 #3 (1967) 450.

2) The discussion in this paper neglects "space charge" acceleration effects. This important topic is treated in a separate paper at this conference by M. M. Gordon.

3) W. P. Johnson and P. K. Sigg, IEEE Trans. on Nucl. Sci. NS-16 #3 (1969) 492.

4) P. K. Sigg (private communication).

5) H. L. Hagedoorn (private communication).

6) H. G. Blosser, M. M. Gordon and M. Reiser, CERN 63-19 (1963) 193.

7) W. I. B. Smith, Nucl. Instr. and Methods 9 (1960) 49.

8) D. J. Cluxton, Michigan State University Report MSUCP-25 (1969).

9) M. L. Mallory and H. G. Blosser, IEEE Trans. on Nucl. Sci. NS-13 #4 (1966) 163.

Table I: Summary of emittance data from most recent MSU DC ion source tests—D. J. Cluxton (ref. 8). Ion source slit 0.5 mm with 30° recess per Fig. 7. Gas flow 1.5 cc/min. Extraction voltage 35 kV. Currents in milliamps unless otherwise indicated.

Arc		Radial Emittance					Axial Emittance				
Cur. amps	Volts	100%		reduced area			100%		reduced area		
		mm-mr	cur.	%	mm-mr	cur.	mm-mr	cur.	%	mm-mr	cur.
1.0	100	48	0.9	96	36	.86	114	0.9			
2.0	125	41	1.1				207	1.1	61	32	0.85
3.0	150	69	3.2	96	34	3.1	245	3.2	82	89	2.7

FIGURE CAPTIONS

Fig. 1. Top—schematic drawing of central region arrangement in the MSU cyclotron including computed central ray trajectory for the first two turns. Bottom—voltage vs. time for the two dees with numbered arrows indicating the phase relationship of successive accelerations.

Fig. 2. Phase difference, $\phi_i - \phi_o$, vs. turn number for a family of central rays. Ray o leaves the source at $\tau_o = -28°$, rays 1, 2...6 leave the source at $\tau_o = -34°$, $-32°$, $-30°$, $-26°$, $-24°$, and $-22°$ respectively.

Fig. 3. Radius difference, $r_i - r_o$ at $\theta = 180°$ vs. turn number for the same family of rays as in Fig. 2.

Fig. 4. Phase difference, $\phi_i - \phi_o$, vs. turn number for a family of rays leaving the source at $\pm 90°$ to the central ray direction. Ray o is the same as in Fig. 2 rays 7, 8,..., 12 have $\tau_o = -32°$, $-32°$, $-28°$, $-28°$, $-24°$, and $-24°$ respectively with positive initial P_r for odd numbered rays and negative for even numbered rays. Initial energy 20 ev. See text for discussion of inset.

Fig. 5. Radius difference, $r_i - r_o$, at $\theta = 180°$ vs. turn number for the same family of rays as in Fig. 4.

Fig. 6. Gamma ray yield vs. rf time for beam hitting the internal probe, the main curve being with the 18th and 28th turn slits out, the inset at the upper right with the slits in (on a 5 times magnified scale). The largest observed current transmitted by these slits is 15 μa, the narrowest time group 0.15 nanoseconds fwhm (R. St.Onge, private communication).

Fig. 7. Median plane cross section view of the source-puller geometry employed by D. A. Cluxton (ref. 8) in most recent MSU DC ion source emittance measurements. The major design change from previously studied sources is the use of a knife edged tantalum extraction slit in place of the previous square edged graphite slit.

Fig. 8. Graph of radius vs. radial momentum in the extracted beam for rays leaving the ion source at rf times as labeled (all times are negative). The circled points joined by the line entered the deflector on turn 212, and are at 1° intervals in τ_o. Other rays entered the deflector on turns as follows: $|\tau_o|$ = 10°→217, = 11°→216, = 14°→214, = 29°, 30°→213.

Fig. 9. Graph of final energy vs. position on dispersion curve S (defined in Fig. 8) for the same rays as in Fig. 8 plus a group of rays run at various rf voltages with τ_o fixed at -23°.

Fig. 10. Right—measured radial distribution of the cyclotron external beam (100% of beam). Left—computer calculation of expected beam distribution due to combined emittance and dispersion.

Fig. 11. Current transmitted thru a 1 in 6000 energy analysis versus the aperture of a slit located at the position of the emittance measurement of Fig. 10.

Fig. 12. Final energy vs. initial time for a family of central rays tracked from ion source to extraction. The upper pair of horizontal lines mark off a 1 in 6000 energy interval with the bite positioned for maximum transmission and duty cycle. The shaded areas mark the time intervals when beam would be transmitted. The lower pair of horizontal lines show the effect of a misset energy analysis on the time distribution which also is equivalent to the effect of a change in the rf voltage.

Fig. 13. Gamma ray yield vs. rf time for beam reaching the scattering chamber after 1 in 6000 energy analysis with the 18th and 28th turn phase selection slits in and out. Removing the slits greatly reduces the transmission efficiency from cyclotron center to scattering chamber without appreciably improving the scattering chamber duty cycle even though the internal beam duty cycle has broadened in the manner indicated in Fig. 6.

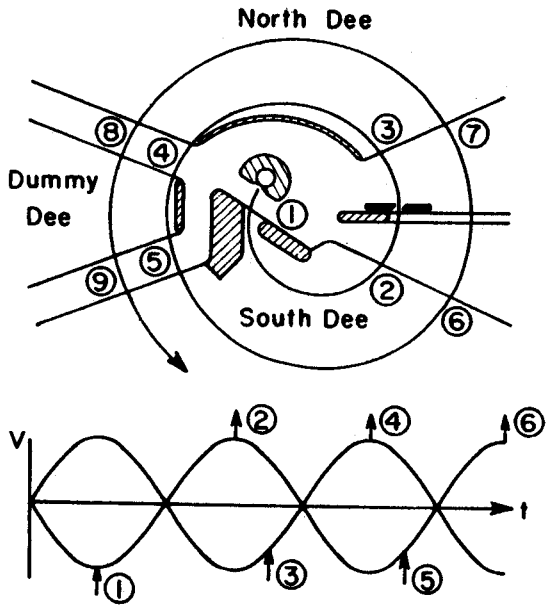
North Dee
Dummy
Dee
South Dee
V
t

Fig. 1

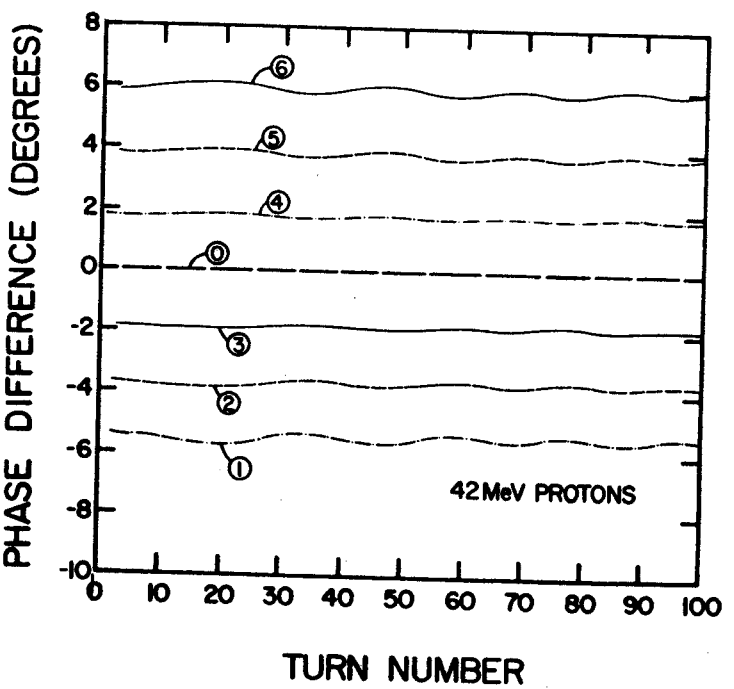
PHASE DIFFERENCE (DEGREES)
TURN NUMBER
42 MeV PROTONS

Fig. 2

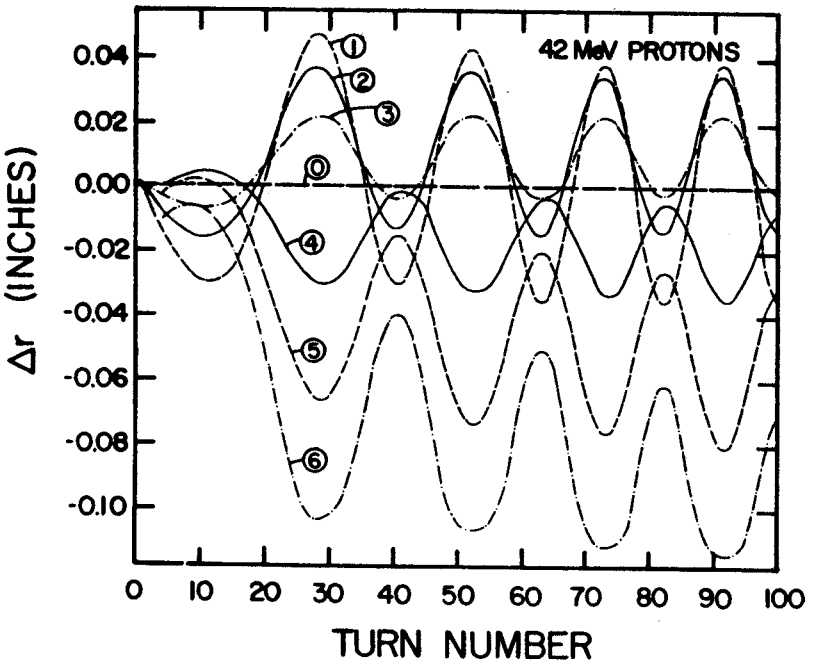
42 MeV PROTONS
Δr (INCHES)
TURN NUMBER
0.04
0.02
0.00
-0.02
-0.04
-0.06
-0.08
-0.10
0
10
20
30
40
50
60
70
80
90
100
①
②
③
⓪
④
⑤
⑥

Fig. 3

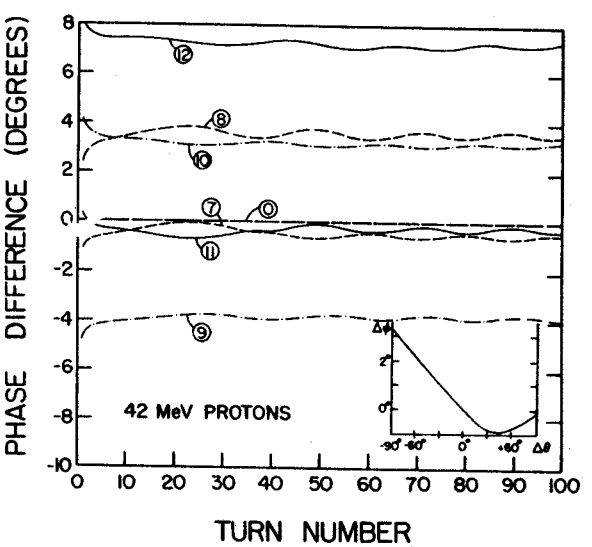
PHASE DIFFERENCE (DEGREES)
TURN NUMBER
42 MeV PROTONS
8
6
4
2
0
-2
-4
-6
-8
-10
0
10
20
30
40
50
60
70
80
90
100
⑫
⑧
⑩
⑦
⓪
⑪
⑨

Fig. 4

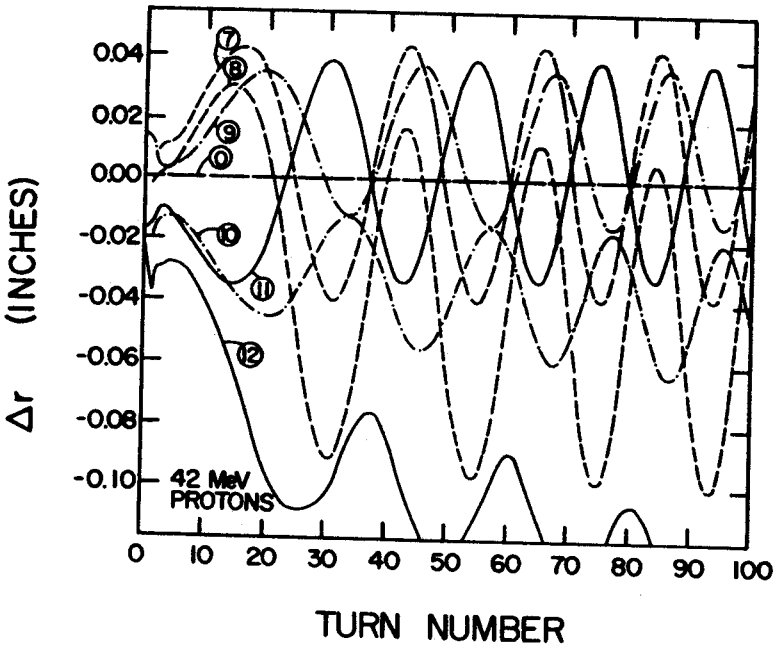
Δr (INCHES)
0.04
0.02
0.00
-0.02
-0.04
-0.06
-0.08
-0.10
42 MeV
PROTONS
0 10 20 30 40 50 60 70 80 90 100
TURN NUMBER

Fig. 5

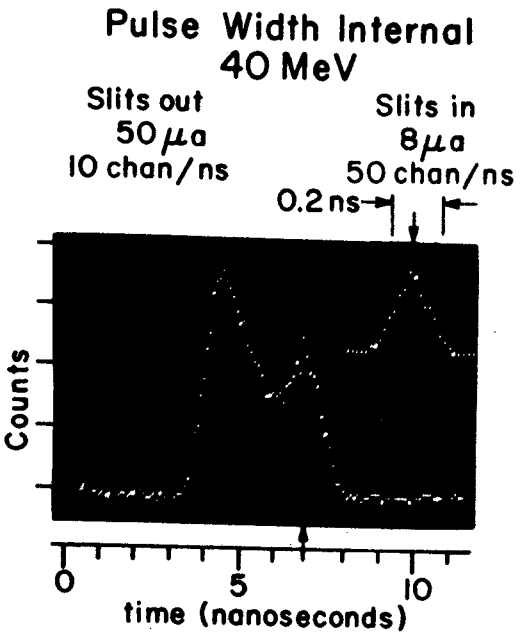
Pulse Width Internal
40 MeV
Slits out
50 μa
10 chan/ns
Slits in
8 μa
50 chan/ns
0.2 ns
Counts
0
5
10
time (nanoseconds)

Fig. 6

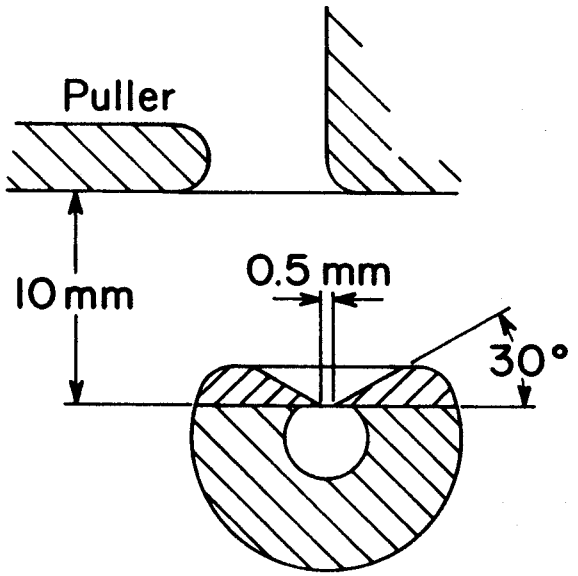
Puller
10 mm
0.5 mm
30°

Fig. 7

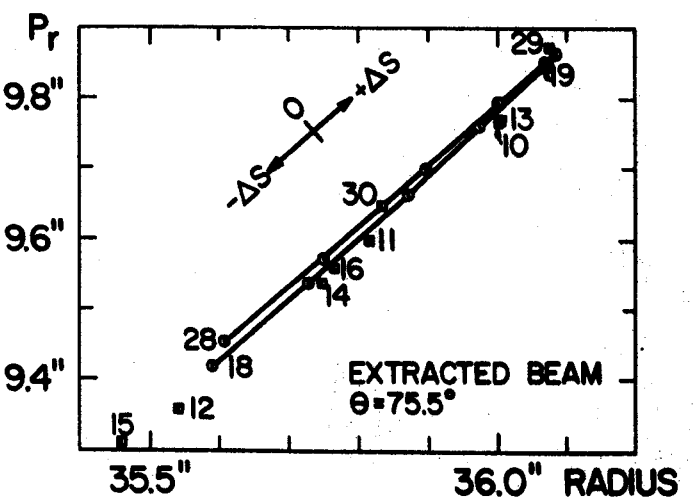
P_r
9.8"
9.6"
9.4"
0
+ΔS
-ΔS
29
9
13
10
30
11
16
14
28
18
12
15
EXTRACTED BEAM
θ=75.5°
35.5"
36.0" RADIUS

Fig. 8

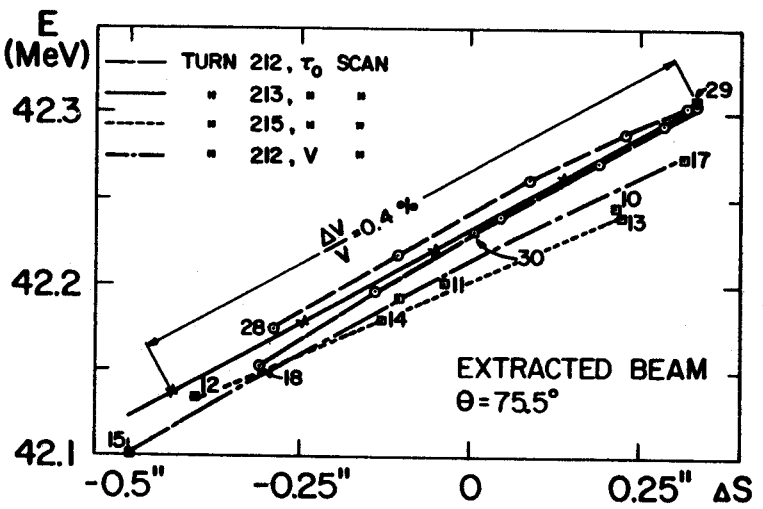
E
(MeV)
42.3
42.2
42.1
TURN 212, τ_0 SCAN
" 213, " "
" 215, " "
" 212, V "
$\frac{\Delta V}{V}$ = 0.4 %
29
17
10
13
30
11
28
14
12
18
15
EXTRACTED BEAM
θ = 75.5°
-0.5"
-0.25"
0
0.25"
ΔS

Fig. 9

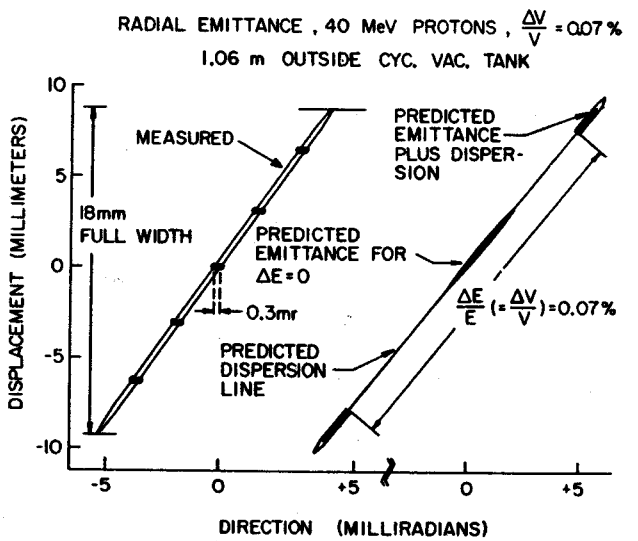
RADIAL EMITTANCE, 40 MeV PROTONS, $\frac{\Delta V}{V}$ = 0.07 %
1.06 m OUTSIDE CYC. VAC. TANK
DISPLACEMENT (MILLIMETERS)
10
5
0
-5
-10
MEASURED
18mm
FULL WIDTH
PREDICTED
EMITTANCE FOR
ΔE = 0
0.3mr
PREDICTED
EMITTANCE
PLUS DISPER-
SION
$\frac{\Delta E}{E}$ ($= \frac{\Delta V}{V}$) = 0.07 %
PREDICTED
DISPERSION
LINE
-5
0
+5
0
+5
DIRECTION (MILLIRADIANS)

Fig. 10

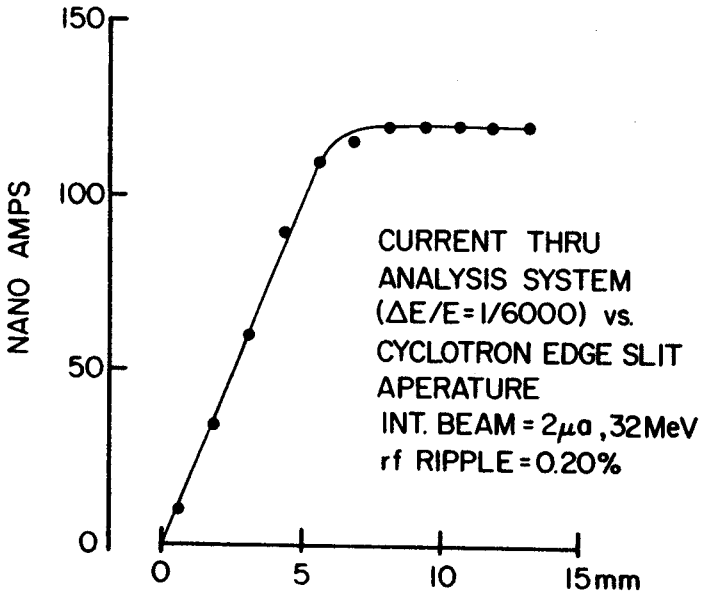
150
100
50
0
NANO AMPS
CURRENT THRU
ANALYSIS SYSTEM
(ΔE/E=1/6000) vs.
CYCLOTRON EDGE SLIT
APERATURE
INT. BEAM = 2μa, 32MeV
rf RIPPLE = 0.20%
0
5
10
15mm

Fig. 11

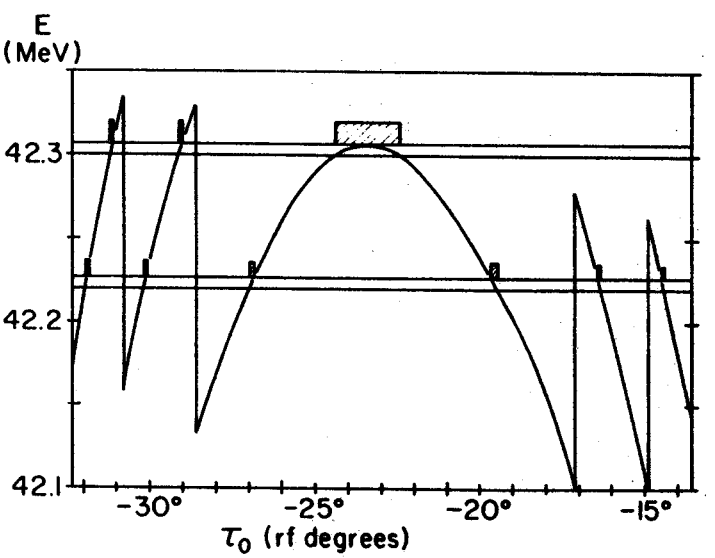
E
(MeV)
42.3
42.2
42.1
-30°
-25°
-20°
-15°
τ_0 (rf degrees)

Fig. 12

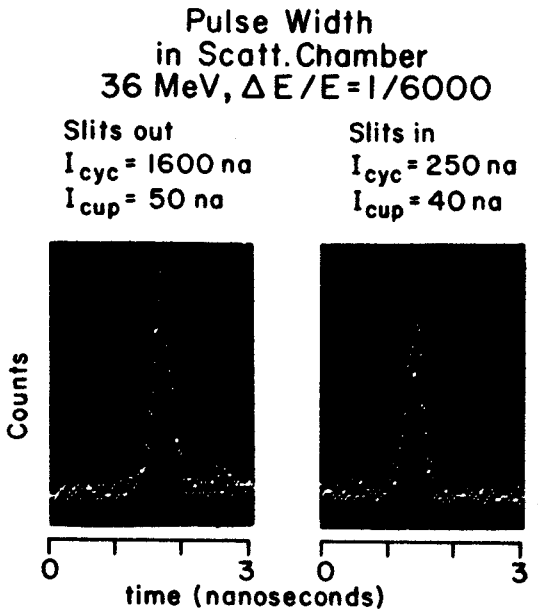
Pulse Width
in Scatt. Chamber
36 MeV, ΔE/E = 1/6000
Slits out
I_{cyc} = 1600 na
I_{cup} = 50 na
Slits in
I_{cyc} = 250 na
I_{cup} = 40 na
Counts
0
3
0
3
time (nanoseconds)

Fig. 13

High Resolution Nuclear Studies Using Cyclotron Beams*

E. Kashy, G. F. Trentelman, and R. K. Jolly
Cyclotron Laboratory and Department of Physics
Michigan State University
East Lansing, Michigan 48823

ABSTRACT

Various types of nuclear experiments which require high resolution particle beams are described. Examples of the performance of the MSU Cyclotron in providing such beams are given. Proton beam currents of approximately 200 na for $\frac{\Delta E}{E} = 1/6000$ resolution are easily obtained at $E_p \geq 25$ MeV with internal beam currents of only 3 μa. The role of dispersion matching is discussed and preliminary results using the laboratory broad range magnetic spectrograph are shown.

1. INTRODUCTION

The imporatnce of high resolution beams and detection systems in the study of the nucleus has been apparent for many years, especially in nuclear spectroscopy, i.e., the classification of nuclear levels, their excitation energies, decay properties, spin, parity, etc. More recently high resolution beams have proved to be essential in certain aspects of the study of Isobaric analog levels. Up to now these studies have been the exclusive domain of Electrostatic accelerators, mostly the VandeGraff type, which have in many ways the most desirable beam properties. In this paper it is shown that cyclotrons like the MSU sector focused cyclotron when used with a highly dispersive beam analyser such as the one presently in use in the MSU Cyclotron Laboratory[1] can compete successfully in a field previously reserved to electrostatic machines, and in some instances improve upon such machines.

2. TYPES OF EXPERIMENT

We can divide the high resolution experiments into two broad types: (a) where energy resolution is required on target and (b) where energy resolution of reaction product is desired. An example of the first requirement is the reaction:

*Supported by the National Science Foundation.

$$^{28}_{14}Si + p \rightarrow ^{29}_{15}P^{*} \rightarrow ^{28}Si + p_o$$
$$\rightarrow ^{28}Si^{*} + p_1$$

Here, a compound system is formed and one is studying energy levels of ^{29}P which then decays to either the incoming or other allowed channels. Detection of the outgoing particles needs only to be good enough to separate various modes of the decay. Since the ^{28}Si + p system can have resonances corresponding to levels of ^{29}P which have width of a few keV or even less[2,3] high resolution of the incident beam is essential to the understanding of the resonance phenomenon.

In the second type of experiment high resolution of reaction product is desired. For example, in the reaction

$$^{28}Si + p \rightarrow ^{28}Si + P_0$$
$$\rightarrow ^{28}Si^{*} + P_1$$
$$\rightarrow ^{28}Si^{*} + P_2, \text{ etc.}$$

one is investigating levels of ^{28}Si target nucleus by the inelastic scattering of protons. Where the ^{28}Si excited levels are closely spaced, the detector resolution rather than the beam resolution is usually the limiting factor. Modern solid state devices and magnetic spectrographs have adequate resolution for studying most low lying levels. Indeed, when using a magnetic spectrograph one can effect dispersion matching and obtain separation of particle groups from levels whose energy difference is smaller than the spread of energy on target.

3. MSU CYCLOTRON AND BEAM ANALYSER

Figure I shows the layout of the MSU Cyclotron and of the beam analysing and switching system. The excellent beam properties of the MSU Cyclotron have been previously reported and new data is being presented at this conference.[4] The properties of the analysing system can be found in Ref. 1. Fig. 1 shows the separated function analysing system, (dipoles, quadrupoles, sextupoles) which provides a highly dispersed beam ($\frac{\Delta E}{E} = \frac{3}{10^4}$ per mm) at its focal plane (S3).

FIGURE 1

The following tabulation presents the results of two recent beam transmission studies with 36 MeV protons for energy resolution on target (full width at half maximum of 1/6000 or 6 keV)

Table I

Date	Run N.	Internal Beam (na)	External Beam (na)	Target Beam (na)
8-6-69	1	900	900	130
8-6-69	2	2800	2800	250
8-20-69	3	700	700	135
8-20-69	4	6300	6300	600

The late August data indicates transmission close to the theoretical limit.[4]

As can be seen from Table I, the beams provided are more than adequate in quantity and quality for the purpose of high resolution nuclear experiments.

4. PERFORMANCE AND RESULTS

Figure 2 shows data taken on the ^{28}Si + p reaction going over a 3 keV resonance at $E_p \simeq 5.2$ MeV. The beam current for an energy spread of 1 keV(FWHM) was approximately 20 na, reflecting principally the fact that at the time of these experiments the cyclotron magnetic field had not been measured at these very low excitations. The data of Fig. 2 is of particular

FIGURE 2

interest in that it displays nearly true line shape of the reaction cross sections, as both beam resolution and target straggling are small compared to the 3 keV resonance width. This data was taken using a simple post acceleration system surrounding the target, i.e. a Faraday cage surrounding the target whose potential could be changed from +3 to -3 kV. It is also worth noting that when taking such data with a very thin, nonuniform target rotation of the target is often necessary to smooth out fluctuation due to changes of the position of the beam on target.[5] In the present instance, both rotating and stationary targets were used, with no noticeable gain seen from using target rotation. This reflects the unusual degree of spatial stability in the cyclotron beam.

Fig. 3 shows scattering cross sections of protons from ^{28}Si around 5.8 MeV. Two very narrow resonance are seen in the Figure. The one at 5.834 MeV is of special interest to the nuclear structure physicist as it is identified[3] as the isobaric analog to the ^{29}Al ground state, with a width of approximately 170 ev. The data of Fig. 3 shows the highest resolution

FIGURE 3

obtained so far for these resonances. The contributions from both straggling and beam exceed the 170 ev value considerably, but it is hoped that both can be reduced in the near future.

Fig. 4 shows proton spectra recently obtained by C. R. Gruhn and collaborators for the reaction $^{64}Ni(p,p')^{64}Ni$ with an overall resolution of 21 ± 2 keV.[7] Using laboratory made Ge(Li) detectors they were able to achieve these excellent results, quite comparable to those achieved by magnetic spectrographs. The cyclotron beam contribution amounted to 6 keV at the incident proton energy of 40 MeV.

FIGURE 4

It is possible to use a highly dispersed beam of incident particles in conjunction with a magnetic spectrograph to resolve reaction particles from nuclear states whose energy difference is less than the energy spread of incident beam. The technique is called dispersion matching[7], and is accomplished by making the energy dispersion of particles on target equal to the natural dispersion of the spectrograph. The result is a reduced image width for a given energy reaction particle, and hence greater resolution.

Fig. 5 shows two monoenergetic rays A and B passing from the target to the focal plane of a spectrograph. If the incident energy along the target varies smoothly making the rays from A more energetic than those from B, the radius of curvature of A will increase slightly, that of B will decrease, and the image width A'B' will be reduced. The beam dispersion apparent to the spectrograph is adjusted by changing the target angle relative to it. Since the spectrograph sees the projection of the beam spot normal to it, this procedure changes the apparent beam spot size for a constant energy spread, and therefore changes the incident dispersion $\Delta E/\Delta X$. The dispersion matching can only be optimized for a limited range of angles of target and spectrograph, but partial matching is realized at all angles.

FIGURE 5

This phenomena was tested by observing elastically scattered protons from ^{209}Bi detected in a 120 micron position sensitive detector. Fig. 6 shows three spectra taken at a bombarding energy of 5.83 MeV, the first two with non-dispersed 3 keV beams of high and low divergence respectively, the third with a 9 keV beam dispersed across the target.

The comparison of the calculated resolution to that observed is shown in Table 2. The resolution in the dispersion matched beam situation is approximately 3 keV better than that calculated for a 9 keV non-dispersed beam. Since the target angle used was not the optimum angle, it should be possible to achieve even better results. Thus, one is able to use much larger beams on target with only small degradation of the resolution.

Table 2

Calculated Contributions to the Experimental Resolution of 5.83 MeV Proton in $^{209}Bi(p,p)$ Scattering

Detector and Electronics	3.0 keV
Beam Incoherence	3.0 keV
Straggling	2.0 keV
Source Size for ΔE_{Beam}=3 keV	2.9 keV
Source Size for ΔE_{Beam}=9 keV	8.7 keV

	Total Resolution Calculated Assuming No Dispersion Matching	Experimental Resolution Obtained
Spect a.	5.5 keV	5.5 keV
Spect b.	5.5 keV	5.7 keV
Spect c.	9.9 keV	7.0 keV

In conclusion, it is clear that the modern cyclotron performs very successfully in high resolution nuclear experiments at low energy while achieving comparable results at energy above those available to electrostatic accelerators. It does this while retaining all the advantages usually associated with cyclotrons, such as high intensity beam at moderate energy resolution.

REFERENCES

1. G. H. Mackenzie, E. Kashy, M. M. Gordon and H. G. Blosser, IEEE Trans. on Nucl. Sci., 450 NS15 (1967).
2. M. W. Brenner, A. M. Hoogenboom and E. Kashy, Phys Rev. 127 947 (1962).
3. B. Teitelman and G. M. Temmer, Phys. Rev. 177, 1657 (1969).
4. H. G. Blosser, Invited paper at this conference.
5. D. R. Maxson, R. K. Jolly and K. C. Krox, Nucl. Instr. and Methods 62, 276 (1968).
6. Gruhn, Invited paper, BAPS 13 1363 (1968)
7. B. L. Cohen, RSI 30 415 (1959).

FIGURE CAPTIONS

Fig. 1 Experimental area of MSU Cyclotron Lab. The arrows indicate the elements which constitute the analysing system.

Fig. 2 Excitation function for the reaction $^{28}Si + p$ at $E_p \sim 5.2$ MeV showing a resonance in the ^{29}P compound system. The solid lines are drawn to guide the eye. (The energy scale should read approximately 10 keV higher than shown.)

Fig. 3 Excitation function for the reaction $^{28}Si + p$ at $E_p \sim 5.83$ MeV showing two compound resonances. For both resonances the experimental resolution is affecting the line shape.

Fig. 4 Spectra of proton inelastically scattered from a ^{64}Ni target. The incident protron energy is 40 MeV.

Fig. 5 Dispersion Matching: If energy on target increases from B to A image width A'B' will be reduced.

Fig. 6 Spectra are $^{209}Bi(p,p)$ with $E_p=5.83$ MeV measured at spectrograph focal plane with position sensitive counter. Spectra A and B were taken with 3 keV beam and divergence limits of ± 3 mr and ± 1 mr respectively; spectrum c with 9 keV dispersed beam incoherent to 3 keV.

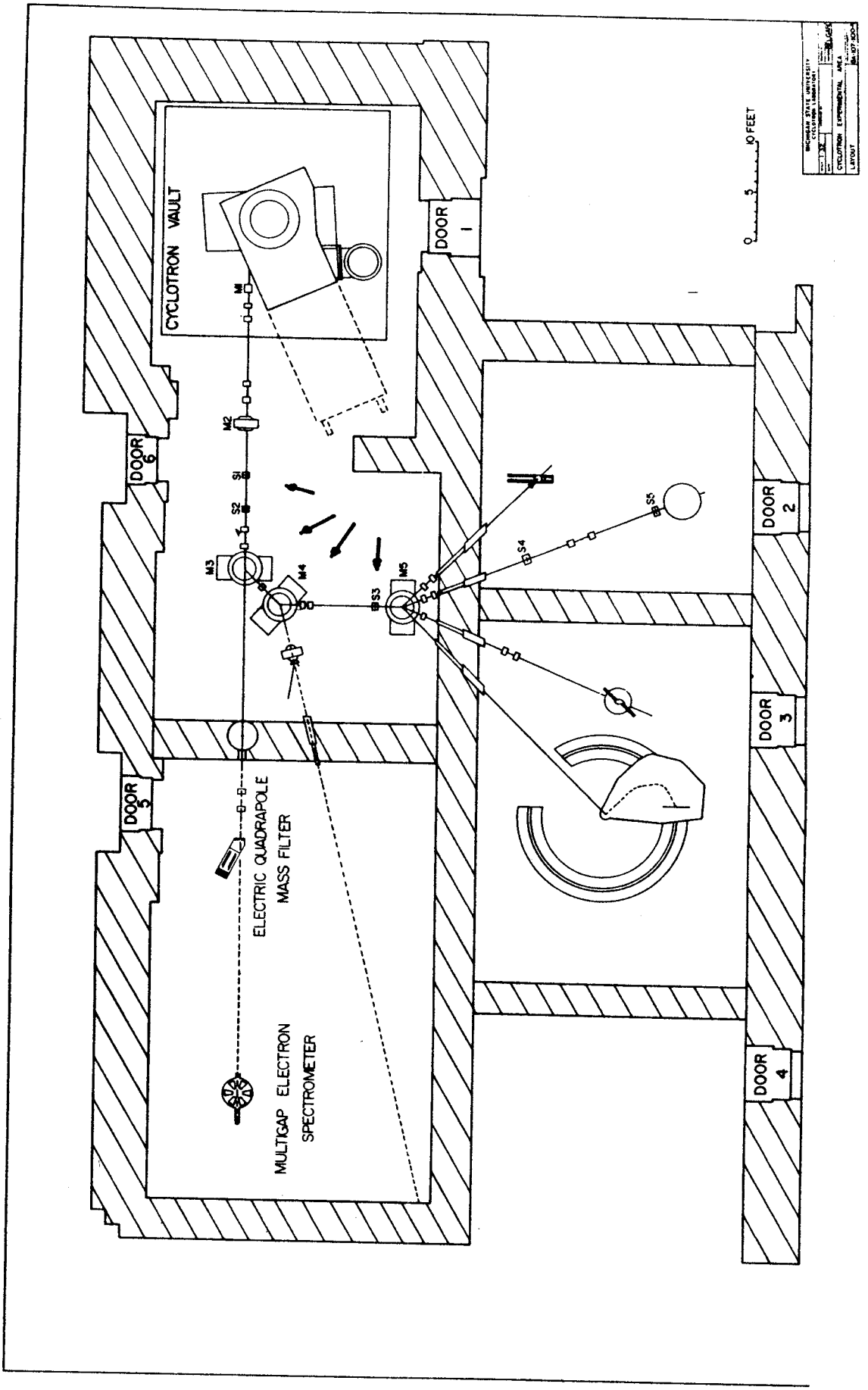
CYCLOTRON VAULT
DOOR 1
DOOR 2
DOOR 3
DOOR 4
DOOR 5
DOOR 6
M1
M2
M3
M4
M5
S1
S2
S3
S4
S5
ELECTRIC QUADRAPOLE MASS FILTER
MULTIGAP ELECTRON SPECTROMETER
0
5
10 FEET

Figure 1

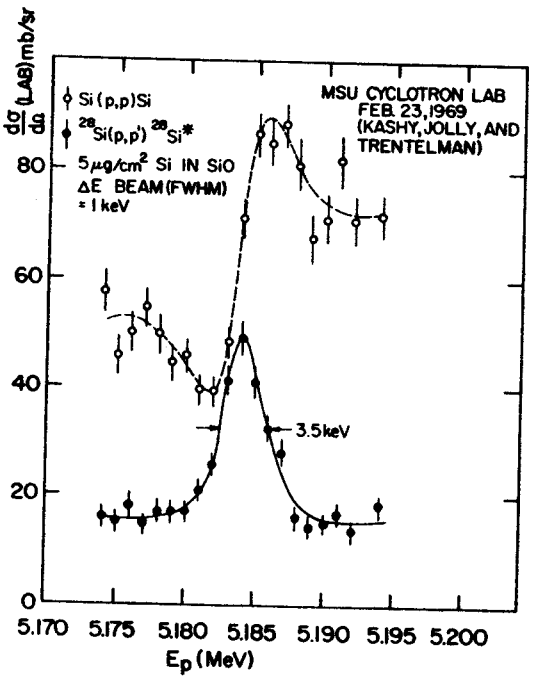

Figure 2

Figure 3

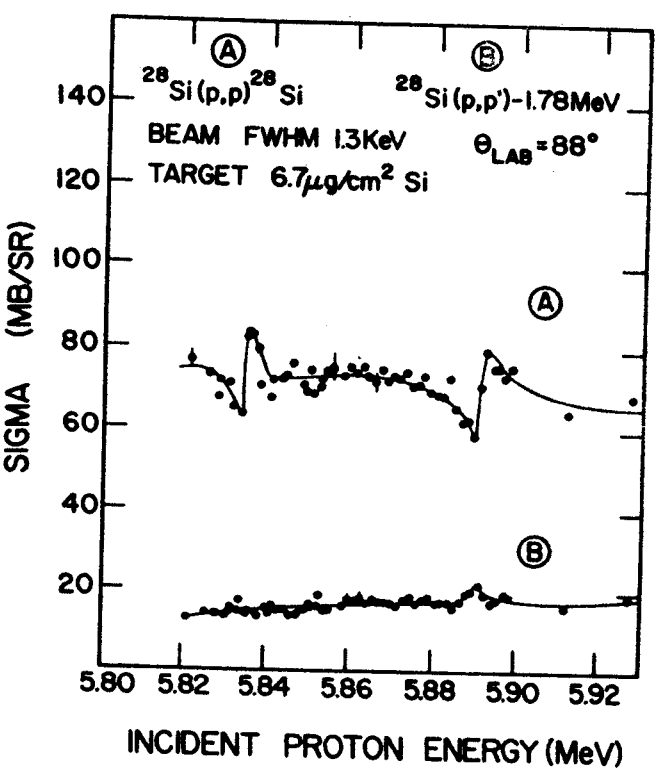

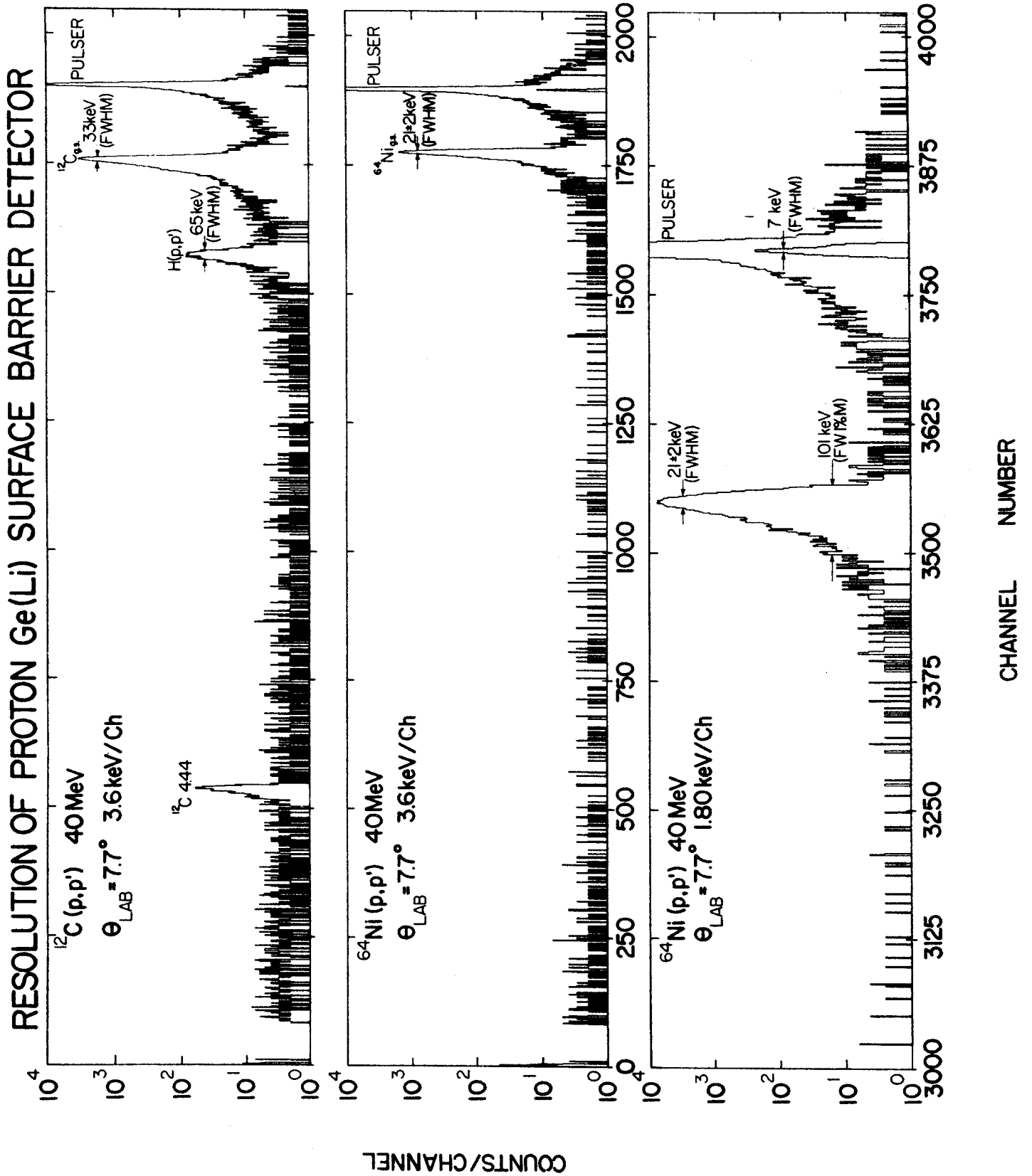
RESOLUTION OF PROTON Ge(Li) SURFACE BARRIER DETECTOR
^{12}C(p,p') 40MeV
θ_{LAB}=7.7° 3.6keV/Ch
^{12}C 444
H(p,p')
65keV (FWHM)
^{12}C$_{gs}$
33keV (FWHM)
PULSER
^{64}Ni(p,p') 40MeV
θ_{LAB}=7.7° 3.6keV/Ch
^{64}Ni$_{gs}$
21±2keV (FWHM)
PULSER
^{64}Ni(p,p') 40MeV
θ_{LAB}=7.7° 1.80keV/Ch
21±2keV (FWHM)
101 keV (FWHM)
7 keV (FWHM)
PULSER
COUNTS/CHANNEL
CHANNEL NUMBER

Figure 4

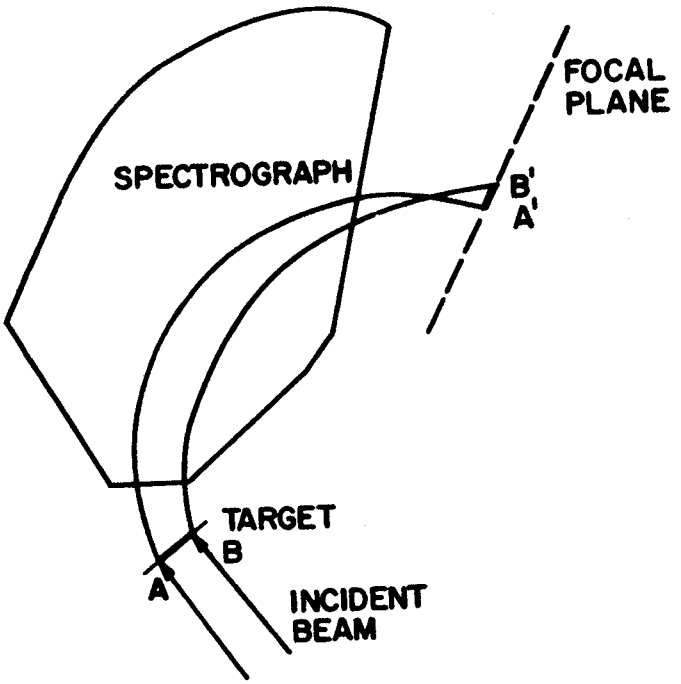

Figure 5

Figure 6

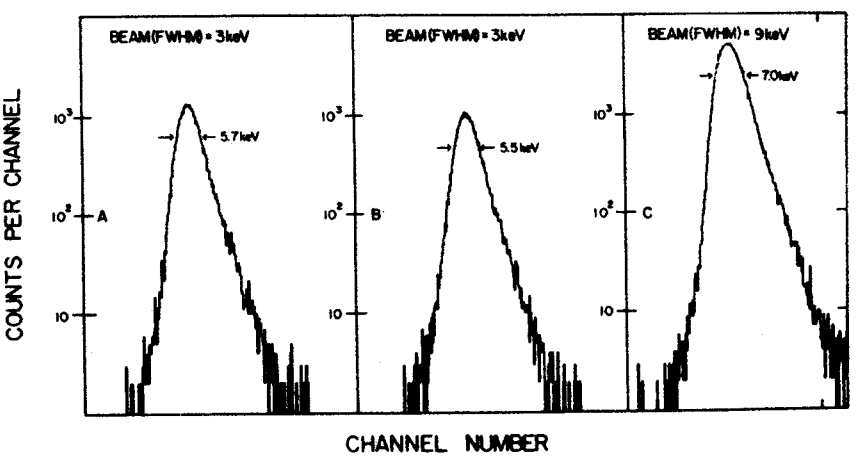

Oxford Cyclotron Conference,
September 1969

The Longitudinal Space Charge Effect and Energy Resolution*

M. M. Gordon
Cyclotron Laboratory, Michigan State University
East Lansing, Michigan, 48823, USA

1. INTRODUCTION

In the design of isochronous cyclotrons with distinctly separated turns at extraction, calculations of energy resolution are customarily based solely on considerations of the beam phase width, the rf voltage and its resultant wave form.[1] Machines of this type have been proposed which aim at 100μA currents with an energy resolution of 10^{-3} or better, and it appears quite likely that the hitherto neglected longitudinal space charge effect will determine the actual current or energy resolution achievable in such cyclotrons.[2] The longitudinal space charge effect was first discussed by T. A. Welton who explained how this effect tends to destroy turn separation by increasing the energy spread within a turn.[3] Welton also pointed out that this effect could be alleviated by accelerating the beam off the peak of the rf wave.[4] More recently, W. B. Powell carried out approximate calculations which indicate that the longitudinal space charge effect could nevertheless still be very serious.[5] The present paper summarizes an extensive analysis of the longitudinal space charge effect and provides formulas for calculating the resultant energy spread within a turn under certain conditions.

The MSU cyclotron has been operating successfully in a separated turn mode with 100% extraction for the past three years and therefore constitutes a real prototype for the "separated turn isochronous cyclotron". Recently, the phase selection technique used in this machine has been refined so that proton beams up to 10μA can be obtained with a phase width of 1.4°(fwhm).[6] This narrow phase width implies an energy resolution of: $\Delta E/E=10^{-4}$ attainable under operating conditions computed to minimize this quantity at extraction.[7] However, the dee voltage has so far been regulated only to: $\Delta V/V=2$ to 6×10^{-4}, so that this parameter restricts the energy resolution achievable in the external beam. Experimental measurements of the longitudinal space charge effect have recently been carried out for the

first time in any cyclotron. Although these results are still preliminary, they demonstrate conclusively that the properly minimized energy resolution increases with beam current. The explicit calculations presented here are aimed toward accounting for these observations.

2. VORTEX MOTION

Consider the nonrelativistic motion of a charge q in the isochronous magnetic field B as viewed in a reference frame rotating with constant angular velocity $\underline{\omega}$ whose direction is antiparallel to B and whose magnitude is the isochronous angular frequency. If there are no electric fields present, then on a time-average basis the charge q will be at rest. Considering the electric field vector $\underline{F}$ as a perturbation, the steady-state (nonoscillatory) velocity vector $\underline{v}$ is then given by:

$$m_o \underline{\omega} \times \underline{v} = q\underline{F}; \tag{1}$$

that is, the Coriolis force has the effect of reversing the magnetic field direction as seen by q in the rotating frame. Since this steady-state velocity is perpendicular to both $\underline{\omega}$ and $\underline{F}$, it is directed along the equipotential curves associated with $\underline{F}$. In the rotating frame the rf electric field has a time-average component in the azimithal direction given by: $V_1/(2\pi r)$, and Eq. (1) shows that this field causes the particles to move radially outward with the velocity: $dr/dt = qV_1/2\pi m_o \omega r$, so that qV_1 is the average energy gain per turn. If the rf electric field is absent, the $\underline{F}$ is produced entirely by the space charge and Eq. (1) indicates that the charges will then circulate clockwise about the point of maximum potential, thereby establishing a "vortex" in the space charge cloud as viewed in the rotating frame. This vortex motion is depicted in Fig. 1. Since both

FIGURE 1

electric fields are actually present, the resultant steady-state motion is a superposition of these two phenomena.

The longitudinal space charge effect has been extensively investigated for other types of accelerators.[8] Synchrotron oscillations as viewed in the appropriate rotating reference frame also constitute a type of vortex motion. In a synchro-cyclotron, for example, the vortex motion produced by the space charge force reinforces the vortex motion associated with the synchrotron oscillations thereby increasing the frequency of these oscillations.

3. ENERGY CHANGES

A properly relativistic treatment of the problem can be achieved by introducing the polar angle transformation: $\theta = \omega t + \phi$, where the phase ϕ gives the azimithal position of the particle in the rotating frame. Treating the electric fields as perturbations, the steady-state motion is then described by:

$$d\phi/dt = -(q/m\omega R)F_r(R,\phi), \tag{2a}$$

$$dE/dt = (qV_o\omega/2\pi)\cos\phi + q\omega RF_\theta(R,\phi), \tag{2b}$$

where: m, E are the relativistic mass and energy of the particle, R is the mean orbit radius, qV_o is the peak energy gain per turn produced by the rf voltage, and F_r, F_θ are the components of the electric field produced by the space charge. These then are the equations for the longitudinal motion appropriately modified to include the space charge force.

Assuming the field is perfectly isochronous, then the space charge cloud has the "sector" shape depicted in Fig. 1, and F_r has an appreciable value only near R=0 and $R=R_{max}$. Eq. (2a) shows that F_r acts like an error in the isochronous field given by: $\delta B = -(c/\omega R)F_r$, and estimates of this error for the MSU cyclotron yield: $\delta B/B \sim 10^{-6}$ which is quite trivial. Moreover, F_r acts over relatively few turns and under these conditions only the component F_θ will have a significant effect. If the magnetic field deviates substantially from the isochronous value as a function of radius, then there is an additional term in Eq. (2a) which produces large excursions in the values of ϕ. In such cases, the shape of the space charge cloud will be considerably deformed from the simple shape shown in Fig. 1, and the calculation of the longitudinal space charge effect will consequently be greatly complicated. For the 36 MeV proton field considered here later, the ϕ variation in the region of significance (R=25 to 71 cm) is less than $\pm 5°$,[9] and will therefore have a negligible effect. Hence, we assume hereafter that the magnetic field is perfectly isochronous and that the values of ϕ are therefore constants.

If only the space charge force is considered, then Eq. (2b) yields the following value for the energy of the particle:

$$E_{sc}(\phi,\tau) = 2\pi q\int RF_\theta d\tau, \tag{3}$$

where: $\tau = \omega t/2\pi$ is the "turn number". Taking $\phi=0$ at the azimuthal center of the space charge distribution, it then follows from symmetry that both F_θ and E_{sc} are odd functions of ϕ, and that $E_{sc}(\phi=0) = 0$. Consequently, the space charge force causes the particles with positive/negative ϕ values to gain more/less energy than those at the central $\phi=0$ value thereby increasing the energy spread within a single turn; this result coincides with that found by Welton.[3] The value of F_θ falls off with increasing $|z|$, and if this decrease is significant, then the value of F_θ should be properly averaged over the particle's axial oscillations before calculating E_{sc}.

The energy of the particle is: $E=E_{sc}+E_{rf}$, where E_{rf} is the energy acquired from the rf voltage. In the formulation of Eq. (2b) it was assumed that the particles with $\phi=0$ have the maximum energy gain per turn, and this choice minimizes the energy spread in the absence of the space charge force. The additional energy spread produced by the space charge force can be partially cancelled by a suitable decrease in the rf frequency. If the rf angular frequency is changed from ω to $\omega(1-\varepsilon)$, then the factor $\cos\phi$ in Eq. (2b) is replaced by $\cos(\phi+\varepsilon\omega t)$, and integration of Eq. (2b) then yields:

$$E_{rf}(\phi,\tau_o)=E_o[\cos\phi - (\alpha\tau_o/J)\sin\phi], \qquad (4)$$

where $\alpha = 2\pi\varepsilon$, $J = 1+(1-\alpha^2\tau_o^2)^{1/2}$, and $E_o=qV_o\tau_o$, with $\tau_o = (\sin\alpha\tau)/\alpha$ being the "original" turn number. The frequency shift method for cancelling the space charge effect has limitations. The ϕ dependence of E_{sc} and E_{rf} are generally quite different so that the cancellation can only be partial. Moreover, this frequency shift amplifies E_{sc} since it increases the total number of turns inside the cyclotron and thereby increases both the strength and duration of F_θ. Nevertheless, the frequency shift method has been successfully used in the MSU cyclotron to maintain turn separation when the beam current is increased.

4. CHARGE DENSITY

In characterizing the charge density it is convenient to introduce an electric field unit: $F_o = IB/cDV_o$, which is specified by the following operational parameters: I = time-average beam current, $B = (m_o c\omega/q)$, D = duty-factor $=\Delta\theta/2\pi$, and V_o is given in Eq. (2b). In terms of conventional units, we have:

$$F_o(V/m) = (0.9)I(\mu A)B(kG)/DV_o(kV), \qquad (5)$$

where the symbols in parentheses give the units for each quantity. For the 36 MeV proton beam considered later with: I = 7.2 μA, $\Delta\theta = 1.4°$, B = 11.4 kG, and V_o = 170 kV, we have: F_o = 110 V/m.

Ignoring temporarily the discrete turn structure in the sector-shaped space charge cloud (Fig. 1), the charge density ρ can be written as:

$$\rho(R,\phi,z) = F_o(\Delta\theta)K(R)\,\sigma_2(\phi)\,\sigma_3(z), \tag{6}$$

assuming that the functional dependence of ρ can be split into three separate factors and where: $\int\sigma_2(\phi)d\phi = \int\sigma_3(z)dz=1$, $K(R) = (V_o/V_1)\gamma^3$, with $\gamma = (1-\omega^2R^2/c^2)^{-1/2}$ and qV_1 is the actual energy gain per turn. If the angular width of the beam is sufficiently large to make the ϕ dependence of V_1 significant, then this dependence should be incorporated into $\sigma_2(\phi)$. For conditions obtaining in the MSU cyclotron, the ϕ dependence of V_1 is insignificant. The phase distribution within the internal beam has been measured and found to be symmetric and triangular in shape with $\Delta\theta = 1.4°$, full width at half maximum.[6] These data then imply:

$$\sigma_2(\phi)d\phi = (1-|\phi|/\Delta\theta)(d\phi/\Delta\theta), \tag{7}$$

for $|\phi|<\Delta\theta$, and $\sigma_2=0$ for $|\phi|>\Delta\theta$.

In order to obtain a realistic form for $\sigma_3(z)$, the axial phase space distribution of the particles should be considered. Data on this distribution obtained from both internal and external beam measurements are available for the MSU cyclotron.[6] These data suggest a form for $\sigma_3(z)$ having a symmetric trapezoidal shape with a full width of 0.75 cm and with Δz=0.5 cm, full width at half maximum. The results obtained for E_{sc} are insensitive to the detailed shape of σ_3 and depend mainly on the value of Δz.

Because of the separated turn structure of the beam, the microscopic charge density is a rapidly oscillating function of radius. In the MSU cyclotron, the radial width of a single ion pulse is $\delta R \cong 0.8$ mm while the radius gain per turn is ΔR = 2.5 mm at R = 50 cm. Calculations of the longitudinal space charge effect which include this turn structure have also been carried out, and the results indicate that this microstructure is not significant when: $\delta R << \Delta z$, and $\Delta R << R\Delta\theta$. These calculations are complicated and will not be discussed here.

5. ELECTRIC FIELD CALCULATIONS

In calculating the electric field we assume a two dimensional cartesian model in which $y = R\phi$ and $\rho = \rho(y,z)$ at a given R value. Here, $F_\theta(R,\phi,z)$ is replaced by $F_y(y,z)$ and R becomes simply a parameter. Eq. (6) is replaced by:

$$\rho(y,z) = F_o(\Delta y)\ K(R)\sigma_2(y)\sigma_3(z), \tag{8}$$

with $\Delta y = R\Delta\theta$, and $\int\sigma_2(y)dy=1$. This model greatly simplfies the field calculation and can be justified when $\Delta\theta$ is small. The analysis includes the effect of image charges by assuming that conducting planes at $z = \pm z_d$ enclose the beam. In the MSU cyclotron, the two dees and one dummy dee, which have an aperture of 3.81 cm, enclose the beam for 320° of azimuth; it therefore seems reasonable to neglect the remaining 40° and to simply take $2z_d = 3.81$ cm. These conducting planes are quite important since they cause the field contribution from distant charge elements to fall off exponentially with distance, which then improves the validity of the model.

Assuming $\rho(y,z)$ is an even function of z, then the electrostatic potential is given by the real part of the following function:

$$W(y,z) = -2 \int dy'\ dz'\ \rho(y',z')\ \ln[\tan k'(\zeta - \zeta')], \tag{9}$$

where $k' = \pi/4z_d$, $\zeta = z+iy$, $\zeta' = z'+iy'$. Taking the real part of $(-\partial W/\partial y)$ yields:

$$F_y(y,z) = 2 \int dy'\ dz'\ \ \rho(y',z')(L_1/L_2), \tag{10}$$

where: $L_1 = k \cos\xi \sinh\eta$, $L_2 = \sin^2\xi + \sinh^2\eta$, $\xi = k(z'-z)$, $\eta = k(y-y')$, and $k = \pi/2z_d$.

The above expression can be cast into a form more suitable for computation by using Eq. (8) and introducing $f(y-y',z)$ given by:

$$f(y-y',z) = (\Delta y) \int\sigma_3(z')(L_1/L_2)dz', \tag{11}$$

with L_1 and L_2 given above. This function, which is proportional to the field produced by an infinite charge strip of thickness dy' located at y', is an odd function of (y-y') and has a discontinuity at y=y' for $z \simeq 0$. To remove any difficulty arising from this discontinuity, the function G(y,z) is calculated from:

$$G(y,z) = \int[\sigma_2(y')-\sigma_2(2y-y')]\ f(y-y',z)\ dy', \tag{12}$$

where the integration extends from $y' = -\infty$ only up to $y'=y$. A comparison with Eq. (10) then yields:

$$F_y(y,z) = 2F_o K(R) G(y,z), \tag{13}$$

so that G is a dimensionless field function which is specified by the geometric parameters: $R\Delta\theta$, Δz, z_d.

Fig. 2 shows curves for G vs. ϕ for R=25 and 71 cm (τ= 25, 200). These curves were obtained for the triangular σ_2 and the trapezoidal σ_3 discussed in Sec. 4. These curves show that $G(\phi)$ varies slowly with R; indeed, the curve for R = 50 cm (τ = 100) is almost indistinguishable from that shown for R = 71 cm (τ = 200). The function $G(\phi)$ always approaches an asymptotic limit for $R|\phi|>z_d/2$; this is an important consequence of the image forces, which holds independent of the detailed shape of σ_2 or σ_3. Making use of this conclusion and the definition of G in Eq. (13), we can then rewrite Eq. (3) as:

$$E_{sc}(\phi) = 4\pi q F_o \, G(R_o\phi) \int RK(R)d\tau, \tag{14}$$

with $R_o \tilde{=} 0.7\, R_{max}$. Thus, the ϕ dependence of E_{sc} is nearly identical to that of G evaluated at R_o.

For a given axial beam width Δz, the values of $G(\phi)$ decrease substantially as $\Delta z \to 2z_d$, the aperture of the surrounding conductors. This is shown in Fig. 3 which presents curves of G vs. ϕ obtained for: $2z_d = \infty$, 3.81, 1.27 cm, and with Δz = 1 cm. Moreover, the value of G falls off more sharply with increasing $|z|$ when $\Delta z \to 2z_d$. These conclusions, which result from the effect of the image charges, hold quite generally and clearly indicate how the longitudinal space charge effect can be rendered harmless. When $\Delta z << 2z_d$, as is the case for the MSU cyclotron, then only $G(\phi)$ values for z=0 need be considered. Excessively small values for Δz should certainly be avoided since G diverges logarithmically as $\Delta z \to 0$.

Fig. 4 presents G vs. ϕ curves for three different distributions: rectangular, trapezoidal, and triangular, all having $\Delta\theta = 4°$(fwhm). These curves clearly demonstrate that the ϕ dependence of G, and hence also that of E_{sc}, is quite nonlinear and strongly dependent on the form of $\sigma_2(\phi)$.

FIGURES 2, 3, 4, & 5

6. DISCUSSION OF RESULTS

The experimental data and associated calculations presented here pertain specifically to the 36 MeV proton configuration of the cyclotron in which the peak energy gain

per turn is 170 kV. The phase distribution within the beam is given by Eq. (7) with $\Delta\theta = 1.4°$; this implies a full energy width of 11 kV, and a width of 2.8 kV for 75% of the protons. Fig. 5 displays three "turn patterns" obtained with the differential probe which cover about the last 50 turns inside the machine. The top pattern is for I = 1μA with rf frequency f = 17.65 MHz adjusted to yield minimum turn width at extraction. The middle pattern was obtained under identical conditions but with ion source output increased so that I = 7.2μA; the loss of turn separation here clearly demonstrates the longitudinal space charge effect. The bottom pattern was obtained under the same conditions as the middle one but with a frequency shift $\Delta f = -2.8$ kHz, so chosen as to obtain again the sharpest turn definition; this result indicates that the space charge effect can be compensated by an appropriate frequency shift as discussed in Sec. 3. These figures are copies of the output from a strip chart recorder with a moving pen of limited resolution so that details of turn structure are lost. When these patterns were observed, the dee voltage regulation was $\Delta V/V \triangleq 6 \times 10^{-4}$, corresponding to an energy variation $\Delta E \triangleq 22$ kV. Note that beyond $\nu_r = 1$ some turns are missing from these patterns because of the precessional motion of the orbits which are driven off-center at this resonance. Also, the differential probe is located 160° upstream from the deflector entrance.

More recently, the dee voltage regulation has been improved to: $\Delta V/V = 2 \times 10^{-4}$, corresponding to an energy variation of about 7 kV. With the slits of the beam transport-analyzing system set to pass an energy slice of only $\Delta E = 6$ kV, it was observed that for an internal beam of 0.75μA, a current of 0.15μA was transmitted, and when the internal beam was increased to 6μA, the transmitted current became 0.6μA. In each case the rf frequency was adjusted to yield the maximum transmission. Since the percentage transmission decreased from 20% to 10% when the internal beam current was increased, it must be concluded that the rf frequency adjustment only partly cancels the energy spread produced by the space charge effect.

Values of E_{sc} *vs.* ϕ were calculated using Eqs. (3, 5, 13) with $G(R\phi)$ functions displayed in Fig. 2. Because of the phase selection slits, the first 28 turns constitute the "injector" for the remainder of the cyclotron; hence, the calculation of E_{sc} justifiably omitted these first 28 turns. In addition, the calculation approximated the contribution from the last

20 turns where the beam is in the nonisochronous extraction region and where F_θ falls off to zero. A correction factor was also included which takes account of the increased number of turns produced by an rf frequency shift. The values of E_{rf} vs. ϕ were calculated from Eq. (4) with E_o = 36 MeV. The resultant value of $E - E_o = E_{sc} + E_{rf} - E_o$ then represents the energy displacement of particles with given ϕ from those at the central phase evaluated at extraction.

The three $(E - E_o)$ vs. ϕ curves presented in Fig. 6 were obtained for I = 1μA and for frequency shifts: $-\Delta f$=0.3, 0.9, and 1.5 kHz. In these three cases, the total energy spread is: 38, 26, and 50 kV respectively; while the percentage of particles with ΔE<6 kV is: 5, 28, and 69% respectively. These results show why the rf frequency shift cannot fully compensate for the energy spread produced by the space charge effect.

FIGURES 6 & 7

The $(E - E_o)$ vs. ϕ curves displayed in Fig. 7 represent an attempt to account for the observations reproduced in Fig. 5 and discussed above. It was assumed that the energy spread for I = 1μA could be neglected so that the curves shown for ΔI = 6.2μA should actually correspond to the I = 7.2μA data. Although the observed frequency shift was Δf = -2.8 kHz, additional curves are shown for twice and thrice this value. These curves yield a full energy spread of ΔE = 193, 128, and 310 kV respectively, with 50% of the particles having ΔE<152, 96, and 62 kV in the three cases. Since the observed frequency shift has only a small uncertainty, it must be concluded that the calculated E_{sc} values are about twice as large as required to fit this observation. This discrepancy may be accounted for by a partial neutralization of the space charge produced by negative ions in the residual gas; at I = 7.2μA, the beam density is 2×10^7 protons/cm^3 which corresponds to a pressure of only 10^{-9} torr, while the vacuum attained in the beam space is about 10^{-5} torr; thus, if about one negative ion per 10^4 neutrals is present, these negative ions would significantly reduce the longitudinal space charge effect. Experimental and theoretical work on this problem will continue.

I am indebted to my colleague H. G. Blosser for supplying the experimental data and for his helpful discussions and suggestions. I am also grateful to D. A. Johnson for carrying out the computer work and preparing the figures.

7. APPENDICES

The subsection 7.1 below should be appended to Sec. 2 following the first paragraph there. The subsection 7.2 below should be appended at the end of Sec. 5.

7.1. Local Vortices

In an isochronous cyclotron with separated turns the charge density and resultant electrostatic potential have local maxima at the center of each ion bunch or turn. As a result, the central region of each turn will execute a local vortex motion in which the ions remain within the same turn; the ions outside this region, however, will partake in the overall vortex motion of the total charge cloud and it is only this motion which tends to destroy the turn separation. Since the length $r\Delta\theta$ of the turn is generally much greater than the radius gain per turn, the local vortices are so small and feeble that their presence can be neglected entirely. This rule may not apply when the cyclotron operates under pulsed conditions; in the MSU cyclotron, for example, where nine out of ten ion pulses can be completely rejected, the radial separation between ion bunches is then always greater than the length $r\Delta\theta$, so that the local vortices are quite significant in this case. However, this special situation will not be treated here. It should be noted that in those cases where the vortex motion seriously changes the charge distribution, an iterated calculation may then be necessary to achieve adequate self-consistency.

7.2. Special Formulas

For the rectangular distribution: $\sigma_3(|z| < z_o) = 1/2\ z_o$ and $\sigma_3(|z| > z_o) = 0$, the function f of Eq. (11) becomes simply:

$$f_o(y-y',z) = (\Delta y/2z_o)[\tan^{-1} X_1 + \tan^{-1} X_2], \qquad (15)$$

where $X_{1/2} = [\sin k(z_o \pm z)]/\sinh \eta$, and $|\tan^{-1} X_{1/2}| < \pi/2$. In this case, the evaluation of G(y,z) via Eq. (12) requires only one integration. If in addition, $\sigma_2(y)$ is also a rectangular distribution with $\Delta y = 2y_o = 2R\Delta\theta$, then the following approximate formula for G(y,z=0) is obtained:

$$G_o(y) = U_2 \tan^{-1}(1/U_2) - U_1 \tan^{-1}(1/U_1) + (1/2)\,\ell n[(1+U_2^2)/(1+U_1^2)] - \ell n(T_1/T_2), \qquad (16)$$

where: $U_{2/1} = (y_o \pm y)/z_o$, and $T_{2/1} = [\tanh k'(y_o \pm y)]/(y_o \pm y)$,

with $k' = \pi/4z_d$. The terms involving $U_{2/1}$ represent an exact evaluation of the contribution from the charges between the conducting planes, while the last term is the contribution from all the image charges calculated only to zero order in z_o; hence, this expression is valid only if $z_o << z_d$. This $G_o(y)$ can be used to quickly obtain estimates of the longitudinal space charge effect. It should also be noted that G can be explicitly evaluated (by solving Poisson's equation) for $\sigma_3 \sim \cos(nkz)$ where n is any odd integer, with $\sigma_2(y)$ having any simple analytical form.

REFERENCES

* This work was supported by the National Science Foundation.

1. M. M. Gordon, Nucl. Instr. and Meth. 58, 245 (1968).
2. Rickey, Sampson, and Bardin, IEEE Trans. Nucl. Sci., (1969); to be published.
3. T. A. Welton, Sector-focused Cyclotrons, Nucl. Sci. Ser. Report No. 26, NAS-NRC-656, p. 192 (Wash., D.C., 1959).
4. T. A. Welton, private communication, 1958.
5. W. B. Powell, private communication, September 1967.
6. H. G. Blosser, preceding paper at this conference.
7. M. M. Gordon, IEEE Trans. Nucl. Sci. NS-13, 48 (1966).
8. E. D. Courant, Ann. Rev. of Nucl. Sci. 18, 435 (1968).
9. Berg, Blosser, and Gordon, Nucl. Instr. and Meth. 58, 327 (1968).

FIGURE CAPTIONS

Fig. 1 Vortex motion within the space charge cloud in an isochronous cyclotron. The electric field $\underline{F}$ is that produced exclusively by the space charge itself. Angular velocity: $\underline{\omega} = -(q/mc) \langle \underline{B} \rangle$.

Fig. 2 Plots of field function G vs. phase ϕ at z=0, obtained for R =25 cm and 71 cm. Charge distribution has triangular shape in azimuthal direction and trapezoidal shape in axial direction. Figure demonstrates slow variation of $G(\phi)$ with R between turns 25 and 200.

Fig. 3 Plots of field funtion G vs. phase ϕ at z=0 and R = 50 cm. Charge distribution has triangular shape in azimuthal direction and rectangular shape in axial direction. Curves demonstrate dependence of G on conductor aperture: $\Delta z_d = \infty$, 3.81, 1.27 cm when beam height is Δz = 1 cm.

Fig. 4 Plots of field function G vs. ϕ at z=0 and R = 50 cm. Charge distribution has rectangular shape in axial direction, and different curves shown correspond to following shapes in azimuthal direction: rectangular, trapezoidal, and triangular.

Fig. 5 Three differential probe "turn patterns". Top and middle pattern demonstrate that the longitudinal space charge effect destroys turn separation when the beam current increases from 1 to 7.2μA, while bottom pattern shows that turn separation can be restored by an appropriate frequency shift: Δf = -2.8 kHz. Arrow at r=28.61 inches shows location of the ν_r=1 resonance.

Fig. 6 Plots of energy displacement $(E-E_o)$ vs. phase ϕ at E_o = 36 MeV as calculated from theory for I = 1μA beam current. Different curves correspond to frequency shifts: $-\Delta f$ = 0.3, 0.9, and 1.5 kHz. Figure demonstrates that frequency shift only partly cancels space charge effects.

Fig. 7 Plots of $(E-E_o)$ vs. phase ϕ at E_o = 36 MeV as calculated from theory for ΔI=6.2μA increase in beam current. Different curves correspond to frequency shifts: $-\Delta f$ = 2.9, 5.9, and 8.8 kHz. Compare with Figs. 5 and 6.

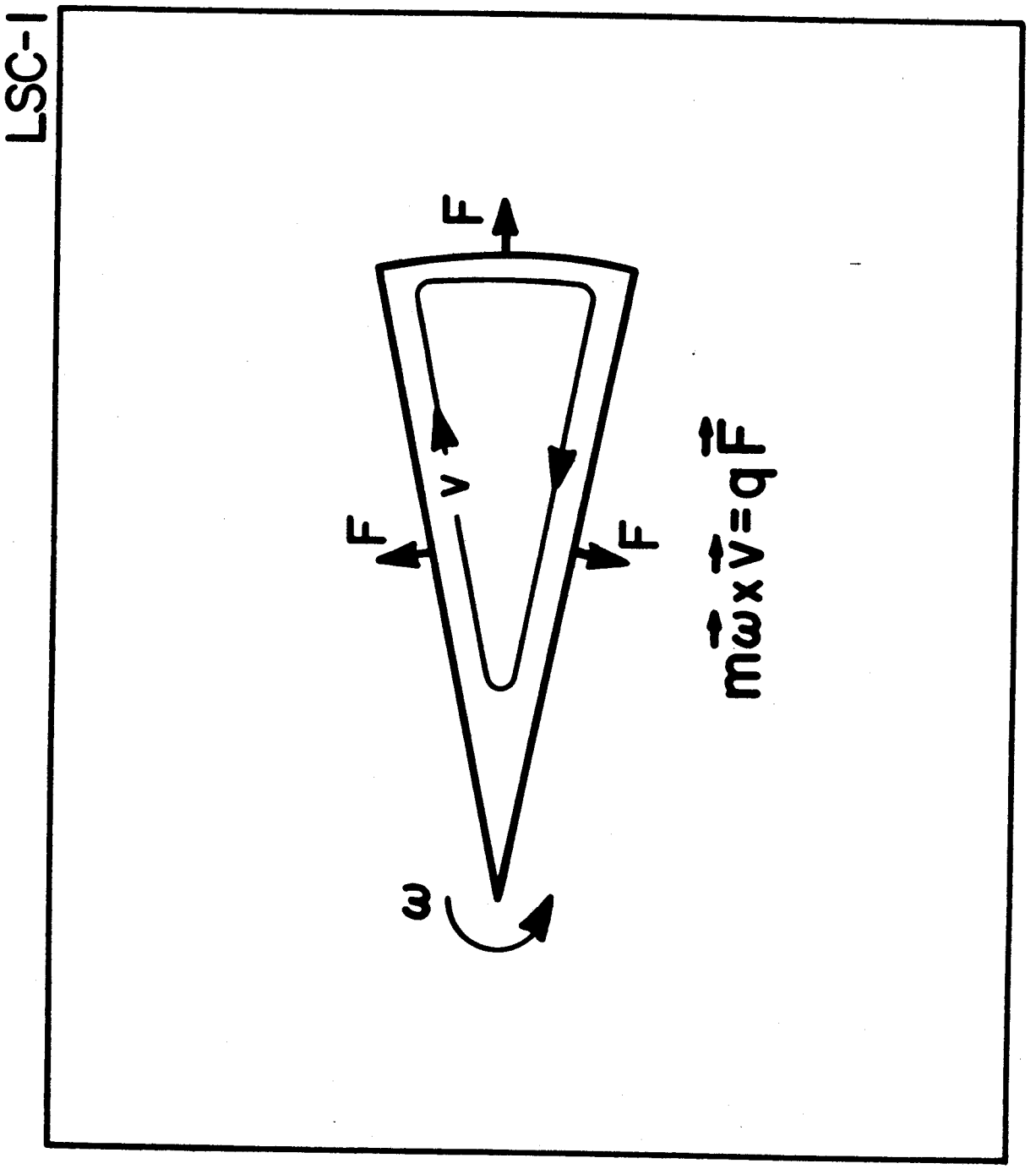

Figure 1

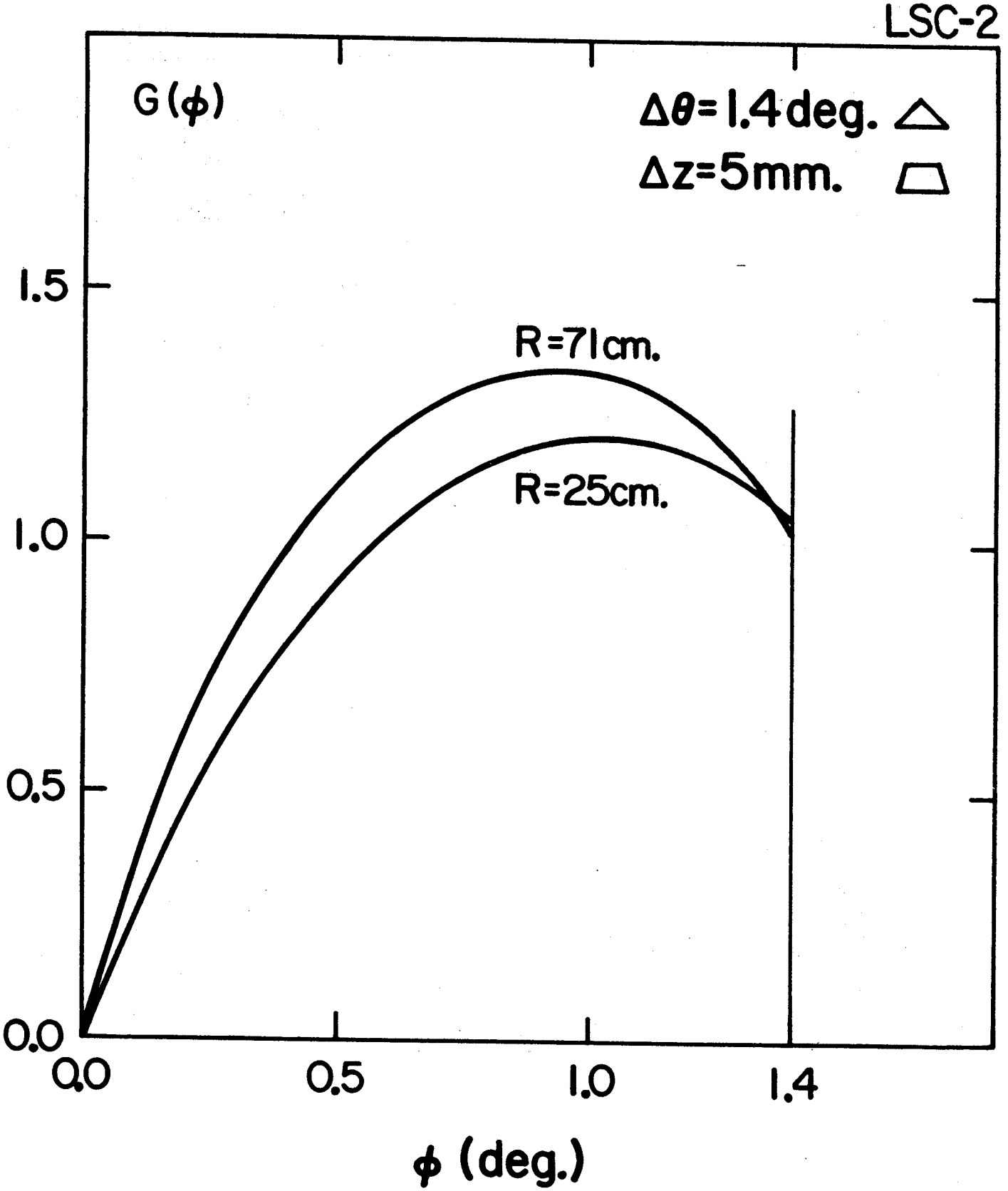

Figure 2

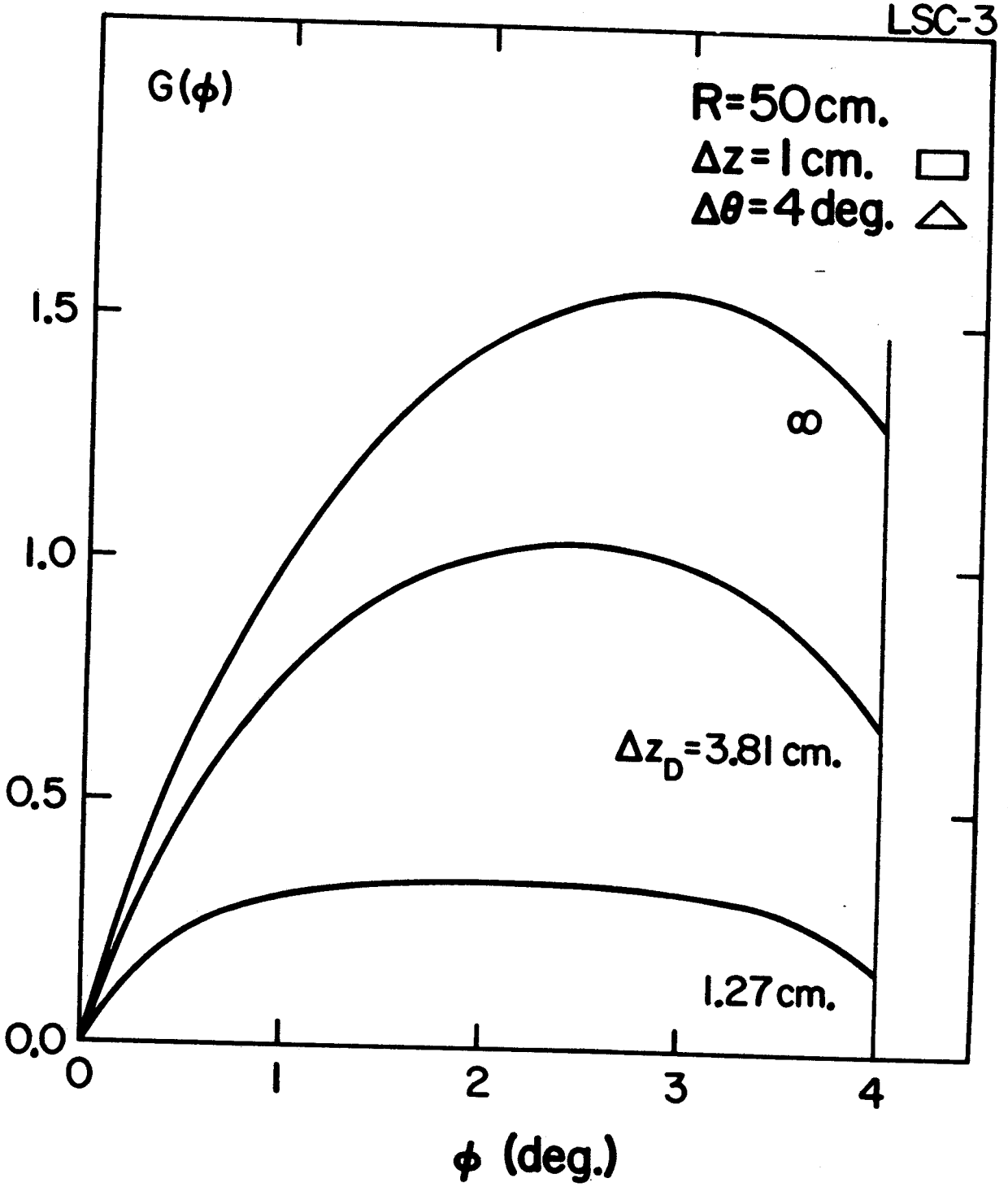
LSC-3
G(φ)
R=50cm.
Δz=1cm.
Δθ=4deg.
1.5
1.0
0.5
0.0
∞
Δz_D=3.81cm.
1.27cm.
0
1
2
3
4
φ (deg.)

Figure 3

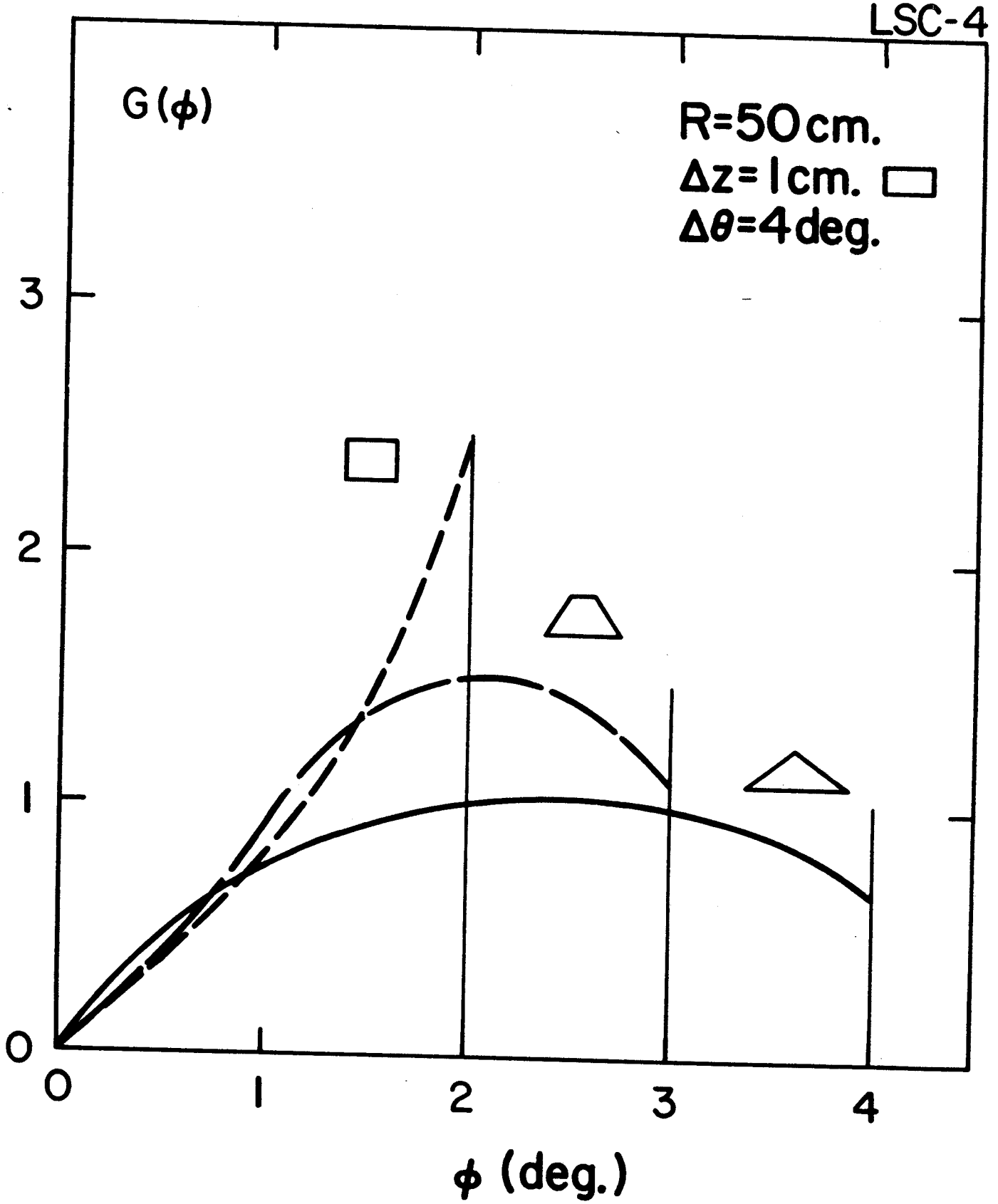

Figure 4

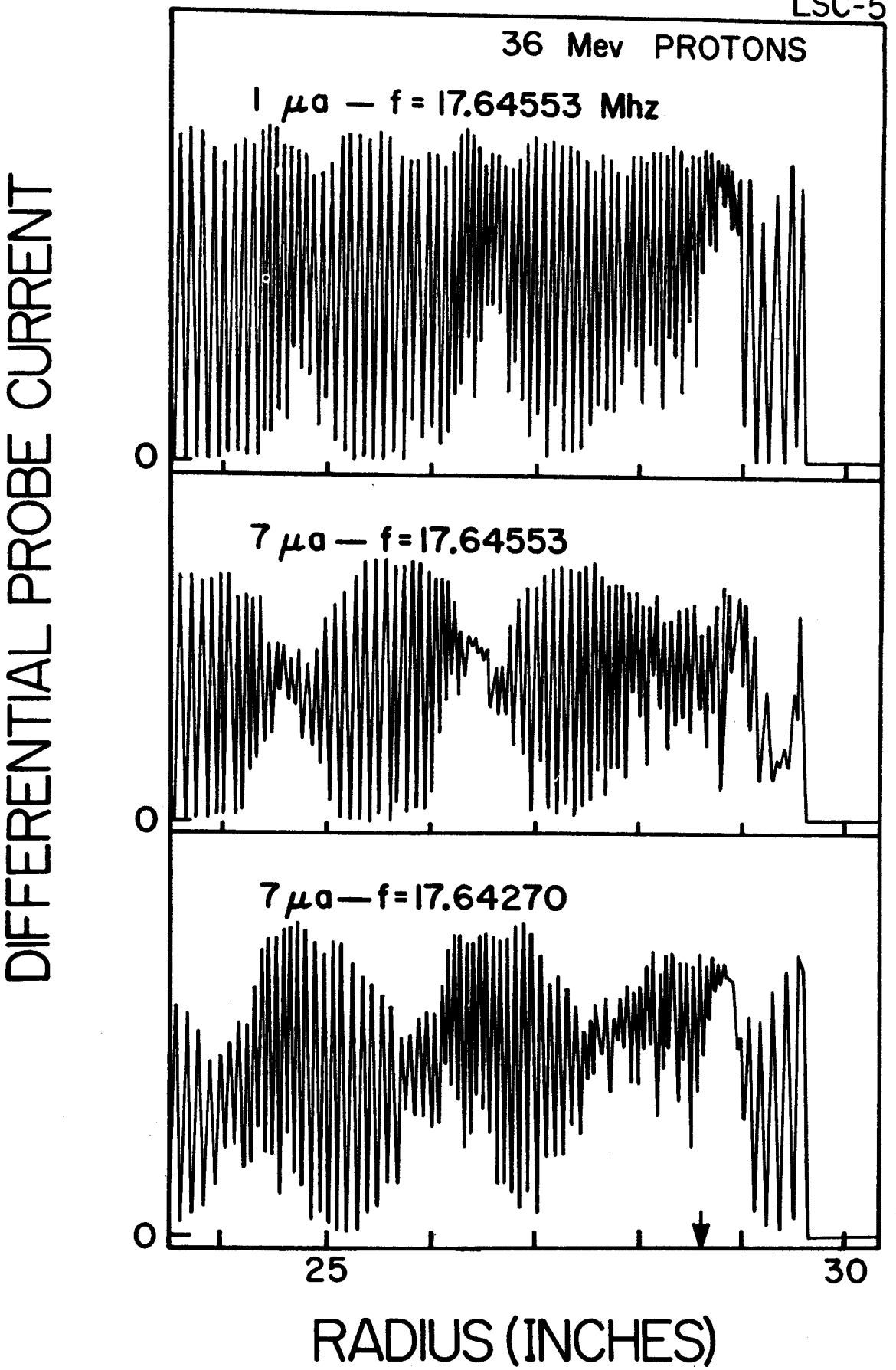
LSC-5
36 Mev PROTONS
1 μa — f = 17.64553 Mhz
7 μa — f = 17.64553
7 μa — f = 17.64270
DIFFERENTIAL PROBE CURRENT
0
0
0
25
30
RADIUS (INCHES)

Figure 5

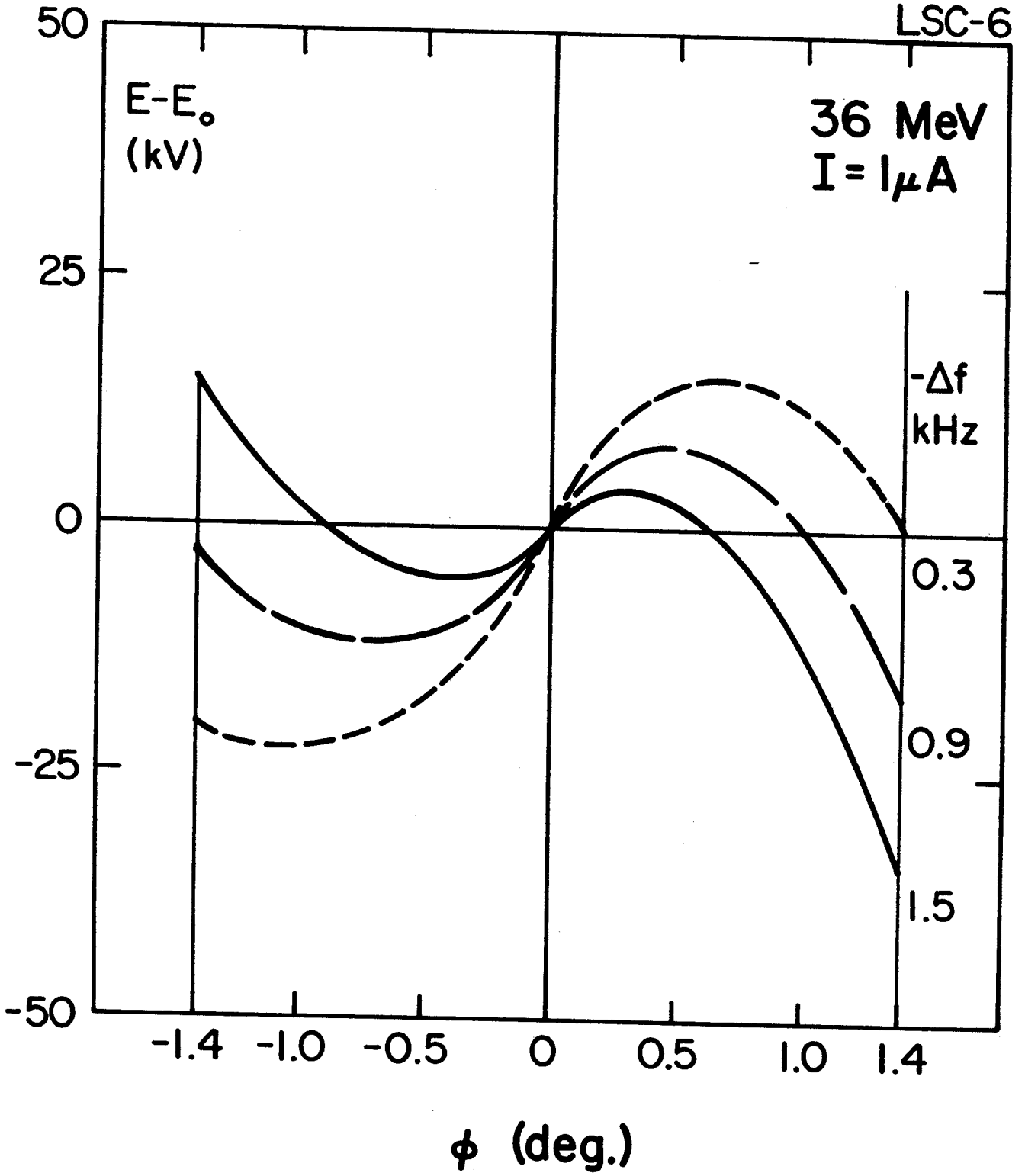
LSC-6
E-E₀
(kV)
36 MeV
I = 1μA
50
25
0
-25
-50
-Δf
kHz
0.3
0.9
1.5
-1.4
-1.0
-0.5
0
0.5
1.0
1.4
φ (deg.)

Figure 6

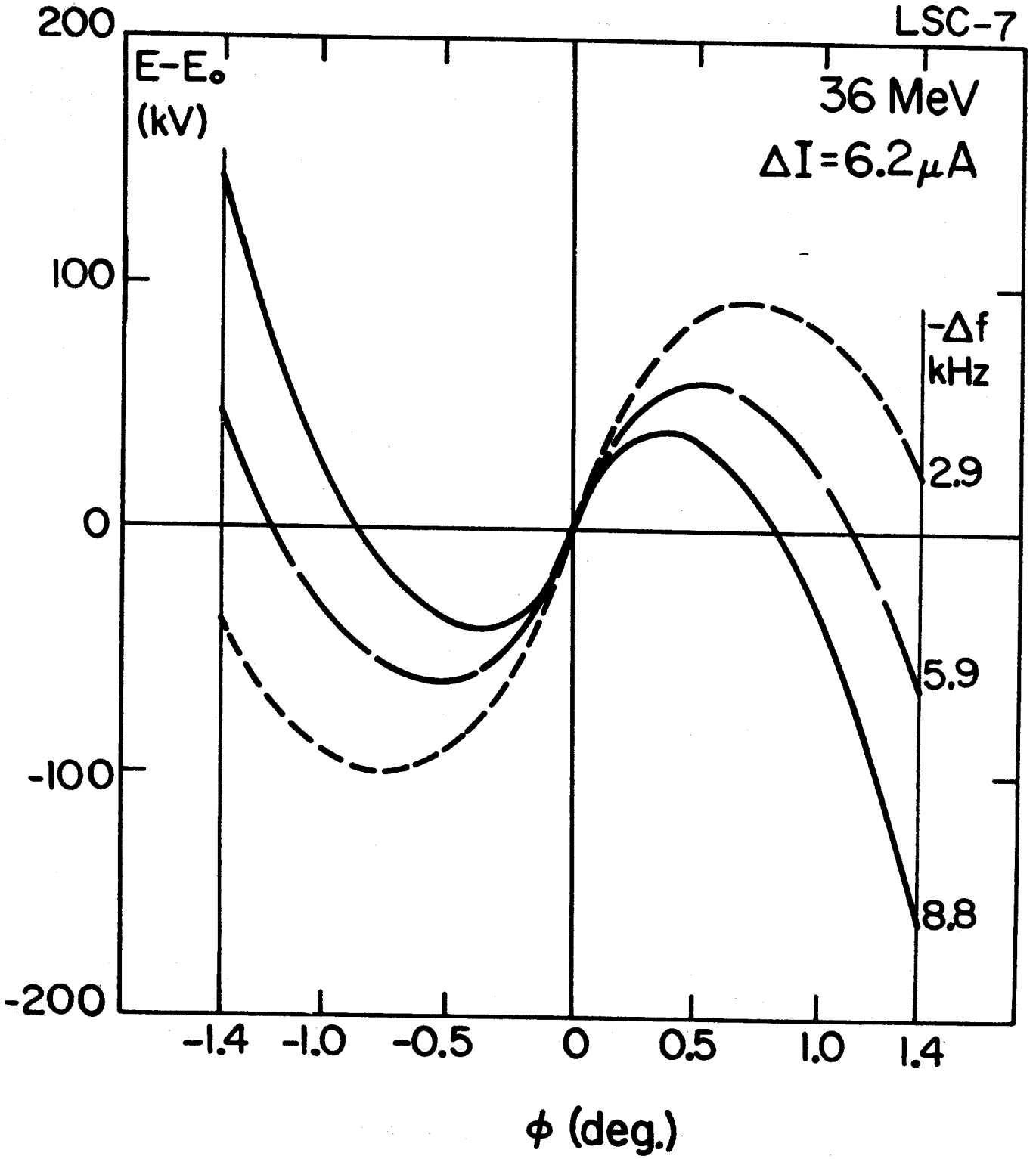
LSC-7
E-E₀
(kV)
36 MeV
ΔI=6.2μA
200
100
0
-100
-200
-Δf
kHz
2.9
5.9
8.8
-1.4
-1.0
-0.5
0
0.5
1.0
1.4
φ (deg.)

Figure 7

The Cyclotron and the Computer, a Look at the Present and the Future*

R. A. deForest
Cyclotron Laboratory and Department of Physics
Michigan State University
East Lansing, Michigan 48823

ABSTRACT

This paper shows that current approaches to computer control are philosophically the same and that there is a second approach which the author hopes to see implemented in the future, since it offers advantages in both cost and flexibility. Some details of computer hardware and software are described because they are of importance to persons making long range decisions. At this time, without sophisticated systems of logging and analysis which future cyclotron control systems will have, it is not possible to forecast in detail changes computer control will bring to beam quality; however, computer control will dictate more careful attention to the engineering details of beam defining devices and beam measuring devices.

1. FUNDAMENTAL CONTROL CRITERIA

Two basic and obvious principles have dictated all control systems whether computerized or not. 1) All important settings of cyclotron parameters must be available to the human operator at all times. 2) The operator must be able to alter those settings without introducing undesirable step changes.

These two criteria have been responsible for the complexities of current systems in which the computer is an appendage rather than an integral part of control systems. We can not do away with these criteria, but we can alter the method of control to eliminate complexity and duplication of hardware.

2. GENERALIZATION OF THREE BASIC CONCEPTS

It is important to note that initial set-up of an accelerator (before twiddling) is a digital process as far as the operator is concerned. For example, RF frequency is set to some number of Herz; trim coil currents are set to some number of amperes; etc.

*Supported by the National Science Foundation.

The human operator must know what the existing settings are, so he gathers this information through "analog to digital converters', ADC's, if we generalize the term ADC to its broadest sense. In this sense a panel meter indicating a number of amperes is an ADC just as much as a digital voltmeter is.

The same generalization applies to the "digital to analog converter', DAC. Hence, we may refer to a console knob as a DAC. The human operator inputs a number of turns of the knob. The result of his action will be the setting of some analog quantity, for example, the mechanical aperture of a collimating slit.

To clear up any possible confusion about terminology—the words digital quantity refer to any numerical expression of some physical situation. Analog quantity refers to the physical situation itself. Although the origin of the word "analog" would not imply this interpretation, it has historical reasons for its existence and, if we are going to talk computer language, it is best to stick with it.

The third concept is that of the multiplexor, MUX. In its broadest sense, it is a device which can route information from many sources to a single receiver or from a single source to many receivers. In this sense, the human operator is serving as a part time multiplexor when he reads first one panel meter and then another.

All set-up operations may be described in terms of these three concepts if we include the human as part of some of the control loops. Someone who holds down a toggle switch until he sees a given number on a digital display is himself part of a DAC.

3. THE CLASSICAL CYCLOTRON CONTROL SYSTEM

The generalizations made above allow us to describe the conventional control system by the diagram in Fig. 1.

FIGURE 1

It is important to notice the duplication of equipment. Any single direct ADC is read very seldom on the average. Yet it and its associated hardware must be paid for in installation costs.

It is also important to note that the human is performing a task which is trivial for electronic equipment but to which he is not well suited. He is working as a multiplexor, a very bad

multiplexor. He is slow; sometimes he turns the wrong knob; sometimes he forgets a set-point altogether. Who would want to buy a human multiplexor when it has these specifications?

I think we are all agreed that it would be wiser to let computer hardware take care of the trivia and leave the human to perform as decision-maker and analyst, a role in which he has at least a statistical chance of doing some good.

4. PRESENT CONCEPTS OF COMPUTER CONTROL

The preceding remarks have gone through many people's minds with the result that there has been much talk about computer control but, to my knowledge, very little implementation.

Berkeley[1] introduced computer controlled set-pointing on the 88" and MSU has implemented set-pointing and data gathering via their computer -beam probe collaboration (this is not to say that MSU has any intentions of standing still at its present level of accomplishment). The Maryland Cyclotron envisions computer control[2] and the SIN group in Zurich has been making studies[3]. All of these sytems are essentially the same in basic philosophy. They consider the computer as an appendage to the control system. They do not see it as an integral part. Figure 2 illustrates the current philosophy.

FIGURE 2

Figure 2 is not the simple structure it appears to be, because the box labeled Manual Console is in fact a duplication of the complicated structure of Figure 1. Figure 3 shows the same system as Figure 2 with sufficient detail added to allow us to look at the inefficiencies of current systems.

Now we come back to the two basic criteria mentioned earlier. The operator must have all settings available to him and must be able to intervene to change them. There have been two approaches to this problem, both within the context of the computer appendage. LRL, Berkeley and MSU have used helipots driven by motors to perform as both DAC's and set-point indicators. The proposals of Maryland and the SIN group use digital switches on the manual console exchangeable with digital output from the computer to set electronic DAC's which perform as references for various devices. In the Maryland-SIN system, another path must be provided to inform the human operator of any current set point.

This approach invokes considerable duplication of hardware. If one has plans for beam optimization, the same information which

is supplied to the human must be supplied to the computer, but via a second path. The human-computer interface implies some communications device. At its simplest level a teletype or electric typewriter. But, if the computer is able to keep tabs on everything, why not let it report information through its own link to the human? Why supply a second information reporting path? Further, the information reporting system on the manual console uses a large number of ADC's whereas the computer can get by with one or two. This extra equipment is outlined with the dashed line you see in Figure 3.

FIGURE 3

5. A NEW APPROACH TO COMPUTER CONTROL OF CYCLOTRONS

The approach I am going to present is not new in itself; it is only new to Cyclotrons. The idea is to eliminate the manual console altogether and carry on all communications through the computer. This is illustrated in block diagram form in Figure 4 and in some greater detail in Figure 5. Note that this approach implies no more DAC's than the totally computerized control system and has reduced ADC's to one.

FIGURE 4 and 5

The Los Alamos LINAC group has done considerable investigation of this control method[4,5,6]. Butler reports[4] that a study by EG & G indicates that the fully computerized system with no manual console costs the same to construct as a manual console system without computer. This study was a quantitative measurement of points we have just discussed qualitatively.

6. SOME DETAILS

A. If the computer is to have full control and is to be able to handle abnormal situations:

1. Interlock status of each controllable device must be available to the computer,
2. The computer must be able to turn devices on and off;

B. There are always special devices which deliver many data points at a time, for example a beam probe or a beam scanning wire. The interface to such devices should be constructed so that they can "take care of themselves". In other words, the software should be able to request a block of data from the device without having to supervise the collection of that data. If

this policy is not followed, the computer will be wasting valuable computing time on a trivial operation. The MSU implementation will be discussed below as an example.

7. TYPES OF COMPUTER

A. A complete cyclotron laboratory requires the following computer services:

1. Processing of codes of the type most installations take to a computing center, e.g. DWBA codes for the experimenters and orbit codes for the machine development people.
2. Real-time data collection. At MSU we have demonstrated that the computer is a more useful and flexible tool for data collection than specialized devices like hardwired multichannel analysers.
3. Real-time data analysis. The experimenter should be able to determine if he is getting reasonable data during the course of his experiment.
4. Off-line data analysis. The experimenter should be able to make detailed analyses of previously recorded data.
5. Control of the cyclotron and the experiments.

I mention all of these computer uses because they enter into decision making when one is planning a laboratory. It is reasonable to ask, "Should I do all of these jobs with one computer or should I use more than one?"

At the present time, the multi-machine approach has many advantages because of the recent strides which have been made in process control. Several vendors[7,8,9] offer monitors and compilers which allow process control software to be written in a high level language. These are supplied for process control machines. The vendors of big machines capable of multi-programming and time-sharing are not yet to my knowledge offering such a software package. Michigan State was able to use the single computer approach only because a number of clever graduate students were available to conceive and to implement our own systems software[10,11] but most people I believe would hesitate to attempt third generation systems software without the support of a very sophisicated staff of programmers.

8. WHAT WILL THE COMPUTER DO FOR US?

A. Once the hardware and software for cyclotron data collection and set-pointing are available, closed-loop control will no longer be a wild dream. At MSU, for example a simple call from FORTRAN will initiate the measurement of two beam traces using the differential beam probe. The data so acquired are analysed and produce corrections for five cyclotron parameters, main field, Dee voltage, beam phase, x centering, y centering.[12] At present, insufficient set-pointing hardware is available to completely bypass the human operator in making the corrections to the settings; however, it is only a matter of time before that will be available.

B. With the computer at hand, gathering and processing of information can be speeded up to the point that analyses previously too time-consuming to be worthwhile will become routine. Again, I refer to our experience with the beam probe as an example of this.

C. Data logging and monitoring will provide a useful tool for trouble shooting and machine improvement. At present, only the well trained operator can quickly pinpoint what malfunction is causing beam troubles. The ever watchful computer will be able to spot drifts in equipment immediately and report this. If the drifts are not due to a major malfunction, the computer will be able to correct for them.

D. I firmly believe the computer will mean faster machine improvement from initial startup, more extensive investigations of machine behavior resulting in better machines, faster trouble shooting and faster set-up resulting in more useful up-time.

9. BRIEF DESCRIPTION OF THE MSU SYSTEM

At the present time, the analog input path and the analog output paths have been implemented.

The differential beam probe is using the analog input in a manner very similar to the Karlsruhe hardware[13]. The probe is mounted on a lead screw driven by a stepping motor. The data sampling is synchronized to the stepping motor.

The analog output path has been coupled to the trim coils through motorized helipots. Most of the hardware has been installed to extend the analog output to control of the RF set-pointing and the internal beam-slit set-pointing.

At present we can take a beam trace by executing the FORTRAN statement "CALL PROBE (NERROR)". NERROR is a flag used to indicate whether or not meaningful data has been returned. Data is retrieved by a function subroutine call to NPASS1(I) or NPASS2(I), which yield the Ith datum in the first or second pass respectively. When CALL PROBE is executed, the probe will move from outer radius to inner radius and back again. Data is taken on both passes. Data transfer is handled by two interrupt routines thereby allowing the computer to do other work concurrent with gathering data from the probe. The above mentioned calls will retrieve data collected and stored by the interrupt routines.

To the FORTRAN programmer, setting a trim coil simply requires the statement CALL POTSET (NPOT, VALUE). NPOT identifies which potentiometer is to be set and VALUE indicates the desired setting.

A FORTRAN program called CYCSET (CYClotron SETup) generates set-up sheets for each desired energy and makes calls to set point where hardware has been implemented. In the event a hardware failure has occurred, the library routine POTSET, described above, will generate an error message which is printed on the set-up sheet, thus calling the operator's attention to a malfunction.

It should be pointed out, to the credit of our graduate student programmers[10,11], that the above described cyclotron-computer interrelationships are time-shared with other jobs.

Further work in progress will enable automatic control of our new scattering chamber. The experimenter will be able to request either set-pointing or end-of-run data on the four parameters of the scattering chamber.

At present, the experimenter, with four on-line ADC's at his disposal can communicate with the computer via his own teletype and CRT display. This same teletype will give him control of the scattering chamber.

10. CONCLUSIONS

The author feels that the time has come to throw away our conservatism and make a step jump into the type of control system proposed in section 5. Since initial costs should be comparable to a system with no computer, and since the proposed system offers ease in collecting large quantities of data, automatic monitoring, and all necessary hardware for closed loop

optimization, wherever studies show this to be possible, one can see the proposed system offers a lot more for the same price as the cost of a classical control system.

Those groups who do not yet have any control hardware are in the enviable position of being able to implement third generation cyclotron control. First generation control was straight forward and practical. Second generation with the appended computer has been rewarding but not spectacular. Now it is time to take full advantage of the technology which has been racing forward during the last ten years.

REFERENCES

1. Automatic Control of the Trim-coil Power Supplies at the Berkeley 88 inch Cyclotron, David R. Struthers, IEEE Trans. Nucl. Sci. NS-14, No. 3, p1044.
2. Computer Control of the Maryland Cyclotron, J. Etter, K. Jenkins, D. Nelson, Particle Accelerator Conference, Shoreham Hotel, Washington, D.C., March 1969, IEEE Transactions on Nuclear Science, Vol NS-16, No. 3, p 873.
3. Einige Grundgedanken zum SIN-Kontrollsystem, L. Besse, SIN, Zurich, Internal Report TM-13-03.
4. Computer Control of the Los Alamos Linear Accelerator, H. S. Butler, National Particle Accelerator Conference, Washington, D.C., 1967
5. Computer Control of a Linear Accelerator, H. S. Butler, R. A. Gore, D. T. VanBuren, IFAC-IFIP Symposium, Toronto 1968.
6. A Compact Data Acquisition and Control Terminal for Particle Accelerators, D. R. Machen, R. A. Gore, D. W. Weber, IEEE Trans. Nucl. Sci., Vol NS-16, No. 3, p 883, 1969
7. Control Data 1700, Autran-PIA.
8. Honeywell DDP-516, OLERT
9. IBM 1800, PROSPRO
10. Janus: A flexible approach to realtime time sharing, J. O. Kopf, P. J. Plauger, Fall Joint Computer Conference, 1968.
11. Michigan State University Time Sharing, R. Au, W. Merritt, unpublished presentation at Scientific Data Systems Users Group Meeting, Boston, May 1969.
12. Private communication, H. G. Blosser.
13. Control of Betatron Oscillations in a Cyclotron by Use of an On-Line Computer, M. D. Loesel, G. Schatz, H. Schweickert, documentation obtained directly from Karlsruhe.

FIGURE CAPTIONS

Fig. 1 Classical computer control

Fig. 2 Current concept of computer control

Fig. 3 Complexities of current computer control -

Fig. 4 Simplified control concept

Fig. 5 Some details of simplified control concept

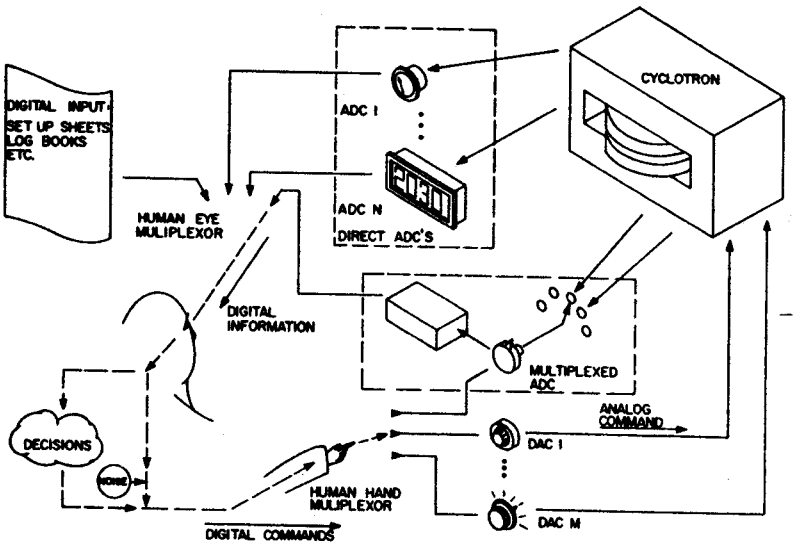

Figure 1

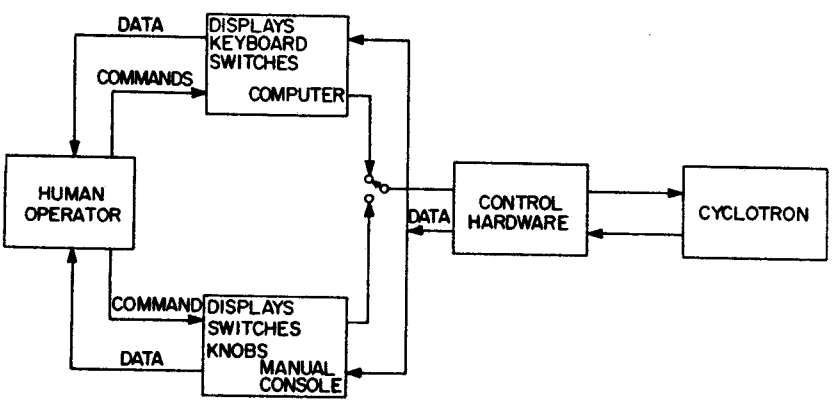

Figure 2

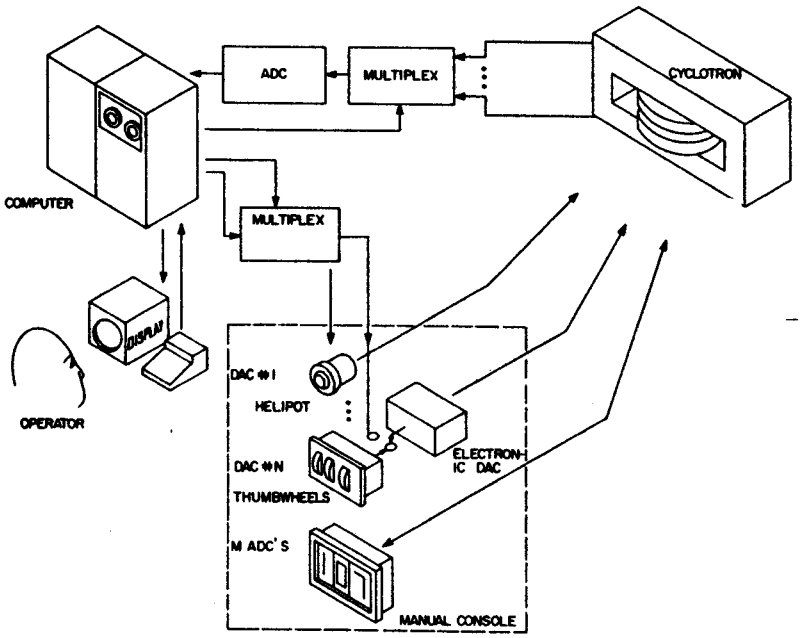

Figure 3

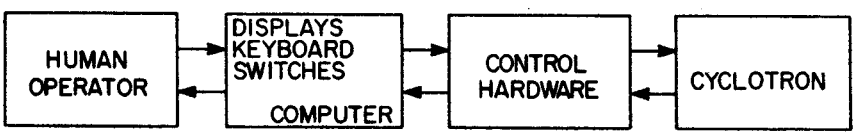

Figure 4

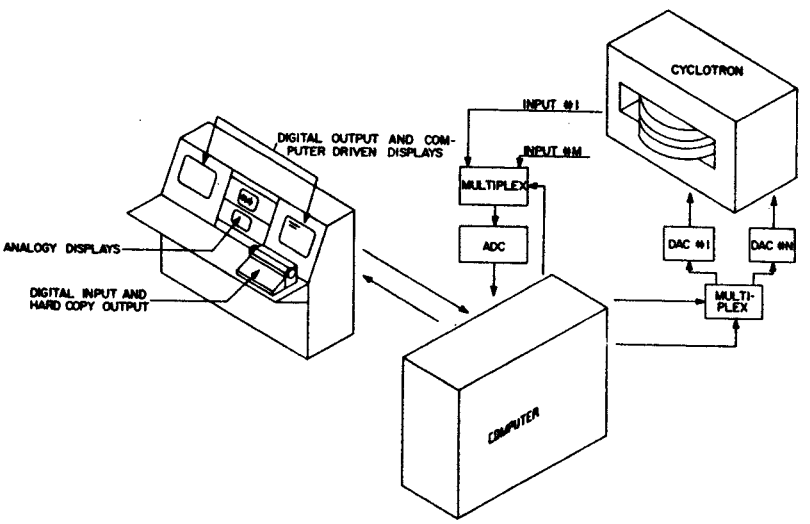
CYCLOTRON
INPUT #1
INPUT #M
DIGITAL OUTPUT AND COM-
PUTER DRIVEN DISPLAYS
MULTIPLEX
ADC
DAC #1
DAC #N
ANALOGY DISPLAYS
DIGITAL INPUT AND
HARD COPY OUTPUT
MULTI-
PLEX
COMPUTER

Figure 5

CYCLOTRON BEAM PULSER FOR PARTICLE TIME-OF-FLIGHT EXPERIMENTS*

W. P. Johnson†, H. G. Blosser and P. Sigg
Michigan State University
East Lansing, Michigan
U.S.A.

*Work supported in part by the National Science Foundation.
†Now at the University of Maryland

ABSTRACT

The energy resolution in time-of-flight experiments performed on a cyclotron is limited by the reaction product flight times of approximately 60 nsec associated with the beam microstructure. A scheme for eliminating N-1 out of every N micropulses from the external beam has been developed for the Michigan State University Cyclotron. The internal beam is stopped on a collimator on the first one-half turn by applying a DC voltage to a radially deflecting plate located in the dee between the ion source and collimator. A 60 nsec wide pulse, synchronized with the dee voltage, but with $1/N^{th}$ the repetition rate cancels the DC deflection voltage allowing single micropulses through the collimator. Beam currents of 1 μamp time-average have been obtained with pulse widths of 0.4 nsec at one-tenth the RF repetition rate. By removing a set of phase selecting slits inside the cyclotron, time-average currents of 10 μamps have been obtained at 10% duty cycle with pulse-widths of approximately 1.5 nsec.

1. INTRODUCTION

Time-of-flight experiments require very short bursts of particles with long waiting periods between bursts. Cyclotrons produce such short beam pulses, but the repetition rates, typically on the order of 50-100 nsec, are often too high. It is possible to eliminate some of the bursts by sweeping the beam across a collimator synchronously with the orbital frequency in such a manner that only one out of N micropulses pass through the collimator and reach the experimenter's target. This can be done in two ways: by blocking the external beam or by stopping the beam near the ion source. The former has the great disadvantage that the beam thrown away activates whatever it hits and produces annoying background for the experimenter and a health hazard for the accelerator operations group.

At the Michigan State University Cyclotron, N-1 out of N particle micropulses are stopped by a collimator on the first one-half turn by applying a DC voltage to a radially deflecting plate located in the dee between ion source and collimator (see Fig. 1). A 60 nsec wide pulse, synchronized with the dee voltage but with $1/N^{th}$ the repetition rate, cancels the DC deflection voltage allowing single microbursts of particles through the collimator. Eliminating unwanted pulses near the cyclotron center greatly reduces the internal circulating beam current for a given peak current on target.

2. ELECTRONICS

A block diagram of the pulser electronics which consists of a frequency divider, variable delay line, pulse generator, amplifier, and

assorted pulse-amplitude regulators is shown in Figure 2. While the frequency divider used at present is a divide-by-ten fast pre-scaler, any type of divider can be used provided the time jitter in the output pulse is smaller than a few nanoseconds. The variable delay serves to adjust the position of the pulse relative to the dee voltage so that the DC voltage on the deflection plates is cancelled when the beam is passing through.

Signals from the delay trigger a pulse generator[2] that delivers a 40 volt, 50 nanosecond wide pulse, to a preamplifier. The preamplifier (Figure 3) is a variable gain untuned amplifier feeding an inverting 200 ohm to 50 ohm transmission-line-type transformer. The gain is varied by adjusting the grid bias; this is used as the pulse amplitude regulating element.

The distributed amplifier in the final stage (Fig. 4) operates with 10 parallel 4CW2000A tubes interconnected by lumped-constant delay lines and is capable of delivering 20 amperes into a 75 ohm transmission line. Because the deflection plates represent an open-circuited load to the transmission line, reflection produces a 3000 volt pulse at the plates. The grid and plate delay lines are built from a design used at the Princeton-Pennsylvania Accelerator.[3] To simplify construction and to improve symmetry, each delay line consists of two parallel lines of twice the desired impedances: 100 ohm for grid line and 150 ohms for the plate. The reflected pulse from the deflection plates is dissapated in the back terminating resistor of the anode line.

Figure 5 shows the feedback circuit that varies the grid of the preamplifier. Pulses from the anode are rectified by a peak detector and filtered by a 150 Hz low-pass filter. It was found that most of the 360 Hz ripple on the output comes from the distributed amplifier anode power supply. Thus,

by summing a ripple signal from the anode power supply with the signal from the pulser output, stable, ripple-free pulses are produced.

The pulser is connected to the deflection plates through a 75 ohm coaxial cable inside the dee stem and a 75 ohm strip-line lying along the inside bottom of the dee. The positive DC deflecting voltage is applied to the same line through an RC de-coupling network.

3. RESULTS

Tests on the operation of the pulser were first made with the dees removed from the cyclotron. The 14 nsec risetime pulses, observed on a sampling oscilloscopes showed no appreciable ringing or overshoot. With a pulse width of 60 nsec (FWHM), the top of the pulse was flat to within a few percent for the period of time that the beam spends between the deflection plates. Since the beam responds to the time-average electric field in the gap, flatness of the pulse is not essential. However, any "rounding" of this pulse does make phasing relative to the dee voltage more critical.

Beam tests with the pulser were made using a standard time-of-flight (TOF) electronic set up. Gamma rays produced when the beam strikes a target are detected by a fast scintillator. The resultant signal was used as the "start" pulse for a time-to-amplitude converter (TAC). The stop signal was the same pulse used to trigger the pulse generator. The output from the TAC was shaped and displayed on a multi-channel analyzer. A spectrum was obtained that showed the time distribution of particles striking the target. The time resolution of the TOF electronics was sufficient to indicate particle pulse widths on target of 0.2 nsec (corresponding to approximately

a 1^{o} phase width). Figure 6 shows a TOF spectrum taken with an external proton beam. The lower figure gives data taken with the pulser off, showing gamma rays produced in the target at sharply defined times determined by the orbital frequency of acceleration. The spectrum in the upper half of Figure 6 taken with the beam pulser on, clearly indicates that proton pulses have been effectively removed. The pulser was being operated at one-tenth the RF frequency and so nine out of every ten beam pulses were eliminated. (Only a portion of the spectrum has been shown in Fig. 6 to emphasize the clean removal of unwanted beam pulses.)

Provided the cyclotron is setup carefully to optimize extraction efficiency, operation of this beam pulser is stable, often running for periods of 2 hours without any adjustment of amplitude or delay. Preliminary measurements of the effect of the pulser on the phase width of the beam indicated no distortion of the particle pulse to within the resolution of the TOF electronics (0.4 nsec FWHM phase width with and without the pulser). Beam currents of 1 μamp time-average have been obtained with the 0.4 nsec pulse width and one-tenth the RF repetition rate. By removing a set of phase selecting slits inside the cyclotron, time-average currents of 10 μamps were measured with pulse widths of approximately 1.5 nsec.

ACKNOWLEDGMENTS

The authors wish to express their thanks to Drs. A. Galonsky and R. St. Onge for the use of some of their time-of-flight data. A special acknowledge is given to W. Harder who constructed a major portion of the pulser electronics.

REFERENCES

[1]General Radio, Model 1156-A, West Concord, Mass., U.S.A.

[2]Data Pulse, Model 108, Culver City, Calif., U.S.A.

[3]Private communication from Mr. Jack Riedel, Princeton University, Princeton, New Jersey, U.S.A. See also W. Gagnon and B. Smith, IEEE Trans. Nucl. Sci. NS-16, No. 3, 551 (1969).

FIGURES

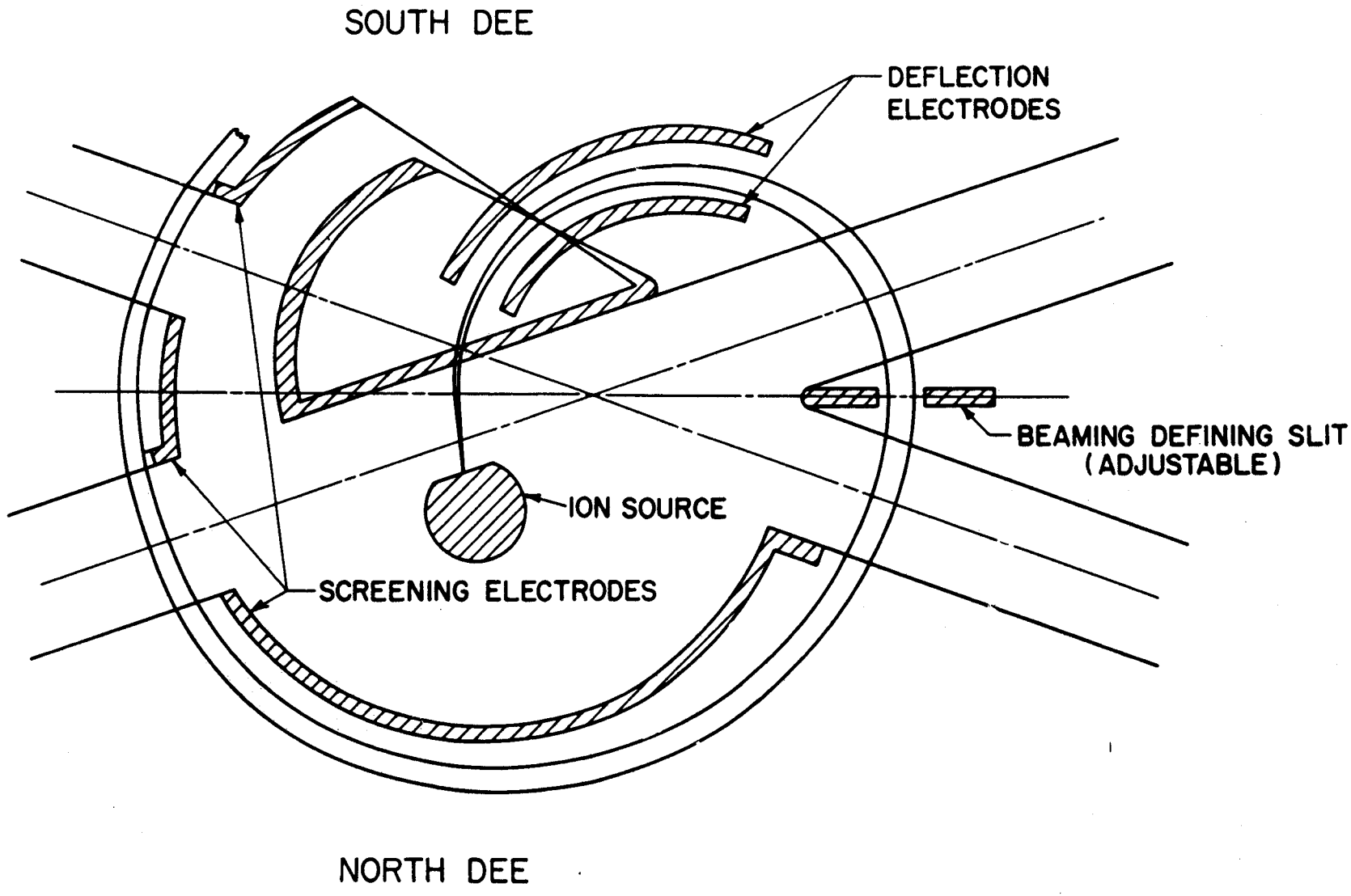
SOUTH DEE
DEFLECTION ELECTRODES
BEAMING DEFINING SLIT (ADJUSTABLE)
ION SOURCE
SCREENING ELECTRODES
NORTH DEE

Fig. 1

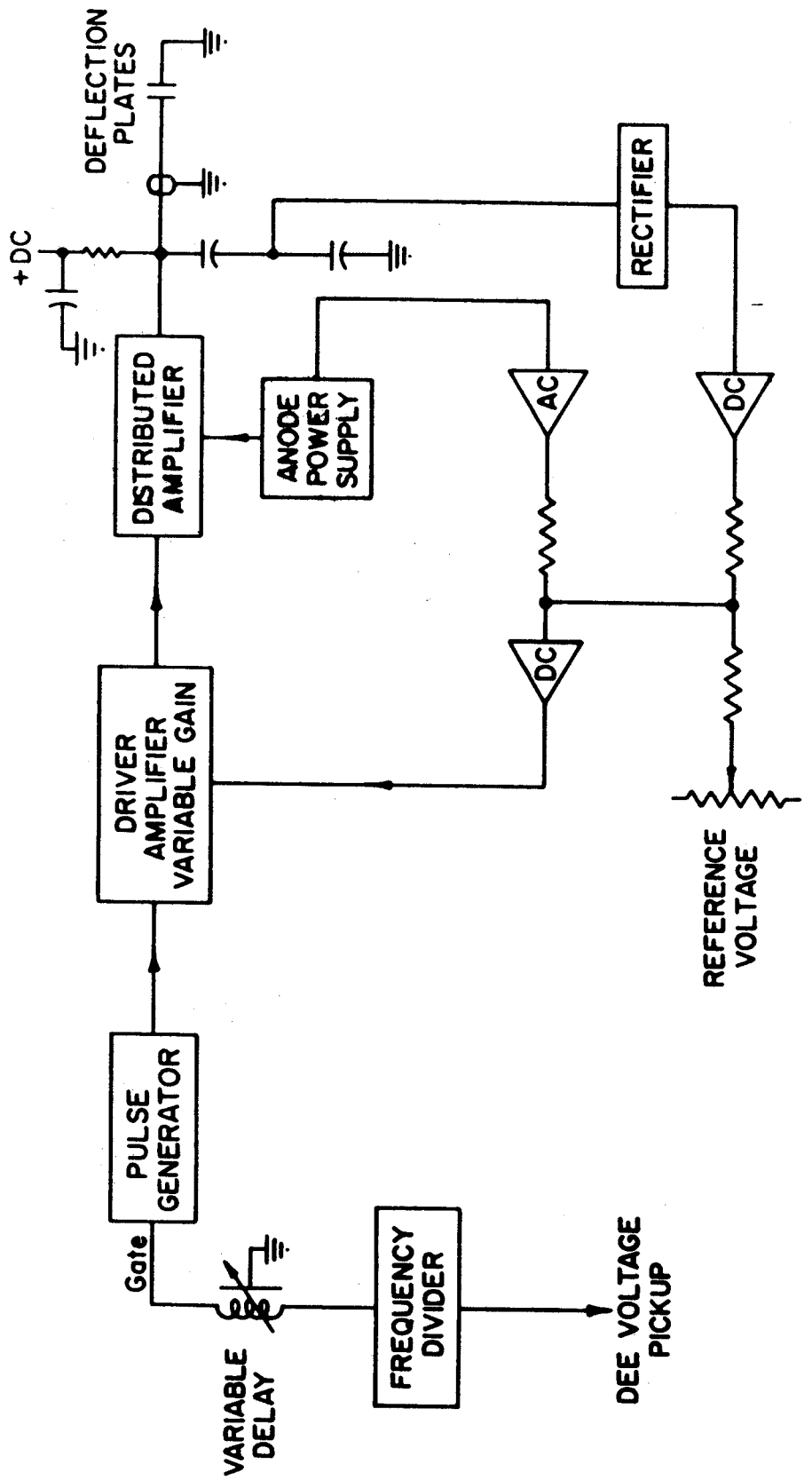
DEFLECTION PLATES
+DC
RECTIFIER
DISTRIBUTED AMPLIFIER
ANODE POWER SUPPLY
AC
DC
DC
DRIVER AMPLIFIER VARIABLE GAIN
REFERENCE VOLTAGE
PULSE GENERATOR
Gate
VARIABLE DELAY
FREQUENCY DIVIDER
DEE VOLTAGE PICKUP

Fig. 2

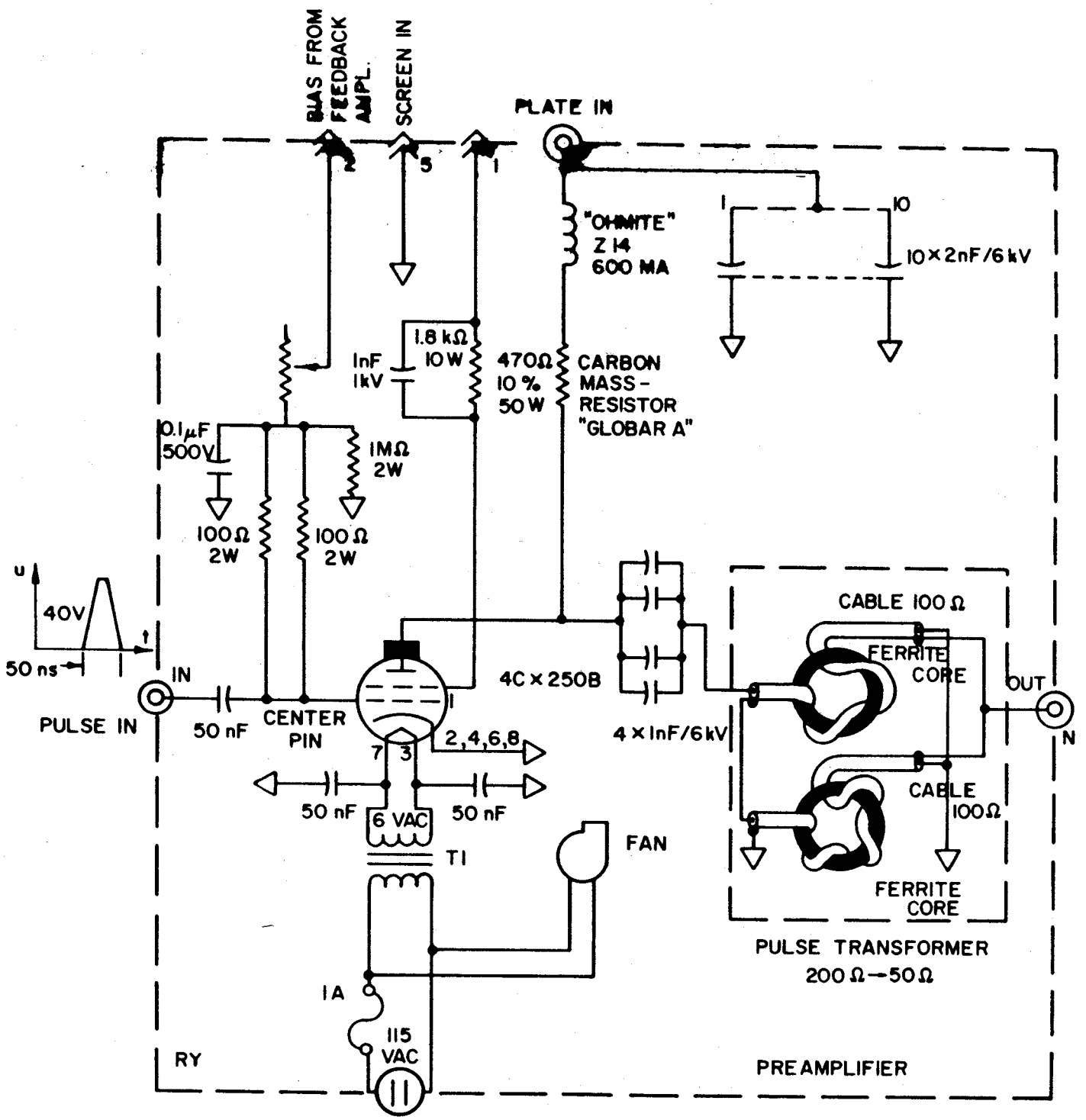
BIAS FROM FEEDBACK AMPL.
SCREEN IN
PLATE IN
2
5
1
"OHMITE" Z 14 600 MA
1
10
10×2nF/6kV
1.8 kΩ 10W
1nF 1kV
470Ω 10% 50W
CARBON MASS-RESISTOR "GLOBAR A"
0.1μF 500V
1MΩ 2W
100Ω 2W
100Ω 2W
u
40V
t
50 ns
IN
PULSE IN
50 nF
CENTER PIN
4C×250B
1
7
3
2,4,6,8
50 nF
6 VAC
50 nF
T1
FAN
4×1nF/6kV
CABLE 100Ω
FERRITE CORE
OUT
N
CABLE 100Ω
FERRITE CORE
PULSE TRANSFORMER 200Ω→50Ω
1A
115 VAC
RY
PREAMPLIFIER

Fig. 3

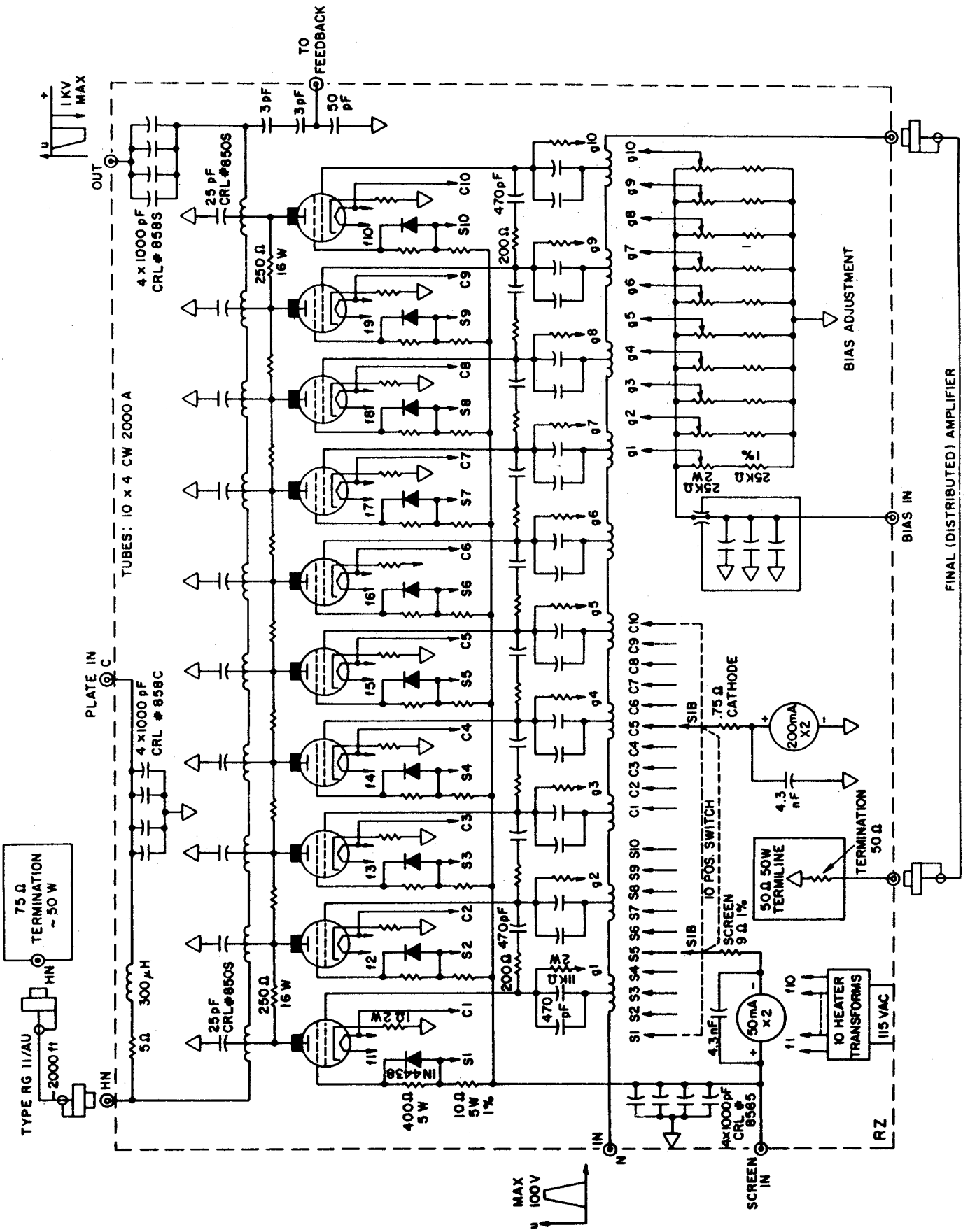
TUBES: 10 x 4 CW 2000 A
FINAL (DISTRIBUTED) AMPLIFIER
BIAS ADJUSTMENT
BIAS IN
PLATE IN
SCREEN IN
OUT
TO FEEDBACK
1KV MAX
MAX 100V
75 Ω TERMINATION ~50 W
TYPE RG 11/AU
2000 ft
300 μH
5Ω
4 x 1000 pF CRL # 858S
4 x 1000 pF CRL # 858C
4 x 1000 pF CRL # 8565
25 pF CRL # 850S
250 Ω 16 W
200 Ω 470 pF
400Ω 5W
10Ω 5W 1%
IN4438
10 POS. SWITCH
SCREEN 9Ω 1%
.75Ω CATHODE
50mA X2
200mA X2
4.3 nF
50Ω 50W TERMILINE
TERMINATION 50Ω
10 HEATER TRANSFORMS
115 VAC
25KΩ 2W P
RZ

Fig. 4
197

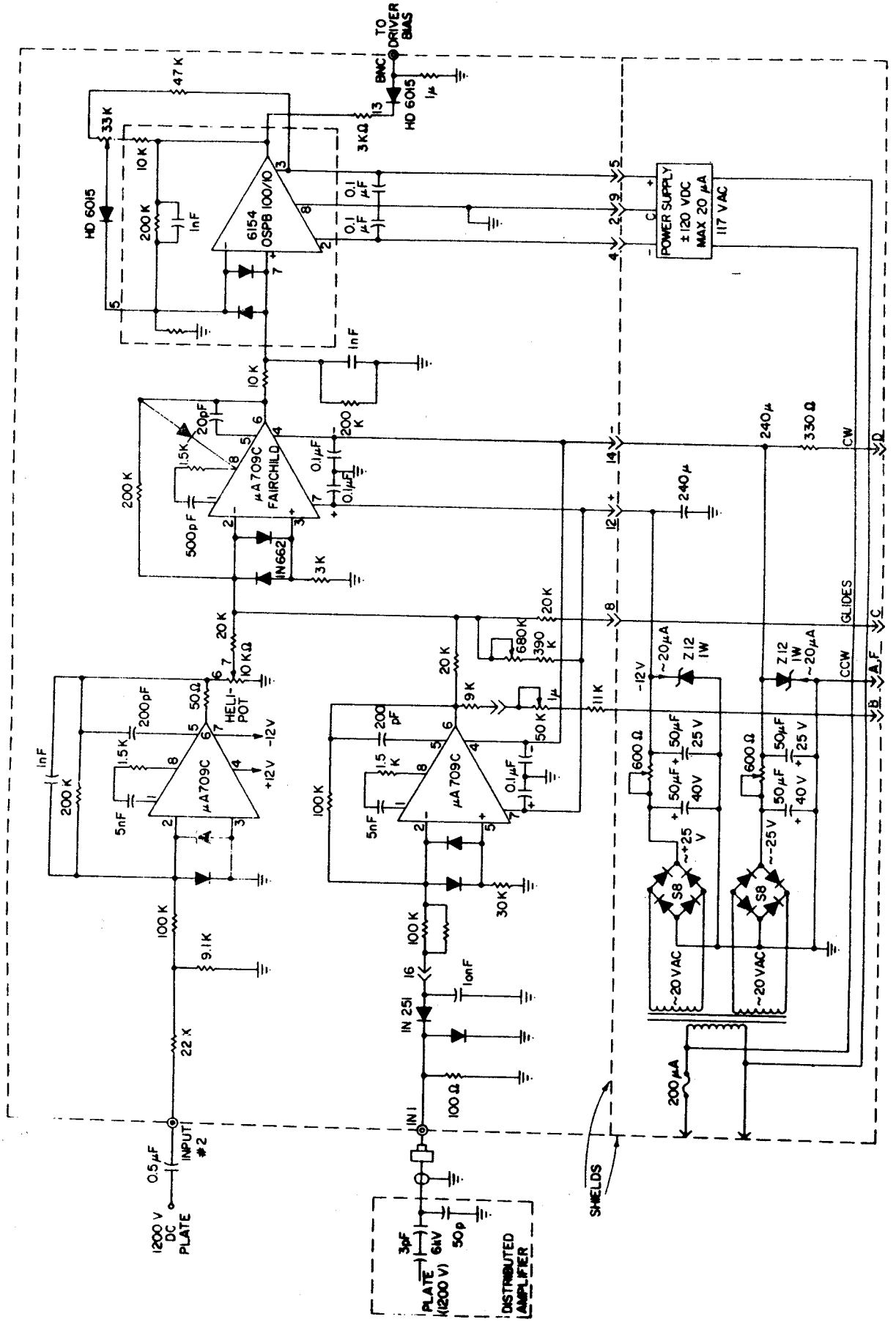
TO DRIVER BIAS
BNC
HD 6015
1μ
47 K
33 K
10 K
200 K
1nF
3KΩ
6154 OSPB 100/10
0.1 μF
POWER SUPPLY ± 120 VDC MAX 20 μA
117 VAC
20pF
1.5K
μA 709C FAIRCHILD
0.1μF
500pF
IN662
3K
20 K
10 KΩ
HELI-POT
680K
390 K
50 K
9K
11K
240μ
330 Ω
CW
CCW
GLIDES
-12V
Z 12 1W ~20μA
600 Ω
50μF 25 V
50μF 40V
~+25 V
~-25 V
S8
~20 VAC
200μA
200pF
50Ω
5nF
100 K
9.1K
22 K
30K
IN 251
10nF
100 Ω
IN 1
INPUT #2
0.5 μF
1200 V DC PLATE
3pF
50p
PLATE (1200 V)
DISTRIBUTED AMPLIFIER
SHIELDS

Fig. 5

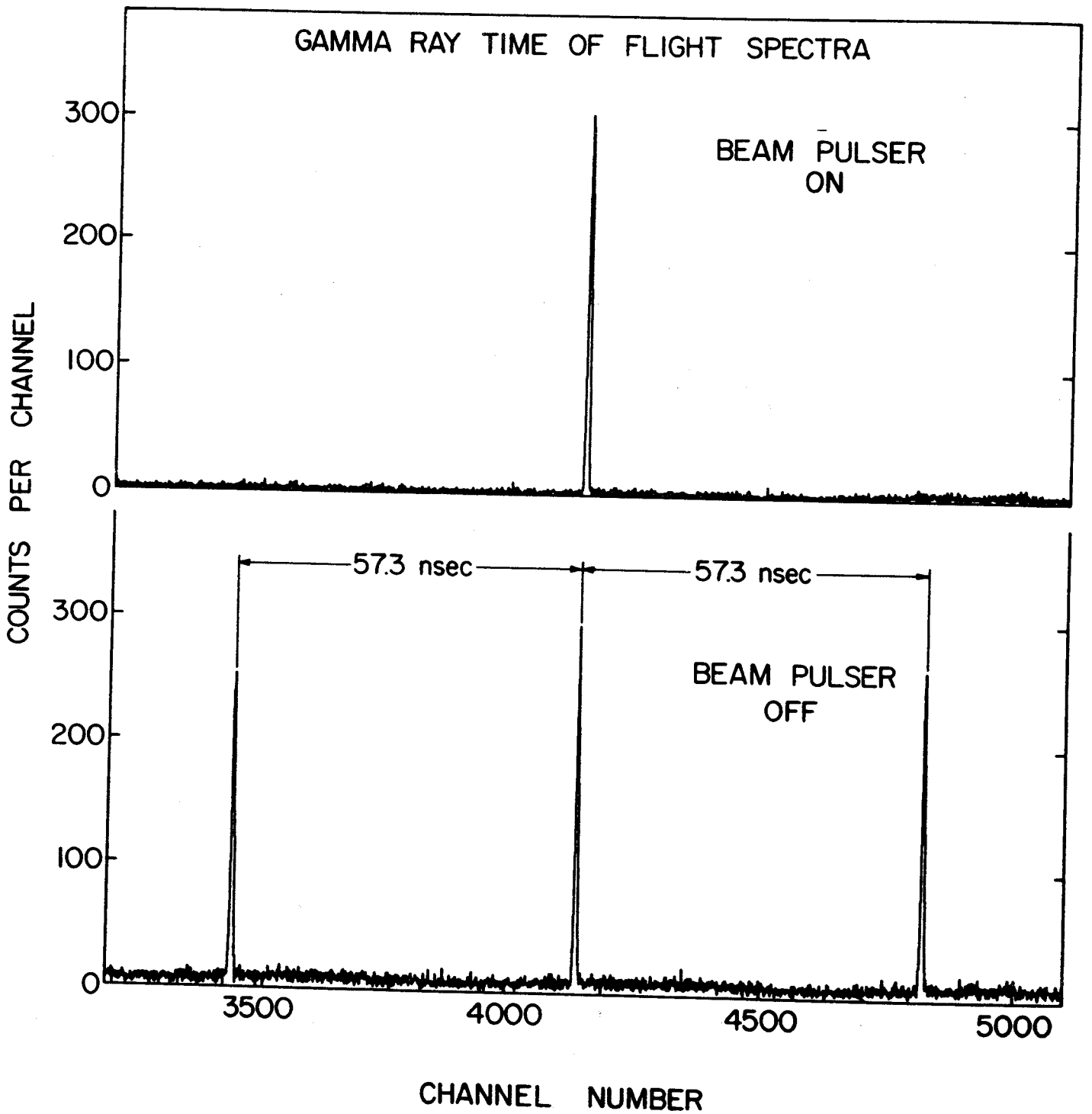
GAMMA RAY TIME OF FLIGHT SPECTRA
BEAM PULSER ON
BEAM PULSER OFF
57.3 nsec
57.3 nsec
COUNTS PER CHANNEL
CHANNEL NUMBER
0
100
200
300
3500
4000
4500
5000

Proposed Michigan State University Transuranic Accelerator Facility

H. Blosser, M. M. Gordon and D. A. Johnson
Cyclotron Laboratory, Michigan State University
East Lansing, Michigan 48823, USA

ABSTRACT

This paper briefly describes the design of a versatile facility for accelerating ions of every element to energies sufficient to produce nuclear reactions on any target. The design utilizes a large six sector ring cyclotron with ∿40 kilogauss-meter average bending capability for the main acceleration. The present MSU cyclotron would be the light ion (p,d,^{3}He,^{4}He) injector. A number of possible heavy ion injectors are discussed, the field trimming problem is reviewed and initial studies of resonance transitions are described.

1. INTRODUCTION

The possible existence of "islands" of nuclear stability well beyond the region of presently known nuclei is a topic of great current interest to physicists and chemists.[1] The most likely production processes for such super heavy nuclei appear to be transfer reactions between a massive projectile and a massive target, such as $^{238}U(^{238}U, ^{178}Yb)^{298}114$, etc. Due to the large coulomb repulsion, such a reaction will only take place at bombarding energies in the range of 6-9 MeV/nucleon which is well beyond the capability of present accelerators (assuming realistic values for the ion charge state). A number of groups are hence currently planning accelerators to produce the desired energetic ions—several of these are described in other papers at this session.

The major difference between the proposed MSU facility and those envisaged by other cyclotron groups is the much larger final stage cyclotron (40.7 kG-m vs. 29.4, 27.0, 26.5 etc.). This large final stage cyclotron can produce the required energy using ions in a much lower charge state (for Uranium 24+ is adequate vs. 33, 36, 45 etc.). The costly heavy ion injector can therefore be smaller leading to a system which we believe

to be less expensive in total and with a very elegant light ion capability as an important bonus (protons up to 600 MeV, deuterons to 360 MeV, etc.). The MSU plans also give very serious consideration to use of a third cyclotron as the heavy ion injector whereas other U.S. groups plan to employ a large VandeGraff for this purpose.

A brief paper such as this cannot give a complete description of the facility—for this, interested readers are referred to the MSU proposal document.[2] In this paper we briefly discuss several of the crucial problems of the design, namely: (a) the compatibility constraints of such a multi-accelerator system, (b) the field trimming requirements and limitations and (c) the tolerances associated with resonance transitions.

2. SYSTEM CONSTRAINTS

If all cyclotrons in a multi-cyclotron system are operated at the same rf frequency numerous advantages accrue, namely: (a) phasing problems are minimized, (b) all buckets are filled, (c) space charge effects are minimized, (d) harmonic jumps occur at the same point in all the accelerators, (e) orbit scaling is maximized, etc. Given the single rf frequency, the rotation frequency of the particles in any of the cyclotrons must be an integer submultiple of the rf and one can proceed to draw the very useful dimensionless diagram given in Fig. 1 in which possible

FIGURE 1

isochronous magnetic fields are plotted vs. radius. The various harmonics give the curves labeled n=1, 2, 3, 6, 8...etc. Any cyclotron in the system must operate on one or the other of these isochronous field curves—at any transition point from one cyclotron to the next the harmonic number can change if desired as can the charge state of the ion. Such a transition does not however involve an energy or velocity change and if the field and radius are plotted on log scales as in Fig. 1 then lines of constant energy are straight and slant upward to the left. The energy scale for these curves is given in $m_o c^2$ units by the heavy straight line slanting up to the right in the Fig. Any transition from one cyclotron to the next must go along one of the constant energy lines and the ratio of radii in the two cyclotrons is hence completely determined by the selection of the harmonic number and is independent of field or charge state. Given a particular harmonic curve the magnetic field required to accelerate some selected ion in a specified charge state is obtained by reading the dimensionless field value from the graph

and then converting to real units by inserting the A and Z of the ion into the expression for the field unit. The rf frequency appears in both field and radius units and a higher frequency is seen to linearly increase required fields and reciprocally decrease radii. The scale at the top of the graph gives radius in real units (meters) for a frequency of 18.8 MHz which is the maximum energy frequency for the proposed MSU facility.

Using the diagram, possible injection and radius options for the MSU proposal can be readily understood. We first somewhat arbitrarily select a trial Z/A of 0.1 for Uranium and making allowance for flutter adequate for any ion we select harmonic 18 near the bottom of the diagram for acceleration of these ions. On this harmonic we reach the desired energy of 8.5 MeV/nucleon at a radius of 2.3 cyc. units (or 6.0 meters for f=18.8 MHz with a required field of ∿7 kilogauss average or 17 kilogauss peak). Fixing the maximum radius for the final cyclotron at this point and moving up the right hand vertical dashed line, r_f, we see that n=3 is the highest usable harmonic and for Z/A=1 the required magnetic field at 18.8 MHz is nearly the same as for 24/238 on n=18. (The protons and Uranium ions hence both require about the same magnet power supply capacity.) We wish to use the present cyclotron with r_{max}=70 cm as the proton injector and we can accelerate protons on either first or second harmonic in this cyclotron out to point $_1A$ or $_2A$. In either case the transfer to the ring must go along the diagonal constant energy direction as indicated by the heavy double lines. Proton injection radii for the ring of 2.2m or 1.1m then result for the two cases and are indicated by the two heavy dashed lines $_1r_i$ and $_2r_i$ in the figure. These two radius lines intersect the n=18 field line at energies of 1.0 and 0.3 MeV/nucleon which (not accidentally) are good energies for producing the 24+ charge state in a gas or foil respectively.

The 1.0 MeV/nucleon option of course requires a larger injector—two of the most interesting possibilities are indicated by the points B and C which are respectively a converted synchrocyclotron (point B almost exactly matches the parameters of the Carnegie Tech. synchrocyclotron[3] for example) or a 1 meter radius 30 kilogauss superconducting or cyrogenic cyclotron. This last option appears clearly feasible with present magnet technology[4] and is particularly valuable and appropriate for a heavy ion cyclotron where the extreme rigidity and low rotation frequency of the ions are always severe problems. (A previous MSU study

has determined coil configurations appropriate for producing the necessary field flutter.[5])

The 0.3 MeV/nucleon needed for injection radius option $_2r_i$ is much easier to obtain—possible cyclotron options are indicated by points D and E and the zigzag line indicates an FN tandem. Note also that with option E the conservative choice of a 9+ charge state is compatible with existing field technology whereas the 12+ charge state presumed for the other cyclotron options represents a modest extrapolation beyond presently proved source technology. (For any of the heavy ion cyclotron injector options we assume a positive ion source located in the terminal of a Cockcroft-Walton and injecting into the cyclotron via a Saclay type system[6]—the initial radius is thus large enough to avoid gap factor problems even on the high harmonics contemplated—also the complete source and Cockcroft-Walton assembly could be readily set up in duplicate to allow for concurrent maintainance and operation.)

Finally, it should be noted that in the discussion herein we have effectively imposed one unneccessary constraint, namely that the rf frequency for the protons is taken to be the same as for the heavy ions. For our propsal this is natural since the required maximum magnetic field comes out to be nearly the same for both protons and heavy ions even with the constraint imposed. If this were not so one would certainly be strongly inclined to lift the constraint and assume different maximum energy frequencies for the light ions and the heavy ions. Two versions of Fig. 1 would then be necessary and also harmonic relationships might have to change in order to vary the final energy over a wide range.

3. FIELD TRIMMING REQUIREMENTS

Two key questions must be answered to establish the feasibility of trimming a field for both 600 MeV protons and heavy ions, namely: (a) can the trimming be accomplished with sufficient accuracy and (b) can the trim coil power be held to a reasonable level. Model magnet studies of coil effectiveness are of course necessary to establish a firm answer to these questions—until such studies are accomplished, which is a long term process, a reasonably accurate guess as to the severity of the trimming problem can be obtained from air core coil calculations.

To perform such calculations we have constructed an assumed "iron" field, using the magnet shape shown in Fig. 2 which is a

FIGURE 2

plan view of the large cyclotron, and using fringe field data

from our small cyclotron which has the same minimum gap. We then introduce an array of air core coils and perform a least squares fit to trim the assumed iron field for proton and heavy ion operation. In these calculations the number of trimming coils is a parameter of crucial importance. If too many coils are employed, adjacent coils will frequently work against each other to achieve a minor improvement in the fit at enormous cost in kilowatts. If too few coils are used, the residual coil spacing ripple which is always left in the field becomes too large and produces excessive phase and focusing frequency excursions. After some searching a network of 44 coils spaced roughly according to turn density was selected as the best initial design configuration. This set of coils produced a fitted field for protons with closed orbit properties as shown in Fig. 3, and indicated a power requirement

FIGURE 3

of about 1 mega-watt for the complete coil network. Results for heavy ions are similar and are not shown.

A crucial feature of the Fig. 3 results are the oscillations in Q_r, Q_z, and F(E)* due to the coil structure. The focusing frequency oscillations which are typically ± 0.04 mean that "smooth" field operating points which pass close to a resonance may in fact for a real field result in large numbers of turns just on the resonance and may well therefore require a much higher degree of magnet and orbit perfection than passing briskly thru the resonance.

The F(E) oscillations imply a phase excursion of $\pm 22°$ for the design energy gain per turn. This is quite acceptable for normal sinusoidal acceleration since, as is well known,[7] the linearity of the derivitive of a sine wave over such an interval allows the effect of sliding off on one side of the wave to be compensated by a corresponding slide to the other side and, if an appropriate frequency adjustment is made, the beam energy spread is essentially identical to that in a perfectly isochronous field. In contrast if the rf were "flat-topped" by addition of a second or third harmonic such a phase excursion would be catastrophic as regards the energy homogeneity since the strong nonlinearity of the derivitive of a flat-topped wave means that the beam must remain continuously on the flat top or the energy smoothing benefit of the flat top is lost. To accomplish this with a reasonable phase interval for the beam would require a ten-fold reduction in the

*The function F(E) is defined such that $\sin \phi(E) - \sin \phi_o = F(E)/V$ where V is the energy gain per turn.

F(E) oscillations. In the absence of any realistic proposal for accomplishing such a reduction, we have omitted rf flat topping from the design.

4. RESONANCES

The relatively simple magnet shape envisaged in the proposed design leads to a high flutter which for heavy ions or low energy protons produces a $Q_z>1$. On the other hand for high energy protons Q_z drops rapidly with energy due to the rapidly increasing radial gradient of the isochronous field and as seen in Fig. 3, the integral resonance $Q_z=1$ must be passed at intermediate energy.

Guided by our experience in the existing cyclotron which passes the integral resonance $Q_r=1$ at two locations without detectable beam disturbance, we propose to establish appropriate tolerances on magnet construction to eliminate beam disturbance at the $Q_z=1$ resonance. At the same time, as a backup, we have established the existence of a simple two parameter correction for possible residual effects of the resonance.

Results of initial studies of this type on $Q_z=1$ are shown in Figs. 4 and 5 which are results of tracking of accelerated orbits

FIGURES 4 & 5

in the same magnetic field as in Fig. 3. For Fig. 4 two opposite magnets have been displaced up and down by ± 0.25 mm. The induced Z amplitude at the resonance implies that magnet mounts should be designed to hold this error to ± 0.03 mm which is quite practical with modern techniques. Fig. 5 shows that even with ± 0.25 mm magnet displacements the effect of the resonance can be largely eliminated by a simple two parameter trim coil compensation thus establishing the existence of the backup correction procedure. On the basis of these results we believe that $Q_z=1$ can be passed with no great difficulty and with beam disturbances just as small as for the now customary $Q_r=1$ transitions in smaller cyclotrons.

As expected comparable computer studies for the $Q_r+Q_z=2$ and $Q_r=Q_z$ coupling resonances indicate these to be much less severe than $Q_z=1$ and detailed results are therefore omitted.

REFERENCES

1) G. T. Seaborg and J. L. Bloom, Scientific American 220 #4, 57 (1967).

2) Proposal for a Versatile TransUranic Research Facility, Michigan State University document, May 1969.

3) F. T. Howard, ORNL-2644, 197 (1958).

4) W. Chamberlain, IEEE Trans. on Nucl. Sci. NS-16, 732 (1969).

5) R. Berg, Michigan State University document, MSUCP-14 (1963).

6) R. Beurtey and J. M. Durand, Nucl. Instr. & Meth. 57, 313 (1967).

7) H. G. Blosser and M. M. Gordon, Nucl. Instr. & Meth. 13, 115 (1961).

FIGURE CAPTIONS

Fig. 1—Generalized logarithmic graph of isochronous magnetic fields vs. radius for various harmonics n=1, 2, 3...etc. m_oc^2 = 931 MeV, f_o=rf accelerating frequency, and Z and A are charge and mass numbers for the accelerated ions. Fractional labels 1/1, 12/238 on some curves give design Z/A values for the proposed MSU facility. Straight lines slanted to the top left connect points of equal energy on the various field curves, the energy scale being as indicated on the γ-1 axis (m_oc^2 units).

Fig. 2—Plan view of proposed ring cyclotron with central region option $_1$r.

Fig. 3—Graph of energy, radial and axial focusing frequencies and phase slip integral vs. radius in the trimmed magnetic field with trim coil currents set for proton operation. With an energy of 600 keV per turn the F(E) curve gives a phase excursion of $\pm$22°.

Fig. 4—Plot of Z vs P_z on successive revolutions for an orbit accelerated trhough the Q_z=1 resonance. Two magnets 180° apart are displaced up and down by 0.01 inches respectively.

Fig. 5—Repeat of the acceleration run of Figure 4 but with the median plane correcting coil turned on and roughly optimized. (Note the change in scale relative to Figure 4.)

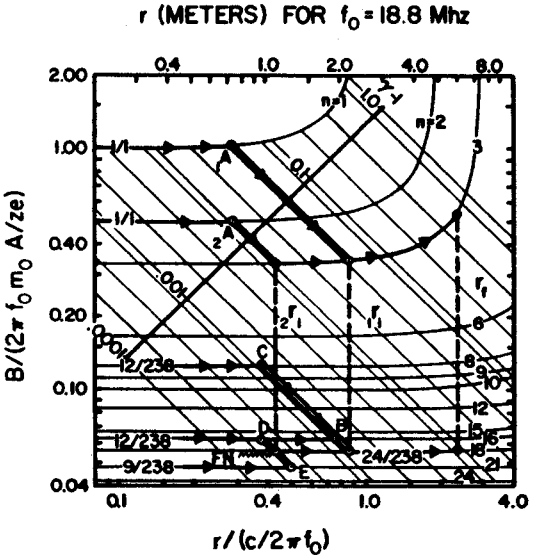
r (METERS) FOR f_0 = 18.8 Mhz
0.4
1.0
2.0
4.0
8.0
2.00
1.00
0.40
0.20
0.10
0.04
n=1
n=2
1/1
12/238
9/238
24/238
FN
0.1
0.4
1.0
4.0
$B/(2\pi f_0 m_0 A/ze)$
$r/(c/2\pi f_0)$

Fig. 1

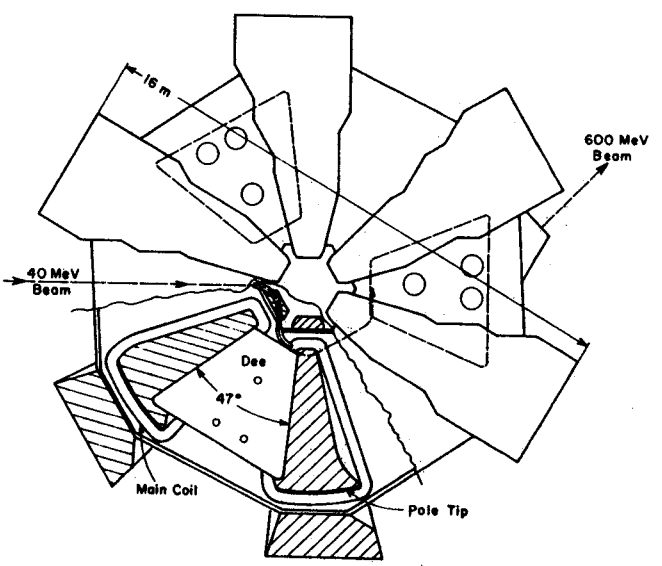
16 m
600 MeV Beam
40 MeV Beam
Dee
47°
Main Coil
Pole Tip

Fig.2

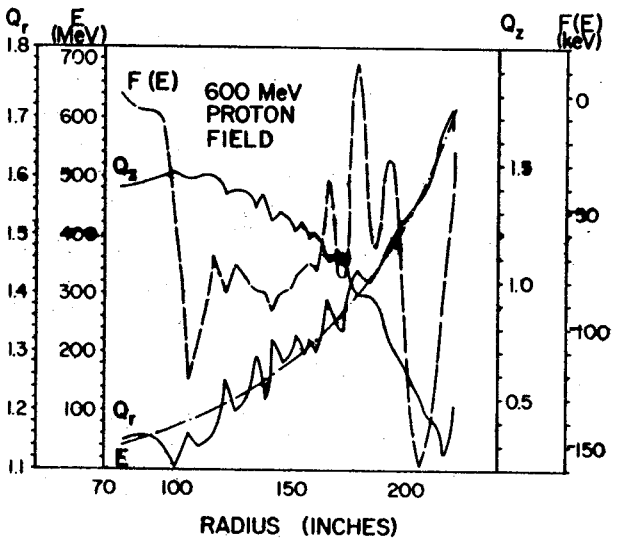
Q_r
E (MeV)
Q_z
F(E) (keV)
F (E)
600 MeV PROTON FIELD
Q_z
Q_r
E
RADIUS (INCHES)

Fig. 3

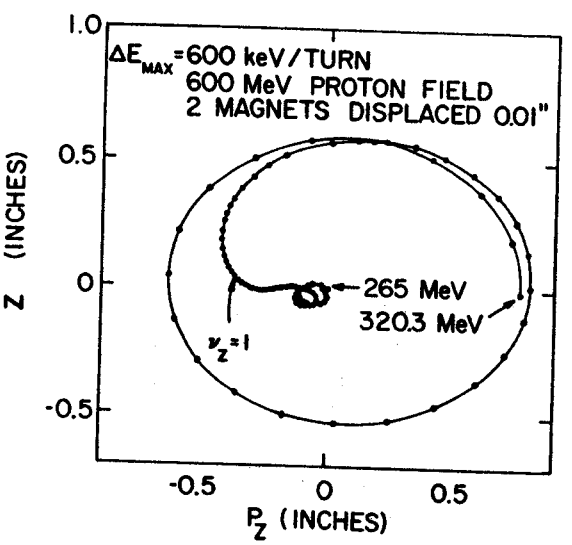
ΔE_{MAX} = 600 keV/TURN
600 MeV PROTON FIELD
2 MAGNETS DISPLACED 0.01"
265 MeV
320.3 MeV
$\nu_z = 1$
Z (INCHES)
P_Z (INCHES)

Fig. 4

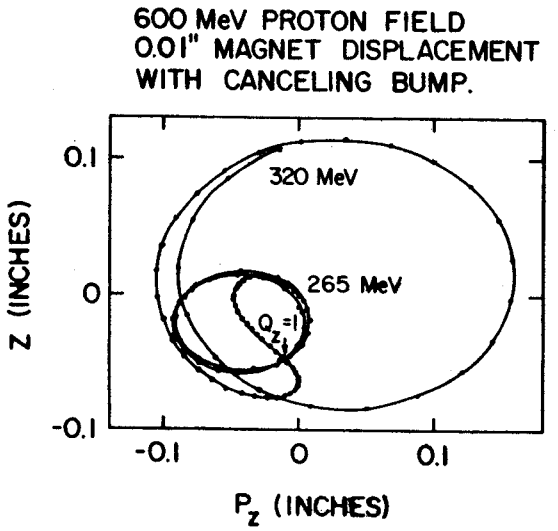
600 MeV PROTON FIELD
0.01" MAGNET DISPLACEMENT
WITH CANCELING BUMP.
320 MeV
265 MeV
$Q_z = 1$
0.1
0
-0.1
-0.1
0
0.1
Z (INCHES)
P_z (INCHES)

Fig. 5

40 MeV Proton Inelastic Scattering on ^{50}Ti, ^{51}V, and ^{52}Cr and its Microscopic Description*

B. M. Preedom, C. R. Gruhn, T.Y.T. Kuo, and C. J. Maggiore
Department of Physics, Michigan State University
East Lansing, Michigan 48823

ABSTRACT

Proton inelastic scattering from ^{50}Ti, ^{51}V, and ^{52}Cr has been measured at 40 MeV. Angular distributions have been obtained from 10° to 80° for states up to 8 MeV of excitation in ^{50}Ti and ^{52}Cr and to 4.5 MeV in ^{51}V. The cross-sections for exciting the low-lying states that have relatively simple wave functions were analysed in terms of a microscopic model using realistic nucleon-nucleon forces. Core polarization is shown to be important and it is seen that a strength obtained from the bound-state matrix elements of Kuo and Brown is adequate to describe the observed scattering. A macroscopic collective model analysis of the data is also presented.

---

*Supported in part by the National Science Foundation.

High-Resolution 5000μ Silicon Surface-Barrier Detectors

E. D. Klema, Tufts University, G. M. Crawley*, Michigan State University, G. T. Garvey and C. C. Foster, Princeton University

The advances in lithium drifting of silicon and germanium have made possible the production of thick solid-state particle detectors with good energy resolution. Surface-barrier detectors fabricated from high-resistivity n-type silicon and operated at large reverse bias voltages have the advantages of greater radiation resistance, stability of their properties with time, and the possibility of being stored at room temperature. Previously it has proved difficult to produce these detectors in thicknesses greater than 2000μ. The present paper describes the results of tests on three 5000μ silicon surface-barrier detectors whose FWHM energy resolution for protons of energy of the order of 30 MeV is of the order of 30 keV.

The techniques for the fabrication of such detectors have been described previously.[1] An important characteristic of these devices is the extremely high reverse bias voltage which can be applied without drawing excessive leakage current and without breakdown. The detectors are operated with negative bias on the gold surface and with the pulse taken off the bulk silicon at ground potential to prevent the collection of low-energy electrons on the bias lead, an effect which can limit the resolution attainable at accelerators.

The detectors are tested in our laboratory with 1 MeV electrons and 6 MeV alpha particles. The 1 MeV electrons from a Bi^{207} source enable one to measure the effective resistivity of the silicon of the detector. The number of pulses in the full-energy peak can be obtained for a run of a given duration. The variation in this number is found as a function of the reverse bias applied to the detector. As the reverse bias is increased, the number will rise, become constant as all the electrons entering the detector are recorded by it, and then decrease as the system noise increases at large reverse biases. One then can use the bias at which the counting rate becomes constant as a measure of the effective resistivity of the silicon. It is not possible to measure easily the capacitance of the detector as a function of reverse bias with high-resistivity material because of the large series resistance of the undepleted material. It is often found in practice that one obtains pulses corresponding to the full energy of the electrons at reverse biases for which the depletion depth is most probably less than the range of the electrons in silicon. The most likely explanation for this result is the possibility that charge pairs are in fact produced beyond the depletion layer, diffuse back into the high-field region, and are collected in the pulse, The very long lifetimes

of the minority carriers in silicon, of the order of several thousand microseconds, makes this effect quite probable. It is generally found that the energy resolution as measured with 1 MeV electrons and the electronic system resolution as measured with a mercury-wetted relay pulse generator correspond quite closely.

The alpha particle groups from the ground and first-excited states of transuranium nuclides such as Am^{241} provide two calibration points which are separated in energy by 42 keV and are very convenient for the calibration of systems with good energy resolution. The three detectors discussed below, which were used for the measurements with protons at Michigan State University and Princeton University, have very poor alpha resolution, of the order of 40 keV. These detectors are 7 mm in diameter and are made of 90,000 ohm cm silicon whose minority carrier lifetime is 3000 microseconds.

Tests on these detectors were carried out using the magnetically-analyzed proton beam of the Michigan State University Cyclotron. The resolution was set by the slit system of the analyzing magnets to be less than 10 keV in all cases. Targets of thin carbon and gold foils were used for these tests. The carbon foil allowed the depth of the detector to be probed by using the kinematics for the elastic and inelastic scattering from carbon to check the linearity of the detector. When the elastic protons begin to penetrate through the depleted region of the detector, they lose less energy in that region and so depart from the linear calibration line. The thickness of the detector can then be calculated from the point at which the elastic peak just remains on the linear calibration.

An example is shown in the figure below in which the proton bombarding energy was 35 MeV. At a laboratory angle of 100°, the carbon elastic peak just loses all its energy in the detector. The thickness in this case was then calculated to be 4700μ.[2)]

The maximum reverse bias applied to this detector was 1500 volts and at this point the leakage current was less than one-half microampere. At lower bias the peaks showed marked tails and double peaking, which decreased with larger bias. These tails, presumably due to change collection effects in the deep detector, were also decreased by using longer time constants in the main amplifier.

A spectrum taken at a bombarding energy of 25 MeV with the gold target to minimize kinematic broadening is shown in the figure below. The FWHM resolution of the gold peak was 31 keV. At this point the electronic noise of the system was 16 keV. Both differentiating and integrating time constants of 3 microseconds were used for this measurement.

Two detectors, one of those used at Michigan State University, and another one made from the same crystal of silicon, were tested

with the proton beam at the Princeton University Cyclotron using a natural magnesium target on a carbon backing. In these measurements data on the elastic and inelastic proton spectra were taken under conditions approximating as closely as possible those of an actual experiment. One of the spectra taken at 90° with a proton beam of 30 MeV is shown in the figure below. The overall FWHM resolution of the proton peaks is 30 keV. The various components of this observed energy resolution are as follows: energy spread due to the reaction kinematics, 18 keV; beam energy spread, 13.5 keV; electronic noise, as determined with a pulser, 12 keV; and the detector resolution, 16 keV. The bias on the detector was 2100 volts, and the differentiating and integrating time constant was 2.4 microseconds.

On the basis of the measurements described above, it seems possible to say that the present state of the art is that protons up to 30 MeV can be measured with silicon surface-barrier detectors with an energy resolution of 0.1%.

1) E. D. Klema, Nuclear Instr. and Meth. 26, 205 (1964).
2) C. F. Williamson, J. P. Boujot, and J. Picard, CEA Report R3042, July 1966.

* Work supported in part by the U.S. National Science Foundation.

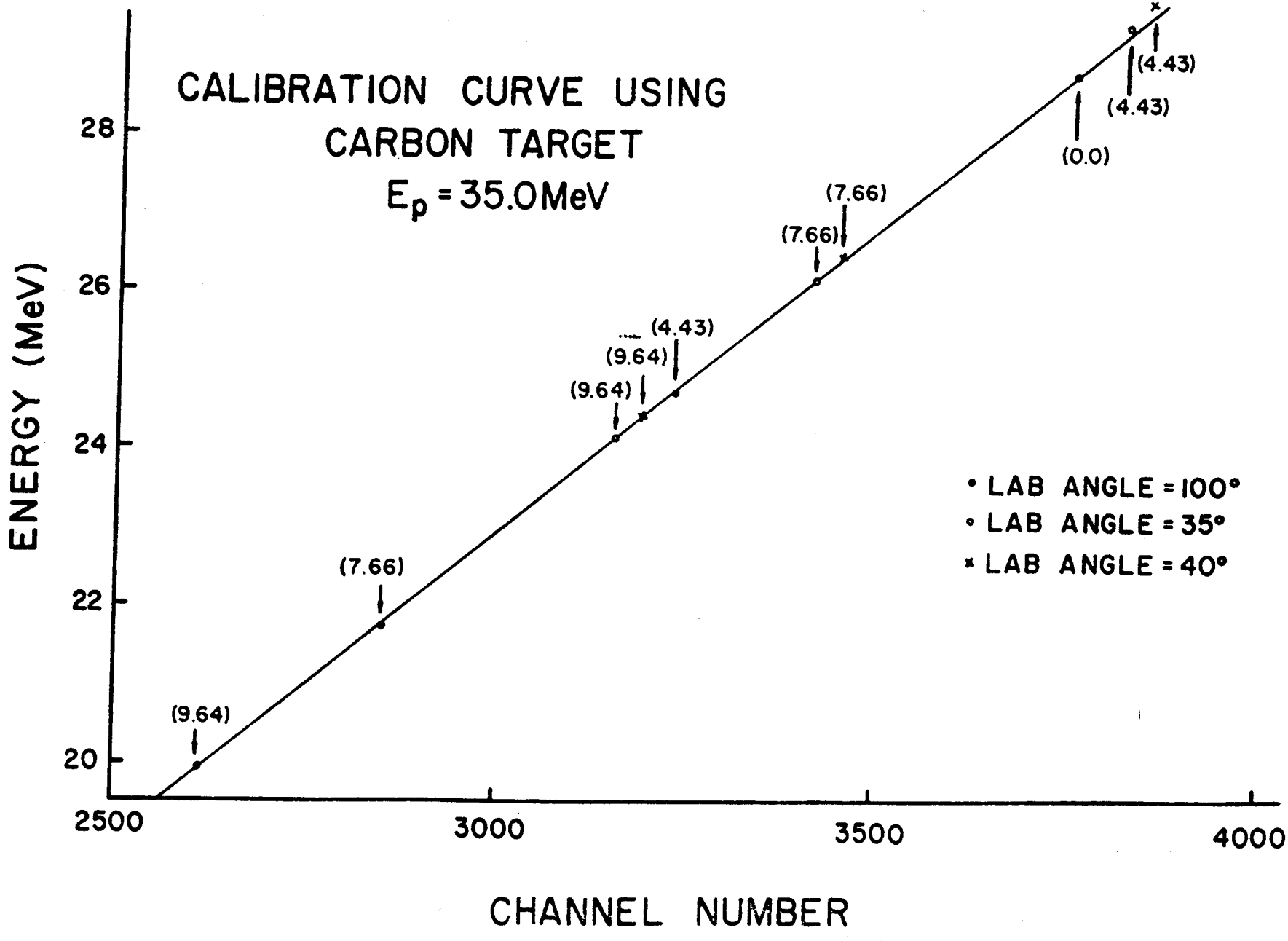
CALIBRATION CURVE USING
CARBON TARGET
E_p = 35.0MeV
ENERGY (MeV)
CHANNEL NUMBER
28
26
24
22
20
2500
3000
3500
4000
(9.64)
(7.66)
(9.64)
(9.64)
(4.43)
(7.66)
(7.66)
(0.0)
(4.43)
(4.43)
• LAB ANGLE = 100°
∘ LAB ANGLE = 35°
× LAB ANGLE = 40°

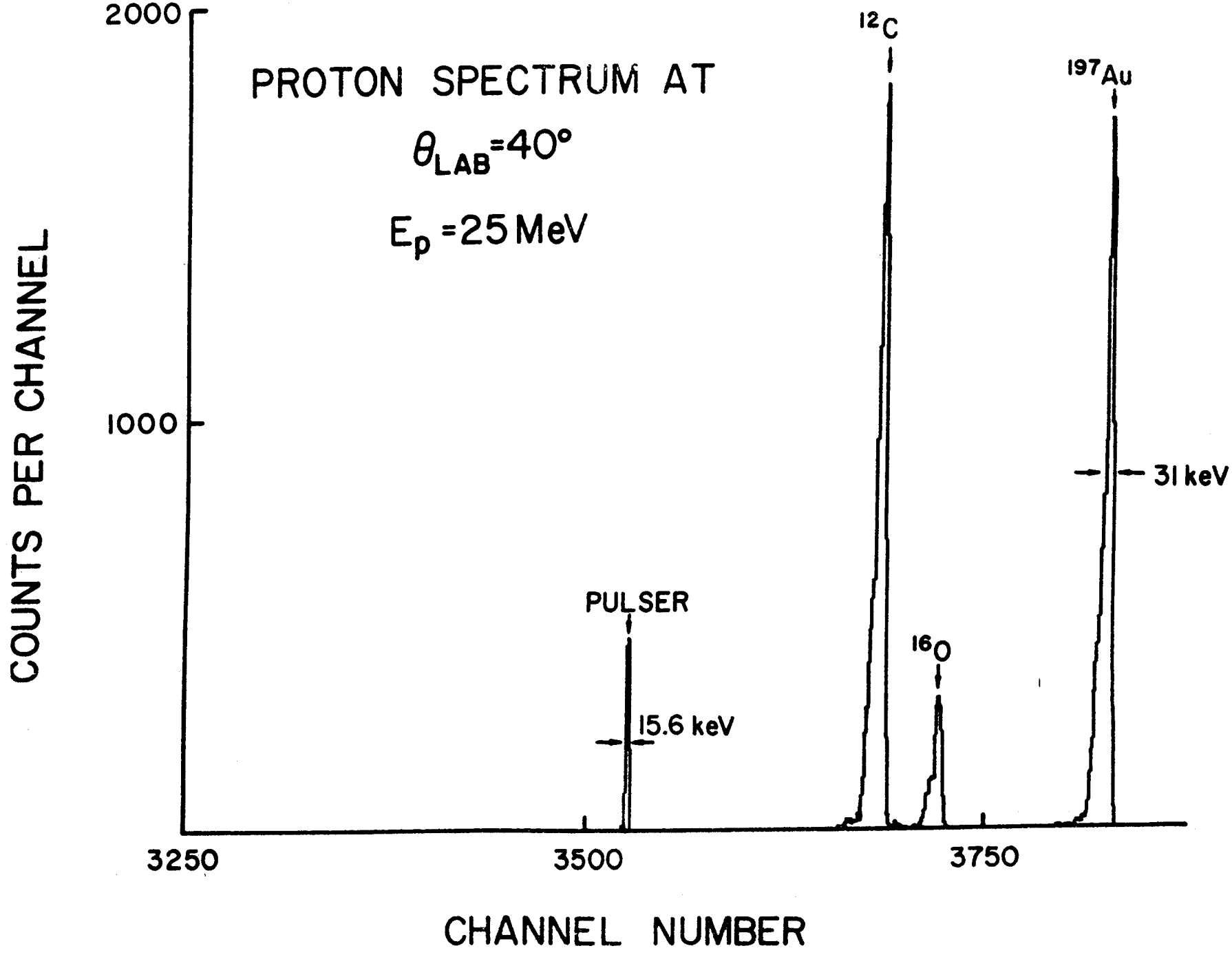
PROTON SPECTRUM AT
θ_{LAB}=40°
E_p =25 MeV
2000
1000
COUNTS PER CHANNEL
^{12}C
^{197}Au
31 keV
PULSER
15.6 keV
^{16}O
3250
3500
3750
CHANNEL NUMBER